Structural and functional aspects of RET receptor tyrosine kinase maturation, signalling and chemical inhibition

Emily May Burns

University College London

and

Cancer Research UK London Research Institute

PhD Supervisor: Neil McDonald

A thesis submitted for the degree of

Doctor of Philosophy

University College London

September 2014

Declaration

I Emily Burns confirm that the work presented in this thesis is my own. Where information has been derived from other sources, I confirm that this has been indicated in the thesis.

Abstract

The RET receptor tyrosine kinase (RTK) is crucial for embryonic and adult development of multiple organs, tissues and neurons. Gain-of-function mutations in the RET gene are found in human cancer, while loss-of-function mutations are associated with congenital anomalies of the kidney and urinary tract (CAGUT) and Hirschsprung's Disease (HSCR). Previous work has identified that some HSCR RET mutations result in a bottleneck in RET folding and a subsequent loss of RET export. This thesis presents work examining the characteristics of wild type (WT) and HSCR RET maturation, export and signalling in stably transfected mammalian cell lines. High throughput siRNA screening was used to identify components involved in WT and HSCR RET maturation and export; preliminary validation has implicated Endoplasmic Reticulum associated degradation (ERAD), autophagy and the N-glycosylation pathway.

RET is also a validated cancer target, as a driver of cancers including multiple endocrine neoplasia (MEN) 2A and B. While there are several FDA-approved RET inhibitors available, their lack of specificity and potency has resulted in high levels of off-target toxicity and low life expectancy extensions. As such, a new generation of more optimal inhibitors is required. This thesis presents the investigation of the molecular basis of RET kinase inhibition, through the elucidation of the RET kinase domain (KD) structure bound to several ATP-competitive chemical inhibitors that are known to inhibit RET *in vitro*. Preliminary development of an updated RET pharmacophore is described, defining key residue interactions and combining observations with biochemical and thermal stability data.

Acknowledgement

I am eternally grateful to every member of the McDonald Laboratory, with whom I have thoroughly enjoyed spending the last four years. Thank you Neil, for supporting and challenging me, and for your constant enthusiasm throughout the project. Thank you Phil, for teaching me with ceaseless patience. Thank you Andy, for the long nights at the synchrotron and your positive guidance through every aspect of crystallography. Thank you Svend, for all of your work that has heavily influenced my project. This project would not have been possible without the efforts of Rachael Instrell, Ming Jiang and Becky Saunders from the HTS laboratory - thank you. A special thanks to Mike Howell, for refreshingly frank advice.

To my friends at the LRI: you have kept me working and smiling, thank you!

My family and friends, thank you for your unwavering support throughout the last four years. Thank you for lending your ear, making me laugh and making life outside of the laboratory so satisfying.

Mum and dad, thank you for everything.

Table of Contents

Table of figures

List of tables

Abbreviations

4-PBA	4-Phenylbutyric acid
DAPI	4',6-diamidino-2-phenylindole
AMPPNP	5'-Adenylylimidodiphosphate
ATF6	Activating transcription factor 6
A-loop	Activation loop
ATP	Adenosine 5'-triphosphate
ADP	Adenosine diphosphate
AMP	Adenosine monophosphate
APE motif	Alanine-Proline-Glutamate motif
N-lobe	Amino-terminal lobe
ARTN	Artemin
DFG motif	Aspartate-Phenylalanine-Glycine motif
AURKA	Aurora kinase A
ATG	Autophagy-related protein
BiP	Binding immunoglobulin protein
BSA	Bovine serum albumin
CHIP	C-terminus of Hsc70 Interacting Protein
CLD	Cadherin-like domain
Cadherin	Calcium-dependent adhesion
CNX	Calnexin
CALR	Calreticulin
C-lobe	Carboxy-terminal lobe
Cbl	Casitas B-lineage Lymphoma
C-spine	Catalytic spine
ΔTm	Change in melting temperature
CMA	Chaperone-mediated autophagy
CMML	Chronic myelomonocytic leukaemia
CCV	Clathrin coated vesicle
COP	Coat protein complex
CAKUT	Congenital anomalies of kidney and urinary tract

COPS6	COP9 signalosome subunit 6
cAMP	Cyclic adenosine monophosphate
CypB	Cyclophilin B
CRD	Cysteine-rich domain
CFTR	Cystic Fibrosis Transmembrane Regulator
DSF	Differential scanning fluorimetry
DDOST	Dolichyl-diphosphooligosaccharide-protein glycosyltransferase
DMEM	Dulbecco's modified eagle medium
EE	Early endosome
EM	Electron microscopy
ER	Endoplasmic reticulum
ERAD	Endoplasmic reticulum associated degradation
ERLEC1	Endoplasmic reticulum lectin 1
ERp44	Endoplasmic Reticulum Protein 44
Erp	Endoplasmic reticulum resident protein
ERN1	Endoplasmic reticulum to nucleus signalling 1
ERGIC	Endoplasmic-reticulum-golgi intermediate compartment
ESCRT	Endosomal sorting complexes required for transport
ET-3	Endothelin 3
EDNRB	Endothelin receptor B
ECE1	Endothelin-converting enzyme 1
EphR	Ephrin receptor
EGFR	Epidermal growth factor receptor
EDEM	ER degradation enhancer, mannosidase alpha-like
ERAA	ER-associated autophagy
ERAD	ER-associated degradation
ERQC	ER-associated quality control
EC	Extracellular cadherin
ECD	Extracellular domain
ERK	Extracellular signal-related kinase
FMTC	Familial medullary thyroid carcinoma
FBS	Fetal Bovine Serum
FGFR	Fibroblast growth factor receptor
FACS	Fluorescence-activated cell sorting

GABARAP	GABA-A receptor associated protein
Gal	Galactose
GFL	GDNF family ligand
GFRα	GDNF family receptor alpha
GDNF	Glial cell-line derived neurotrophic factor
GST	Glutathione S-transferase
GRL	Glycine-rich loop
GTP	Guanosine 5'-triphosphate
IC_{50}	Half maximal inhibitory concentration
Hsc70	Heat shock cognate 70
Hsp90	Heat shock protein 90
HSCR	Hirschsprung's disease
hERG	Human Ether-a-go-go-Related Gene
HYOU1	Hypoxia up-regulated 1
IP3R	Inositol 1,4,5-triphosphate receptor
IR	Insulin receptor
IGFR	Insulin-like growth factor receptor
ICD	Intracellular domain
ILV	Intraluminal vesicle
JAK	Janus kinase
JM	Juxtamembrane
KD	Kinase domain
LE	Late endosome
LMAN1	Lectin, mannose-binding 1
LRRK2	Leucine-rich repeat kinase 2
LC3	Light chain 3
LAMP	Lysosomal associated membrane protein 2
M-CSFR	Macrophage colony stimulating factor receptor
mTOR	Mammalian target of rapamycin
MRH	Mannose-6-phosphate receptor homology
MAN1B1	Mannosidase, alpha, class1B, member 1
MTC	Medullary thyroid carcinoma
Tm	Melting temperature
MESDC2	Mesoderm development candidate 2

MAPK	Mitogen-activated protein kinase
MVB	Multi vesicular body
MEN2	Multiple endocrine neoplasia type 2
MOI	Multiplicity of infection
GalNAc	N-acetylgalactosamine
GlcNAc	N-acetylglucosamine
NGFR	Nerve growth factor receptor
NRTN	Neurturin
NSCLC	Non-small cell lung cancer
NUAK1	NUAK family SNF1-like kinase 1
OST	Oligosaccharyltransferase
OTP	ON-TARGETplus non-targeting control pool
OPTN	Optineurin
OS-9	Osteosarcoma amplified 9
PTC	Papillary thyroid carcinoma
PFA	Paraformaldehyde
PenStrep	Penicillin & Streptomycin
POC	Percentage of control
PFPE	Perfluoropolyether
PSPN	Persephin
PBS	Phosphate buffered saline
PI3K	Phosphatidylinositol 3-kinase
pTyr	Phospho-tyrosine
PTB	Phospho-tyrosine binding
pRET	Phosphorylated RET
PDGFR	Platelet-derived growth factor receptor
P4H	Prolyl 4-Hydroxylase
PPIase	Prolyl peptidyl cis-trans isomerase
PDI	Protein disulphide isomerase
Rab	Ras-related in the brain
Rab7	Ras-related protein 7
RET	Rearranged during transfection
RTK	Receptor tyrosine kinase
R-spine	Regulatory spine

SEL1L	Sel-1 suppressor of lin-12-like
SPC	Signal peptidase complex
STAT	Signal transducer and activator of transcription
SAD	Single wavelength anomalous dispersion
siRNA	Small interfering RNA
SAXS	Small-angle X-ray scattering
SDS	Sodium dodecyl sulphate
SDS-PAGE	Sodium dodecyl sulphate polyacrylamide gel electrophoresis
SNARE	Soluble NSF Attachment protein Receptor
SE	Sorting endosome
SH2	Src homology-2
SCF	Stem cell factor
SPFH	Stomatin/prohibitin/flotillin/HflK/C
SAR	Structure activity relationships
TBK1	TANK-binding kinase 1
TPR	Tetratricopeptide
TSA	Thermal shift assay
TM	Transmembrane
TRAPP	TRAnsport Protein Particle
TrkA	Tropomyosin receptor kinase
Tie2	Tunica interna endothelial cell kinase
UBE2D1	Ubiquitin-conjugating enzyme E2D 1
UPS	Ubiquitin/proteasome system
UGT1	UDP-glucose:glycoprotein glucosyltransferase 1
UDP	Uridine diphosphate
V-ATPase	Vacuolar-type H+ -ATPase
VEGFR	Vascular endothelial growth factor receptor
WT	Wild-type

C	Cysteine
K	Lysine
N	Asparagine
D	Aspartate
E	Glutamate

L	Leucine
F	Phenylalanine
Y	Tyrosine
V	Valine
A	Alanine
I	Isoleucine
H	Histidine
S	Serine
T	Threonine
R	Arginine
M	Methionine

Asp	Aspartate
Asn	Asparagine
Glu	Glutamate
Leu	Leucine
Met	Methionine
Val	Valine
Lys	Lysine
Ala	Alanine
Ser	Serine

Chapter 1. Introduction

1.1 Receptor tyrosine kinase structure, regulation and function

Receptor tyrosine kinases (RTKs) are type 1 transmembrane receptors that sense and respond to extracellular stimuli by transducing an activating signal across the plasma membrane. This signal is transmitted by either allosteric activation or dimerisation of RTK extracellular domains to stimulate their intrinsic tyrosine kinase activity. RTKs have many crucial biological roles, allowing cells to respond to changes in their environment and make contacts with their surroundings. The intracellular signalling pathways activated by RTKs regulate processes such as cell proliferation, differentiation and survival and are extremely important during development and homeostasis. Catalytic activation of RTKs is therefore tightly regulated by auto-inhibitory mechanisms preventing aberrant activation. However, many diverse mechanisms are found to subvert RTK control – including missense mutations, fusion and over-expression – frequently resulting in deregulation (Gschwind et al., 2004).

The coupling of extracellular ligand binding and stimulation of the autocatalytic tyrosine kinase activity occurs through transmembrane signalling, a poorly defined but presumably conformational switch. The repertoire of human RTKs – numbering almost 60 in the human genome – shows considerable diversity within their extracellular domains (ECD), reflecting the broad spectrum of polypeptide ligands recognised (examples are shown in Figure 1.1). In contrast, their single transmembrane-spanning (TM) and intracellular domains (ICD) show marked sequence and structural similarities. The kinase domain (KD) is highly conserved, while the juxtamembrane (JM) region and C-terminal tail flanking the KD are often more divergent (Lemmon and Schlessinger, 2010).

In view of the structural similarities of RTKs from the TM through to the ICD, the presumption has been that a unifying activation mechanism common to all RTKs would be found; for example, ligand-induced dimerisation of RTKs. While common principles have been uncovered in some instances, many RTKs of therapeutic importance do not follow these principles and exhibit their own private activation

mechanisms, the epidermal growth factor receptor (EGFR) being a prime example (Lemmon et al., 2014). It therefore follows that parallel structural, mechanistic and cell biology studies are required on the twenty discrete subfamilies of RTKs to establish their architecture, their ligand recognition properties and their mechanism of ligand-dependent activation.

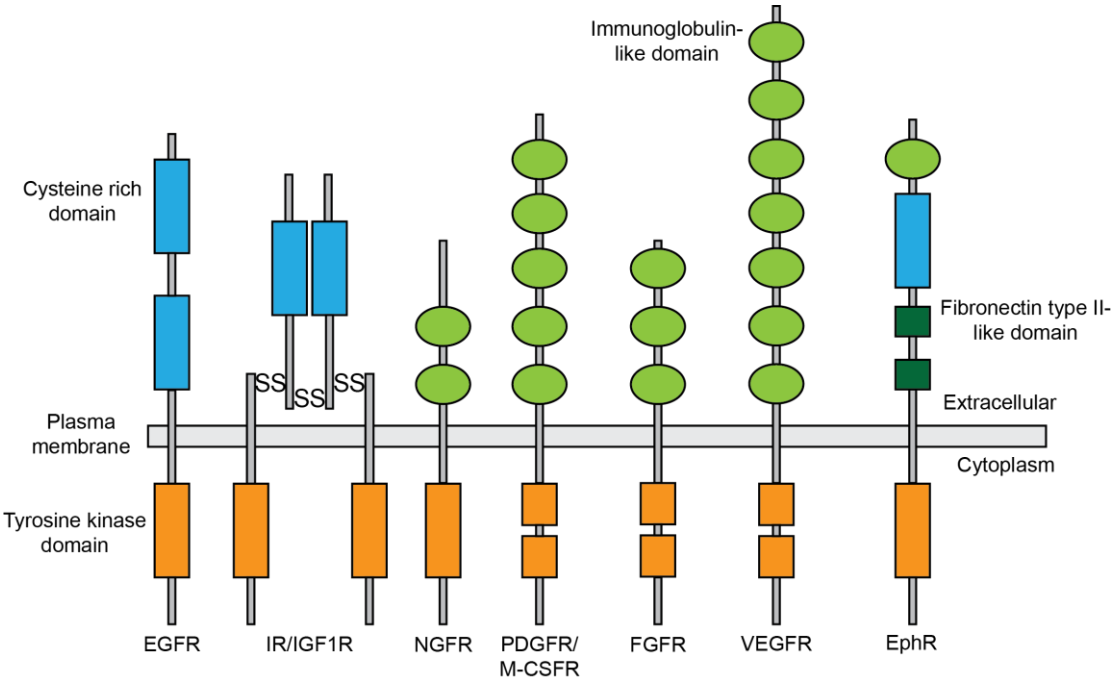

Figure 1.1 Schematic of growth factor receptor tyrosine kinases

The RTK family demonstrates great diversity in their ECD structures, while the TM and ICD regions are very similar both in sequence and structure. Adapted from (Lemmon and Schlessinger, 2010).

RTKs respond to ligand binding through activation of their intracellular kinase activity, often associated with dimerisation of the receptor (Lemmon and Schlessinger, 2010). RTK activation frequently has two components; removal of auto-inhibitory elements and enhancement of catalytic activity, frequently 100-1000-fold. Activation results in precise sequential trans auto-phosphorylation of tyrosine residues within the RTK ICD, which enhance the kinase activity of the receptor and act as docking sites for downstream signalling molecules that bind via SH2 (Src homology-2) or PTB (phospho-tyrosine binding) domains (Furdui et al., 2006).

1.1.1 RTK KD structure and phosphorylation

Tyrosine kinases carry out a phosphoryl transfer reaction in which a tyrosine nucleophile on a substrate protein accepts the transfer of a terminal γ-phosphate from an ATP moiety (Lassila et al., 2011). The reaction requires a catalytic base within the kinase to deprotonate the tyrosine acceptor, permitting nucleophilic attack by the tyrosine oxygen towards the electrophilic phosphorous atom of the γ-phosphate (Figure 1.2). The catalytic cycle is completed by release of phospho-tyrosine product and ADP prior to binding another ATP to continue further rounds of catalysis.

The KD of RTKs is composed of a predominantly β-strand N-lobe and a larger α-helical C-lobe, a structure that is well conserved within serine/threonine and tyrosine kinases. A hinge region between the two lobes allows a certain degree of flexibility within the kinase, which is crucial for successful catalytic function. A cleft exists between the two lobes to accommodate ATP (Knighton et al., 1991). ATP binds within this cleft, below a phosphate-binding loop that contains a glycine-rich sequence motif (GXGXφG; φ is usually tyrosine or phenylalanine), known as the glycine-rich loop (GRL) (Huse and Kuriyan, 2002). The activation loop (A-loop) is located between the N- and C-lobes, beginning with a conserved DFG motif and ending with a conserved APE motif. The loop usually contains between one and three tyrosine residues that can become phosphorylated (Nolen et al., 2004).

1.1.2 Structural elements required for catalytic mechanism

There are several structural elements required for a catalytically productive kinase. The αC-helix must be close to the catalytic centre, so that the conserved lysine residue (Lys758 in RET numbering) within the ATP cleft is organised as such to interact with the α and β phosphate groups of ATP, through a salt bridge with the conserved glutamate residue (Glu775 in RET numbering) extending from the αC-helix. The A-loop must be in an ‘active’ conformation to facilitate substrate binding and catalysis (Hubbard, 1997). The DFG motif must be arranged to allow the aspartate to coordinate magnesium binding; the N- and C-lobes must be correctly

oriented, positioning crucial catalytic residues in both lobes (Huse and Kuriyan, 2002, Cowan-Jacob, 2006).

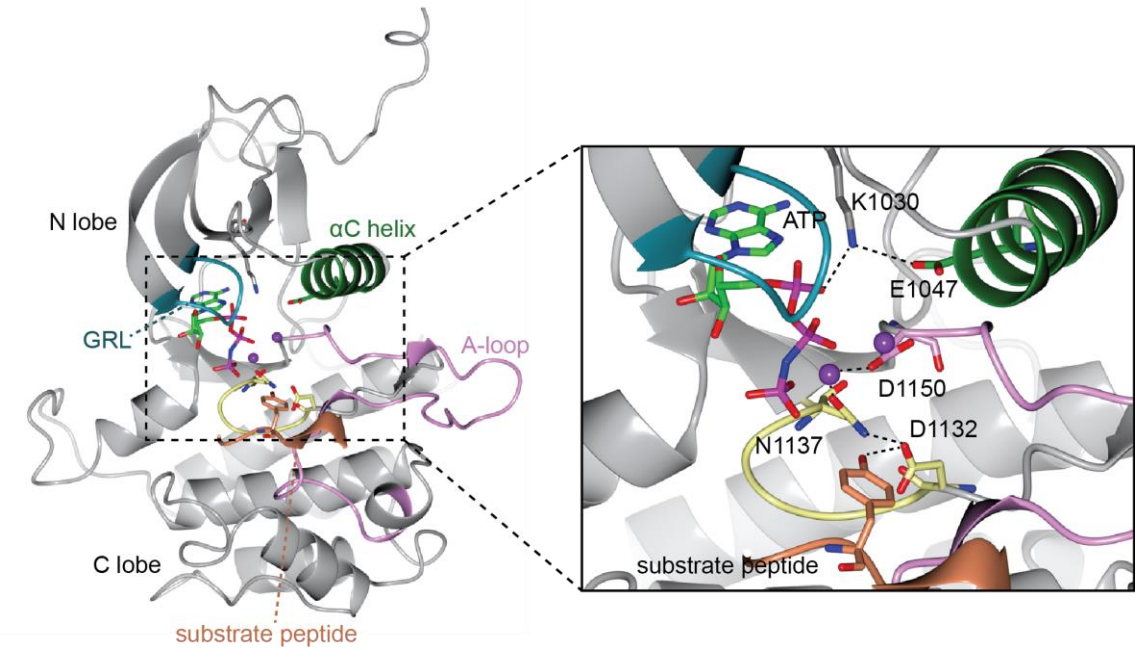

Figure 1.2 Protein tyrosine kinase active conformer

The crystal structure of the insulin receptor (PDB code 1IR3) with an ATP analogue bound within the active site and key structural elements highlighted (Hubbard, 1997). Protein – light grey ribbon; substrate peptide – coral; ATP analogue – green & purple sticks; magnesium ions – purple; activation loop (including substrate-binding P+1 loop) – pink; αC helix – green; glycine-rich loop – cyan. On the right-hand side, key residues are indicated and interactions represented using dotted black lines. The catalytic base (Asp1132) interacts with the attacking nucleophilic hydroxyl group of the substrate peptide tyrosine residue. Asn1137 is required for positioning of both Asp1132 and the magnesium ions.

The glycine residues within the GRL coordinate the ATP phosphate positions via interactions with the loop's backbone, and result in loop flexibility in the absence of ATP binding (Huse and Kuriyan, 2002). The A-loop is a regulatable element bearing tyrosine residues that act as auto-phosphorylation sites. Phosphorylation of the tyrosine residues within the A-loop stabilises the kinase in an 'active' conformation, boosting enzymatic activity by several orders of magnitude in many RTKs. The auto-phosphorylated tyrosine residues within this loop also frequently release the loop from an inactive conformation and serve to recruit downstream effector molecules that recognise the phospho-tyrosine side chains (Cowan-Jacob, 2006).

1.1.3 RTK autophosphorylation and regulation

The phosphorylation of three regions within a tyrosine kinase domain – the activation loop, the JM region and the C-tail – can occur upon ligand activation and RTK dimerisation. This process results in a far less flexible conformer, as the flexible regions within phosphorylation sites become tethered to phospho-binding pockets (Chen et al., 2007). While inactive kinases appear to have the A-loop in a position that occludes the ATP pocket, phosphorylation of the tyrosine residues within the loop prevents binding to the cleft and stabilises an active conformation (Hubbard et al., 1994, Hubbard, 1997).

The JM region and C-tail of tyrosine kinases can also be phosphorylated and are involved in the regulation of kinase activity. Phosphorylation of two tyrosine residues within the JM region results in dissociation, allowing the αC helix to move into an active conformation (Wiesner et al., 2006, Wybenga-Groot et al., 2001). In the case of Tie2, the C-tail has been found to block substrate binding of the kinase domain in its unphosphorylated form (Niu et al., 2002).

1.1.4 Regulation of RTK activity

While a great deal of progress has been made towards the understanding of how many RTKs regulate their activity, the details for several RTKs (e.g. EGFR and RET) are far from fully understood. However, there appear to be common mechanisms of regulation; namely autophosphorylation (as discussed above), allostery and dimerisation. Allostery can be defined as communication between the active site of a protein and a distant site of modification or binding. When an event occurs at this distant site, it results in a change in structural conformation or flexibility. In turn, this change regulates the activity at the active site (Kuriyan and Eisenberg, 2007). As an example, ligand-induced dimerisation of EGFR results in allosteric activation of the alternate KD (Zhang et al., 2006).

While mechanisms of ligand-dependent dimerisation differ amongst the RTK superfamily (Lemmon and Schlessinger, 2010), the process of dimerisation itself appears to be required for both allosteric and *trans*-phosphorylation activation of the KD (Chen et al., 2007, Zhang et al., 2006). Several mechanisms have been

identified, with examples including: TrkA/NGF: dimeric-ligand mediated dimerisation (Wehrman et al., 2007); KIT/SCF: dimeric-ligand and receptor mediated dimerisation (Yuzawa et al., 2007); FGFR/FGF: monomeric-ligand and receptor mediated dimerisation (Schlessinger et al., 2000); EGFR/EGF: receptor-mediated dimerisation (Ogiso et al., 2002).

In the case of receptor-mediated dimerisation, the ligand is still relevant due to its role in the stabilisation of an active receptor arrangement (Lemmon and Schlessinger, 2010). By deduction, receptors that rely on ligand-dependent dimerisation for activation need to have mechanisms of inhibition in the absence of ligand. Examples include charge repulsion of membrane-proximal Ig-like domains in the KIT-ECD and an inaccessible 'dimerisation arm' in EGFR (Yuzawa et al., 2007, Ogiso et al., 2002). Alternatively, dimerisation can be ligand-independent, as is the case for the disulphide-linked dimers of the insulin receptor family (McKern et al., 2006). There are suggestions that receptors that rely on ligand-dependent dimerisation for activation can exist in preformed dimers, with ligand-binding resulting in oligomerisation (Whitty and Riera, 2008, Clayton et al., 2005). Again, mechanisms of inhibition are required to prevent aberrant activation of the KD. In the case of preformed complexes, allosteric activation of the kinase domain would be required (Hubbard and Miller, 2007).

1.1.5 The regulatory spine

While the majority of conserved motifs within a protein can be defined as linear motifs (such as DFG) or an assembly of structural elements, several structural motifs have been identified within kinase domains that do not fall under these definitions. The F-helix (coloured blue in Figure 1.3) is considered the central scaffold of the kinase domain for extending regulatory motifs, due to its rigid and central buried position within the C-lobe relative to crucial areas such as the substrate binding residues (Kornev et al., 2008, Kannan and Neuwald, 2005).

Protein kinase sequential and structural alignments have led to the discovery of a hydrophobic spatial motif consisting of four residues: L96 (αC-helix), L106 (β4 strand), Y164 (catalytic loop) and F185 (activation loop) (Kornev et al., 2006). The

motif is known as the regulatory R-spine and its position (Figure 1.3) – connected to the F-helix via D220 – is thought to regulate the activity of the kinase. The formation of this spine is influenced by several structural elements within the kinase, including the configuration of the activation loop and the position of the αC helix (Kornev et al., 2008). In comparison, another hydrophobic spatial motif termed the catalytic C-spine was found to form in the presence of ATP (Figure 1.3). The C-spine connects to the F-helix via Met231, with the motif composing of: Leu227 and Met231 (F-helix); Met128 (D-helix); Leu172, Leu173 and Ile174 (β7 strand); and Val57 and Ala70 (contacting adenine ring of ATP). In the presence of ATP, this C-spine connects the N- and C-lobes together (Kornev et al., 2008).

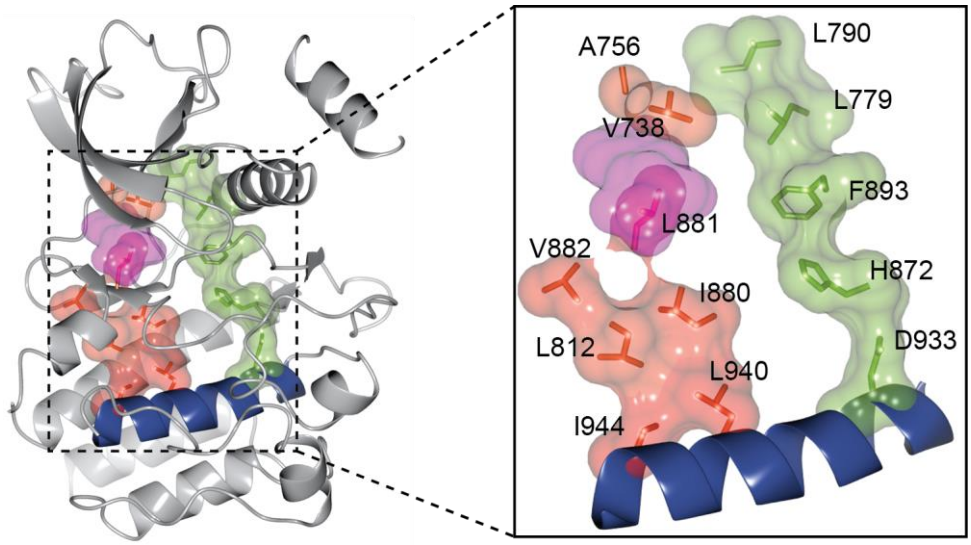

Figure 1.3 Catalytic and R egulatory spines highlighted within the RET kinase domain

Ribbon representation of the RET kinase domain (light grey) with the F helix (dark blue), C-spine (coral) and R-spine (light green) highlighted. Residues within the spine are annotated. The position of adenine within the ATP structure is highlighted in magenta.

1.2 Synthesis, trafficking and degradation of RTKs

The process of intracellular trafficking is crucial in the transport of RTKs to appropriate sites for synthesis, maturation and export to be exposed to ligands. The nascent polypeptide is inserted into the endoplasmic reticulum (ER) to be correctly folded and modified, before being transported to the Golgi apparatus and on to the plasma membrane. Once at the cell surface, RTKs are internalised and either recycled once more to the plasma membrane or targeted for degradation

(Goh and Sorkin, 2013). Studies have demonstrated that RTKs can transmit signals intracellularly, as well as from the plasma membrane, and the subcellular location can dictate the signalling specificity (Lemmon and Schlessinger, 2010, Miaczynska et al., 2004). The location of the RTK can result in the association of different signalling molecules. This entire process determines the half-life of an RTK in a particular cell type; for example, the EGFR half-life in carcinoma cells is 24 hours (Stoscheck and Carpenter, 1984). In the case of RET, a combination of findings from studies examining RET maturation and degradation suggest a half-life of approximately 10 hours (Tsui et al., 2006, van Weering et al., 1998). To understand RTK maturation, a brief overview of protein folding, glycosylation and transport of glycoproteins is given.

1.2.1 Protein folding and quality control within the ER

After synthesis on ribosomes, proteins are translocated into the ER, where they are folded and modified into their correct structure before being transported to the correct cellular compartment (Figure 1.4). Most proteins are targeted to the ER via amino-terminal signal sequences that are cleaved co- or post-translationally (Wang et al., 2005, Land et al., 2003). Growing evidence suggests that this signal sequence is not only responsible for the ER-targeting of proteins, but also important for folding and modification of the polypeptide (Piersma et al., 2006, Tamura et al., 2011).

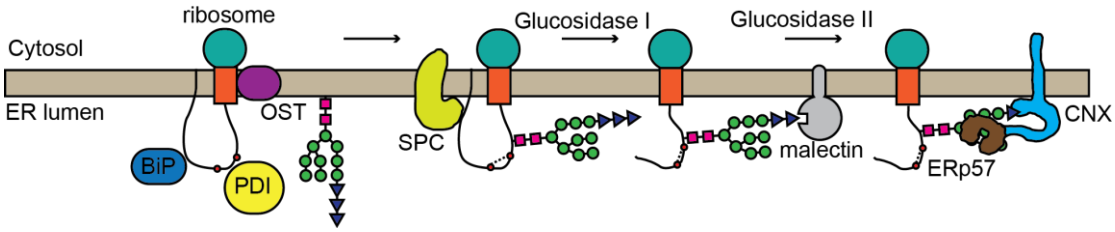

Figure 1.4 Cotranslational protein folding within the ER

The nascent polypeptide is inserted into the ER by the ribosome (cyan), through the Sec61 translocon (orange). The oligosaccharyltransferase (OST; purple) attaches the glycan chain to Asn on the polypeptide, while BiP and PDI are involved in protein stability and disulphide bond formation. The N-terminal sequence is cleaved by the signal sequence peptidase complex (SPC; lime green) and glucosidase I removes the terminal glucose molecule. The trimmed polypeptide can then bind to the membrane-associated lectin (malectin; grey) and glucosidase II removes another glucose molecule. The monoglucosylated glycan binds to calnexin (CNX; blue) and the oxidoreductase ERp57 (brown). This process continues until glucosidase II removes the final glucose molecule. Adapted from (Braakman and Hebert, 2013).

Upon entering the ER, a large number of proteins are modified by N-linked glycans that are attached to the asparagine side chain present in the NXS/T motif (where X is any amino acid). This process often occurs during translation into the lumen via the enzyme oligosaccharyltransferase (OST) (Nilsson and von Heijne, 1993). The carbohydrate attached initially comprises of three glucoses, nine mannoses and two N-acetyl glucosamines (Figure 1.5). Glycosylation of a protein can have effects on both the final function and the physical properties: N-linked glycans have been shown to improve stability, kinetics of folding, solubility and resistance to degradation (Hanson et al., 2009).

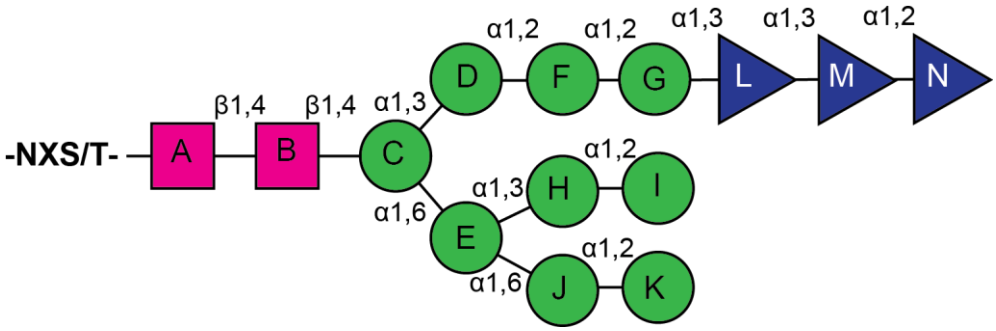

Figure 1.5 Structure of the N-glycan core

The oligosaccharide is made up of two N-acetylglucosamine (pink squares), nine mannose (green circles) and three glucose residues (blue triangles). A-G are added on the cytosolic side of the ER membrane, while H-N are added once the substrate is flipped in the membrane. The linkages are annotated. Adapted from (Aebi et al., 2010).

Nascent polypeptides are found in the ER at such a high concentration that misfolding is very likely to occur without the assistance of a number of ER molecular chaperones (Ellis and Hartl, 1999). Two types of chaperones exist: classical chaperones bind directly to the protein and can be found outside of the ER as well, while carbohydrate-binding chaperones are ER-specific and interact with the glycan moieties (Braakman and Hebert, 2013). Classical chaperones comprise of heat shock protein (Hsp) 70 and 90 family members, recognising exposed hydrophobic regions on substrates that are indicative of an incorrectly folded state. One such chaperone is known as BiP (binding immunoglobulin protein), a nucleotide-binding ER-specific protein that binds to substrates and protects them from premature folding (Suzuki et al., 1991). BiP is believed to be a crucial regulator of ER function due to its roles in protein translocation, protein folding, ERAD and activation of the unfolded protein response (Hendershot, 2004).

Carbohydrate-binding chaperones include calnexin (membrane-bound) and calreticulin, which facilitate the folding of glycoproteins. These chaperones bind to folding substrates and stabilise them, preventing aggregation and premature exit from the ER (Hebert et al., 1996, Rajagopalan et al., 1994). They also facilitate the formation of disulphide bonds and the isomerisation of rare *cis-trans* Pro peptide bonds (Oliver et al., 1997, Kozlov et al., 2010). The N-linked glycan attached to a substrate is first trimmed by glucosidase I, reducing affinity for OST, followed by further trimming by glucosidase II. The monoglucosylated protein is then able to enter the carbohydrate-binding chaperone pathway and can only leave when glucosidase II removes the final glucose. At this point, the substrate protein is checked by UGT1 (UDP-glucose:glycoprotein glucosyltransferase 1) and reglycosylated if further attempts at folding are required (Labriola et al., 1995, Hebert et al., 1995).

These chaperone systems are required for the retention of proteins within the ER, to allow for protein folding. The folding process is facilitated by a host of ER-localised enzymes that are either protein disulphide isomerases (PDIs) or prolyl peptidyl *cis-trans* isomerases (PPIases). PDIs catalyse the formation, isomerisation and reduction of disulphide bonds and there are currently more than 20 mammalian family members identified (Wallis and Freedman, 2013, Ellgaard and Ruddock, 2005). PPIases are responsible for the inter-conversion of *cis* and *trans* Pro-peptide bonds, a rate-limiting step in protein folding due to the unconventional conformation of the bond (Lang et al., 1987, Brandts et al., 1977). It should be noted that proline residues are often found in close proximity to disulphide bonds, suggesting an inter-related function for each class of enzyme.

The folding and chaperone systems of the ER can persist in futile attempts of protein folding for a finite time, before ER-associated degradation (ERAD) takes over. ERAD involves the recognition of a misfolded substrate, the transfer of the substrate across the ER lipid bilayer, ubiquitylation and proteasomal degradation (Olzmann et al., 2013). Problematic proteins that are assessed by UGT1 and re-entered into the carbohydrate-binding chaperone pathway must eventually be removed. While glucosidases are responsible for the trimming of glucose residues,

mannosidases – MAN1B1, EDEM1 and EDEM3 – are responsible for demannosylation that results in substrates that can no longer be recognised by UGT1 (demonstrated in Figure 1.6) (Hosokawa et al., 2010, Gonzalez et al., 1999, Hirao et al., 2006). The substrates are instead recognised by OS-9 (osteosarcoma amplified 9) and ERLEC1 (endoplasmic reticulum lectin 1) via mannose-6-phosphate receptor homology (MRH) domains (Hosokawa et al., 2008, Hosokawa et al., 2009).

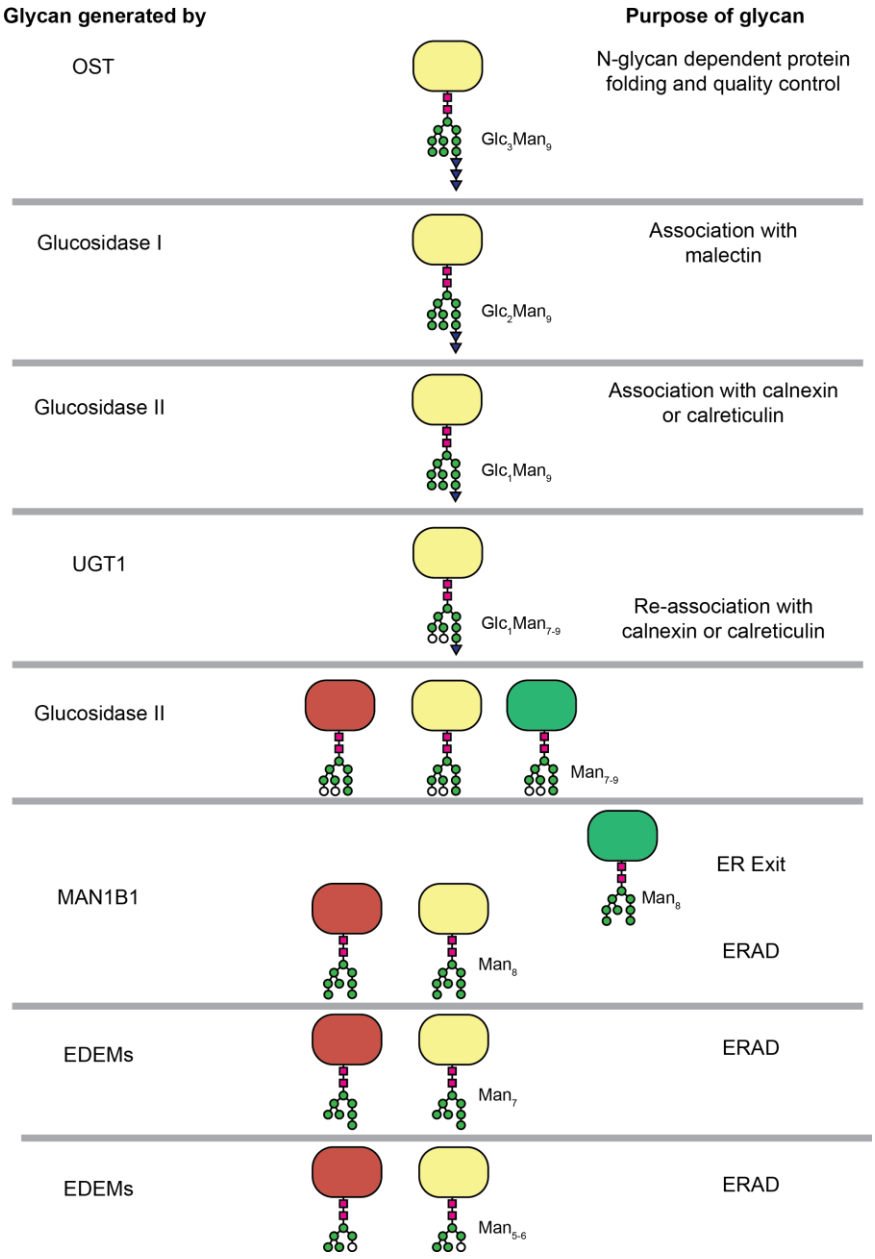

Figure 1.6 Glycan processing within the ER

N-glycan trimming and modification is carried out by a number of enzymes within the ER (left). The N-glycan dictates the fate of the protein: exit or ERAD. Yellow: immature substrate; red: misfolded substrate; green: folded substrate. Adapted from (Aebi et al., 2010).

Once recognised, the misfolded substrates need to be exported from the ER. This is facilitated by the interaction of misfolded protein-recognition factors with SEL1L (sel-1 suppressor of lin-12-like), a transmembrane glycoprotein that in turn organises the clustering of essential ERAD components required for substrate dislocation (Olzmann et al., 2013). While the entire ER 'dislocon' has not been identified, several components – such as the Derlin protein family and E3 ligase Hrd1 – have been proposed to be involved (Ye et al., 2004, Carvalho et al., 2010). Following removal from the ER, substrates are ubiquitinated and degraded via the cytosolic 26S proteasome. A large number of E3 ligases have been implicated in the ubiquitination of misfolded ERAD substrates, although it is thought that Hrd1 and gp78 carry out the majority while other ligases have more selective clientele (Olzmann et al., 2013, Kikkert et al., 2004, Fang et al., 2001).

1.2.2 ER to Golgi apparatus transport

Cell surface proteins that successfully reach their native fold may be transported from the ER to the Golgi apparatus, where they are modified further and can then continue on to the plasma membrane. This process requires the formation of the COPII coat on the cytosolic side of the ER membrane, defining transport vesicles that carry proteins forward. The cytoplasmic G-protein Sar1 is activated by ER membrane protein Sec12, triggering a conformational shift in Sar1 that is thought to result in membrane curvature. The activated and now membrane-bound Sar1 then recruits Sec23 and Sec24, a complex that is required for both cargo-binding and recruitment of the outer coat components Sec13 and Sec31 (Lord et al., 2013). After membrane curvature has been induced and ER cargo has been recruited, the vesicle must be excised from the membrane, a process that is thought to be driven by Sar1 itself (Lee et al., 2005). Once excised, the vesicles move towards an intermediate compartment known as ERGIC (ER-Golgi intermediate compartment), where preliminary sorting of substrates can occur. ER-resident proteins can be transported back (retrograde transport) and proteins destined for the secretory pathway can move forward to the *cis*-Golgi (anterograde transport). Retrograde transport is mediated by the COPI coat complex (Martinez-Menarguez et al., 1999). The COPII coated vesicles tether to and fuse with the accepting membrane with

the aid of the TRAPP (TRAnsport Protein Particle) and SNARE (Soluble NSF Attachment protein Receptor) complexes (Cai et al., 2007).

1.2.3 Functions of the Golgi

Proteins that reach the Golgi apparatus are modified further through a range of complex glycosylation processes. The Golgi is a host for many glucosyltransferases, glucosidases and nucleotide sugar transporters that are located throughout the *cis*- and *trans*-Golgi. Glycoproteins arrive in the *cis*-Golgi with N-glycans attached, high mannose sugar moieties that can be modified further by the Golgi resident UDP-GlcNac into complex N-glycans (Lau et al., 2007). O-linked glycosylation – single sugar moieties added to Ser/Thr – also occurs within the Golgi, and is mainly applicable to mucin type glycans and proteoglycans (Schachter and Williams, 1982, Esko and Selleck, 2002). Proteins move through the Golgi, from *cis* to *trans*, into the *trans*-Golgi network (TGN): the hub of cargo sorting for the early secretory pathway. The presence of sorting motifs and glycosylation can act as signals that target cargo proteins to the plasma membrane (Yeaman et al., 1997).

1.2.4 RTK endocytosis and receptor recycling

Once at the cell surface, RTKs can be internalised and degraded via the process of endocytosis (Figure 1.7). Increased activation of cell surface RTKs leads to increased turnover, thus controlling the level of RTK signalling. The receptors are endocytosed by both clathrin-dependent and –independent mechanisms, with the resulting vesicles fusing with the early endosomes (EEs). At this point, some ligands dissociate from the receptor in the acidic endosome and both ligand-occupied and –unoccupied RTKs can be recycled by EE-plasma membrane fusion or retro-endocytosis in endosomal-derived vesicles. Slower recycling also occurs in EEs that have matured into sorting endosomes (SEs) and multivesicular bodies (MVBs), which gradually lose their ability to recycle and mature into late endosomes (LEs). LEs fuse with lysosomes containing proteolytic enzymes required to degrade the receptors and ligands (Goh and Sorkin, 2013). Several Rab GTPases are involved in the endo-lysosomal pathway; particularly, Rab5 is found on early endosomes and is crucial for the biogenesis of endosomes, while

Rab7 replaces Rab5 on matured late endosomes and is involved in endo-lysosomal fusion (Gautreau et al., 2014).

Clathrin-mediated endocytosis has been identified as the major internalisation pathway for ligand-activated RTKs, with the small interfering RNA (siRNA) knockdown of clathrin resulting in the inhibition of EGFR, VEGFR2 and TrkB internalisation (Huang et al., 2004, Lampugnani et al., 2006, Zheng et al., 2008). Specific motifs within the cytoplasmic domains of RTKs are recognised by components of the clathrin coat, along with mono-ubiquitination of lysine residues within the auto-phosphorylated kinase domain by E3 ligases such as Cbl (Casitas B-lineage Lymphoma) (Goh and Sorkin, 2013, Marmor and Yarden, 2004). It is thought that the ubiquitin moieties attached to activated RTKs target the receptors to clathrin-coated pits via ubiquitin binding proteins within the pits and are involved in the late sorting events of RTKs within MVBs (Hawryluk et al., 2006, Marmor and Yarden, 2004).

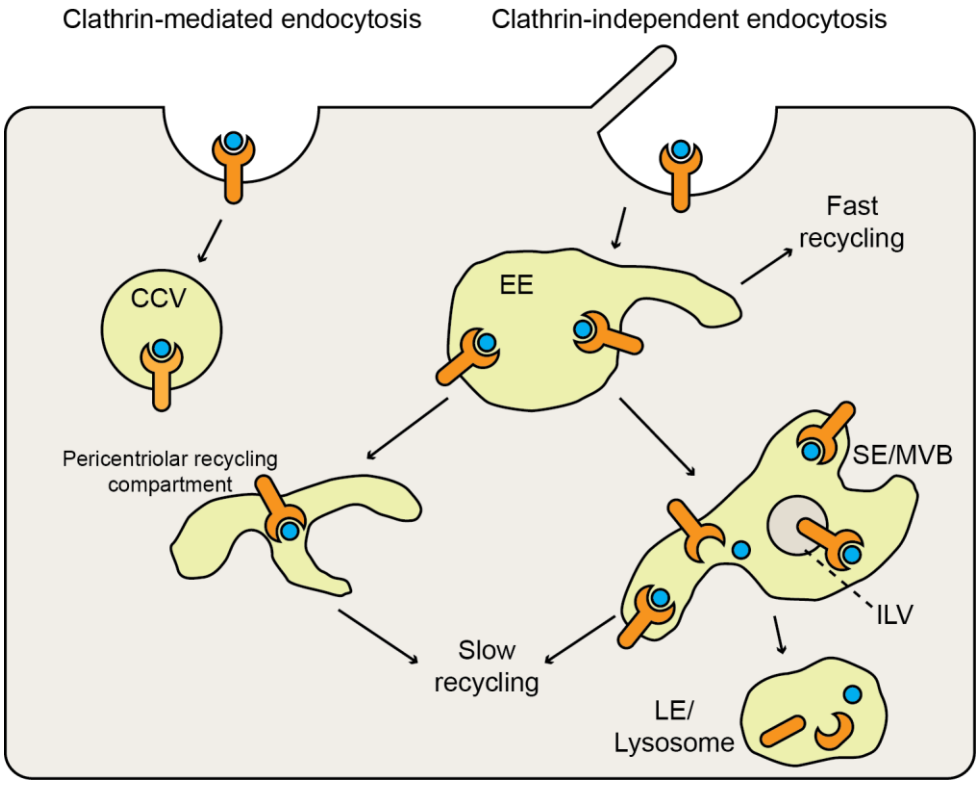

Figure 1.7 RTK endocytosis

A schematic model of RTK (orange) endocytosis upon ligand (blue) binding. The receptors and ligands are recycling or degraded via the lysosome. CCV – clathrin coated vesicle; EE – early endosomes; SE – sorting endosome; MVB – multivesicular bodies; ILV – intraluminal vesicles; LE – late endosome. Adapted from (Goh and Sorkin, 2013).

RTKs that are subsequently located within the membrane of EEs and MVBs can be recycled back to the plasma membrane, while those located within MVB intraluminal vesicles (ILVs) cannot be recycled back and are degraded once the MVBs mature into LEs. It is currently believed that the ubiquitinated RTKs are held back from the recycling process within MVBs by components of ESCRT (endosomal sorting complexes required for transport), resulting in their packaging into ILVs (Teis et al., 2009).

Receptor recycling has been demonstrated for EGFR, TrkA and the insulin receptor (IR), although the mechanisms behind recycling are less well understood (Sorkin et al., 1991, Zapf-Colby and Olefsky, 1998, Huecksteadt et al., 1986). Recycling appears to be the standard pathway for RTKs that have not been trapped within MVBs, with studies based on the EGFR suggesting that saturation of the RTK degradative pathway results in higher levels of receptor recycling (Goh and Sorkin, 2013, French et al., 1994).

1.2.5 Mechanisms of RTK degradation

RTK degradation within the mammalian cell can occur via three pathways: (1) endocytosis and lysosomal degradation, (2) chaperone-mediated autophagy (leading to lysosomal degradation) and (3) the ubiquitin-proteasome system (UPS) (Figure 1.8). The decision as to which pathway to select is made depending on the location of the protein. For example, activated RTKs at the cell surface are internalised and degraded via the lysosome to regulate signalling levels (Goh and Sorkin, 2013); misfolded and therefore defective RTKs are often exported from the ER via ERAD, ubiquitinated and degraded via the proteasome (Olzmann et al., 2013); and it is now believed that misfolded and aggregated proteins can be targeted for selective autophagy or the ‘aggresome’ (Hyttinen et al., 2014).

1.2.5.1 Lysosomal degradation

Proteins can be targeted for lysosomal degradation from both the endocytic and autophagic pathways. The lysosome itself, a crucial digestive compartment of the cell, has an acidic internal environment containing acid hydrolases that are used to digest imported components (Appelqvist et al., 2013). There are approximately 60

different hydrolases contained within the lysosome – such as proteases, nucleases and phosphatases – with their own specific targets that result in the breakdown of all macromolecules (Bainton, 1981).

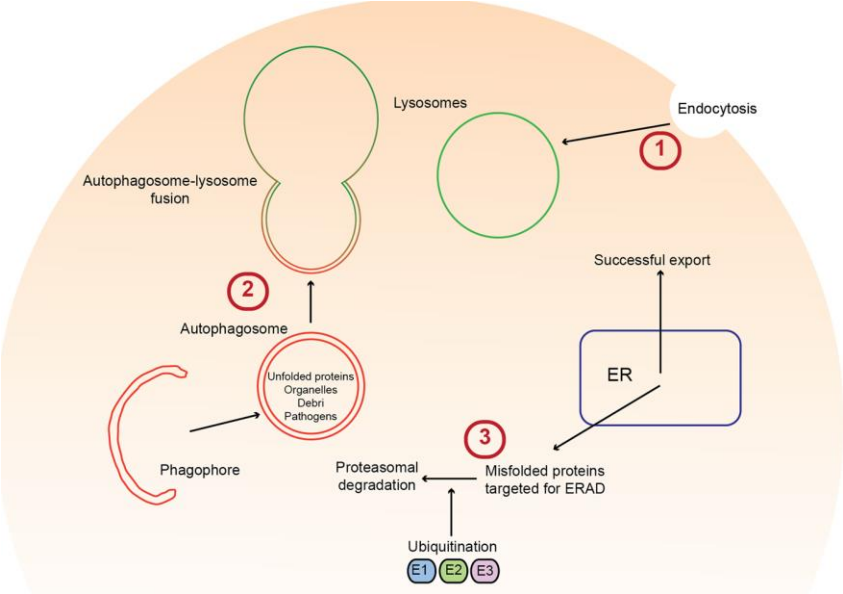

Figure 1.8 Degradative pathways targeting RTKS

The three pathways involved in RTK degradation: (1) Endocytosis and lysosomal degradation; (2) Autophagy and lysosomal degradation; (2) Proteasomal degradation.

1.2.5.2 Proteasomal degradation

The ubiquitin/proteasome system (UPS) is the other main proteolytic system of the eukaryotic cell. While many proteases are present within the lysosome, the UPS has only one: the 20S proteasome. Degradation via the proteasome requires target proteins to be tagged with ubiquitin, a process that requires three enzymes. The E1 ubiquitin-activating enzyme is first bound to the ubiquitin protein before transferring it to an E2 ubiquitin-conjugating enzyme; an E3 ligase then catalyses the transfer from the E2 to (primarily) a lysine residue on the target protein. Poly-ubiquitination can occur due to the presence of lysine residues within the ubiquitin molecule itself (Wong and Cuervo, 2010). The process of ubiquitination is crucial in the end fate of the substrate protein. Due to the presence of lysine residues within ubiquitin, several modes of ubiquitination can occur. Mono-ubiquitination tends to result in regulation of the substrate protein – through endocytosis, trafficking or transcription – while poly-ubiquitination can occur in several ways. Firstly, ubiquitin chains

occurring through Lys48 tend to result in proteolysis of the substrate, while chains occurring through Lys63 are more associated with signalling and endocytosis. Branched ubiquitination through Lys11 has recently been reported to result in proteolysis of the substrate as well (Johnson et al., 1996, Winter et al., 2013).

Substrate specificity is regulated by the presence of degradative signals on target proteins that are recognised by the array of E3 ligases, known as E3 ligase substrate recognition components (Ravid and Hochstrasser, 2008). Alternatively, the E3 ligases can be assisted by cytosolic chaperones. For example, the E3 ligase CHIP recognises Hsp90 and Hsc70 and can then target the chaperones' client proteins (Murata et al., 2001). Proteins that have been Lys48-linked with at least four ubiquitin molecules are classed as substrates for the 26S proteasome (Thrower et al., 2000). Substrates are either escorted to the proteasome by shuttle factors or they can bind directly to ubiquitin receptors on the proteasome itself (Finley, 2009). Deubiquitinating enzymes then remove the poly-ubiquitin chains and the substrate can enter the 20S catalytic core of the proteasome for degradation (Wong and Cuervo, 2010).

1.2.5.3 Autophagy

Autophagy is a crucial degradative process required for the removal of both proteins and organelles through the action of lysosomes. The autophagic pathway can be divided into three types: macroautophagy (the sequestering of a region of the cytosol into a double membrane that is carried to the lysosome); microautophagy (the lysosomal membrane itself invaginates around the surrounding cytosol to internalise it within the lumen); and chaperone-mediated autophagy (CMA) (motifs on substrate proteins are recognised by chaperones that target it directly to the lysosome) (Wong and Cuervo, 2010).

Macroautophagy requires the formation of the phagophore; a double-membrane structure that engulfs portions of the cytosol and ultimately closes to become a vesicle known as the autophagosome. The autophagosomes are then transported by microtubules to the late endosomes or lysosomes. This process initially involves the formation of the ATG5-ATP12-ATG16L complex, which is required for the

conjugation of ATG8 family proteins (divided into the LC3 and GABARAP subfamilies) to the phagophore membrane. The ATG8 family members then act as receptors for specific proteins until they are released by ATG4B when the phagophore closes into the autophagosome (Lamark and Johansen, 2012).

The identification of chaperone-mediated autophagy has altered the conception that autophagy is an unselective process. In the case of selective autophagy, autophagy receptors identify protein substrates and can bind directly to ATG8 homologues on the phagophore membrane. Misfolded and aggregated proteins can be targeted through this mechanism, which has been termed aggrephagy (Overbye et al., 2007). As discussed earlier, aberrant proteins within the ER are targeted for ERAD and retrotranslocated into the cytosol for degradation. At this point, the presence of cytosolic chaperones such as Hsp70 can induce the binding of CMA receptors (such as LAMP2) or E3 ligases (such as CHIP). Alternatively, specific aggrephagy receptors (such as Optineurin) can bind to the aggregated protein or pathogens (Lamark and Johansen, 2012).

1.3 RET structure, ligands-co-receptor partners and biological functions

This laboratory has been actively studying the structure and biochemistry of the RET (**RE**arranged during **T**ransfection) receptor tyrosine kinase. This project has arisen from a long standing interest in the cystine knot superfamily of growth factor ligands that include the glial cell-line derived neurotrophic factor (GDNF), and their interactions with partner proteins. RET has an unusual level of importance as an RTK, as it is essential for vertebrate development and contributes to multiple human diseases including several forms of cancer, Hirschsprung's disease and congenital anomalies of kidney and urinary tract (CAKUT). The diseases associated with RET are discussed later in section 1.4.

1.3.1 Biological functions of RET

RET plays a crucial role in development, with RET function being required for spermatogenesis and the development of the kidneys and nervous system. RET is expressed in the cells of both the central and peripheral nervous systems, and its

inactivation has been shown to result in renal agenesis, due to a loss of ureteric bud development (Schuchardt et al., 1994a). RET can display multiple alternative splicing variants, resulting in three different carboxyl termini: 9 terminal amino acids (RET9), 43 terminal amino acids (RET43) and 51 terminal amino acids (RET51) (Myers et al., 1995). It has been suggested that there are isoform-specific roles for splicing variants RET9 and RET51 during this development (Jain et al., 2006). Along with defects in kidney development, mice lacking RET were found to lack enteric neurons throughout the digestive tract (Schuchardt et al., 1994b). This lack of neural crest development also occurs in humans and was identified in the mid 1900's as Hirschsprung's disease (HSCR) (Whitehouse and Kernohan, 1948).

RET is also expressed in the motor neurons of the spinal cord, with GDNF found to be required for their survival during embryogenesis (Oppenheim et al., 2000). GDNF appears to be required for the survival of several types of neuron, with RET/GDNF signalling shown to protect midbrain dopaminergic neurons from chemically-induced cell death (Trupp et al., 1996). The beneficial effect of GDNF on neuronal survival results in the implication of the ligand in the treatment of Parkinson's disease, and some loss-of-function studies have shown that RET or GDNF ablation results in defects within dopaminergic neurons (Kramer et al., 2007, Pascual et al., 2008). RET, GDNF and GFRα have all been shown to be required for spermatogenesis: a process that is essential for reproduction (Naughton et al., 2006, Jain et al., 2004).

1.3.2 RET evolution

Only one *RET* gene is known to exist in mammals, lower vertebrates and arthropods; the gene is absent from other phyla of the animal kingdom (Shiu and Li, 2004). The *RET* gene can be found in *Drosophila melanogaster*, but the fly appears to lack genes encoding GDNF or GFRα and *Drosophila* RET cannot interact with the mammalian ligand or co-receptor (Abrescia et al., 2005). However, the RET expression pattern is similar to that of mammals, and a *Drosophila* model for RET-associated multiple endocrine neoplasia type 2 (MEN2) has been developed for drug profiling (Hahn and Bishop, 2001, Dar et al., 2012, Das and Cagan, 2010). The zebrafish (*Danio rerio*) has been used as a model organism for studying RET,

in which it was shown that the function of RET and its bipartite ligand (defined as two GDNF and two GFRα1 molecules) is conserved in enteric nervous system development (Shepherd et al., 2004, Shepherd et al., 2001, Marcos-Gutierrez et al., 1997).

1.3.3 RET ligands and co-receptors

RET binds to a GDNF family ligand (GFL) – GDNF, neurturin (NRTN), artemin (ARTN) or persephin (PSPN) – and a corresponding GDNF family receptor (GFRα) co-receptor (1-4) that is GPI-linked to the plasma membrane (Figure 1.9) (Klein et al., 1997, Treanor et al., 1996). Assembly of the GDNF-GFRα–RET ternary complex leads to RET activation by transmembrane signalling. The current model for RET activation involves a disulphide-linked ligand homodimer, two membrane-associated GFRs and two RET molecules. In the case of ARTN/GFRα3, the order of assembly has been determined as: 1 GFRα3 + ARTN dimer + 1 RET + 1 GFRα3 + 1 RET (Schlee et al., 2006).

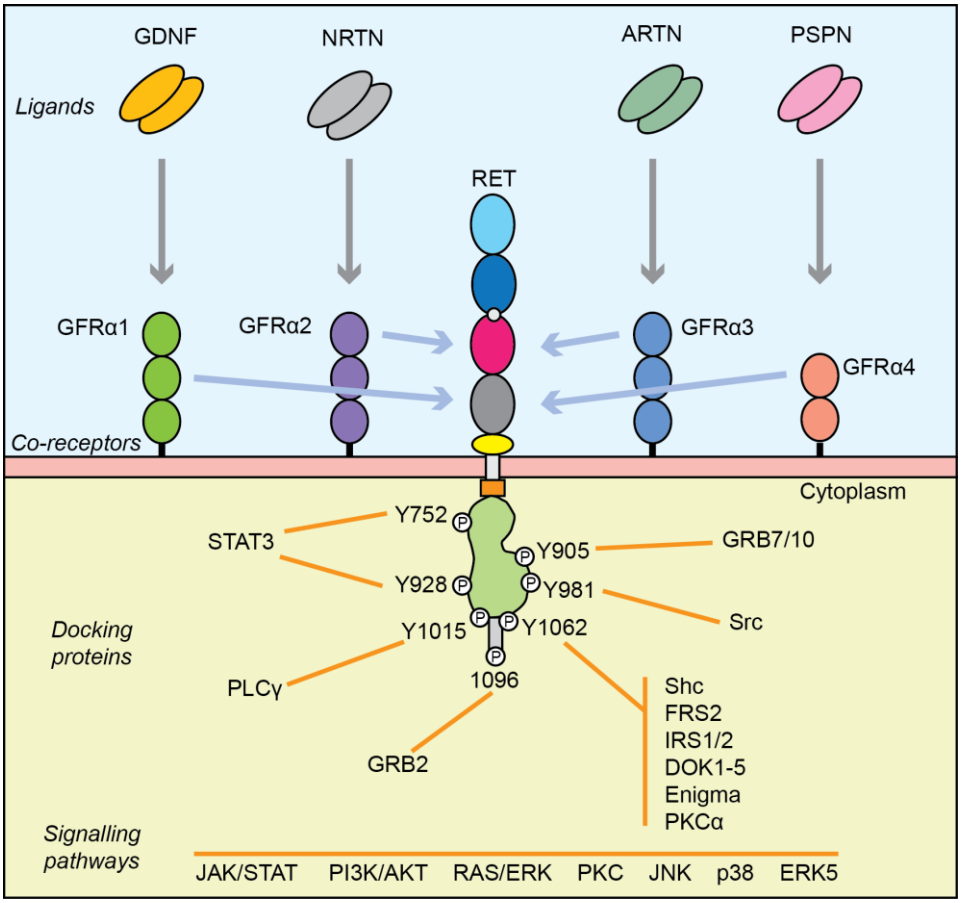

Figure 1.9 Schematic of RET/ligand/co-receptor interactions & downstream signalling pathways

Disulphide-linked homodimer ligands and their corresponding GPI-anchored co-receptor bind to RET and induce kinase activation. Tyrosine residues within RET-ICD become auto-phosphorylated and act as docking sites for scaffold and downstream signalling proteins. This recruitment leads to the activation of particular downstream signalling pathways.

There are currently two distinct models of RET/GFL/GFRα signalling. The first model involves RET and GFRα expression in the same cell, with GFRα localised to lipid rafts: signalling compartments within the membrane that have high levels of cholesterol and sphingolipids to accommodate for membrane-associated signalling molecules (Lingwood and Simons, 2010). Upon GFL/GFRα binding, GFRα recruits RET to the lipid raft, allowing for *in cis* RET activation (Sariola and Saarma, 2003). The second model is based on GFRα1 being cleaved from the membrane by phospholipases, resulting in a soluble GFRα1 that can bind to GDNF before binding to and activating RET (Paratcha and Ledda, 2008).

Alongside the canonical RET/GFL/GFRα signalling mechanism, there are several other proposed RET ligands and co-receptors. Ephrin-A has been proposed as a novel RET co-receptor, competing with GFRα1 to mediate the Ephrin-A signalling in motor axons (Bonanomi et al., 2012). It has also been shown that RET51 can be indirectly activated by nerve growth factor (NGF) in sympathetic neurons (Tsui-Pierchala et al., 2002). RET has been found to bind to and phosphorylate protocadherins – cadherin-like TM proteins – along with GDNF, suggesting that they are components of a signalling complex (Schalm et al., 2010). Independent of RET, GDNF and GFRα1 are thought to signal through the neural cell adhesion molecule (NCAM). NCAM interacts with a GDNF-GFRα dimer, leading to the activation of the Src-like kinase Fyn in the cytoplasm and Focal Adhesion Kinase (FAK) (Sariola and Saarma, 2003, Paratcha et al., 2003).

1.3.4 RET-specific signalling pathways

RET activation stimulates similar downstream signalling responses to those of other RTKs, such as the MAPK/Ras, PI3K/Akt and STAT3/JAK pathways. Activation of RET is defined by phosphorylation of its tyrosine residues within the ICD. Eight tyrosine residues (Y806, Y809, Y900, Y905, Y981, Y1062, Y1090 and Y1096) have been identified by mass spectrometry and found to be phosphorylated upon bipartite ligand binding (Kawamoto et al., 2004). Other auto-phosphorylation sites – Y687, Y752, Y928, Y1015 and Y1029 – have also been observed in separate studies (Liu et al., 1996, Salvatore et al., 2000, Schuringa et al., 2001). Y1090 and Y1096 are only found in the RET51 splice variant, due to its extended carboxy-terminus.

RET activation leads to the activation of the mitogen-activated protein kinase (MAPK) pathways (rat sarcoma oncogene/extracellular signal-related kinase (RAS/ERK), p38 MAPK and ERK5), the janus kinase/signal transducer and activator of transcription (JAK/STAT) pathway, the phosphatidylinositol-3-kinase (PI3K)/Akt pathway, a protein kinase C (PKC) pathway and the c-Jun N-terminal kinase (JNK) pathway (see Figure 1.9) (Mulligan, 2014). The phospho-tyrosine residues mentioned above act as docking sites for a host of signalling molecules, with pathway activation specific to the tyrosine residue phosphorylated.

1.3.5 Ligand and co-receptor structures

The crystal structures of GDNF from rat and human ARTN have been previously solved (Wang et al., 2006, Eigenbrot and Gerber, 1997). The structures reveal that each monomer contains a cystine knot fold between two β-sheet 'fingers' and an α-helix 'heel'. Dimerisation of the ligand results in a two-fold symmetry with intertwined 'fingers' and projecting 'heels' towards the co-receptor.

While GFL ligands are mostly specific to canonical GFRα components (GDNF-GFRα1, NRTN-GFRα2, ARTN-GFRα3, PSPN-GFRα4), there appears to be a degree of crosstalk (Airaksinen et al., 1999). GFRα1-3 contain three domains (D1-3), while GFRα4 contains only D2 and D3 (Hatinen et al., 2007). The structures of the D2-D3 domains from GFRα1 and GFRα3 have been solved, revealing a five-helix bundle constrained by disulphide bonds within each domain (Parkash et al., 2008, Wang et al., 2006). D1 is predicted to share the same fold, but is not essential for RET binding (Leppanen et al., 2004, Scott and Ibanez, 2001).

The crystal structures of GDNF-GFRα1(D2D3) and ARTN-GFRα3(D2D3) have been solved, revealing the D2 domain of GFRα binds to each projecting 'finger' region at either end of the GFL dimer (Wang et al., 2006, Parkash et al., 2008). Domain D3 makes no contacts with the GFL. GFRα1 D2-3 has been proposed as the primary RET-binding region, with several residues implicated in RET activation (Parkash et al., 2008, Scott and Ibanez, 2001). Differences in flexibility of GFL ligands when in complex with GFRα have been proposed to influence RET signalling outputs (Parkash and Goldman, 2009).

1.3.6 RET ectodomain structure

RET is the only RTK to contain calcium-dependent adhesion like domains (CLDs) and has co-opted these domains to form a binding site for its cognate ligands. The receptor contains four CLDs (CLD1-4) with a calcium-binding site conserved only between CLD2 and 3 (Schneider, 1992, Anders et al., 2001a). Other sites have lost calcium-binding function. CLD1-4 is followed by a cysteine-rich domain (CRD) that precedes the transmembrane (TM) region of the receptor.

The CLDs share similarity with extracellular cadherin (EC) domains, which adopt a seven-stranded β-barrel fold. EC domains are arranged end-to-end, with conserved calcium-binding regions at the junctions (Boggon et al., 2002, Harrison et al., 2011). Calcium binding motifs are generally composed of acidic residues (motifs: E, EN, DRE, DXNDN, DXD, D) at the junction of two consecutive cadherin domains. Indeed, the junction of CLD2-3 contains almost all of these motifs, lacking only the D. It has therefore been proposed that these two CLDs will have a linear arrangement with a calcium-binding site at the junction (Anders et al., 2001a).

The calcium-binding property of the RET-ECD is required for proper folding, processing, ligand recognition and signalling. In the absence of calcium, the receptor fails to be exported to the cell surface – potentially due to protein misfolding within the ER and subsequent degradation (van Weering et al., 1998). Further evidence for this can be found in HSCR mutations within the calcium-binding region of RET that lead to defective RET export (Pelet et al., 1998). In terms of RET signalling, it has been shown that calcium is required for GDNF-RET binding, RET KD auto-phosphorylation and activation of the downstream MAPK signalling pathway (Anders et al., 2001a, Nozaki et al., 1998).

In 2010, Dr Svend Kjaer solved the structure of human RET CLD1-2 (hRET CLD1-2) in the McDonald Laboratory (Figure 1.10) (Kjaer et al., 2010). The structure revealed a clamshell-like fold, stabilised by two disulphide bonds within CLD2 and one within CLD1. There is a hydrophobic interface between the two CLDs, with the N-terminal β-strand of CLD-1 buried within this interface. The similarity between EC domains and the RET CLDs was confirmed by the presence of a seven-stranded β-barrel fold within CLD1 and 2. Several structural elements were identified that appear to be conserved only among higher vertebrates: an anti-parallel β-strand (βC'- βC''), a short α-helix (α1) and a six-residue loop containing a *cis*-proline (*cis*-Pro loop) constrained by a disulphide bond (Kjaer et al., 2010). The *cis*-Pro loop cannot form in lower vertebrates because one of the cysteine residues is absent and an alternative 'swapped' disulphide is formed, while both cysteine residues are absent in arthropods (Figure 1.10c). These mammal-specific structural elements have been implicated in RET ternary complex formation and were found to be

involved in the hRET CLD1-2 dimeric interface (Figure 1.10b) (Kjaer and Ibanez, 2003, Kjaer et al., 2010). The implications of this evolution of RET cannot be fully understood until the structure of the human ECD is compared to that of a lower vertebrate.

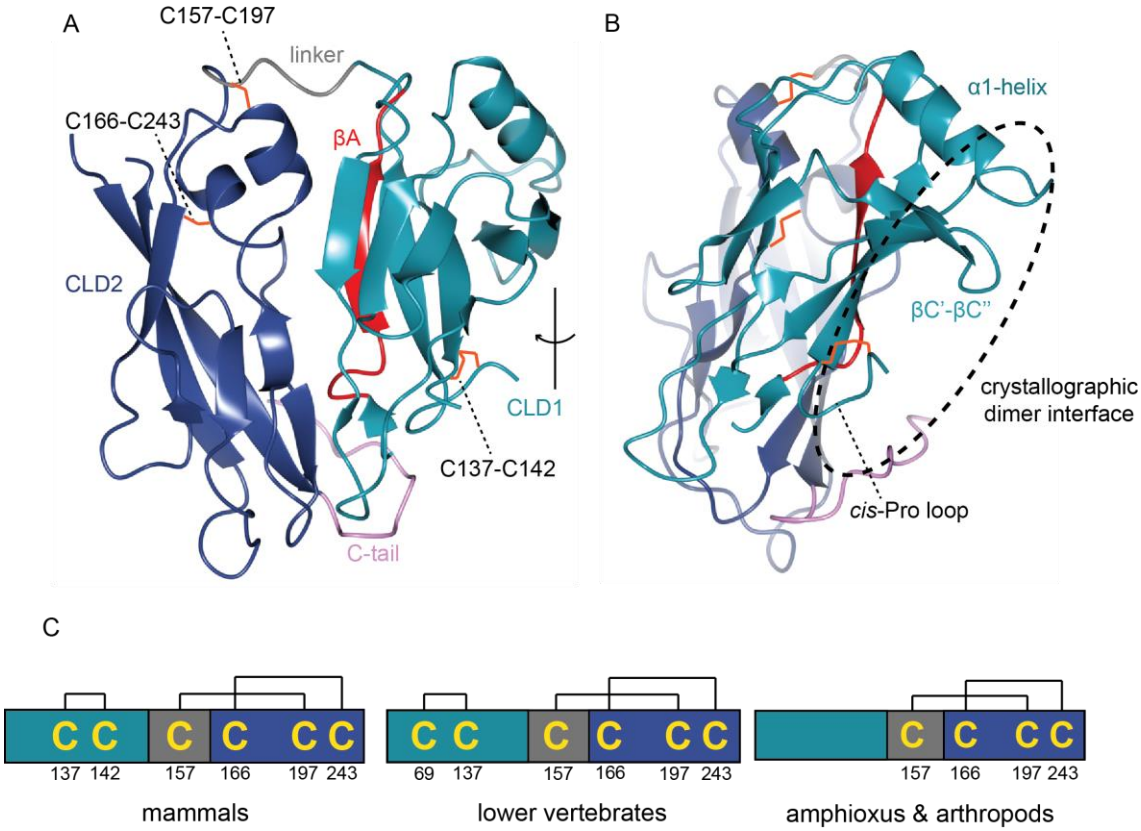

Figure 1.10 The human RET CLD1-2 crystal structure with mammal-specific structural elements and disulphide swapping
(A) Ribbon view of the hRET CLD1-2 crystal structure (PDB code 2X2U), revealing a clamshell-like arrangement of CLD1 (cyan) and CLD2 (dark blue). The N-terminal βA strand (red) is buried within the interface. Disulphide bonds are represented in orange and the C-tail is pink. **(B)** Side view of the CLD1-2 structure, revealing the crystallographic interface. The highlighted structural elements are not seen in classical cadherin structures. **(C)** Schematic representation of the disulphide bond swapping that occurs between mammalian, lower vertebrate and amphioxus/arthropod RET CLD1-2 (Kjaer et al., 2010).

1.3.7 RET ternary complex formation

As mentioned previously, RET activation requires the formation of a ternary complex comprised of a GFL homodimer, two GFRαs and two RET monomers. Several studies – the latest of which was recently published by the McDonald Laboratory – have identified regions within the receptor, ligand and co-receptor that are believed to be required for this ternary complex formation.

A previous study proposed that CLD1, 2 and 3 were required for bipartite ligand interactions and identified regions within CLD1-2 that were necessary for GDNF/GFRα1 binding. They used a loss-of-function human/*Xenopus* RET chimera to identify regions required for ligand-co-receptor binding (Kjaer and Ibanez, 2003). Three of the predicted regions within CLD1-2 were found to lie within the crystallographic dimer interface of hRET CLD1-2, consistent with the conclusion that this interface occurs within the context of GDNF-GFRα1 binding (Figure 1.10b) (Kjaer et al., 2010). A subsequent study – based on mass spectrometry of the cross-linked ternary complex – found three interactions between RET, GDNF and GFRα1 that were not present between ligand and co-receptor alone (Amoresano et al., 2005). These interactions were all localised to the GFRα1 domain D1, which cross-linked with RET CRD, the N-terminus of GDNF and the base of CLD4. Interestingly, the primary RET binding region within GFRα1 D2-3 was not identified. They also showed that CLD4-CRD is important for ternary complex formation, as RET CLD1-3 could not compete with RET for GDNF-GFRα1 binding.

A more recent structural analysis has led to the creation of an EM structural model of the RET ECD-GDNF-GFRα1 ternary complex, providing an insight into the basis of RET ligand recognition (Figure 1.11). Coordinates for the GFRα1D2-D3-GDNF dimeric ligand (PDB code 3FUB) were placed into the model by aligning the bipartite ligand symmetry axis with the 2-fold symmetry axis of the EM map. This resulted in the bipartite ligand being placed in the centre of the complex, with GDNF closest to the base of the electron density map. The position of RET CLD1-4 could be identified from architectural knowledge obtained from the zebrafish SAXS-derived model. The interdomain CLD angles observed in zebrafish RET CLD1-4 SAXS data were preserved within the EM map, validating the SAXS-derived model and confirming the position of CLD1-4 within the map (Goodman et al., 2014 (In press)).

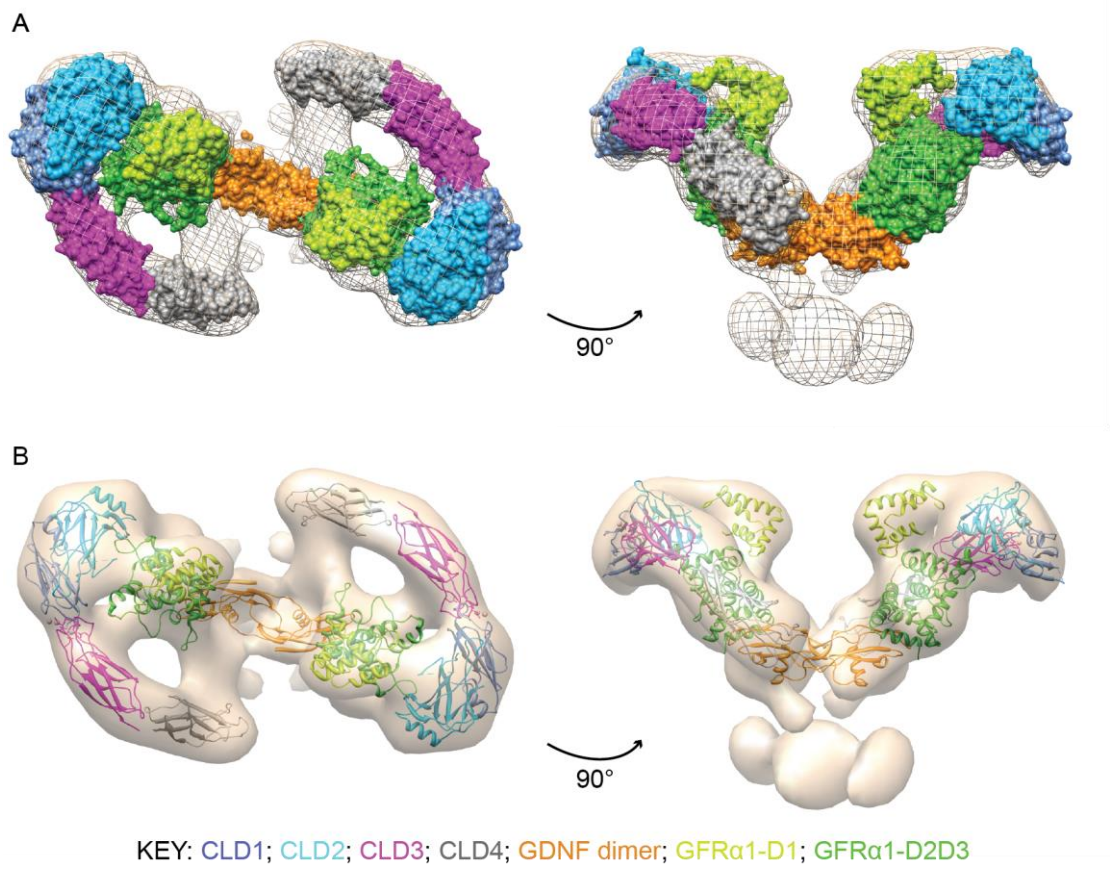

Figure 1.11 Model of RET/GDNF/GFRα1 ternary complex derived from EM map

(A) Grid view of mammalian ternary complex reconstitution in figure-of-eight (left) and wing (right) positions. Structures of RET, GDNF and GFRα1 (surface view) are fitted into the map. **(B)** Surface view of the mammalian ternary complex reconstitution with structures of RET, GDNF and GFRα1 (ribbon view) fitted in.

1.3.8 RET kinase domain structure and regulation

The binding of GFL/GFRαs to the RET ECD results in rapid auto-phosphorylation of the RET KD and subsequent activation RET-specific downstream signalling pathways. To understand the molecular mechanisms involved, I will first discuss what is currently known about the structure of the RET KD. The structures of the non- and phosphorylated forms of the RET KD were elucidated in 2006 by the McDonald Laboratory (Knowles et al., 2006). The bilobal domain comprised of the canonical protein kinase structural elements: an N-lobe consisting of five anti-parallel β-strands and the αC helix between strands β3 and β4, a flexible GRL above the nucleotide-binding pocket, and a predominantly helical C-lobe.

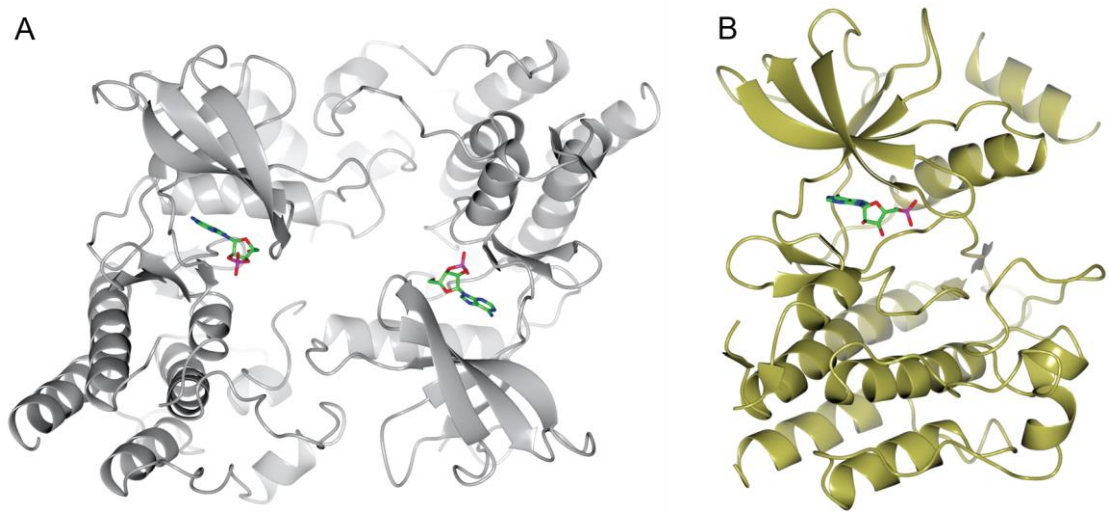

Figure 1.12 Two structural orientations of the RET KD

(A) Ribbon view of non-phosphorylated RET (light grey) as two protomers within the asymmetric unit related by non-crystallographic symmetry, with 2',3'-cAMP in the active site (PDB code 2IVS) **(B)** Ribbon view of phosphorylated RET (gold) in a head-to-tail dimer containing a single monomer, with AMP in active site (PDB code 2IVT) (Knowles et al., 2006).

Published crystal structures (Figure 1.12b) of the RET KD revealed a head-to-tail crystallographic dimer (or in some cases a non-crystallographic symmetry (NCS) dimer, Figure 1.12a) (Knowles et al., 2006, Mologni et al., 2010). The appearance of this RET KD dimer led to the hypothesis that the dimer interface could be relevant *in vivo*, as the formation would occlude the substrate binding region and prevent kinase activity through a *trans*-inhibitory mechanism (Knowles et al., 2006). This dimer has not yet been validated.

1.4 The role of RET in human disease

RET is a critically important RTK, due to its involvement in the development of a number of human diseases, as discussed earlier. The receptor appears to have several signalling thresholds that dictate the phenotypic outcome: excessive signalling through over-expression or constitutive activation results in the development of a number of cancers, while reduced RET signalling leads to Hirschsprung's disease in humans. The absence of RET is embryonically lethal in knockout studies due to the lack of kidney development.

1.4.1 Loss-of-function mutations and Hirschsprung's disease

Harold Hirschsprung first described Hirschsprung's disease (HSCR) in 1888, when two boys died of severe constipation resulting from congenital megacolon (abnormal dilation of the colon) (Hirschsprung, 1888). However, the absence of intramural ganglion cells in the colon was not identified as the cause of the disease until the mid-20th century (Whitehouse and Kernohan, 1948). HSCR is now defined as a congenital malformation of the colon, caused by an absence of enteric ganglia within the length of the hindgut (Amiel et al., 2008). HSCR can be divided into three subtypes dependent on the severity of the phenotype: short-segment HSCR, where the rectum and anus are affected by aganglionosis; long-segment HSCR, where a larger proportion of the colon is affected; and total colonic aganglionosis, the most severe form lacking a functional enteric nervous system for the entire colon (N-Fek, 1986, Neilson and Yazbeck, 1990).

While the *RET* gene is most commonly mutated in HSCR – accounting for approximately half of familial cases and 15-20% of sporadic cases – there are several other genes implicated in HSCR development: *GDNF*, *NRTN*, *endothelin receptor B (EDNRB)*, *endothelin 3 (ET-3)*, *endothelin-converting enzyme 1 (ECE1)*, *SOX10*, and *ZFHX1/SIP1* (Asai et al., 2006, Heanue and Pachnis, 2007). A large number of loss-of-function RET mutations have been associated with the development of HSCR and can be separated into five classes (Figure 1.13) (Plaza-Menacho et al., 2006, Carlomagno et al., 1996).

Class one mutations are found within the RET ECD and affect the transport of the receptor to the cell surface. It is believed that this reduction in cell surface expression is caused by a lack of proper folding and processing within the ER, and some of the mutations have been shown to affect calcium-binding and N-linked glycosylation (Kjaer et al., 2010, Kjær and Ibanez, 2003b, Pelet et al., 1998). Kjaer *et al.* developed a mammalian RET ECD secretion assay to investigate the effect of a range of HSCR mutations (Kjaer et al., 2010). Mass spectrometry was used to identify unpaired cysteine residues in the recombinant protein that may be involved in the formation of aberrant disulphide bonds during protein folding. Two unpaired cysteine residues were subsequently mutated (C87R and C216S) in an effort to

improve protein folding and export. Their mutation led to the export of some HSCR mutant forms of the RET ECD that were usually exported unsuccessfully.

The severity of the disease phenotype was found to correlate with the ability of the cysteine mutations to restore RET export: RET G93S (a mutant that causes total colonic aganglionosis, a very severe disease phenotype) could not be rescued through the elimination of the unpaired cysteines, while the export of RET S100M (a mutation resulting in a milder disease phenotype) could be completely restored.

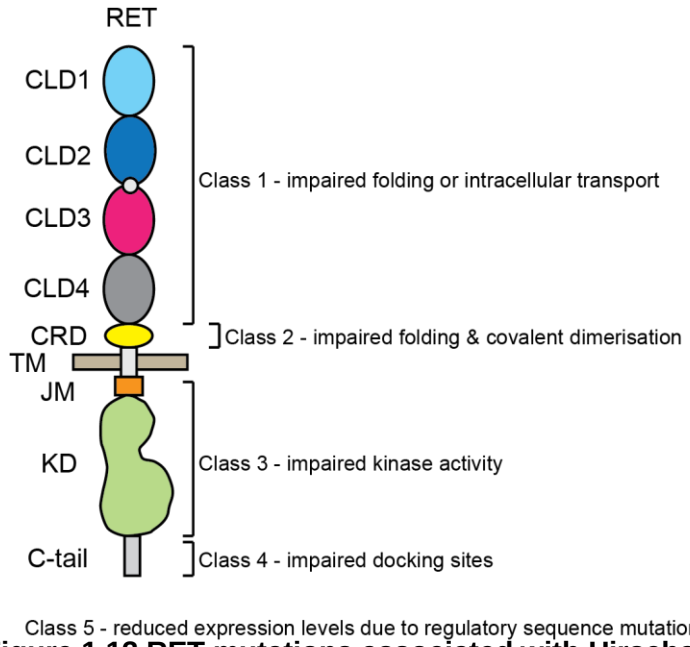

Figure 1.13 RET mutations associated with Hirschsprung's disease

Point mutations associated with Hirschsprung's disease can be divided into five classes, four of which can be localised to a region of the RET receptor. CLD – cadherin like domain; CRD – cysteine rich domain; TM – transmembrane domain; JM – juxtamembrane domain; KD – kinase domain; C-tail – carboxy-terminal tail. Figure adapted from (Plaza-Menacho et al., 2006).

Class two mutations are located within the CRD and result in the presence of an unpaired cysteine residue. This unpaired cysteine can cause reduced folding efficiency, resulting in a loss of receptor export, but it can also cause covalent dimerisation. This dimerisation can lead to constitutive activation of the receptor, as seen in multiple endocrine neoplasia type 2A (MEN2A). These are more complex mutant phenotypes, as the families affected can demonstrate the occurrence of both HSCR and MEN2A (Kjær and Ibanez, 2003b, Pelet et al., 1998).

Class three mutations are found within the kinase domain of the receptor and disrupt the kinase activity. They tend to target essential catalytic residues, charged residues or bulky hydrophobic groups (Knowles et al., 2006). Class four mutations also affect the activity of the receptor by targeting docking sites within the C-terminal tail, disrupting downstream signalling events (Geneste et al., 1999). Finally, class five mutations are located within the regulatory sequences within introns separating exons of the *RET* gene, reducing *RET* expression levels.

1.4.2 RET gain-of-function mutations and MEN2

Medullary thyroid carcinoma (MTC) is a malignant cancer that arises from calcitonin-producing thyroid parafollicular C cells, with around 25% of cases being familial. The carcinoma is a component of multiple endocrine neoplasia 2 (MEN2), a syndrome divided into three disorders: MEN2A, MEN2B and familial MTC (FMTC) (Santoro and Carlomagno, 2013, Donis-Keller et al., 1993, Hofstra et al., 1994). FMTC is characterised by the presence of MTC itself, while MEN2A is characterised by MTC, pheochromocytoma, or parathyroid hyperplasia/adenoma. MEN2B is the most aggressive of the three subtypes, with an earlier MTC onset and pheochromocytoma. Other developmental problems can arise as well, including mucosal neuromas, intestinal ganglioneuromatosis, and ocular and skeletal abnormalities (Arighi et al., 2005). RET mutations that are associated with MEN2 have been schematically annotated in Figure 1.14.

MEN2A mutations target the extracellular cysteine residues, with the most common being C634. These CRD-localised mutations result in disulphide-linked homo-dimerisation of the receptor and subsequent constitutive activation (Santoro et al., 1995). The ability of the RET TM regions to self-associate has been shown to underlie this oncogenic activity, as homo-dimerisation via the TM brings the unpaired cysteine residues within the CRD in close proximity with one another (Kjaer et al., 2006). There are suggestions that RTK signalling may not be as simple as the current dimerisation model, and could involve oligomerisation of many dimers at the cell surface (Wu, 2013). As such, the CRD-localised mutations may also increase the prevalence of this oligomerisation at the plasma membrane and lead to heightened activation. As mentioned above, the mutation of some

cysteine residues – C609, C611, C618 and C620 – cause constitutive activation and poor protein folding, resulting in both MEN2A and HSCR (Ito et al., 1997).

In contrast, MEN2B arises from mutations within the RET KD: M918T (95% of cases) and A883F (5%) (Carlson et al., 1994, Smith et al., 1997). These mutations result in a monomeric onco-protein that can signal independently of ligand, although the mechanism by which this occurs is not well understood. The highly conserved M918 maps to the substrate binding P+1 loop of the RET KD and may therefore play a role in substrate selection. For example, the RET M918T mutation within this P+1 loop has been show to result in constitutively phosphorylated STAT3 (Yuan et al., 2004). Recent investigations suggest that the mutation destabilises RET, making it a better substrate for auto-phosphorylation (Plaza-Menacho et al., 2014).

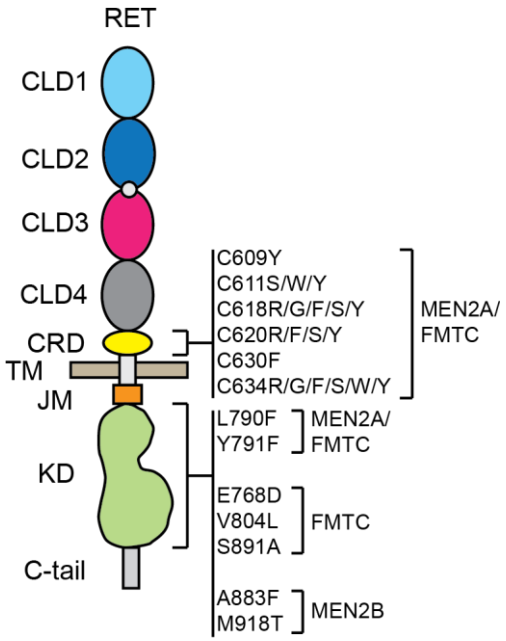

Figure 1.14 RET point mutations associated with cancer

RET schematic with point mutations associated with particular syndromes highlighted. Clinical mutations observed are reported in (Plaza-Menacho et al., 2006, Kodama et al., 2005).

1.4.3 RET fusion mutations and thyroid cancer, lung cancer and leukaemia

A further mechanism of RET deregulation causing disease is found in the case of RET fusion proteins that have been observed in papillary thyroid carcinoma (PTC).

PTC is the most common thyroid cancer and arises from follicular cell tumours that are both benign adenomas and metastatic carcinomas (Arighi et al., 2005). Somatic chromosomal rearrangement results in the fusion of the *RET* kinase region with several genes, creating fusion oncogenes known as *RET/PTC.* 11 *RET/PTC* oncogenes have been identified to date, with fusions to the coiled-coil domain containing gene 6 (*CCDC6*) or nuclear receptor co-activator gene 4 (*NcoA4*) accounting for over 90% of the rearrangements (Santoro et al., 2006). More recently, RET fusion proteins have also been implicated in the development of non-small cell lung cancer (NSCLC) and chronic myelomonocytic leukaemia (CMML) (Ballerini et al., 2012, Takeuchi et al., 2012, Kohno et al., 2012, Lipson et al., 2012). The presumption is that forced dimerisation of the kinase domains results in activation.

1.4.4 Over-expression of RET in breast and colorectal cancer

RET overexpression has been reported in a number of different cancers, including prostate, pancreatic, bile duct, lung and breast cancer (Morandi et al., 2011, Zeng et al., 2008, Dawson et al., 1998). Aberrant RET expression has been investigated further in the case of breast cancer and was found to be specifically associated with oestrogen receptor (ER)-positive breast cancer (Plaza-Menacho et al., 2010, Boulay et al., 2008, Esseghir et al., 2007). RET activation was found to result in oestrogen-independent activation of the ERα, facilitating resistance to endocrine therapy (Plaza-Menacho et al., 2010).

In contrast, RET is believed to play an opposite role as a tumour suppressor in colorectal cancer (Luo et al., 2012). Aberrant methylation of *RET* was found to occur in 27% of colon adenomas and 63% colorectal cancers, with the methylation correlating with reduced RET expression. Furthermore, inactivating *RET* mutations were found in primary colorectal cancer and RET overexpression resulted in apoptosis in colorectal cancer cell lines.

1.5 Targeted therapy towards tyrosine kinases in cancer

The crucial and highly regulated role protein tyrosine kinases play in cell signalling has resulted in their implication in almost every type of cancer. Tyrosine kinases

are therefore highly targeted for cancer therapy development, with a large proportion of that research and development focusing on small molecule ATP pocket inhibitors. The development of Imatinib, a small molecule ATP-competitive inhibitor of the ABL kinase that was first used to treat chronic myeloid leukaemia, pioneered this area of therapy (Druker et al., 2001). Since this time, targeted therapy through the design of specific RTK inhibitors is becoming increasingly prevalent. While a great deal of effort has led to the development of ATP-competitive inhibitors, the high level of sequence conservation within the nucleotide-binding region of tyrosine kinases makes specific inhibitor design extremely challenging. Allosteric inhibitors, RTK ECD-targeted antibodies, aptamers and protein substrate mimics are proving useful alternative strategies (Cowan-Jacob et al., 2009).

RET is a validated cancer target and is a driver of MEN2A & B, FMTC, NSCLC and breast cancers. There were no approved treatments for inoperable MTC until the development of Vandetanib (ZD6474): a small molecule ATP-competitive RET and VEGFR2/3 inhibitor (Thornton et al., 2012, Carlomagno et al., 2002a). The success of Vandetanib as a treatment of MTC has validated RET as a cancer target, but the high number of adverse reactions and poor life expectancy extension of only 6 months in advanced MTC survival suggest that better treatments need to be developed (Thornton et al., 2012).

1.5.1 Chemical inhibition of kinases

Small molecule inhibitors that target the nucleotide-binding pocket of tyrosine kinases can be divided into two groups: type I *DFG-in* inhibitors and type II *DFG-out* inhibitors. Type I inhibitors target the hydrophobic region usually occupied by the adenine ring of ATP, forming multiple hydrogen bonds with the kinase hinge between the N and C lobes (Liu and Gray, 2006). In the presence of type I inhibitors, the conserved DFG motif located at the start of the activation loop is in the active *DFG-in* conformation (Figure 1.15). Several published structures of the RET KD bound to type I inhibitors are available (e.g. PP1 and Vandetanib), with novel structures presented in this thesis (Knowles et al., 2006, Mologni et al., 2010). Type II inhibitors (e.g. Sorafenib) also target the ATP pocket, but displace the DFG

motif into the catalytically incompetent *DFG-out* conformation, disrupting the formation of the hydrophobic R-spine (Liu and Gray, 2006). At present, attempts to crystallise the RET KD bound to a *DGF-out* inhibitor have been unsuccessful. Therefore, models for Sorafenib binding have been built from other RTK-Sorafenib structures, such as VEGFR-2 (McTigue et al., 2012).

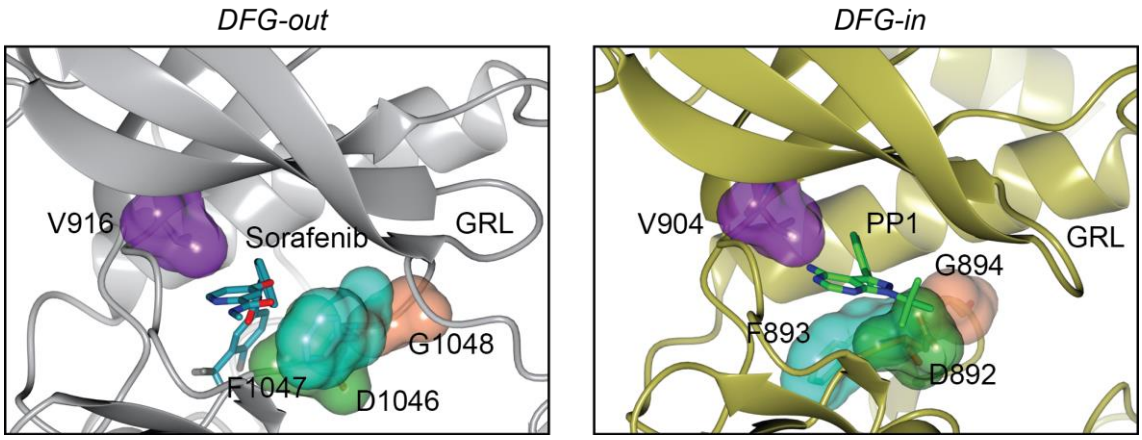

Figure 1.15 Arrangement of the DFG motif in kinases bound to type I and II inhibitors
The left panel displays the *DFG-out* conformation of the VEGFR-2 kinase domain bound to the type II inhibitor Sorafenib (PDB code 4ASD). The right panel displays the *DFG-in* conformation of the RET kinase domain bound to the type I inhibitor PP1 (PDB code 2IVV). The gatekeeper residue is highlighted in purple, and the D (green) F (cyan) G (coral) motif is annotated – along with the GRL – for both kinases.

1.5.2 Clinically approved RET inhibitors

There are several small molecule inhibitors that were originally designed for other tyrosine kinases and have been found serendipitously to target RET. These include: Vandetanib (RET/VEGFR/EGFR), Sorafenib (RET/BRAF/VEGFR/FLT3), Sunitinib (RET/VEGFR/FLT3), Cabozantinib (RET/MET/VEGFR/KIT) and Motesanib (RET/VEGFR/KIT) (Borrello et al., 2013). Vandetanib is an aminoquinazoline compound that has been FDA approved for the treatment of MTC and has been found to be active against the wild-type and M918T mutant form of RET. The inhibitor cannot inhibit RET when the gatekeeper mutation V804M or V804L is present, presumably due to the fact that it binds into the back of RET's ATP pocket behind the gatekeeper residue and would be blocked from binding in the case of a bulky gatekeeper mutation (Carlomagno et al., 2004, Knowles et al., 2006). Sorafenib is a bisarylurea compound that was originally developed against the serine/threonine kinase BRAF and has since been found to

be active against several tyrosine kinases, including RET (Wilhelm et al., 2006). The inhibitor has been FDA approved for the treatment of liver and kidney cancers, and has been found to be active against RET-V804M *in vitro* (Plaza-Menacho et al., 2007). Sunitinib is an indolinone approved for the treatment of Imatinib-resistant GISTs (gastrointestinal stromal tumours), advanced pancreatic and renal cancer. Interestingly, the inhibitor has been found to bind to the KIT KD in the inactive *DGF-out* conformation, while targeting RET in the active *DFG-in* conformation (Goodman, unpublished) (Gajiwala et al., 2009).

1.6 Project Aims

A large number of RET mutations are associated with the development of Hirschsprung's disease. Previous work has demonstrated that the HSCR RET mutations can result in a bottleneck in RET folding and a loss of RET export. Relatively little is known about why RET is so inefficiently folded, despite the obvious relevance to human disease. As such, this thesis aims to further understanding around how RET proceeds from a nascent polypeptide to a cell surface glycoprotein and identify how HSCR RET mutants are targeted by ER quality control mechanisms. A cell-based immunofluorescence assay that could be used to study RET folding, maturation and trafficking to the cell surface was developed. The assay was used to identify factors involved in RET folding, maturation and trafficking, with the aim to understand whether the factors identified could be involved in the development of Hirschsprung's disease.

Secondly, RET is recognised as a valid cancer target. While several FDA-approved RET inhibitors are available, their lack of specificity and potency suggests that the development of a new generation of RET inhibitors is required. This thesis aims to aid this development through the elucidation of the structure of the RET KD bound to several ATP-competitive inhibitors that can be separated into distinct chemical scaffolds. The high-resolution structures presented could be used to explain biochemical and cellular IC_{50} data and define key inhibitor-residue interactions, thus informing further rounds of scaffold modification with the aim of enhance potencies against RET.

Chapter 2. Materials & Methods

2.1 Materials

2.1.1 Reagents

All reagents were purchased from Sigma-Aldrich unless otherwise stated. All primers were obtained from Sigma-Aldrich and all restriction enzymes were from New England Biolabs (NEB).

Reagent	Source
Agarose	UltraPure, Invitrogen
dNTPs	100 mM stock, Invitrogen
Lullaby transfection reagent	OZ Biosciences
Effectene transfection reagent	Qiagen
FuGENE HD transfection ragent	Promega
Full range rainbow marker	Spectra Multicolor, Thermo Scientific
Filter paper	3M
Enhanced Chemiluminescence (ECL) solution	Luminata Classico, Millipore
Nitrocellulose membrane	Amersham HyBond, GE Healthcare
Chemiluminescence film	Amersham Hyperfilm, GE Healthcare
KOD polymerase	Novagen
NuPAGE 4-12% Bis-Tris Gels	Life Technologies
Competent E.coli	NovaBlue, prepared - Promega method - in house (original source: Novagen)
Crystallisation additive screen	Hampton Research
MRC 2 drop 96 well trays	SwissCi
Crystal loops	MiTeGen
Polyperfluoroether oil	Hapton Research
SYPRO Orange Dye	Invitrogen molecular probes (Lot 980228)
rtPCR 96 well trays	MicroAmp Fast Optical, Life Technologies
Glutathione sepharose 4B	GE Healthcare
Vivaspin columns	Sartorius stedium biotechnology
Protein G sepharose beads	GE Healthcare
Express 35S Protein Labeling Mix	PerkinElmer
Coomassie stain	Phastgel Blue, GE Healthcare
PCR tubes	Thermo Scientific
Bradford assay solution	BioRad

Table 2.1 Reagents & consumables

Buffer	Preparation
LB medium	5 g Bacto yeast extract, 10 g Bacto-tryptone, 10 g NaCl, volume adjusted to 1 l with water, autoclaved
LB agar	6 g agar, 400 ml LB medium, autoclaved
SOC medium	20 g Bacto-tryptone, 5 g Bacto yeast extract, 10 mM NaCl, 2.5 mM KCl, 10 mM MgSO4, 20 mM D-glucose, volume adjusted to 1 l with water, autoclaved
DNA 6x sample buffer	0.25% bromophenol blue, 30% (v/v) glycerol
TAE	40 mM Tris-acetate, 0.1 M EDTA
TBS	50 mM Tris HCl, 150 mM NaCl pH 7.5
TBST	TBS and 0.1% (v/v) Tween-20
PBS	8 g NaCl, 0.2 g KCl, 1.44 g Na_2HPO_4, 0.24 g KH_2PO_4, pH 7.4 (with HCl), volume adjusted to 1 l with water, autoclaved
MOPS SDS-PAGE	1x MOPS (NuPAGE, Invitrogen) in water
Transfer buffer	25 mM Tris base, 129 mM Glycine, 10% methanol
Mammalian cell lysis buffer	1% Triton-X100, 20mM Tris (pH 8), 130 mM NaCl, Protease Inhibitor (CoMplete, Roche), Phosphatase Inhibitor Cocktail 2 (SIGMA)
Insect cell lysis buffer	20 mM Tris (pH 8), 100 mM NaCl, 1 mM DTT, 10 mM Benzamidine, 0.2 mM ABSF
RET KD purification buffer	20 mM Tris (pH 8), 100mM NaCl, 1 mM DTT
RET KD TSA purification buffer	20 mM HEPES (pH 8), 100 mM NaCl, 1 mM DTT
Poly-D-Lysine in PBS	10% (v/v) Poly-D-Lysine (SIGMA) in PBS
Immunofluorescence (IF) fixing buffer	3.65% Formaldehyde (SIGMA) in PBS
IF blocking buffer	3% Bovine Serum Albumin (BSA) in PBS
IF staining buffer	1% BSA in PBS
Western blot (WB) buffers	5% (w/v) dried skimmed milk powder (Marvel) in TBST
LDS sample buffer (4x)	Novex®, Life technologies

Table 2.2 Buffers & media

Reagent	Preparation	Provided by
Inhibitor 1	10 mM in 100% DMSO	Dr Nathanael Gray, Harvard Medical School
Inhibitor 3	3.3 mM in 100% DMSO	Dr Allan Jordan, Paterson Institute for Cancer Research UK
Inhibitor 4	25 mM in 100% DMSO	Professor Morten Grötli, University of Gothernburg
Inhibitor 5	10 mM in 100% DMSO	Dr Nathanael Gray, Harvard Medical School
Inhibitor 6	10 mM in 100% DMSO	Dr Nathanael Gray, Harvard Medical School
Inhibitor 7	10 mM in 100% DMSO	Dr Nathanael Gray, Harvard Medical School
Inhibitor 8	10 mM in 100% DMSO	Dr Nathanael Gray, Harvard Medical School
Inhibitor 9	10 mM in 100% DMSO	Dr Nathanael Gray, Harvard Medical School
Inhibitor 10	10 mM in 100% DMSO	Dr Nathanael Gray, Harvard Medical School
Inhibitor 11	10 mM in 100% DMSO	Dr Nathanael Gray, Harvard Medical School
Inhibitor 18 (PP242)	20 mM in 100% DMSO	Selleckchem
Inhibitor 19 (BMS-536924)	20 mM in 100% DMSO	Selleckchem
PP1	10 mM in 100% DMSO	Sigma-Aldrich
Vandetanib	10 mM in 100% DMSO	Selleckchem
Sorafenib	100 mM in 100% DMSO	AK Scientific Inc
Pz-1	100 mM 100% DMSO	Dr Hong-Yu Li, University of Arizona
Sunitinib	37 mM in 100% DMSO	Sigma-Aldrich
Epoximicin	1 µM in 100% DMSO	Sigma-Aldrich
Pitstop2	10 µM in 100% DMSO	Abcam
17-AAG	1 µM in 100% DMSO	Sigma-Aldrich
TBK1 inhibitor (MRT67307)	1 µM in 100% DMSO	Professor Sir Philip Cohen, University of Dundee
TBK1 control inhibitor (MRT199665)	1 µM in 100% DMSO	Professor Sir Philip Cohen, University of Dundee
Recombinant human GDNF	100 µg/ml in sterile PBS + 0.1% BSA	R&D System, 212-GD
Recombinant human GFRα1	100 µg/ml in sterile PBS + 0.1% BSA	R&D Systems, 714-GR

Table 2.3 Pharmacological agents & recombinant reagents

Antibody target	Subset	Description	Source & code	Use	Dilution
RET	mAb718	Mouse monoclonal (Clone 132507)	R&D systems, MAB718	WB	1:500
	C20	Goat polyclonal	Santa Cruz Biotechnology, sc-1290	WB	1:1000
	1D9	Mouse monoclonal	Massimo Santoro (Salvatore et al., 2002)	IF/FACS	1:40
	23C	Mouse monoclonal	In house, Dr Svend Kjaer	IF	
phospho-RET	pYpan	Mouse monoclonal (Clone 4G10)	Millipore, 05-321	WB	1:1000 (WB)
	pYpan	Mouse monoclonal	Santa Cruz Biotechnology, sc-7020	IF	1:100
	pY1062	Rabbit polyclonal	Santa Cruz Biotechnology, sc-20252-R	WB/IF	1:1000 (WB) 1:100 (IF)
phospho-ERK1 (pThr202/pTyr204)/2(pThr185/pTyr187)		Rabbit polyclonal	Sigma-Aldrich, E7028	WB/IF	1:1000 (WB) 1:100 (IF)
ERK1/2		Rabbit polyclonal	Sigma-Aldrich, M5670	WB	1:10000
Actin		Mouse monoclonal (Lot E0610)	Santa Cruz Biotechnology, sc-4778	WB	1:1000
phospho-Akt (Ser473)		Rabbit monoclonal (193H12)	Cell Signaling, 4058	WB	1:1000
Akt		Rabbit polyclonal	Cell Signaling, 9272	WB	1:1000
CHIP		Mouse monoclonal (Clone ST21.55)	Sigma-Aldrich, S1073	WB	1:500
Ube2D1		Rabbit polyclonal	Boston Biochem, A-615	WB	1:500
BiP		Rabbit monoclonal (C50B12)	Cell Signaling, 3177	WB	1:1000
PERK		Rabbit monoclonal (D11A8)	Cell Signaling, 5683	WB	1:1000
Calnexin		Rabbit monoclonal (C5C9)	Cell Signaling, 2679	WB	1:1000

Secondary antibodies	Description	Source & code	Use	Dilution
Alexa® Fluor 488 (anti-mouse)	Donkey polyclonal	Abcam, ab150105	IF/FACS	1:2000
Alexa® Fluor 488 (anti-rabbit)	Donkey polyclonal	Abcam, ab150073	IF	1:2000
Anti-mouse HRP	Goat anti-mouse IgG linked to HRP	Santa Cruz Biotechnology, sc-2031	WB	1:10000
Anti-rabbit HRP	Goat anti-rabbit IgG linked to HRP	Santa Cruz Biotechnology, sc-2030	WB	1:10000
Anti-goat HRP	Mouse anti-goat IgG linked to HRP	Santa Cruz Biotechnology, sc-2354	WB	1:10000

Table 2.4 Primary and secondary antibodies

Item	Preparation	Source
SfIII insect cell media		Invitrogen
Dulbecco's Modified Eagle Medium 1x (DMEM)		Gibco, Life Technologies
Met/Cys-free DMEM		Gibco, Life Technologies
Foetal Bovine Serum (FBS)		Sigma-Aldrich
Penicillin/Streptomycin (PenStrep) 100x		LRI laboratory services
Trypsin		LRI laboratory services
Hygromycin B	50 mg/ml in water	Sigma-Aldrich
Zeocin	100 mg/ml in water	Invitrogen
Blasticidin	10 mg/ml in water	Sigma-Aldrich
Doxycycline hyclate	50 mg/ml in water	Sigma-Aldrich
Gentamicin	10 mg/ml	Gibco, Life Technologies

Table 2.5 Media and antibiotics

2.1.2 Plasticware

All plasticware was purchased from Corning International unless otherwise stated. 96 well plates used for immunofluorescence were obtained from Nunc, Thermo Scientific (96 well optical bottom, polymer base, black).

2.2 Methods

2.2.1 Cell culture

2.2.1.1 Mammalian cell lines

The Flp-In system was utilised in order to create stably transfected mammalian cells that could express various RET species upon the addition of doxycycline (Figure 2.1). Hek293 FlpIn cell lines expressing WT, S100M and S100M* (S100M/C87R/C216S) RET were previously generated by Dr Svend Kjaer (McDonald Laboratory, London Research Institute), with methods detailed in section 2.2.1.3 (Kjaer et al., 2010). DLD-1 and HeLa FlpIn cells were kindly donated by Professor Stephen Taylor (University of Manchester).

Antibiotic requirments of each cell line (µl per 15 ml media)				
Cell line	**Hygromycin (50mg/ml)**	**Blasticidin (10 mg/ml)**	**Zeocin (100 mg/ml)**	**Created by**
Hek293 FlpIn		3.75	30	Dr Svend Kjaer, London Research Institute
Hek293 WT RET	45	3.75		Dr Svend Kjaer, London Research Institute
Hek293 WT* RET	45	3.75		Dr Svend Kjaer, London Research Institute
Hek293 S100M RET	45	3.75		Dr Svend Kjaer, London Research Institute
Hek293 S100M* RET	45	3.75		Dr Svend Kjaer, London Research Institute
DLD-1 FlpIn		12	9	Professor Stephen Taylor, University of Manchester
DLD-1 WT RET	120	12		Emily Burns, London Research Institute
DLD-1 S100M RET	120	12		Emily Burns, London Research Institute
HeLa FlpIn		6	7.5	Professor Stephen Taylor, University of Manchester
HeLa WT RET	60	6		Emily Burns, London Research Institute
HeLa S100M RET	60	6		Emily Burns, London Research Institute
HeLa S100M* RET	60	6		Emily Burns, London Research Institute

Table 2.6 Mammalian cell lines and antibiotic requirements

2.2.1.2 Tissue culture

All cells were grown in T25 flasks, passaged twice every week and were cultured at 37 °C with 10% CO_2. All cells were cultured in DMEM with 10% FBS and PenStrep. Individual antibiotic requirements for each cell line are outlined in the Table 2.6.

2.2.1.3 Establishing stable cell lines

Stable DLD-1 and HeLa FlpIn cell lines expressing WT, S100M (HeLa) and S100M* (DLD-1) were generated as per the Flp-In™ T-Rex™ guidelines. Initially, the pFRT/lacZeo plasmid is randomly integrated into the genome to generate the zeocin-resistant host cell line. This is followed by co-transfection with the pcDNA5/FRT expression vector containing the gene of interest (GOI) and the pOG44 plasmid. Flp recombinase, found within the pOG44 vector, catalyses a homologous recombination event between the FRT sites in the pFRT/lacZeo and pcDNA5/FRT vectors, allowing integration of pcDNA5/FRT. The end result is a stable mammalian cell line that is hygromycin resistant, zeocin sensitive and expresses a gene of interest upon incubation with doxycycline. Successful clones were expanded and tested for zeocin sensitivity and gene expression prior to selection.

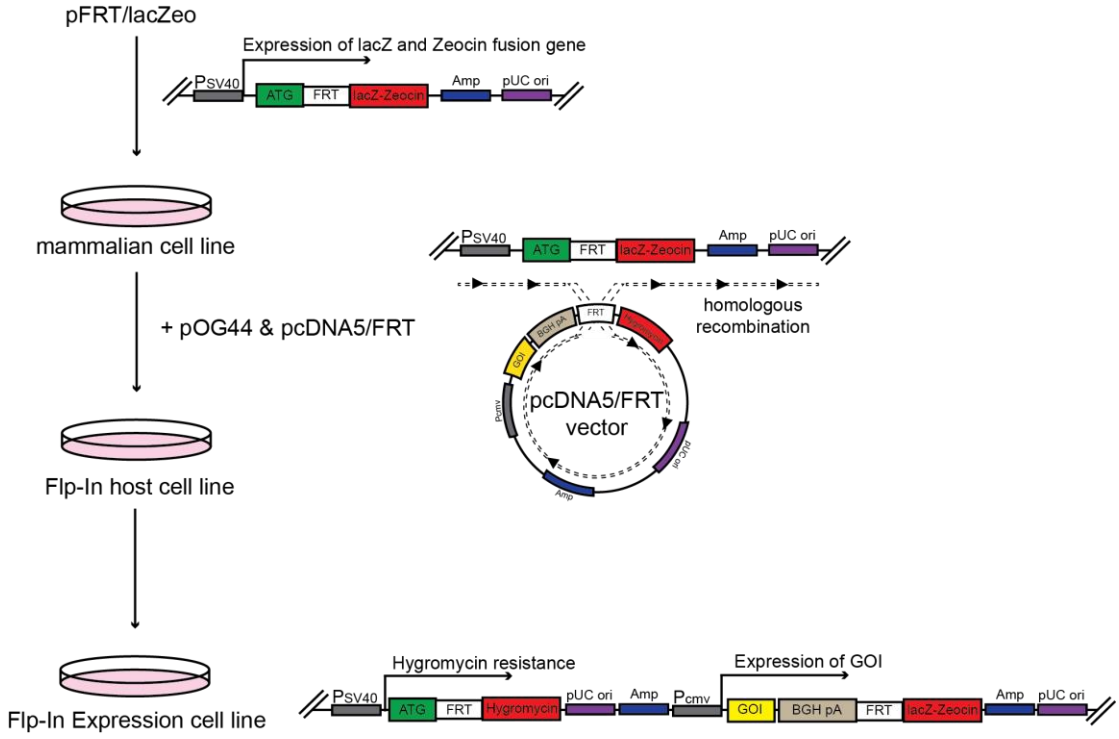

Figure 2.1 Establishment of the Flp-In mammalian cell expression system

The three separate vectors required during the establishment of an inducible mammalian cell line expressing a gene of interest (GOI). Figure adapted from Life Technologies.

Briefly, the Flp-In cell lines (courtesy of Professor S Taylor, University of Manchester) were plated on 10cm dishes and grown to 60% confluency before cotransfection with the vector pOG44 and the pcDNA5/FRT/TO vector containing the gene of interest (WT, S100M or S100M* RET). Ratios from 10:1 to 15:1 (pOG44:pcDNA5) were used – 10:1 is equal to 5 µg pOG44 and 500 ng pcDNA5. 24 hours after transfection, cells were washed and incubated in new DMEM (blasticidin only). 48 hours after transfection, the cells were split to 25% confluency and incubated for 2-3 hours before the media was replaced (hygromycin and blasticidin). The hygromycin concentration required for DLD-1 and HeLa cell lines was previously determined by Professor Stephen Taylor's laboratory. Media was replaced every 3-4 days until visible colonies began to form. Colonies were selected and expanded (approximately 10 per cell line created), before testing for zeocin sensitivity and RET expression.

The transfection was carried out using the Effectene transfection reagent (Qiagen) as per the instructions of the handbook. Briefly, 500 ng pcDNA5/FRT/TO(RET) vector and 5 µg pOG44 was mixed with EC buffer to 150 µl total. 44 µl enhancer (8 µl for every µg DNA) was added and the mixture incubated at room temperature for 5 min. 137.5 µl effectene (25 µl for every µg DNA) was added and the mixture pipetted up and down five times. This was incubated at room temperature for a further 10 min, during which time the cells were washed in PBS and the media replaced. 1 ml media was added to the transfection mixture, which was then added to the cells dropwise.

2.2.2 Monitoring RET maturation

2.2.2.1 Immunoblotting

Cells were harvested and washed with ice cold PBS before resuspension in 1x NuPAGE Sample buffer (Invitrogen). The cells were incubated at 90 °C for 5 minutes and then lysed by sonication for 2 seconds, followed by centrifugation (10,000 x g, 5 minutes). The supernatants were loaded onto SDS-PAGE NuPAGE 4-12% Bis-Tris gels (Invitrogen) with a protein marker and 90 V were applied. Proteins were transferred onto nitrocellulose membranes that had been soaked (along with fibre pads and filter paper) in transfer buffer. The sequence of items,

starting on the side of the black cathode, were: 1) fibre pad, 2) filter paper, 3) the gel, 4) the nitrocellulose membrane, 5) filter paper, 6) fibre pad (at the side of the red anode). Wet transfer was carried out in the cold room at 100 V for 90 min.

Membranes were blocked with 5% non-fat dry milk (in 1x TBST) for 1 hour, washed in 1x TBST and then probed with the relevant primary antibody diluted in 5% milk overnight. Membranes were washed three times in 1x TBST and probed with the corresponding HRP-conjugated secondary antibody for one hour, before washing three times once more in 1x TBST. For development, membranes were developed using the enhanced chemiluminescence (ECL) method. Membranes were incubated with ECL solution and exposed onto ECL film. Using this method, the horseradish peroxidase (HRP) conjugated to the secondary antibodies catalyses the oxidation of luminol, resulting in the emission of light.

2.2.2.2 Pulse chase analysis

Hek293 cells were plated onto 100mm dishes (Corning Costar) and grown in DMEM/10% FCS until they reached 60-80% confluency. Cells were washed three times with pre-warmed PBS and incubated with 5 ml Met-Cys-free DMEM (+ 10% FCS) at 37 °C for one hour. 2 ml of fresh Met-Cys-free DMEM was added to the cells (+ 10% FCS + 100 µCi S^{35}-Met express label) for a further one-hour incubation. The cells were washed in pre-warmed PBS and incubated in 5ml standard DMEM (+ 10% FCS) at 37 °C for 0, 30, 60, 90, 120, 180, 300 min 24 hours. One plate of cells (zero time point) was harvested by cell scraping into 1 ml ice cold PBS and centrifuged (14,000 x g, 45 seconds, 4 °C). The PBS was removed and each cell pellet stored at -80 °C.

Protein G sepharose beads were washed in mammalian lysis buffer and incubated with anti-RET C20 antibody (5 µl per sample) for 1 hour at 4 °C. 0.8 ml mammalian lysis buffer was added to each thawed cell pellet and left for 15 minutes on ice, before centrifugation (10,000 x g, 10 min, 4 °C). The lysate was transferred to a new eppendorf containing the anti-RET antibody and Protein G sepharose bead mixture and incubated at 4 °C for 4 hours with constant rotation. The beads were washed with lysis buffer three times and harvested (centrifugation at 1000 x g, 5

min). The harvested beads were resuspended in 1x Sample Buffer (+ 10% β-Mercaptoethanol), incubated at 90 °C for 5 minutes, and centrifuged (10,000 x g, 1 min). The supernatants were then subjected to SDS-PAGE and nitrocellulose membrane transfer. Resulting membranes were exposed to a phosphor screen for 24 hours, with individual bands quantified by a phosphoimager.

2.2.3 Detecting RET cell surface expression levels

2.2.3.1 FACS analysis

Hek293 cells were plated on 10 cm plates at approximately 60% confluency and RET expression was induced with 2 µg/ml doxycycline for 24 hours. Cells were harvested in trypsin, washed in ice cold PBS and centrifuged at 400 xg for 5 min. Cells were resuspended at 5 x 10^6 cells/ml in FACS buffer (ice cold PBS + 2% FBS + 0.1% sodium azide) to prevent internalisation of surface antigens. 100 µl of the resuspended cells was added to each eppendorf with 2.5 µl 1D9 antibody (an anti-RET antibody binding to the extracellular domain of RET ECD, (Salvatore et al., 2002a)) and incubated for 30 min at 4°C. Cells were washed three times in ice cold PBS (400 xg, 5 min) before incubation with secondary Alexa488 antibody (1:2000 in FACS buffer) for 30 min at 4°C in the dark. Cells were washed three times as before and resuspended in PBS + 2% FBS, in polystyrene round-bottom BD Falcon tubes for immediate analysis.

Samples were analysed in the London Research Institute FACS facility by Marwa Jalal and Sukhveer Purewal using the FACSCalibur (Becton Dickinson). Data was analysed using FlowJo. Cells are initially sorted based on viability (using the DAPI staining at 450/50nm bandpass filter). Live cells were then gated away from doublets and debri, as defined by the side scatter (SSC) pulse width and intensity. Cell number was finally plotted in a histogram against fluorescence intensity at 530/30nm.

2.2.3.2 Immunofluorescence

10,000 DLD-1, Hek293 or HeLa cells were plated in 200 µl DMEM in each well of the Poly-D-Lysine coated 96-well glass bottom plates. Once the cells were adherent, RET expression was induced by replacing the media with that containing

2 µg/ml doxycycline (non-induced controls were also present on the plate). After 24 hours, cells were fixed for 15 minutes in 50 µl/well 3.65% PFA (diluted in PBS) and washed three times in PBS. A portion of each plate was permeabilised using 50 µl/well 0.01% Triton-X100 for 5 min at room temperature. The plate was washed three times and blocked using 50 µl/well 3% BSA for 1 hour, before washing again three times and overnight staining in 50 µl/well 1D9 anti-RET primary antibody (1:40 in 1% BSA). The plate was washed three times and incubated for 1 hour (in darkness) in 50 µl/well Alexa488 secondary antibody (1:2000 in 1% BSA). The plate was washed a further three times and incubated for 1 hour (in darkness) in 50 µl/well 4',6-diamidino-2-phenylindole (DAPI) (1:10,000 in 1% BSA). DAPI is a fluorescent dye that binds to the A-T rich regions of DNA, therefore staining the nucleus. The plate was washed a final three times before 100 µl/well PBS was added to all wells.

Plates were processed by the HTS facility. Images of the cells were taken at 10x magnification of channel 1 (DAPI detection channel) and channel 2 (Alexa488 detection channel) fluorescence, using the Cellomics Arrayscan VTI HCS (High Content Screening) automated microscope (Thermo Scientific). This fully automated and software controlled microscope is designed for high-throughput fluorescence imaging of fixed and live cells. Images were analysed using the Thermo Scientific HSC Studio software platform known as Cellomics iView. The software calculates the number of nuclei (defined as channel 1 fluorescence, stained with DAPI, known as the object count) and the average ring intensity (defined as channel 2 fluorescence surrounding the nuclei, stained with Alexa488 secondary antibody and interpreted as RET staining). These values were used for interpretations of fluorescence levels, normalising against the number of cells in each field of view.

2.2.4 Mammalian cell transfection

2.2.4.1 Transient overexpression of cDNA constructs in DLD-1 cells

Transient transfections of DLD-1 cells were performed using the transfection reagent FuGENE HD. FuGENE HD is a nonliposomal transfection agent; the lipid-based reagent interacts with and forms micelles around the exogenous DNA. The

complex can interact with the cell membrane, allowing for delivery of the DNA into the cytoplasm via endocytosis (Medina-Kauwe et al., 2005).

DNA and FuGENE HD at a ratio of 1:3 were mixed and incubated at room temperature for 15 min, and then added to the adherent cells. Media was replaced 24 hours later, cells were lysed 48 hours post transfection.

2.2.4.2 High-throughput siRNA transfection of 300-candidate siRNA library

Gene expression can be silenced by the addition of double stranded RNA (dsRNA). dsRNA is cleaved by the RNAase enzyme Dicer into small interfering RNAs (siRNAs). These small oligomers are integrated into the multi-subunit complex called RISC (RNAi-inducing silencing complex), which guides them to the target RNA sequence. The siRNA unwinds and the antisense strand remains attached to RISC and directs degradation of the mRNA sequence by endo- and exonucleases (Morris et al., 2004).

The siRNA targets of the four library plates can be found in the appendix of chapter 4. 10 µl of each siRNA (375 nM stock) was plated onto Poly-D-Lysine coated 96-well glass bottom plates . Plates were frozen (-20°C) for storage. Prior to use, plates were thawed for 20 min at room temperature and centrifuged for 1 min at 1000 rpm before removing the seal. 10 µl of Lullaby transfection reagent (pre-diluted in serum-free media Opti-MEM (Life technologies), final concentration 0.2 µl/well) was added to each well using the microplate dispenser Thermo Scientific Matrix WellMate™ and plates were incubated at room temperature for 20 min. 10,000 DLD-1 cells were added to each well. Plates were incubated at 37°C, 10% CO_2 for 48 hours. On the morning of day 3, media was aspirated by the plate washer and 100 µl media containing 2 µg/ml doxycycline was added. 8 hours later, media was aspirated again (from 4-PBA control wells) and replaced with 100 µl media containing doxycycline and 10 mM 4-PBA. On day 4, media was aspirated and 50 µl/well 3.65% PFA was added; plates were incubated at room temperature for 15 min. Plates were washed three times with PBS and 50 µl/well 3% BSA (in PBS) was added for 1 hour (incubated at room temperature). The blocking solution was aspirated and 50 µl/well primary 1D9 anti-RET antibody (diluted 1:40 in 1%

BSA) was added. Plates were incubated at 4°C overnight before washing three times in PBS. 50 µl/well secondary Alexa488 antibody (1:2000 in 1% BSA) was added for 1 hour (in darkness) before washing again and staining with 30 µl/well DAPI (10 mg/ml diluted 1:10,000) for 1 hour (in darkness). Plates were finally washed twice and left in 100 µl/well PBS.

Plates were processed by the HTS facility at 10x magnification using the Cellomics Arrayscan VTI HCS automated microscope (Thermo Scientific). Images were analysed using Cellomics iView; the number of nuclei (channel 1 DAPI, object count) and the average ring intensity (channel 2 RET) were used for interpretations. All images are stored on the HTS server – barcodes in Table 2.7 can be used to access the images of each plate.

HTS barcodes

	Plate	Repeat	Barcode
WT RET	**1**	1	00022138
		2	00022139
		3	00022140
	2	1	00022144
		2	00022145
		3	00022146
	3	1	00022150
		2	00022151
		3	00022152
	4	1	00022156
		2	00022157
		3	00022158
S100M RET	**1**	1	00022153
		2	00022154
		3	00022155
	2	1	00022147
		2	00022148
		3	00022149
	3	1	00022141
		2	00022142
		3	00022143
	4	1	00022135
		2	00022136
		3	00022137

Table 2.7 Barcodes for all siRNA screen plates

2.2.4.3 siRNA transfection of DLD-1 cells

siRNA transfections of DLD-1 cells were performed using the transfection reagent Lullaby. Lullaby is also a lipid-based transfection reagent; lipids form complexes

with the nucleic acids, resulting in the formation of micelles around the exogenous RNA. These micelles gain access to the cytoplasm via endocytosis, delivering the RNA to the cytoplasm (Medina-Kauwe et al., 2005).

For a 96-well plate, 37 nM siRNA and 10 µl Lullaby (prediluted in Optimem, final concentration 0.2 µl/well) were mixed at room temperature for 20 min and added to 5000 cells/well. RET expression was induced 24 hour later with 2 µg/ml doxycycline, with fixing and staining occurring 48 hours post transfection.

siGENOME SMARTpool siRNA	
Target	**Serial number**
RISC-free	D-001220-01-05
OTP Control	D-001810-10-05
RET	M-003170-02-0005
RAB7A	M-010388-00-0005
P4HB	M-003690-01-0005
ATP6V0C	M-017620-02-0005
ATP6V1C2	M-016263-01-0005
ERP44	M-026181-01-0002

Table 2.8 siRNA targets and serial numbers used in chapter 3

2.2.5 Cloning

2.2.5.1 Baculovirus transfer vectors

The hRET KD construct was originally cloned into a pBacPAK-His3 derivative called pBacPAK-GST by Mr Phillip Knowles and was used in the production of hRET KD in the McDonald Laboratory (Knowles et al., 2006). Following this, a codon-optimised version of the hRET KD construct was obtained from Gentech to improve protein expression levels. Dr Kerry Goodman cloned this new construct into the pBacPAK-GST vector. The pBacPAK-GST vector encodes an N-terminal glutathione S-transferase (GST) tag, followed by a 3C cleavage site. Cleavage of this tag with 3C protease results in the residues GPLSL being left at the N-terminus of hRET KD. The recombinant hRET KD protein used spanned from residues 705-1013, with the kinase insert (residues 827-840) removed.

2.2.5.2 Site-directed mutagenesis

Site-directed mutagenesis of plasmids was carried out using KOD Hot Start DNA polymerase (Novagen). Typically, the reaction mixture was composed of 0.3 µM forward and reverse primer, 100 ng template DNA and a 1x KOD mastermix composed of 1 unit KOD polymerase, 150 µM each dNTP, 8 mM $MgCl_2$ and 20 mM Tris HCl pH 7.5. The KOD polymerase chain reactions (PCR) were carried out with an initial polymerase activation temperature of 94 °C for 2 minutes. Denaturation was carried out at 98 °C for 15 sec, annealing at the primer melting temperature for 10 sec, extension at 70 °C for 4 min; 30 cycles were carried out before storage at 4 °C.

The template DNA was removed from the reaction by digestion using 20 units of Dpn1, with incubation at 37 °C overnight. 250 µl of competent NovaBlue cells were transformed with 5 µl of the reaction by incubating on ice for 30 minutes, followed by 42 °C for 45 seconds and 2 minutes on ice. Transformed cells were spread onto LB-agar plates containing 200 µg/ml carbenicillin and incubated at 37 °C overnight. Colonies were selected and grown in LB medium containing 200 µg/ml carbenicillin, ready for plasmid purification using the Qiagen mini-prep kit. This was carried out according to the manufacturer's instructions and the plasmid was subsequently sequenced to determine whether the mutagenesis had been successful.

The Cancer Research UK London Research Institute equipment park staff carried out all DNA sequencing, using the BigDye™ Terminator Cycle Sequencing kit (PE Applied Biosystems) and capillary sequencing on an ABI Prism 3730.

Construct	Expression cassette details	Antibiotic resistance	Created by
pcDNA5/FRT/TO WT RET	pCMV-2xTetOperator-WT RET	Amp (B), Hygromycin (M)	Dr Svend Kjaer, London Research Institute
pcDNA5/FRT/TO S100M RET	pCMV-2xTetOperator-S100M RET	Amp (B), Hygromycin (M)	Dr Svend Kjaer, London Research Institute
pcDNA5/FRT/TO S100M* RET	pCMV-2xTetOperator-S100M* RET	Amp (B), Hygromycin (M)	Emily Burns, London Research Institute
pOG44	pCMV-synthetic intron-FLP	Amp (B)	Life Technologies
pBacPAK-GST-RET KD	GST-3C-$hRET_{705-826;841-1013}$ (codon optimised)	Amp (B)	Dr Kerry Goodman, London Research Institute
pCMV5 CHIP FLAG	CHIP-FLAG tag	Amp (B)	MRC Dundee
pCMV CHIP P269A FLAG	CHIP P269A - FLAG tag	Amp (B)	MRC Dundee
pCMV5-HA UBE2D1	HA tag-UBE2D1	Amp (B)	MRC Dundee
pCMV5-HA UBE2D1 C85A	HA tag-UBE2D1 C85A	Amp (B)	MRC Dundee

Table 2.9 DNA constructs used

pBacPAK-GST = modified pBacPAK-His3 (Clontech) vector; 3C = 3C protease cleavage recognition site; GST = glutathione S-transferase; (B) - in bacteria, (M) - in mammalian cells.

2.2.6 Protein expression

2.2.6.1 Baculovirus production

The production of baculoviruses from baculovirus transfer vector constructs, initial viral amplification and protein expression tests in insect cells were carried out by the Cancer Research UK London Research Institute Protein Production Facility. Baculoviruses were produced in Sf9 cells using the Clontech BacPAK system (BacPAK™ Expression System User Manual, Clontech). Briefly, this system uses the *Autographa californica* (AcMNPV) nuclear polyhedrosis virus to produce recombinant proteins in insect cells. The target gene is inserted into a shuttle vector and cotransfected into the insect cells with linearised BacPAK6 viral DNA; this forces recombination of the virus and shuttle vector. The isolated recombinant virus is then amplified and used for insect cell infection.

2.2.6.2 Insect cell culture

Sf9 cells were cultured in suspension in serum-free SfIII media (Invitrogen) containing 10 µg/ml gentamycin. They were grown at 27 °C with continuous shaking (140 rpm) in 100-500 ml aliquots in 2 l roller bottles, at a maintained density of 1.5-6 x 10^6 cells/ml. Cell density was determined using a Vi-CELL cell counter (Beckman Coulter). The cell counter uses the trypan blue exclusion assay to determine the number of viable cells present, based on the principle that live cells have intact cell membranes that exclude trypan blue dye (Strober, 2001). Cells were only used for baculovirus amplification or protein expression if the viability was above 89% and the doubling time was above 24 hours.

2.2.6.3 Baculovirus amplification

Baculovirus amplification was carried out in Sf9 cells using a baculovirus multiplicity of infection (MOI) of 0.1-0.5 and 250 ml cell aliquots at a density of 1 x 10^6 cells/ml. MOI refers to the ratio of virus particles to cells used, with low MOI used during virus amplification. The culture was incubated at 27 °C with shaking (140 rpm) for 6 days before harvesting the baculovirus-containing media by centrifugation (3000 x g, 20 minutes, 4 °C). This process was often repeated, with baculoviruses used in protein expression being passaged in Sf9 cells 3-5 times.

2.2.6.4 Calculation of viral titre

The High Pure Viral Nucleic Acid Large Volume Kit (Roche) was used to purify baculoviruses from media following the manufacturer's instructions. Briefly, the viral nucleic acids are isolated from the cells by lysing the cells and virus. Centrifugation in the presence of a glass-fibre purification column results in the final isolation of the viral nucleic acids separate from salts, proteins and impurities. The nucleic acids are eluted in nuclease-free water. Reverse Transcription PCR was performed by the Cancer Research UK London Research Institute Protein Production Facility in order to quantify the viral RNA.

2.2.6.5 Protein expression

Sf9 cells at 1 x 10^6 cells/ml in 500 ml aliquots were infected with baculoviruses at an MOI of 2. The infected cells were incubated at 27 °C with shaking (140 rpm) for 3 days before harvesting the pellet by centrifugation. Following purification, the expression yield for hRET KD was approximately 1.5 mg/l culture.

2.2.7 Protein purification and analysis

2.2.7.1 hRET KD protein purification and autophosphorylation

hRET KD protein was purified using essentially the same protocol as was published in 2006 (Knowles et al., 2006). Harvested Sf9 cell pellets were harvested by centrifugation (3000 x g, 15 min, 4 °C), resuspended in cold KD lysis buffer (20ml per 1 l culture) and lysed by sonication for 90 seconds on ice. The lysate was then centrifuged (29220 x g, 30 min, 4 °C) and the supernatant taken forward for purification. Glutathione-sepharose resin (GE Healthcare) was washed in KD lysis buffer and added (0.5ml per 1 l culture) to the supernatant. This lysate-resin mixture was incubated overnight at 4 °C with constant rotation, before the resin was collected in a 10 ml syringe and washed with 20 ml KD buffer. The washed resin was resuspended in 10 ml KD buffer and hRET KD phosphorylation was carried out by adding 5 mM ATP (pH 8) and 10 mM $MgCl_2$. This mixture was incubated on ice for 6 hours before thorough washing of the resin beads with 30 ml KD buffer, to remove excess ATP and magnesium.

The resin was resuspended again in 10 ml KD buffer and GST-tagged 3C-protease was added (100 µg per 1 ml resin). This mixture was incubated at 4 °C overnight with constant rotation, before the cleaved protein was separated from the resin using a 10 ml syringe and the resin washed with 2 volumes of KD buffer. The affinity-purified protein was concentrated in a Vivaspin column at 3000 x g (GE Healthcare). The theoretical protein parameters used in further analysis were calculated using the ProtParam tool in ExPASY (http://web.expasy.org/protparam). hRET KD: 300 amino acids, 34.3 kDa, pI of 9.04, extinction coefficient (*$10^3 M^{-1} cm^{-1}$) of 49.39).

2.2.7.2 Measuring protein concentration

The concentration of purified protein was measured using the Bradford protein assay (Bradford, 1976). A standard assay was carried out using KD buffer with bovine serum albumin (BSA) concentrations of 0, 250, 500, 750 and 1500 µg/ml. 25 µl of each sample was added to 1.3 ml Bradford solution (diluted 1:5 with water). The mixture was incubated at room temperature for 15 min before transfer to a 1.5 ml cuvette for measurement in a spectrophotometer at 595 nm. The absorption reading of each standard was plotted against the concentration and used to calculate the concentration of unknown samples.

2.2.7.3 SDS-PAGE

Sodium dodecyl sulphate polyacrylamide gel electrophoresis (SDS-PAGE) was used to analyse the purity of protein samples. 4-12% NuPAGE gels were used with MOPS running buffer. Protein samples were prepared in 4x SDS loading buffer and incubated at 95°C for 5 minutes, before loading into the wells of the gel. A voltage of 120 V was applied until the SDS loading buffer dye had migrated into the bottom edge of the gel. Gels were stained with coomassie stain for 20 min and destained in water overnight.

2.2.7.4 Differential Scanning Fluorimetry

Differential scanning fluorimetry (thermal shift assay) was used to examine the thermal stability of the WT RET KD in the presence of a range of chemical inhibitors. hRET KD protein was purified in HEPES buffer and diluted to 0.05

mg/ml. The protein was aliquoted (100 µl per tube) into PCR tubes and 1 µl of each inhibitor (100 µM stocks, 1 µM final concentration) was added. For the ATP/Mg^{2+} control, 200 µM ATP and 10 mM $MgCl_2$ was added. The tubes were incubated at 4°C for 2 hours. SYPRO orange dye was diluted 1:100 in HEPES buffer and 5 µl was added to each tube and incubated for a further 15 min. Samples were transferred into an rtPCR plate: 25 µl in each well (4 repeats of each sample). The plate also included a HEPES buffer only, a HEPES buffer + ATP/Mg^{2+} and a KD alone control.

The thermal stability was assessed using the BioRad I-Cycler rtPCR machine, increasing the temperature from 4°C to 90°C over 2 hours. Relative fluorescence units (RFU) at each 0.5°C temperature point were exported and analysed as described in chapter 5.

2.2.8 X-ray crystallography

2.2.8.1 Co-crystallisation of hRET KD with inhibitors

The hRET KD was co-crystallised with several inhibitors designed and produced by our collaborators. The purified and phosphorylated protein was incubated with each inhibitor at a molar ratio of 1:3 (protein:inhibitor) at 4 °C for 2 hours with constant rotation, followed by concentration to 3-4 mg/ml in a Vivaspin column for crystallisation.

2.2.8.2 Crystallisation screening and optimisation

Crystallisation conditions used in prior hRET KD crystallisation (2.2 M sodium formate and 0.1 M sodium acetate (pH 4.5)) were extended upon in 2-drop 96 well MRC plates (Knowles et al., 2006). Conditions were dispensed into the MRC plates (100 µl per well) using a Formulator robot (Formulatrix) and mixed using a Hydra robot (Thermo Scientific). Sitting drops of typically 100 nl of purified protein at 3-4 mg/ml plus 100 or 200 nl of well solution were aliquoted using a Mosquito robot (TTP Labtech). Sealed plates were incubated at 20 °C in a robotic crystal hotel and imager (Rock Imager, Formulatrix).

Crystals were confirmed to be protein using UV absorption (Rock Imager) and a further round of screening was carried out around the most optimal condition, varying the pH, salt concentration and protein concentration for further refinement of the crystallisation conditions. The aim was to produce large three-dimensional single crystals. In the case of inhibitors 1, 7, 9 and ADP, the additive screen kit was also used in optimisation, as per Hampton Research instructions.

2.2.8.3 Cryo-protection and crystal mounting

Before X-ray data collection, crystals were cryoprotected in perfluoropolyether oil (Hampton Research), mounted in litholoops (Molecular Dimensions) and flash-frozen in liquid nitrogen. This cryoprotectant was first tested with 5 min exposure time on the in-house X-ray system (Rigaku) and no ice rings were observed.

2.2.8.4 Diffraction data collection

X-ray data collection was carried out at Diamond Light Source or the European Synchrotron Radiation Facility (ESRF). Details of the beamline used for each dataset are listed in the results section with X-ray data. The loop was mounted onto the goniometer using beamline robotics and the crystal was centred in the X-ray beam. Data collection strategies for each dataset were determined using MOSFLM (Powell, 1999) or EDNA (Diamond Light Source) based on preliminary images at 0 °, 45 ° and 90 ° rotation angles of the goniometer.

2.2.8.5 Diffraction data processing

Data were processed using XDS: diffraction spots were identified on each image, indexed and integrated based on refined unit cell parameters and crystal orientation, and the Laue and space group predicted (Kabsch, 2010). The process of indexing and integration converts 2D coordinates into 3D reciprocal lattice coordinates, providing the unit cell parameters and crystal orientation. The images are then integrated, predicting the position of Bragg reflections and estimating the intensity of each reflection (Leslie, 2006). The integrated spot intensity data were scaled and merged using Aimless and XSCALE (Kabsch, 2010, Evans and Murshudov, 2013). These programs ensure that all of the data are processed on a common scale, with partial reflections and symmetry equivalents merged. The

Laue group (diffraction symmetry) and space group were chosen based on cell dimensions directly in XDS using POINTLESS (Evans, 2006). The output files generated by these programs detailed the data quality metrics against the resolution and image number. They were analysed to determine the resolution limit of each dataset, with poor images being discarded. The data were scaled and merged again to the determined resolution. Data quality details for each dataset are listed in the results section.

2.2.8.6 Molecular replacement

In order to create an electron density map, the phase problem must be solved. In the case of RET KD-inhibitor structures, this was carried out using molecular replacement. All pRET KD-inhibitor structures were solved by molecular replacement using the published pRET KD-adenosine structure (PDB code 4CKJ), with the GRL and αN helix removed as a standard model. The "Cell Content Analysis" tool within the CCP4 suite was used to determine the Matthew's Coefficient and identify the number of molecules in the asymmetric unit (Collaborative Computational Project, 1994, Matthews, 1968). There was only one pRET KD molecule in the asymmetric unit for all pRET KD-inhibitor structures except for pRET KD-I-3, in which there were two. Molecular replacement was carried out using the maximum likelihood program PHASER, with the edited protein coordinates of the pRET KD-adenosine structure (McCoy et al., 2007). One good solution was found for each of the structures, which was taken forward for refinement and model building.

2.2.8.7 Refinement and model building

Refinement and model building were carried out alternately, using the molecular replacement solution electron density map and the protein coordinates. Modifications to the structures were made based on the composite 2Fo-Fc density map (Fo – observed structure factor, Fc – calculated structure factor), used to reduce model bias, and the Fo-Fc difference density map. This process of refinement gradually improves the phases of the data, resulting in an improved electron density map. The structures were refined in PHENIX (Adams et al., 2010), while model building was carried out in COOT (Emsley and Cowtan, 2004). TLS

(translation, libration, screw rotation) groups were defined (N-terminal helix 700-712; N-lobe 716-808; C-lobe 809-1013) in the fourth round of refinement, allowing individual rigid body refinement of the RET KD N- and C-lobes. The Rf_{ree} and R_{work} values were used to determine the quality of the refined model. The R_{work} (also known as R-factor) calculates the discrepancy between the simulated model and the original experimental diffraction data (Rupp, 2010). The R_{free} value is calculated by comparing the simulated model to original experimental observations omitted from refinement, removing some of the bias associated with Rwork (Brunger, 1992). This process was continued until the R_{free} ceased to improve and there was less than 7% difference between the R_{free} and R_{work}. At this point, the electron density map should allow for good interpretation of the structural model.

Chapter 3. Characterisation of the maturation of a RET S100M missense mutation causal in Hirschsprung's disease

3.1 Introduction

This chapter describes the generation and characterisation of stable cell lines producing the mild RET S100M Hirschsprung's disease mutant. The aim was to investigate whether this mutant was transported to the cell surface and to compare its maturation kinetics to those of wild type RET and a potential folding rescue mutant (RET S100M/C87R/C616S, referred to as S100M*). Immunofluorescence, FACS analysis, western blot analysis and S^{35} pulse-labelling methods were used to characterise S100M RET. Chemical chaperones and a double cysteine mutation were each able to restore S100M RET maturation and cell surface localisation. Preliminary efforts to influence RET cell surface levels by siRNA (small interfering RNA) gene targeting are described.

In 2010, the laboratory published the structure of human RET CLD1-2 obtained using x-ray crystallography (Kjaer et al., 2010), revealing a clamshell-like arrangement of the top two domains of the RET extracellular domain (ECD) (Figure

3.1). To produce the recombinant hRET CLD1-2 protein used in crystallisation, two unpaired cysteine residues, identified by mass spectrometry in disulphide swapping experiments, were mutated: C87R and C216S (Figure 3.1). It was reasoned that eliminating potentially problematic oxidised cysteines from the extracellular region of this glycoprotein would be beneficial to protein yields. Western blot analysis of cell lysates showed two species for wild type (WT) RET, corresponding to an immature partially glycosylated 150kDa form and a mature fully glycosylated 170kDa form. Removal of the two unpaired cysteine residues resulted in the loss of the lower molecular weight immature form, suggesting the slow kinetics of WT RET protein folding could be accelerated. Recombinant S100M RET extracellular domain (ECD) was also not efficiently secreted into the media in a surrogate assay used to quantify protein yields (Kjaer et al., 2010), suggesting the presence of a bottleneck in HSCR RET folding. Upon the removal of the two unpaired cysteine residues from the HSCR mutant ECD (S100M*), the protein was found to be fully glycosylated and efficiently secreted. It was also shown to bind to GDNF and GFRα1 with equivalent affinity to WT RET ECD, suggesting the possibility that restoring cell surface expression of mild HSCR mutants could rescue ligand-binding and potentially RET signalling.

As the aim of this chapter was to investigate both WT and HSCR mutant S100M RET maturation and export in more detail, I exploited an inducible mammalian expression system (Flp-In System, Life Technologies) in which the export and signalling capabilities of various RET species could be investigated. Previous experiments with RET from the literature and within the McDonald laboratory have indicated that obtaining good ligand-induced RET activation in transiently transfected cell lines is problematic, due to the high level of basal RET auto-phosphorylation. The inducible Flp-In system was explored as a potential way to alleviate these problems within the field.

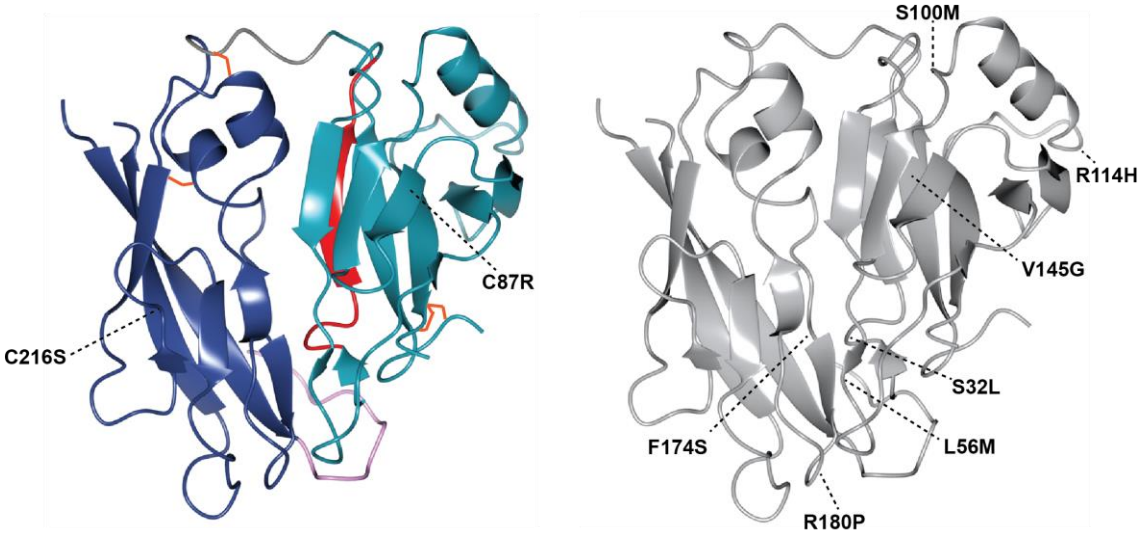

Figure 3.1 Structure of hRET CLD1-2 and relevant HSCR mutations

(A) The structure of hRET CLD1-2 (PDB code 2X2U) with key structural elements coloured and the positions of C87R and C216S highlighted. CLD1 – cyan; CLD2 – dark blue; N-terminal β-strand buried in the interface – red; C-tail – pink; connecting loop – grey; disulphide bonds – orange. **(B)** The structure of hRET CLD1-2 (grey ribbon) with HSCR mutations within this region of RET annotated (Kjaer et al., 2010).

3.2 Structure-based sequence alignments of RET CLD1-2

The sequences of selected RET species are shown in Figure 3.2, highlighting the secondary structural elements of human RET CLD1-2, the location of unpaired cysteines, a glycosylation site mutation and the site of S100M (Figure 3.2).

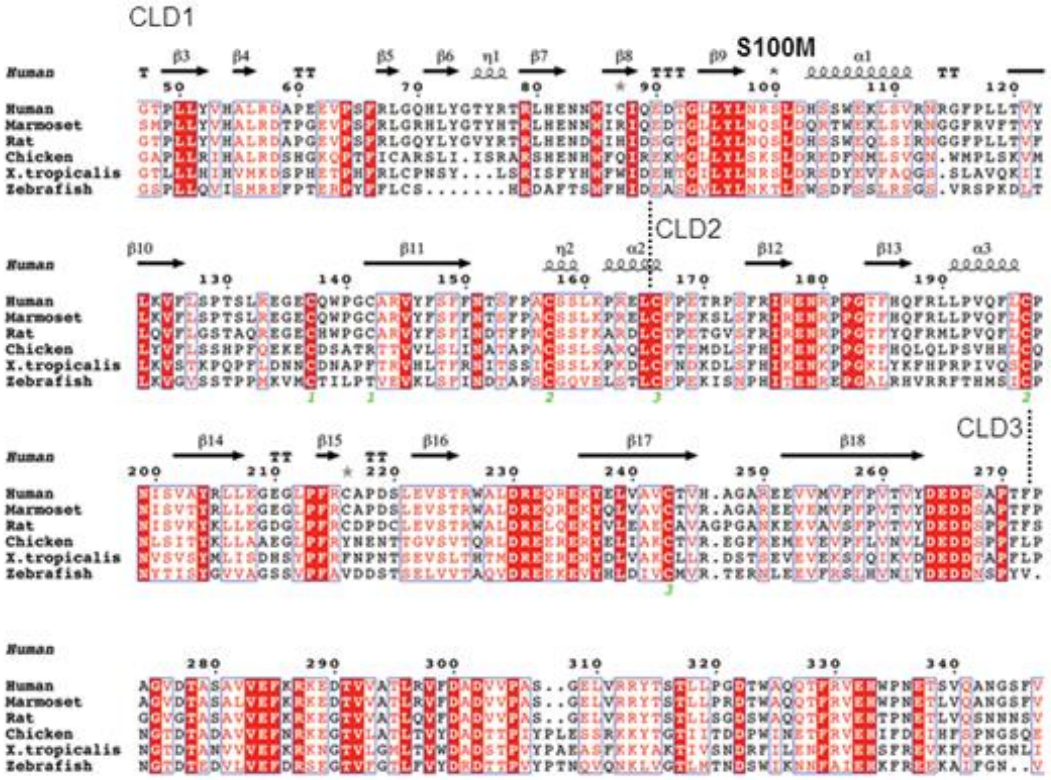

Figure 3.2 ECD sequence alignment for selected RET species

ECD domains from selected species of RET highlighting secondary structural elements from the human CLD1-2 structure. The location of two unpaired cysteines is shown by a grey star above the residue, along with a serine residue at an N-linked glycosylation site mutation. The domain boundaries are based on the alignment of the CLDs to cadherin EC domains (Anders et al., 2001b).

3.3 Generating inducible RET and RET mutant Flp-In stable mammalian cell lines responsive to GDNF-GFRα1

The accumulation of an immature species within the ER in higher abundance than mature processed RET suggests that it has an inherently slow and complex folding trajectory. The rate-limiting step during RET folding and export is not known but could relate to achieving a “native” conformation and correct disulphides, glycosylation processing or the transit from Endoplasmic Reticulum (ER) exit sites. In addition, the ER organelle from different mammalian cell types is known to function with varying levels of efficiency and can be easily become stressed and blocked by misfolded proteins produced by overexpression (van Weering et al., 1998) (Kjaer et al., 2010). We reasoned that transiently transfecting RET constructs into mammalian cells would therefore not be an optimal platform for examining RET

maturation and export, due to potential aggregation and ER stress. While endogenous RET expression can be examined in several neuronal cell lines (Trupp et al., 1999), preliminary investigations showed levels to be far lower than that achieved using an over-expression system. For these reasons, it was determined that an inducible stable cell line expressing RET was required.

The Flp-In system (as seen in Figure 2.1) was utilised in order to create stably transfected mammalian cells that could express various RET species upon the addition of doxycycline. This involves transfecting a mammalian cell line with three separate vectors that will ultimately lead to the creation of a stable cell line expressing a gene of choice (methods are detailed in Chapter 2).

Previously in the laboratory, Hek293 Flp-In stable cell lines expressing WT, WT*, S100M or S100M* RET had been created previously by Dr Svend Kjaer (London Research Institute). While these particular cell lines were sufficient for biochemical analysis of RET maturation, they were not optimal for immunofluorescence assays, due to the heterogeneous RET expression levels and the tendency of the cells to grow very close together, hindering the identification of separate cells during analysis. In order to overcome these issues, DLD-1 and HeLa Flp-In cells were kindly donated by Professor Stephen Taylor (University of Manchester), in order to create cell lines expressing the various RET species that could be used for imaging and future assay development.

The mammalian cell lines used in this thesis are derived from human embryonic kidney cells (Hek293), cancer cells (HeLa) or colorectal adenocarcinoma cells (DLD-1). Human embryonic kidney (HEK) cells were originally exposed to sheared fragments of the human adenovirus type 5 (Ad5) DNA, which resulted in the incorporation of this DNA into the host genome and the creation of the subsequent cell line used today, known as Hek293 (Graham et al., 1977). The cancer cell line known as HeLa is named after Henrietta Lacks, from whom they were originally derived from in 1952. While originally reported as cervical cancer cells, they were later identified as a rare adenocarcinoma and were the first cancer cell line created in the laboratory (Masters, 2002). DLD-1 cells are epithelial cells originally derived from a colorectal adenocarcinoma and are positive for oncogenes *myc*, *myb*, *ras*,

fos, *sis*, and *p53* (Trainer et al., 1988, Rodrigues et al., 1990). They also have a constitutively active PI3K-Akt pathway, but their ligand-responsive pERK1/2 signalling pathway is intact. Hek293 cells were used for primary western blots, FACS and pulse chase analysis; DLD-1 cells were used for immunofluorescence staining and chemical or genetic manipulation experiments. HeLa cell lines stably expressing WT and S100M RET were created as an alternative to Hek293, but DLD-1 cells were selected for future experiments investigating the role of specific factors in RET cell surface expression levels. DLD-1 cells were chosen over HeLa cells due to their higher levels of RET expression.

3.4 Examining RET maturation and cell surface expression levels

In all mammalian cells examined, both the immature 150kDa and mature 170kDa species of WT RET are observed, while S100M RET is only present as the immature species (Figure 3.3a). The 120kDa nascent RET polypeptide is believed to be folded within the ER and partially glycosylated into its immature form. Once correctly folded, the protein can be exported from the ER to travel to the Golgi apparatus, where it is fully glycosylated (by the addition of more complex N-glycans) into the mature 170kDa species that is expressed at the cell surface (Takahashi et al., 1991, Takahashi et al., 1993). Therefore, the existence of S100M RET as an immature form indicates that the mutant receptor may not reach the Golgi apparatus and is not therefore fully glycosylated.

Live-cell FACS analysis was carried out using Hek293 cells stably expressing WT and S100M RET (herein referred to as WT RET or S100M RET Hek293 cells), in order to examine cell surface levels of these receptors. The cells were incubated with the anti-RET 1D9 antibody, before the addition of the Alexa488 fluorescent antibody. The 1D9 anti-RET antibody was kindly donated by Professor Massimo Santoro (Salvatore et al., 2002b). While no fluorescence intensity was found in non-induced WT RET Hek293 cells, a shift in intensity (Figure 3.3b, left and middle histograms) was observed once RET expression had been induced with doxycycline. Comparison of fluorescence intensities for WT and S100M RET

Hek293 cells (Figure 3.3b, right histogram) suggests significantly reduced levels of S100M RET at the cell surface.

RET cell surface expression was also investigated via immunofluorescence in DLD-1 cells stably expressing WT and S100M RET (Figure 3.3c). In non-permeabilised (minus Triton X-100) induced DLD-1 cells expressing either WT or S100M RET, only WT RET was visible at the cell surface. S100M RET staining could only be seen in permeabilised cells, confirming that S100M RET does not reach the cell surface and is trapped within the cell. The peri-nuclear staining observed suggested that S100M RET was localised to the ER. The combined observations from western blot, FACS and immunofluorescence analysis confirm that S100M RET is not fully glycosylated and the majority of the protein does not reach the cell surface. FACS analysis suggests that a very small proportion of the protein may reach the surface, but the levels are greatly reduced in comparison with the WT protein.

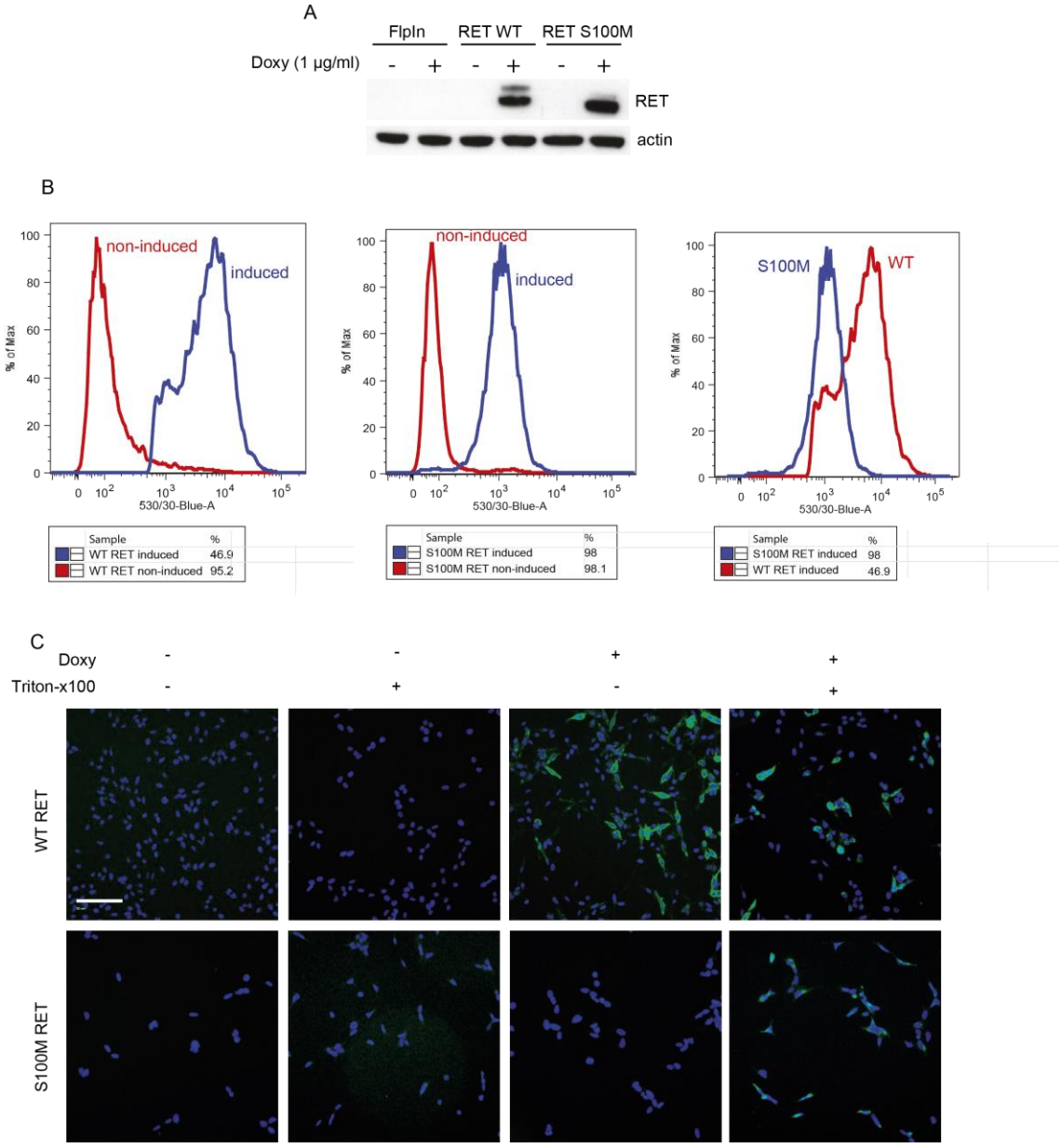

Figure 3.3 S100M RET is not fully glycosylated and is not exported to the cell surface

(A) Western blot of immature and mature RET species in Flp-In, WT RET or S100M RET Hek293 cells. **(B)** (Far left) Histogram displaying fluorescence intensity for non-induced and induced Hek293 cells expressing WT RET obtained via FACS analysis; (middle) Histogram displaying fluorescence intensity for non-induced and induced Hek293 cells expressing S100M RET obtained via FACS analysis; (far right) histogram displaying fluorescence intensity for induced Hek293 cells expressing WT or S100M RET obtained via FACS analysis. The graphs are a representative of three separate experiments. **(C)** Detection of surface and intracellular (+ Triton-X100) RET levels in non-induced and induced DLD-1 cells expressing WT or S100M RET. Scale bar represents 50 µm.

3.5 Investigating the role of unpaired cysteine residues in RET maturation

As mentioned previously, two unpaired cysteine residues (C87 & C216) found within hRET CLD1-2 were mutated to enhance expression yields and allow subsequent crystallisation of the protein (Kjaer et al., 2010). They were also shown to restore full glycosylation of the HSCR mutant S100M RET and allow export of the S100M ECD in a surrogate secretion assay. As seen in Figure 3.4a, S100M RET existed only as the immature 150kDa species, while the mutations C87R and C216S (S100M*) resulted in glycosylation of the receptor into its mature 170kDa form, similar to the WT RET protein.

In order to examine maturation kinetics for each of the RET species, pulse chase analysis was carried out using WT, S100M and S100M* Hek293 cells and radioactive RET levels were examined over a period of six hours. Radioactive RET levels were detected using a phosphor screen (Figure 3.4b) and each band quantified with Image J (Schneider et al., 2012). WT RET maturation – i.e. export from the ER to the Golgi apparatus and glycosylation – appears to occur between 0 and 90 minutes (Figure 3.4c). Since many proteins have been shown to fold and be exported in under a minute (Wiseman et al., 2007), the RET folding/export kinetics of up to 90 minutes highlight the fact that the RET receptor is a slow folding protein even in its non-pathogenic state. S100M RET does not mature over the six hours post radioactive pulse, further indicating that S100M RET does not reach the Golgi apparatus and is not fully glycosylated. In contrast, the S100M* RET is no longer blocked as an immature form but is fully glycosylated and we infer therefore exported to the Golgi apparatus. The kinetics of maturation were calculated by quantifying the band intensities using Image J and normalising the intensity of the lower or upper band against total RET levels at each individual time point. In the case of WT and S100M* RET, the levels of 150kDa RET fall as it is converted into the 170kDa form (Figure 3.4c). This does not occur for S100M RET.

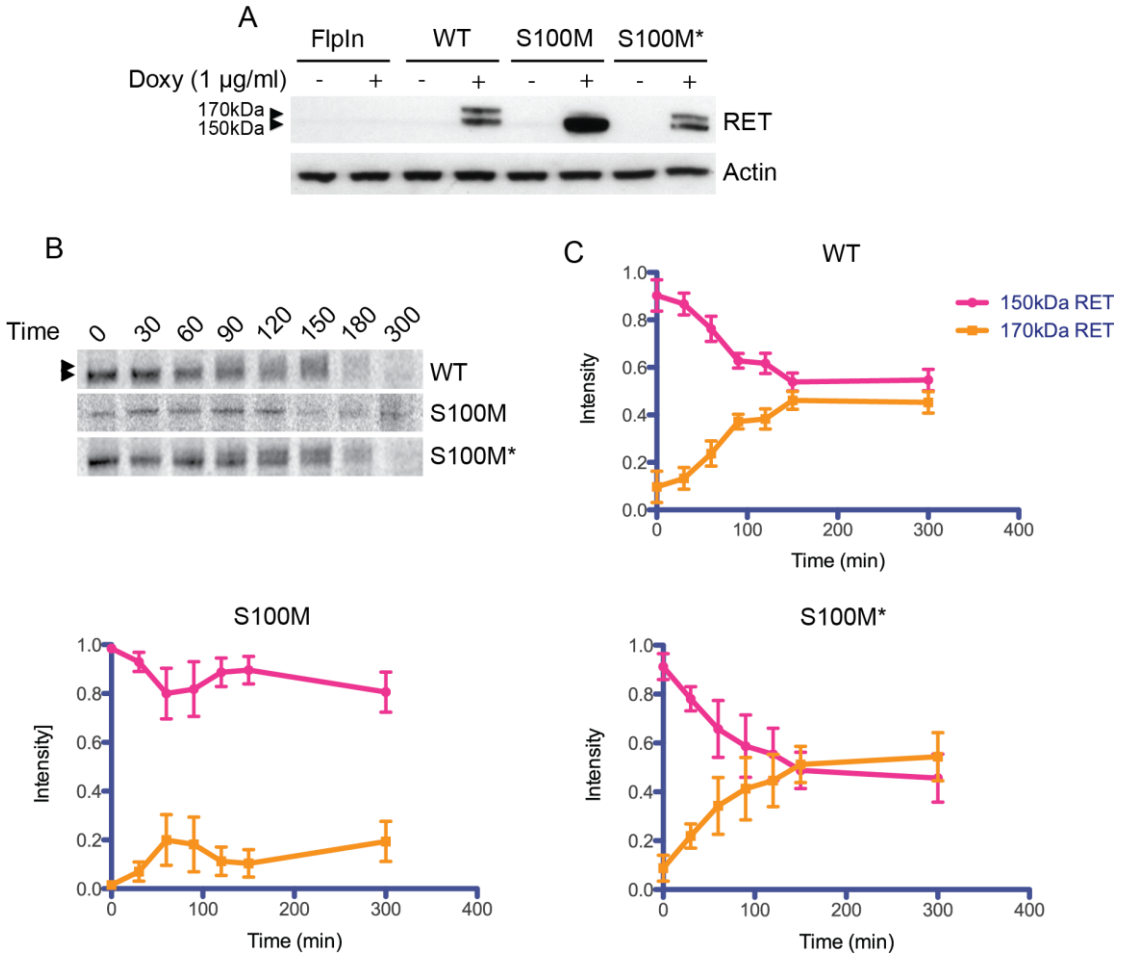

Figure 3.4 Maturation kinetics of WT, S100M and S100M* RET

(A) Cell lysates from Flp-In, WT RET, S100M RET and S100M* RET Hek293 cell lysates were immuno-blotted for RET expression. WT RET and S100M* RET exist as both immature and mature species, while S100M RET can only be found as the immature 150kDa species. **(B)** Phosphor screen detection of immuno-precipitated RET in WT, S100M or S100M* Hek293 cells pulse chased with S^{35}-methionine. **(C)** Analysis of phosphor screen band intensities. The 150kDa or 170kDa band was normalised against the sum of both bands for each time point. N=5 experiments have been performed and standard error of the mean (S.E.M) is displayed.

The pulse chase experiments confirmed that the removal of two unpaired cysteine residues restored a wild type maturation pathway for the RET S100M mutant. A probable explanation is that protein disulphide isomerases within the ER promote the correct disulphide bonds and/or reshuffle incorrect disulphides formed through C87 and/or C216. Removal of two unpaired cysteines reduces the probability of incorrect non-native disulphide bond formation to effectively increase the efficiency and rate of RET folding. Considering this kinetic explanation, S100M RET may have an even slower folding trajectory within the ER, leading to incomplete glycosylation processing; triggering ER associated degradation (ERAD). The

C87R/C216S mutation may assist folding by reducing the number of inappropriately paired disulphide bond possibilities, allowing the protein to exit the ER before ERAD intervenes. This species of S100M can then be processed to a fully glycosylated form within Golgi apparatus (modelled in Figure 3.10 in the conclusion). An alternative explanation is that the mutation of the two RET cysteine residues removes a thiol-dependent ER retention signal as found for unpolymerised IgM molecules (Anelli et al., 2007). Thiol-retention chaperones – such as ERp44 – could interact with S100M RET via the unpaired cysteine residues, retaining the protein within the ER and preventing its export to the Golgi apparatus (Anelli et al., 2003).

To examine the consequences of restoring a wild type maturation path to S100M RET, cell surface levels of S100M* RET were compared to that of WT and S100M RET via FACS analysis. Live cell FACS analysis of WT, S100M or S100M* RET Hek293 cells (Figure 3.5a) showed a fluorescence intensity for S100M* RET similar to that of WT RET, indicating that cell surface RET levels had been restored. Cell surface levels of S100M and S100M* RET was also investigated using immunofluorescence staining. This was carried out in Hek293 cells due to the fact that DLD-1 stable cell lines were only available for WT and S100M RET. Fixed cells were stained with the 1D9 anti-RET antibody, the Alexa488 secondary fluorescent antibody and DAPI. The average ring (the area of the cell surrounding the nucleus) fluorescence intensity values were calculated by the Cellomics iView (Thermo Scientific) and averaged over 12 individual wells of a 96-well plate. Both the surface and intracellular levels of S100M* RET were significantly higher than those of S100M RET (Figure 3.5b). This suggests that S100M RET is degraded at a much higher rate, which could be due to the protein trapped within the ER being targeted for ERAD.

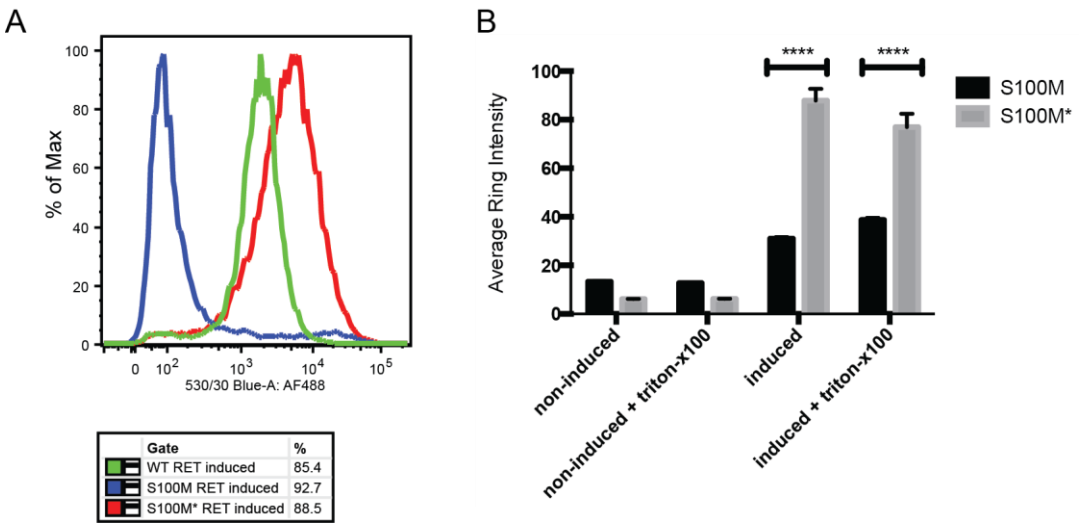

Figure 3.5 Cell surface expression of WT, S100M and S100M* RET

(A) Histogram displaying fluorescence intensity for WT, S100M or S100M* RET Hek293 cells obtained via FACS analysis. This is a representative graph of three separate experiments. **(B)** Graph showing average ring intensity values (channel 2) for Hek293 cells expressing S100M or S100M* RET. S.E.M is calculated from n=12 and statistical significance was calculated using the unpaired t test ($p<0.0001$).

3.6 Investigating RET signalling

Ligand and co-receptor binding to the RET ECD at the cell surface leads to auto-phosphorylation of the intracellular domain (ICD) and activation of its kinase activity. Several sites within the RET-ICD become phosphorylated, with these phosphorylated tyrosine residues serving as docking sites for intracellular signalling proteins (Kawamoto et al., 2004). In order to examine this process of RET activation, recombinant human GDNF and GFRα1 (R&D systems) were added to WT RET and S100M RET DLD-1 cells. Cell lysates were immuno-blotted with antibodies against RET, ERK1/2 and phosphorylated ERK1/2, as the MAPK signalling pathway is known to be stimulated upon RET activation (Besset et al., 2000).

Akt/PKB and MAPK pathway activation was examined to probe for the best marker of RET activation. We found that MAPK responded better to ligand/co-receptor and represented a better surrogate of RET activation (Figure 3.6b). Akt phosphorylation levels were persistently high, most likely due to a PI3K activating mutation in DLD-1 cells (Figure 3.6a). Elevated ERK1/2 phosphorylation (pERK1/2 – upper band) was only detected under the conditions of induced WT RET expression in the presence of recombinant GDNF-GFRα1 (Figure 3.6b). In contrast, this pathway is not activated when S100M RET expression is induced in the presence of GDNF-

GFRα1, suggesting that S100M RET cannot activate downstream RET signalling pathways. This could either be because of its subcellular localisation or alternatively immature S100M RET cannot bind ligand and therefore cannot signal. We therefore wished to explore whether restoring cell surface expression of S100M RET could lead to a functional RET response through the MAPK pathway.

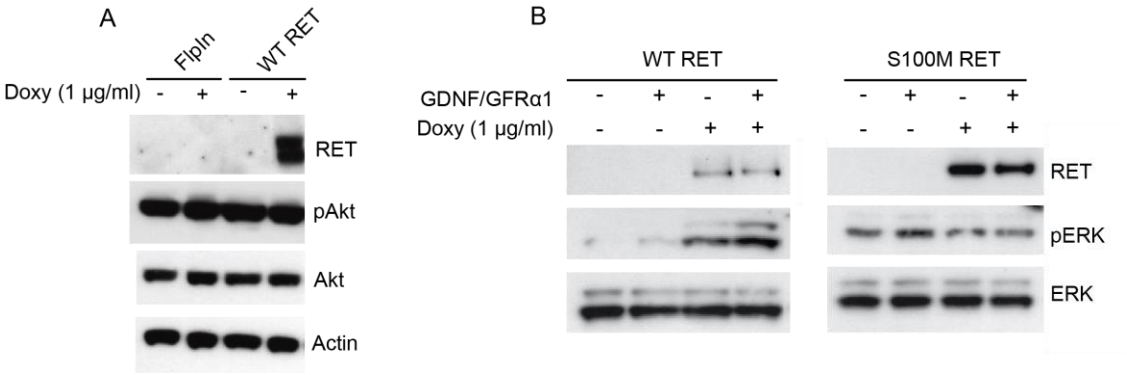

Figure 3.6 Detecting downstream signalling for WT and S100M RET

(A) Western blot analysis of WT or S100M RET DLD-1 cell lysates +/- doxycycline, immuno-blotted for RET, Akt, phosphorylated Akt (pAkt) or Actin. **(B)** Western blot analysis of WT or S100M RET DLD-1 cell lysates +/- doxycycline and recombinant GDNF/GFRα1, immuno-blotted for RET, ERK1/2 and pERK1/2.

Initially, wild type RET, S100M and S100M* RET signalling was investigated in Hek293 cells, but our results were inconsistent and not reproducible. For this reason, experiments were continued in WT and S100M RET DLD-1 cells (as no S100M* DLD cell line was available), with results suggesting the pERK1/2 pathway was a robust indicator of RET activation in this cell line. In order to examine the S100M* RET signalling capabilities, S100M* RET DLD-1 and HeLa cell lines were being created at the time of writing. S100M* HeLa clones had been successfully expanded and were awaiting RET expression and zeocin sensitivity testing.

As recombinantly expressed S100M and S100M* RET ECD were known to bind to recombinant GDNF and GFRα1 as efficiently as the WT RET ECD (Kjaer et al., 2010), it was hypothesised that the restoration of cell surface expression could result in the restoration of downstream signalling activity. In order to investigate this further, both WT and S100M RET folding and export were manipulated using chemical chaperones and siRNA knockdown of a select number of targets, in an attempt to identify factors involved in RET export.

3.7 Efforts to manipulate S100M RET export using chemical chaperones

Aberrant substrate folding within the ER can lead to a build-up of protein in an already crowded organelle and elevated stress levels. The unfolded protein response (UPR) is activated upon such ER stress, resulting in the transcriptional upregulation of folding chaperones and the attenuation of protein import into the ER (Ron and Harding, 2012). It was assumed that the lack of S100M RET maturation (Figure 3.3a) and reduced protein levels compared to S100M* RET (Figure 3.5b) were due to a build-up of partially folded protein within the ER that was subsequently degraded via ERAD. In this instance, it was hypothesised that such an event would result in elevated ER stress levels.

In order to test the effect of RET expression on ER stress levels, WT, S100M and S100M* RET Hek293 cells were immuno-blotted for the stress marker BiP, an ER chaperone that binds to unfolded proteins and regulates the activity of members of the UPR (Bertolotti et al., 2000). BiP levels were found to be elevated upon expression of S100M RET, suggesting that the protein was indeed trapped within the ER due to aberrant folding (Figure 3.7). Expression of WT or S100M* RET did not result in increased BiP levels, presumably due to the protein folding more efficiently and exiting the ER. This preliminary data needs to be built upon in order to confirm the result by investigating the levels of another ER stress marker – such as phosphorylated PERK (ER-localised PKR-like ER kinase). PERK is a mediator of the UPR that is responsible for translation inhibition when activated (Harding et al., 1999).

There are several chemical chaperones known to aid protein folding or alleviate ER stress, including 4-Phenylbutyric acid (4-PBA) and glycerol. 4-PBA is a small molecular weight chemical chaperone that is known to inhibit histone deacetylase, in turn regulating gene transcription (Bolden et al., 2006). The chaperone has been shown to improve the trafficking and function of the ΔF508 mutant Cystic Fibrosis Transmembrane Regulator (CFTR), a protein known to misfold within the ER, but did not appear to have an effect on ΔF508-CFTR gene transcription (Rubenstein et al., 1997). 4-PBA was subsequently found to downregulate the expression of heat

shock cognate protein 70 (Hsc70), a molecular chaperone that belongs to the heat shock protein 70 (Hsp70) family and has been shown to target particular proteins for ubiquitin-dependent degradation (Rubenstein and Zeitlin, 2000). Glycerol has also been shown to rescue cell surface expression levels of ΔF508-CFTR, due to its ability to increase the thermodynamic stability of globular proteins (Sato et al., 1996).

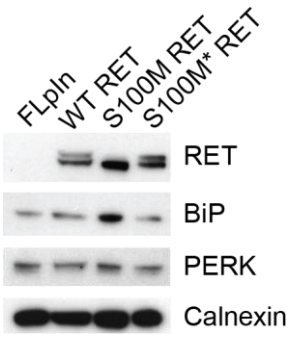

Figure 3.7 Elevated BiP levels in Hek394 cells expressing S100M RET

Western blot analysis of Flp-In, WT, S100M and S100M* RET Hek293 cell lysates. Levels of the folding chaperone BiP were elevated in cells expressing S100M RET.

The effect of 4-PBA and glycerol on S100M RET folding was examined in DLD-1 cells. Cells were grown in a 96-well glass bottom plate (10,000 cells/well) in the presence of increasing concentrations of 4-PBA or glycerol for 24 hours, before fixing, staining and imaging. Both 4-PBA and glycerol resulted in increased S100M RET cell surface expression (Figure 3.8), indicating that HSCR RET cell surface expression could be restored using chemical chaperones.

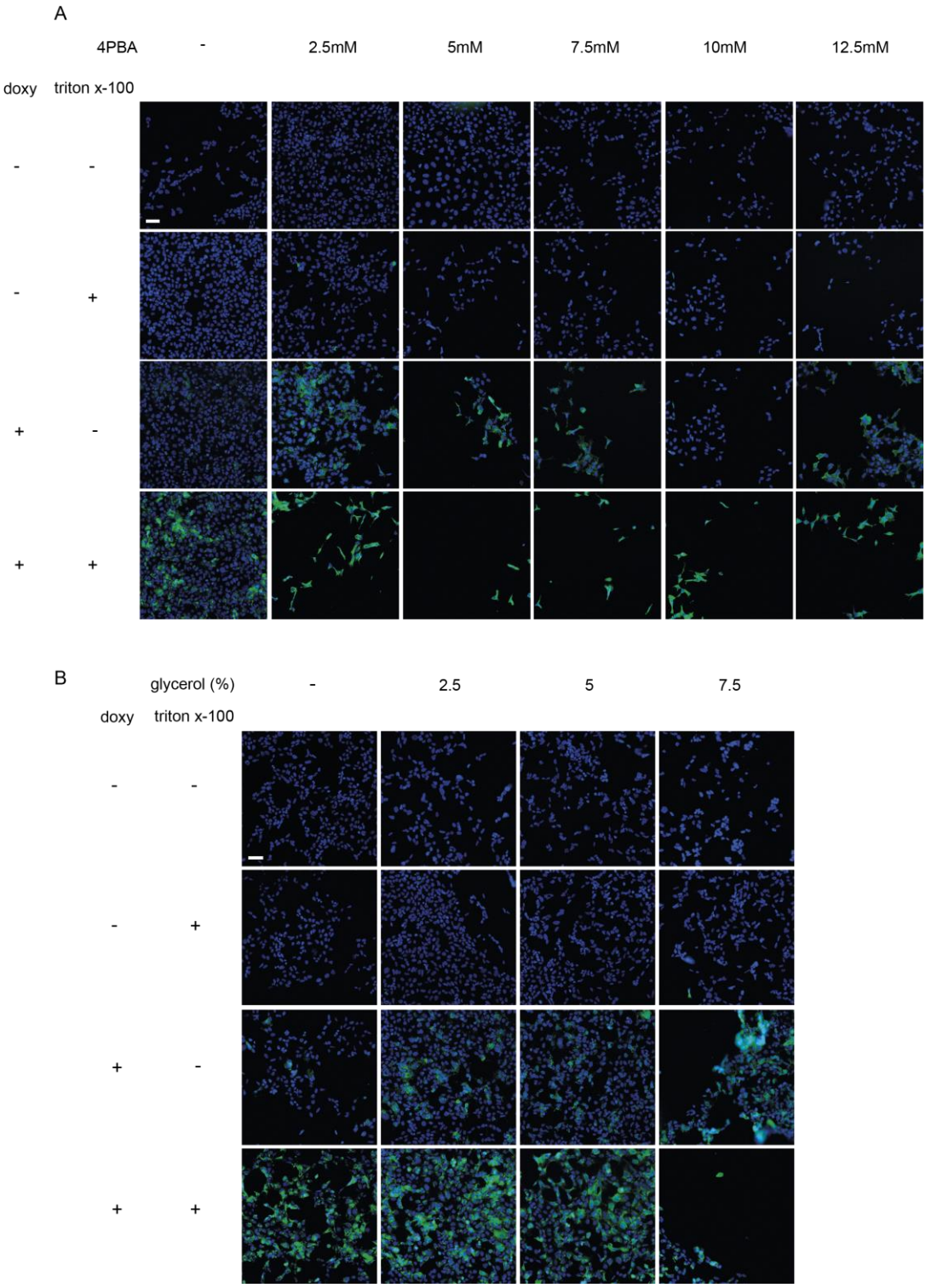

Figure 3.8 Cell surface expression of S100M RET in the presence of chemical chaperones

(A) Images of non- and induced (-/+ doxy) DLD-1 Flp-In S100M RET cells grown in the presence of increasing concentrations of 4-PBA. Non-permeabilised cells (- triton-x100) show increasing levels of fluorescence intensity in the green channel. **(B)** Images of non- and induced DLD-1 Flp-In S100M RET cells grown in the presence of increasing concentrations of glycerol. Images were taken at 10x magnification using the Arrayscan automated microscope (Cellomics). Scale bar represents 50 µm.

WT and S100M RET maturation and phosphorylation (along with pERK1/2 levels) in the presence of 4-PBA must be examined in DLD-1 cells in order to gain insight into both the mechanism of action and the consequences of the chaperone. Preliminary western blot analysis (data not shown) suggests that the increased cell surface levels of S100M RET are not due to restored maturation and no phosphorylated ERK1/2 was observed upon ligand stimulation. 4-PBA may be forcing partially folded RET to the cell surface that is not capable of binding ligand and co-receptor. The experiment needs to be repeated, before subsequent investigation of the mechanism of action by examining RET transcription levels and possible downregulation of Hsc70.

3.8 Manipulation of RET cell surface expression by siRNA knockdown of candidate targets involved in protein folding and export

In order to gain a better understanding of RET's transition through the cell, a 300-candidate siRNA screen comprising of genes involved in protein folding, export and degradation was designed. While the design and implementation of this screen is described in the following chapter, the siRNA knockdown of a small number of potential targets was initially carried out, to test the viability of the design.

Ras-related protein Rab7 (Rab7), Vacuolar-type H^+-ATPase (V-ATPase), Endoplasmic Reticulum Protein 44 (ERp44) and the PDI portion of Prolyl 4-Hydroxylase (P4HB) were chosen as initial knockdown targets. Rab7 is a small GTPase associated with the late endosome/lysosome pathway. Several Rab GTPases are involved in the endocytic process, with Rab5 found on early endosomes (involved in endosome biogenesis) and Rab7 marking matured late endosomes (involved in endolysosomal fusion) (Gautreau et al., 2014). It was hypothesised that the loss of a factor involved in lysosomal targeting may lead to increased RET cell surface levels, and Rab7 silencing has been shown to restore plasma membrane expression of the μ-opioid receptor in diabetic rats (Mousa et al., 2013). V-ATPase is an enzyme found in the membrane of many organelles and is required for organelle acidification (Forgac, 1998). As the enzyme plays many roles

within the cell, there were several hypotheses as to the effect of its inhibition on RET cell surface levels. Firstly, V-ATPase knockdown could result in reduced cell surface levels of the receptor, as acidification of the Golgi apparatus is required for RET maturation, although previous data has shown that the chemical inhibition of V-ATPase does not result in reduced cell surface levels (Hirata et al., 2010). Alternatively, the knockdown could result in increased cell surface levels, due to its role in endocytosis and lysosomal acidification. Similar to Rab7, inhibition of lysosomal degradation of the receptor could result in increased plasma membrane levels. ERp44 is a thiol retention protein found within the ER that is known to interact with and prevent the export of cargo proteins with unpaired cysteines (Anelli et al., 2003). Therefore, the removal of this interaction via siRNA knockdown may increase the export efficiency and cell surface expression of RET. P4H is a multifunctional enzyme that acts as a prolyl hydroxylase and protein disulphide isomerase (PDI) (Kivirikko and Myllyharju, 1998). The knockdown of an important PDI could also affect RET export in two distinct ways: the prevention of efficient RET folding would have a negative impact, while the elimination of the PDI interactions with unpaired cysteine residues could have a positive impact.

WT RET DLD-1 cells were incubated with siRNAs (ON-TARGETplus SMARTpool, Dharmacon) targeting each of these genes, with siRNA against two V-ATPase subunits – ATP6V0C and ATP6V1C (Figure 3.9). The silencing of the RET gene resulted in the loss of WT RET cell surface expression in induced cells (-72% compared to control), confirming the success of the siRNA experiment. ERp44 silencing also resulted in a reduction in WT RET cell surface levels (-46%), which was surprising. The original hypothesis was that ERp44 may be acting as a thiol retention protein and holding RET within the ER, while this suggests that ERp44 may actually be acting as a folding chaperone for RET. P4HB and ATP6V1C2 silencing appeared to have little effect on the export of the receptor, while ATP6V0C silencing resulted in an increase in WT RET cell surface levels (+30%). The differences in effect between ATP6V1C2 and ATP6V0C may be indicative of siRNA inefficiency. The observation that V-ATPase knockdown causes an increase in WT RET cell surface levels suggests that the inhibition of endocytosis or lysosomal degradation has a positive effect, which is as expected. RAB7A silencing also had a modest positive effect on cell surface levels (+14%), which suggests

again that the inhibition of lysosomal degradation can increase RET targeting to the plasma membrane.

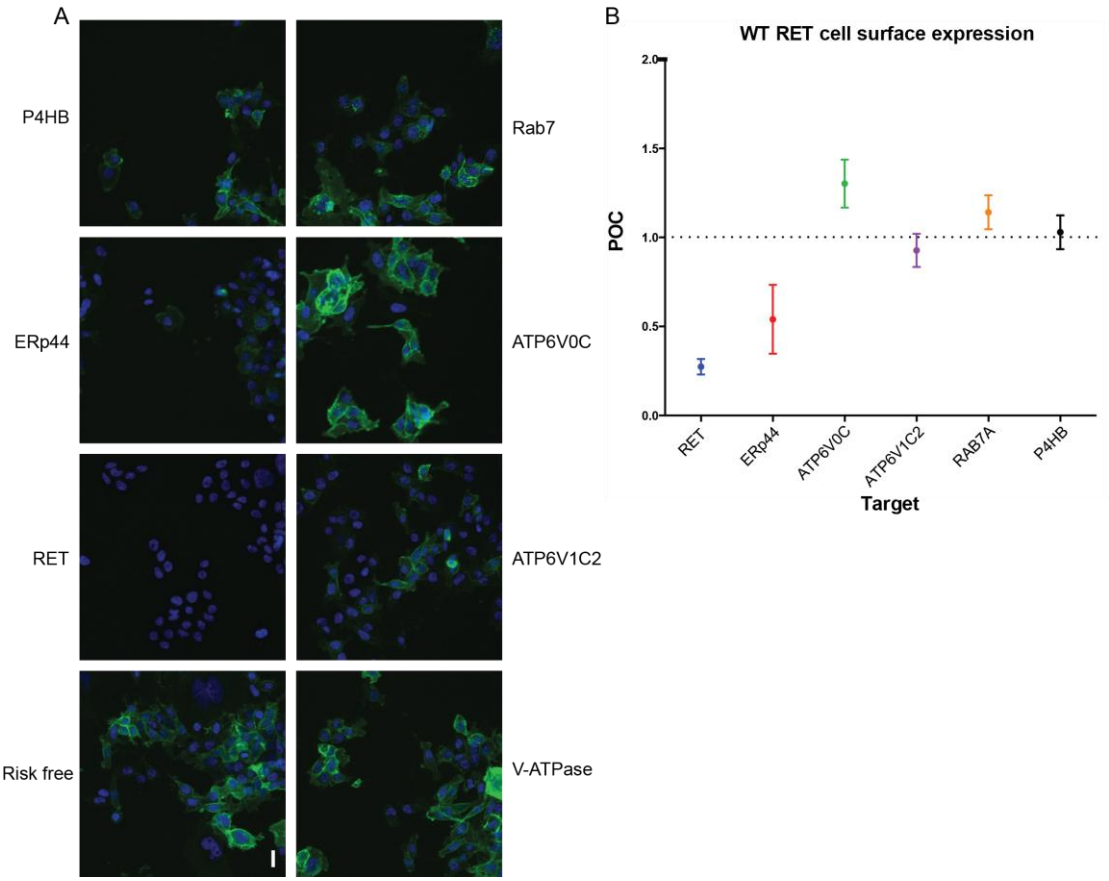

Figure 3.9 Effect of specific target siRNA knockdown on the WT RET surface expression
DLD-1 Flp-In S100M RET cells were grown in the presence of siRNAs (Risc free; RET; ATP6V0C; ATPV1C; ATP6V0C + ATPV1C; ERp44; P4HB; Rab7) for 48 h before the addition of doxycycline for a further 24 h. **(A)** Images taken of RET surface expression (anti-RET 1D9 antibody + Alexa488 fluorescence antibody) at 10 x magnification using the Arrayscan automated microscope. **(B)** Percentage of control (POC) values for each target siRNA. Average channel-2 ring fluorescence intensity values were normalised against the mean control (Risc free). Mean value (n=2, 6 replicates in each experiment) with standard deviation (S.D) error bars displayed. Scale bar represents 50 µm.

3.9 Chapter Conclusion

The aim of the work described in this thesis chapter was to use a variety of methods to investigate RET maturation and export, and to attempt to restore S100M RET cell surface expression. I generated several inducible mammalian cell lines expressing WT and mutant RET to be utilised for this purpose, and have

presented FACS and immunofluorescence data confirming the absence of S100M RET at the cell surface of both Hek293 and DLD-1 cells. WT RET expression in DLD-1 cells in the presence of ligand and co-receptor leads to the activation of the MAPK signalling pathway, while S100M RET expression does not. This is a significant advancement, as these cells are responsive to GDNF-GFRa1 specifically with low background and no apparent basal level of auto-phosphorylation. In marked contrast, the equivalent Flp-In cell line producing S100M RET did not lead to ERK1/2 phosphorylation. Previous data has shown that mature and secreted S100M RET ECD can bind to ligand and co-receptor as efficiently as WT RET, creating the hypothesis that restoring S100M RET to the cell surface may be sufficient to restore RET signalling capabilities.

I describe how S100M RET cell surface levels can be increased via the deletion of two unpaired cysteine residues, potentially increasing the folding efficiency of the protein, and by the addition of chemical chaperones 4-PBA and glycerol. Preliminary investigations – that require further validation – into the maturation and signalling capabilities of S100M RET in the presence of 4-PBA suggest that chemical intervention is insufficient, and may be resulting in partially folded RET at the cell surface. Investigations therefore continued in the direction of gene silencing, identifying a small number of factors that may be involved in RET export and plasma membrane targeting. Gene silencing carried out in WT RET DLD-1 cells has shown that RET can be silenced, ERp44 appears to be required for optimal WT RET expression and inhibition of lysosomal degradation (via the knockdown of V-ATPase or Rab7) results in increased cell surface levels. These observations provide a basis for the next chapter: investigating the effect of silencing of a much larger group of targets. RET and ERp44 will be used as negative controls, and ATP6V0C and RAB7A will be used as positive controls.

3.9.1 A hypothetical model of WT, S100M and S100M* RET folding and export

Pulse chase data suggests that the WT RET protein is an intrinsically poor folding glycoprotein and therefore is a potential substrate for ERAD. A portion of the folded RET is exported from the ER and trafficked to the Golgi apparatus, where it is

glycosylated further (demonstrated by western blot analysis) and transported to the plasma membrane (as seen by FACS and immunofluorescence data). Here, the receptor can bind to ligand and co-receptor, resulting in dimerisation and *trans*-phosphorylation of the kinase domain and subsequent activation of downstream signalling pathways (as seen by western blot analysis of the phosphorylation state of ERK1/2). Following activation, the receptor is subsequently internalised, with some recycling back to the plasma membrane and some lysosomal degradation. This final statement is based on the preliminary findings that V-ATPase knockdown results in increased WT RET cell surface levels.

In the case of HSCR mutant S100M RET, western blot analysis and FACS/immunofluorescence data indicates that the receptor does not reach the Golgi apparatus (as it is not fully glycosylated) and is not exported to the cell surface. Instead, the receptor spends too long in the folding pathway, resulting in the activation of ERAD. This is indicated by the elevated levels of BiP (although further investigations could strengthen this) and has been previously observed (Kjær and Ibanez, 2003b). S100M* RET does not contain two unpaired cysteine residues, resulting in a lower number of possible disulphide bond formations. As such, the receptor folds in a shorter time period and is allowed to exit from the ER and continue its journey. This flow of RET export and subsequent degradation have been visualised in Figure 3.10.

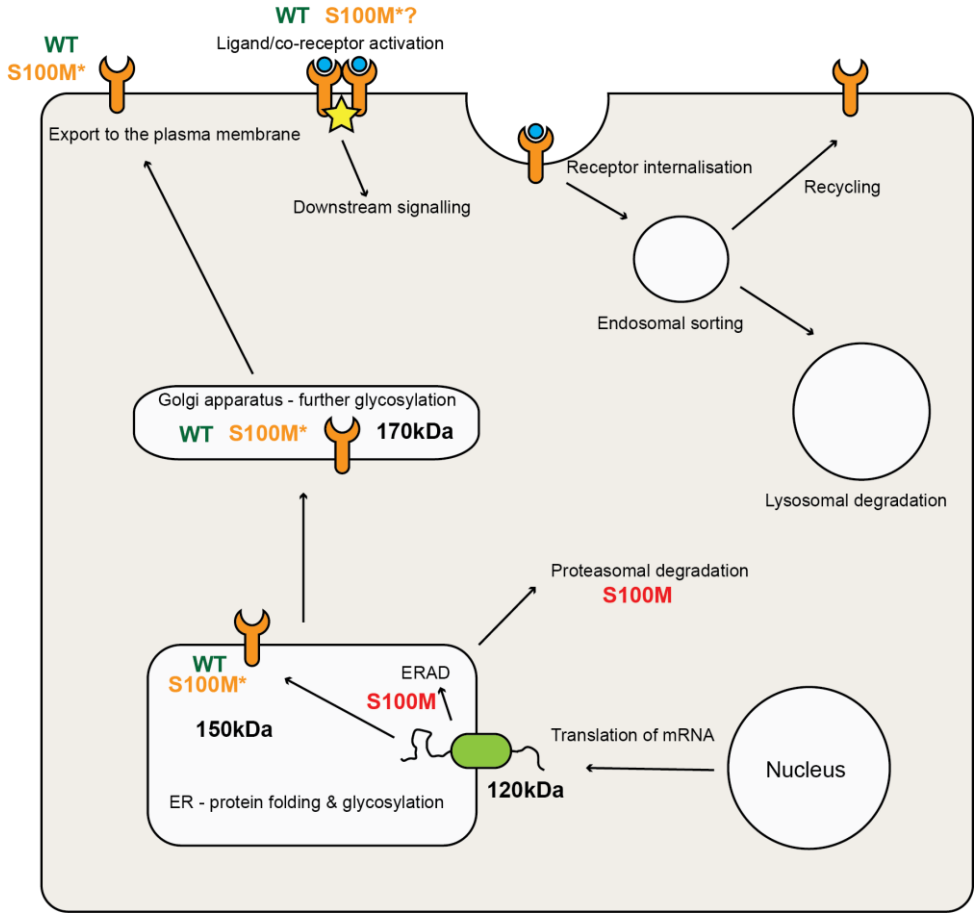

Figure 3.10 A model of WT, S100M and S100M* RET transport through the cell

RET is transformed from a nascent 120kDa polypeptide into a 150kDa folded immature receptor before transportation to the Golgi apparatus for further glycosylation. The mature 170kDa receptor can then be exported to the plasma membrane, ready for ligand/co-receptor binding and subsequent signalling. Receptor activation leads to internalisation and recycling or lysosomal degradation. S100M RET is targeted for ERAD within the ER and degraded via the proteasome. S100M* RET is exported to the Golgi apparatus and the plasma membrane, although signalling capabilities are currently unknown.

3.9.2 Future investigations into RET signalling

As mentioned previously, several clones of S100M* HeLa cell lines were created during the writing of this thesis. Future investigations should first involve the establishment of RET activity in WT, S100M and S100M* expressing HeLa cells; by examining the phosphorylation status of ERK1/2 or Akt in the presence and absence of ligand and co-receptor. While previous data has suggested that S100M and S100M* bind ligand and co-receptor as efficiently as WT, this should be established in a mammalian cell setting with the entire receptor present.

3.9.3 RET evolution: a role for unpaired cysteine residues

Overexpression of RET at the plasma membrane has been observed in several cancer types, such as breast, pancreatic and lung (Morandi et al., 2011, Zeng et al., 2008, Dawson et al., 1998). The observation that even WT RET protein folds at an unusually slow rate could be interpreted as a mechanism for preventing excess receptor expression at the cell surface. As discussed in the introduction, the RET receptor has several structural elements – such as the *cis*-Pro loop and disulphide bonds – that are only present in higher vertebrate species, indicating a level of RET evolution. The two unpaired cysteine residues Cys87 and Cys216 are also only present in higher vertebrates (Figure 3.12). It is plausible to hypothesise that RET acquired unpaired cysteines to control or influence cell surface levels and prevent oncogenic RET signalling.

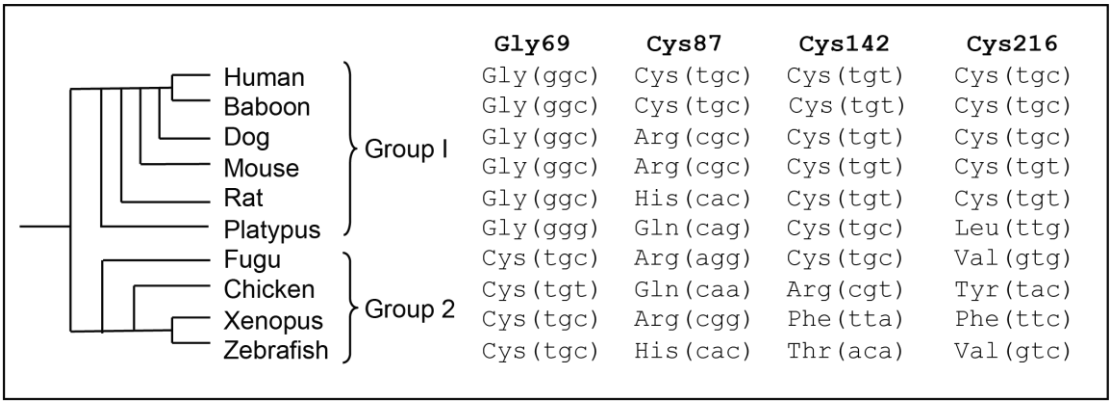

Gly69	Cys87	Cys142	Cys216
Gly(ggc)	Cys(tgc)	Cys(tgt)	Cys(tgc)
Gly(ggc)	Cys(tgc)	Cys(tgt)	Cys(tgc)
Gly(ggc)	Arg(cgc)	Cys(tgt)	Cys(tgc)
Gly(ggc)	Arg(cgc)	Cys(tgt)	Cys(tgt)
Gly(ggc)	His(cac)	Cys(tgt)	Cys(tgt)
Gly(ggg)	Gln(cag)	Cys(tgc)	Leu(ttg)
Cys(tgc)	Arg(agg)	Cys(tgc)	Val(gtg)
Cys(tgt)	Gln(caa)	Arg(cgt)	Tyr(tac)
Cys(tgc)	Arg(cgg)	Phe(tta)	Phe(ttc)
Cys(tgc)	His(cac)	Thr(aca)	Val(gtc)

Figure 3.11 RET evolution in higher vertebrates

The phylogenetic tree of RET with higher (group 1) and lower (group 2) vertebrates. Evolution of the *cis*-Pro loop (Gly69 and Cys142) and unpaired cysteine residues (Cys87 and Cys216) are shown for each corresponding species.

To examine this possibility further, stable DLD-1 cell lines expressing oncogenic RET (such as M918T) and WT RET without the unpaired cysteine residues (WT*) could be produced. In doing so, the signalling properties and subsequent cellular phenotypes (such as differentiation, viability and growth patterns) could be compared.

Chapter 4. Implementation of a cell-based HTS screen to identify factors influencing WT and S100M RET maturation and export

4.1 Introduction

Pathways controlling the maturation and export of receptor tyrosine kinases are poorly understood. RET is unique among receptor tyrosine kinases for its slow and inefficient folding, making it sensitive to loss-of-function mutations causal in at least two human diseases. I have used the mild Hirschsprung's disease mutation S100M as a model for understanding how to restore HSCR RET functionality and will improve knowledge of key components controlling RET maturation and export. The aim of this work was to develop a cell-based assay for monitoring cell surface expression levels of both wild-type (WT) RET and S100M RET. The assay was developed into a high throughput screen using an inducible S100M HSCR mutant cell line and a targeted small interfering RNA (siRNA) library to knock down candidates. In parallel, an siRNA screen was also carried out to investigate the effect of specific gene silencing on WT RET cell surface expression. Both screens targeted 300 candidate genes chosen based on their roles in protein folding, export, ER quality control and protein degradation. A primary hit rate of 10% was found which is high but unsurprising given the biased library used. Positive hits influencing RET cell surface expression were connected to distinct cellular pathways, some expected and others quite unexpected, leading to current efforts into their validation as "true" positives.

The largest effect on WT and S100M RET cell surface levels occurred when genes encoding components of three degradative pathways– proteasomal, lysosomal and autophagosomal – were silenced. Interestingly, optineurin (OPTN) – an autophagy receptor known to target aggregated proteins and *Salmonella* – was identified as a negative regulator of S100M RET (i.e. the knockdown of OPTN enhanced S100M RET surface expression). Furthermore, chemical inhibition of OPTN regulator TBK1 (courtesy of Professor P Cohen, Dundee) indeed boosted S100M levels at the cell surface. However, preliminary validation suggests that the cell surface

S100M RET rescued from these degradative pathways is not capable of restoring receptor maturation or downstream signalling. These findings provide indirect proof that immature S100M RET is not able to bind ligand and co-receptor even when present at the cell surface. The HTS screen also identified proteins involved in ER quality control and glycosylation. These candidate hits are likely to provide a better starting point for functional rescue of S100M RET signalling capabilities. Future directions are discussed, focussing on restoring S100M RET signalling by verifying hits involved in ER quality control and chaperone-assisted folding of WT RET cell surface expression.

The development and implementation of both the siRNA and chemical screen was carried out in collaboration with the HTS facility at the London Research Institute. Mike Howell, Rachael Instrell and Ming Jiang were involved in the design, development and implementation, while Becky Saunders carried out the preliminary statistical analysis.

4.2 Establishment of a cell-based assay to measure cell surface RET

The overall aim was to establish a sensitive and reliable cell-based assay able to detect changes – whether by gene silencing or small molecule inhibition – in the cell surface levels of WT or S100M RET. Reduction, no effect or an enhancement in WT RET surface levels were considered plausible outcomes from the screen given the inducible functional RET present on the cell surface of the cell line used. In contrast, I anticipated either an enhanced cell surface level or no effect as outcomes from the HSCR S100M RET HTS screen. As described in chapter 3, immuno-blotting and pulse chase analysis were sufficient to define the maturation state and kinetics of the receptor. Although the amount of mature RET observed is thought to correlate with cell surface levels, it remains a surrogate assay for cell surface location. To be certain of directly measuring RET surface expression levels, FACS analysis and/or immunofluorescence techniques were used. After successful pilot experiments, immunofluorescence was chosen as the cellular readout for the assay: cells would be plated and the fluorescence intensity in each well used as a

measurement for identifying conditions (gene silencing or chemical inhibition) that positively or negatively affected cell surface levels of the receptor.

With many commercial and academic anti-RET antibodies available, preliminary experiments investigated the optimal antibody staining for the assay (Figure 4.1). Stable Hek293 cells expressing WT RET were plated in glass-bottomed 96 well plates, fixed and stained overnight with a panel of four anti-RET antibodies (including 23C, an in-house RET antibody produced by Dr S Kjaer), before continued staining with the Alexa488 fluorescent secondary antibody and DAPI. At this stage of assay development, inducible Hek293 cells were used because they were the only cell line available. The mAb718 antibody worked well in western blots, but – as seen in Figure 4.1 – a very high background was observed when used for immunofluorescence; high fluorescence intensity was seen in non-induced cells stained with the antibody. In uninduced Hek293 cells, no 1D9 immunofluorescence staining is apparent, whilst clear surface staining is evident on cells in which RET expression has been induced. This antibody was selected for future work and was found to work well in both HeLa and DLD-1 inducible cell lines that became available later in the project, and so optimisation was not repeated.

Rachael Instrell, using siRNA against nuclear lamin A/C and RISC-free control, carried out the transfection optimisation. Fluorescence intensity, transfection efficiency and overall cell number was examined in both HeLa and DLD-1 cells. The most effective transfection reagents were then used to knockdown RET in HeLa and DLD-1 cells, identifying Lullaby® as the most effective transfection reagent (data not shown). As mentioned in the previous chapter, RET expression levels were far more heterogeneous in Hek293 cells than in HeLa and DLD-1 cells, an observation that has been confirmed by Professor Stephen Taylor (University of Manchester). HeLa and DLD-1 cells were therefore deemed optimal for the screen, with DLD-1 cells chosen as the cell line to take forward. This decision was based on a combination of satisfactory fluorescence intensity readouts, relatively homogeneous RET expression levels, high transfection efficiency and the robustness of the cell line during the screening procedure.

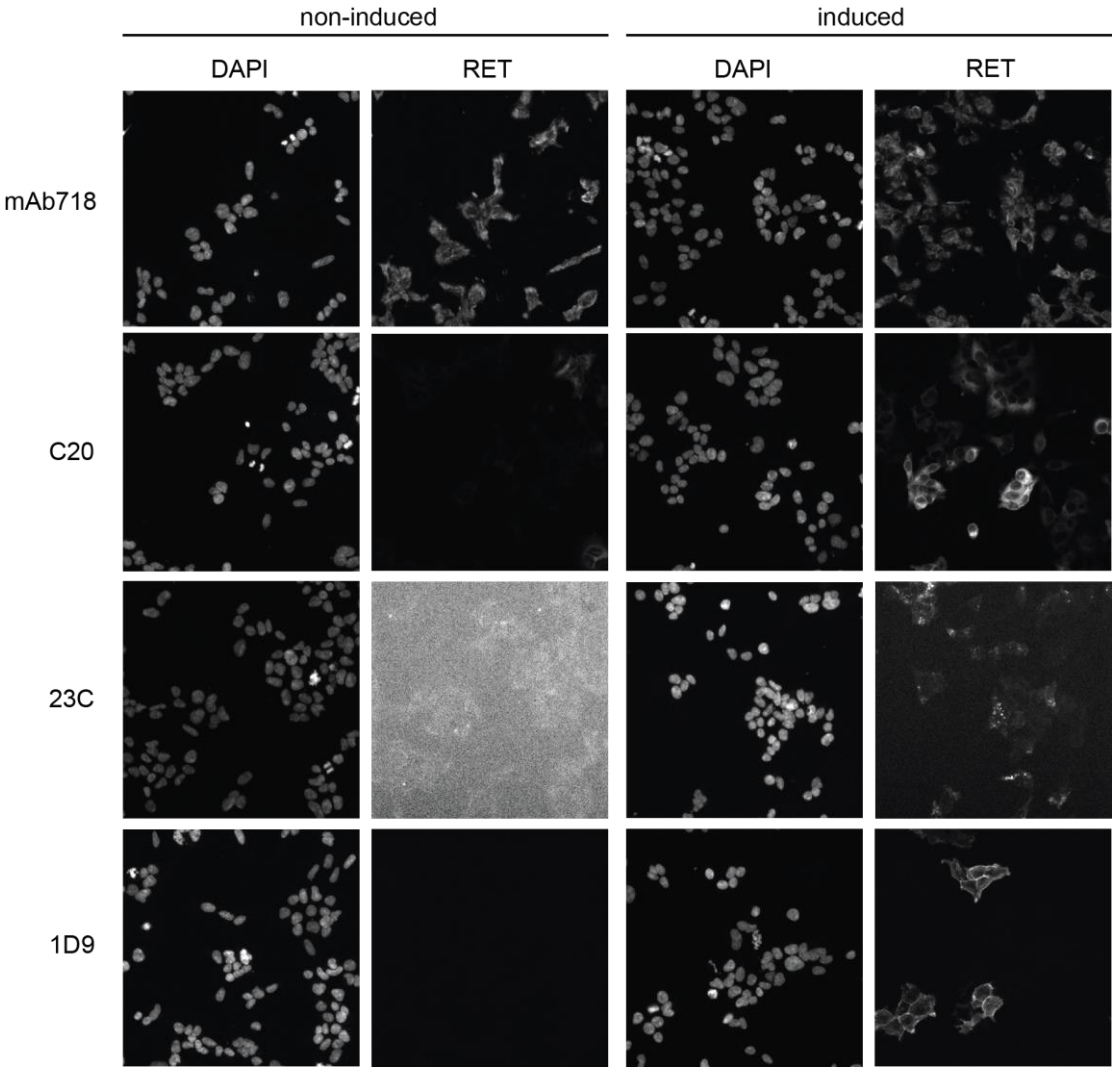

Figure 4.1 Optimising immunofluorescence with a panel of four anti-RET antibodies
Hek293 cells (+/- doxycycline) were stained with four different anti-RET antibodies to examine their effectiveness when used for immunofluorescent studies. Cells were plated in 96-well plates before fixation and staining with each primary antibody, Alexa488 secondary antibody and DAPI nuclear stain. (Figure courtesy of Dr R Instrell, CRUK).

Antibody concentrations and fixation times also required optimisation. DLD-1 cells were relatively sensitive to fixation, with a jump in fluorescence intensity at 30 minutes suggesting cell permeabilisation. For this reason, cells were incubated in 0.1% Triton-X100 for 20 minutes only. Primary antibody (1D9) concentrations of 1:20 and 1:40 were tested, along with secondary antibody (Alexa488) concentrations of 1:1000 and 1:2000. No discernible difference was observed for the each condition, so the lower concentrations were used to conserve antibody.

4.3 Design and implementation of the cell-based immunofluorescence assay

The screen was designed to take place over five days. A model for the assay can be seen in Figure 4.2.

4.3.1 Selecting candidates for a biased siRNA screen

The screen was developed to identify factors involved in RET maturation, folding and export and ER-associated degradation (ERAD). There are direct and indirect ways to accumulate RET at the cell surface; namely through the manipulation of protein glycosylation and folding, the perturbation of receptor internalisation and subsequent lysosomal degradation, or the bypass of the quality control-degradative pathway. As such, hits would be expected to arise from these three particular areas. However, the process of endocytosis is a post-maturation step linked to ligand-dependent downregulation and desensitisation, while glycosylation/folding and ERAD are pre-maturation steps. As the intention of the screen was to identify maturation and export factors, the process of endocytosis was not a priority when selecting candidates.

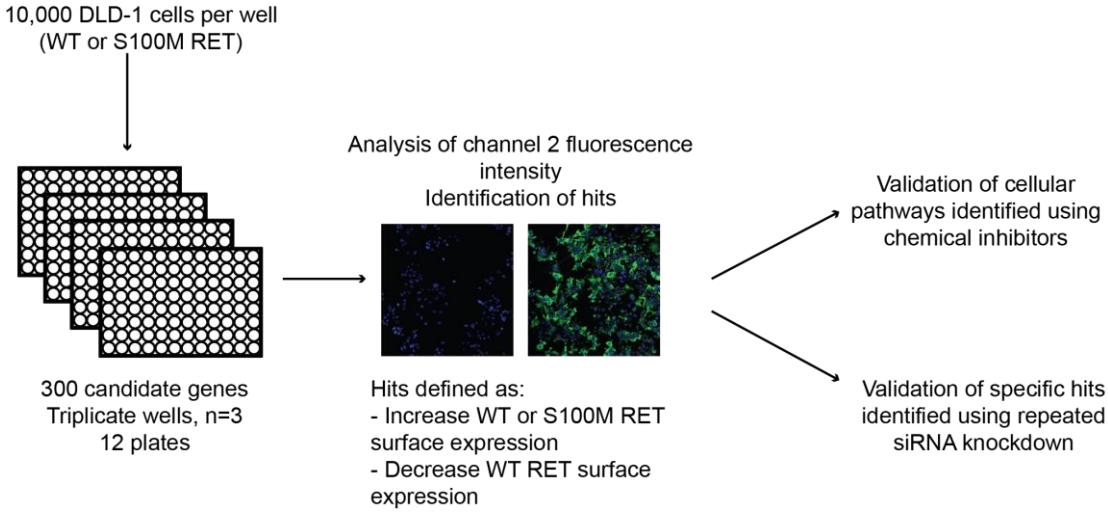

Figure 4.2 Design of the siRNA primary screen, analysis and validation

After siRNA knockdown of 300 candidate genes in DLD-1 cells stably expressing WT or S100M RET (n=3), channel-2 fluorescence intensity would be analysed to identify hits. Validation of true positives would follow by functional rescue experiments to examine GDNF ligand-stimulated auto-phosphorylation and MAPK pathway activation.

The initial candidates were identified via literature searches, selecting genes encoding proteins implicated in protein glycosylation, folding, export, degradation and ER-associated quality control (ERQC that includes ERAD). This preliminary list of approximately 50 genes was then inputted into the STRING (Search Tool for the Retrieval of Interacting Genes/Proteins) database (string-db.org). The database identified proteins that were known or predicted to interact with the initial selection (an example STRING readout using MAN1B1 is shown in Figure 4.3), based on literature searches, and predicted and experimental interactions. This resulted in a pool of 300 final candidates; the list and plate layout can be found in the appendix at the end of this thesis.

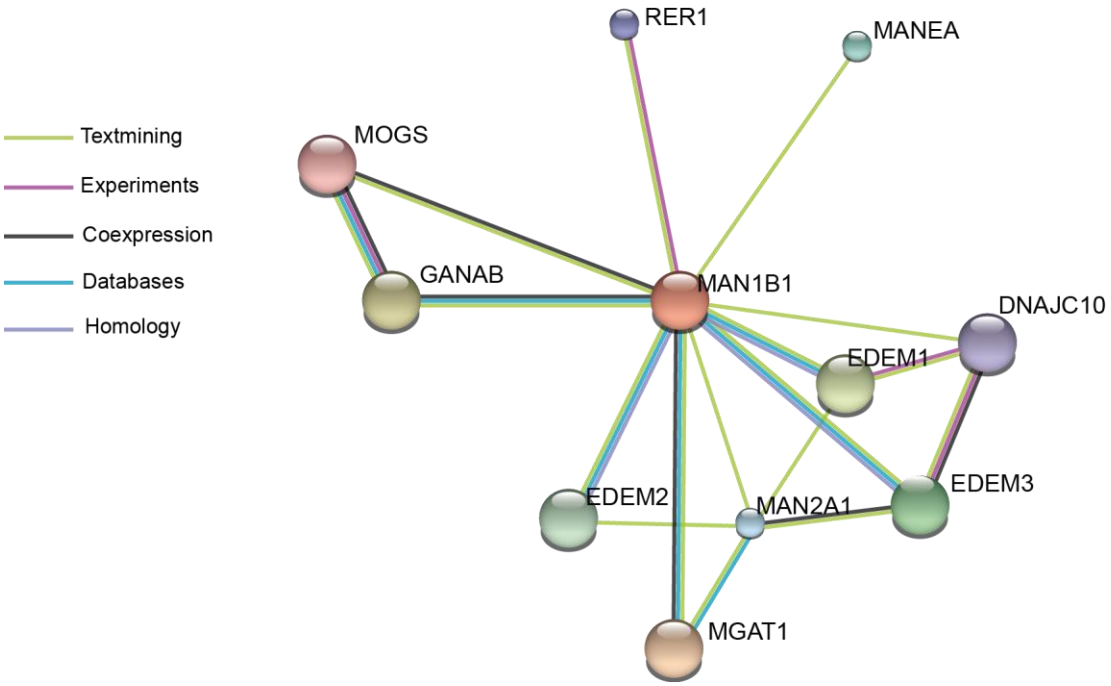

Figure 4.3 Identifying known or predicted protein-protein interactions networks by the use of multiple information sources
Example of network diagram produced when using the STRING database (string-db.org) to identify protein-protein interactions. The database highlights known and predicted interactions with the primary candidate (in this case, MAN1B1), based on known experimental interactions, existing databases, text mining of published literature, interactions predicted *de novo* and interactions observed in one organism (Szklarczyk et al., 2014).

4.3.2 Positive and negative controls

As described in the previous chapter, a small number of siRNAs were tested to examine their effect on the cell surface expression of WT and S100M RET in DLD-1 cells prior to screen development. Chapter 3 presented the effect of siRNA

against RET, V-ATPase, ERp44, the PDI subunit of P4H and Rab7 in WT RET DLD-1 cells. RET and ERp44 knockdown resulted in the reduction of cell surface WT RET levels, while V-ATPase (via the silencing of ATP6V0C) and Rab7 knockdown resulted in increased cell surface levels. It was also identified that the chemical chaperone 4-PBA could restore S100M RET cell surface expression. As such, the positive controls used in the siRNA screen were 4-PBA and siRNA against ATP6V0C and Rab7; the negative controls used were siRNAs against RET and ERp44.

4.4 siRNA screen execution and statistical analysis

The expectation from the siRNA screen was that hits influencing cell surface levels of RET would be those involved in glycoprotein export, glycoprotein maturation by oligosaccharide-processing or ER-associated degradation (ERAD). I anticipated that all of the discrete processes within ERAD could potentially be involved. For example, components involved in the recognition of misfolded proteins; retrotranslocation of unfolded glycoproteins from the ER to the cytosol; or degradation in the cytosol via ubiquitin-proteasome system. The screen was carried out across 12 96-well plates (four plates required for one screen, in triplicate). After the screen was carried out with DLD-1 cells expressing WT or S100M RET, the mean channel-2 ring fluorescence intensity values were used for initial analysis (example immunofluorescence images are shown in Figure 4.5a).

This value takes into account all channel-2 fluorescence of the cell excluding the nucleus, so to remove crossover from channel-1 DAPI staining. A reasonable level of reliability across and within the three replicates was observed and so the values were taken forward for statistical analysis (Figure 4.4). This mean fluorescence intensity value was determined for each well from several field views before processing.

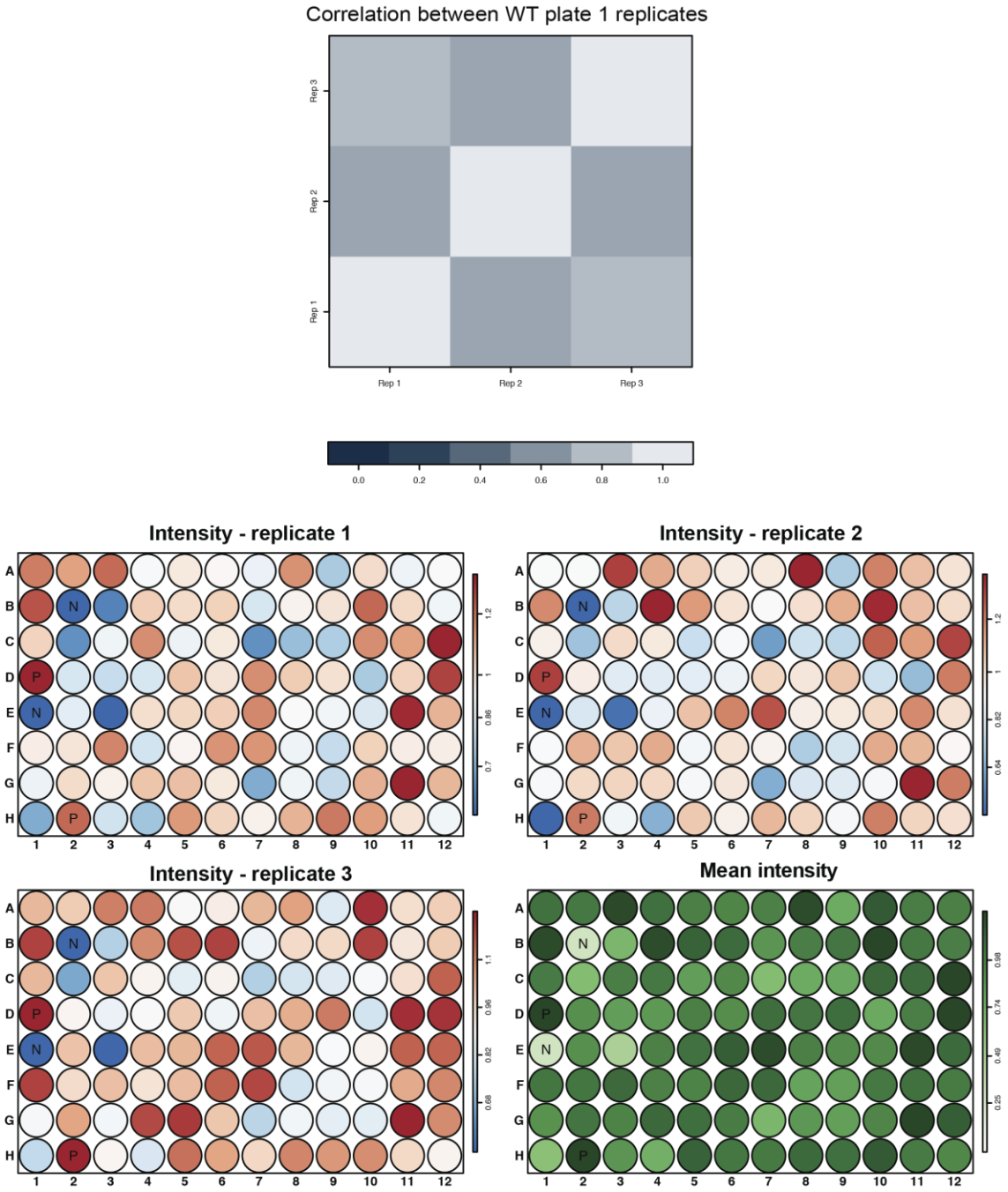

Figure 4.4 Correlation between WT RET plate 1 replicates

The correlation of RET expression levels between replicates was examined using the correlation coefficient, with the example of WT RET plate 1 shown here. At the top, the correlation between WT RET replicates 1-3 is shown (grey), with correlation coefficient values between 0.6 and 0.8. On the bottom, the raw fluorescence intensity measurements for each plate (replicates 1, 2 and 3) are displayed; low fluorescence intensity is depicted as blue and high fluorescence intensity is depicted as red. The mean fluorescence intensity values for WT RET plate 1, calculated using all three replicates, is displayed on the green plate; low fluorescence intensity is depicted as pale green and high fluorescence intensity is depicted as dark green. N - the position of the negative control siRNA within the plate; P - the position of the positive control siRNA within the plate.

High throughput screen data can be pre-processed using three methods. The 'percentage of control' (POC) method corrects for plate variability and normalises each measurement relative to the control; raw measurement values are normalised against the average control value. The 'normalised percentage inhibition' method instead uses the difference between individual measurements and the mean of the positive controls, dividing this value by the difference between the means of the positive and negative controls. The 'Z score' method rescales the plate values by subtracting the average of the entire plate from each measurement and dividing this by the standard deviation estimate of the plate (Malo et al., 2006).

The Z score is commonly used when processing large data sets and the method does not normalise against specific controls, instead assuming that the majority of the siRNAs/compounds will have had no effect and that the whole plate can therefore be used as a control. This method could not be used for this particular screen, as the candidates were pre-selected, therefore introducing bias into the analysis. Instead, the POC scores were calculated by dividing the fluorescence intensity of each well by the mean control intensity (in our case, the ON-TARGETplus non-targeting control pool (OTP) siRNA). Mean values are easily skewed by the presence of outliers, leading to the inclusion of putative hits. To prevent this, the median POC score from the three replicates was chosen to represent each candidate.

Hits were defined as those siRNAs that induced a 25% increase or decrease in fluorescence intensity, as this particular threshold lead to the sectioning of 10% of the candidate targets (Figure 4.5). 300 candidate genes were tested with two species of the RET receptor (600 final measurements), resulting in the identification of 30 'hits': 5% of the overall number of measurements. In Figure 4.6, those candidates above or below this 25% threshold have been annotated. The positive control knockdowns – ATP6V0C (V-ATPase) and RAB7A – were both above of this threshold, suggesting that the screen had been successful. The negative control knockdowns – Erp44 and RET – could also be observed below the 0.75 threshold for WT RET, with only the RET knockdown visible for S100M RET due to the much lower cell surface expression levels. The fact these controls behaved as expected from preliminary tests also suggested that the screen had been successful.

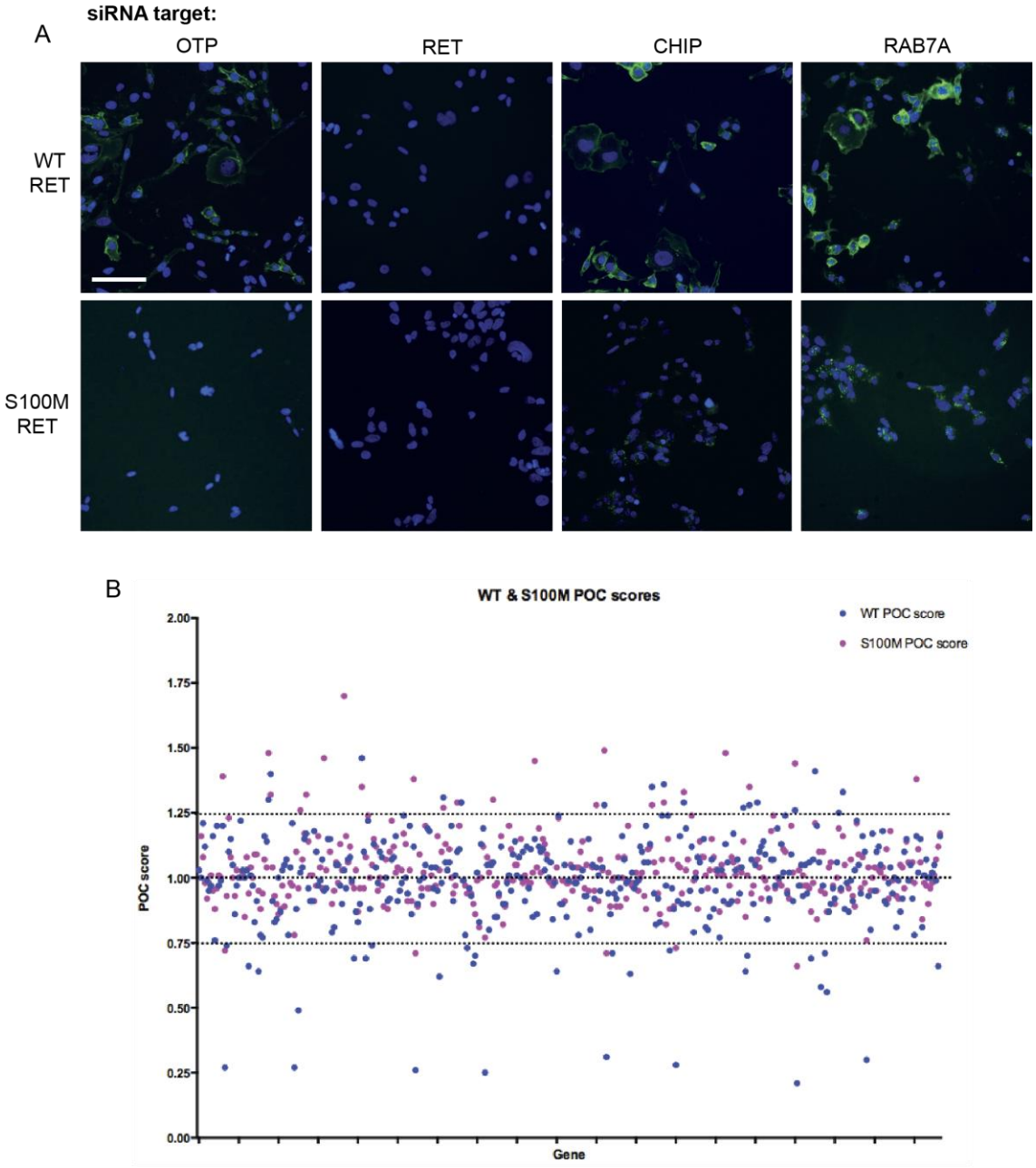

Figure 4.5 POC scores for all candidate genes in DLD-1 WT and S100M cells

(A) Example immunofluorescence images of WT and S100M RET cell surface staining in DLD-1 cells subject to siRNA knockdown of select targets: OTP (control), RET, CHIP and RAB7A. Scale bar represents 100 µm. **(B)** POC scores for all candidate genes are plotted for WT (blue) and S100M (pink) RET screens, with the majority lying between 1.25 (+25%) and 0.75 (-25%). Those each side of this threshold were considered hits. Over the screen, as expected, hits that reduced cell surface WT RET were detected (blue) but no targets reduced S100M RET as levels were already very low.

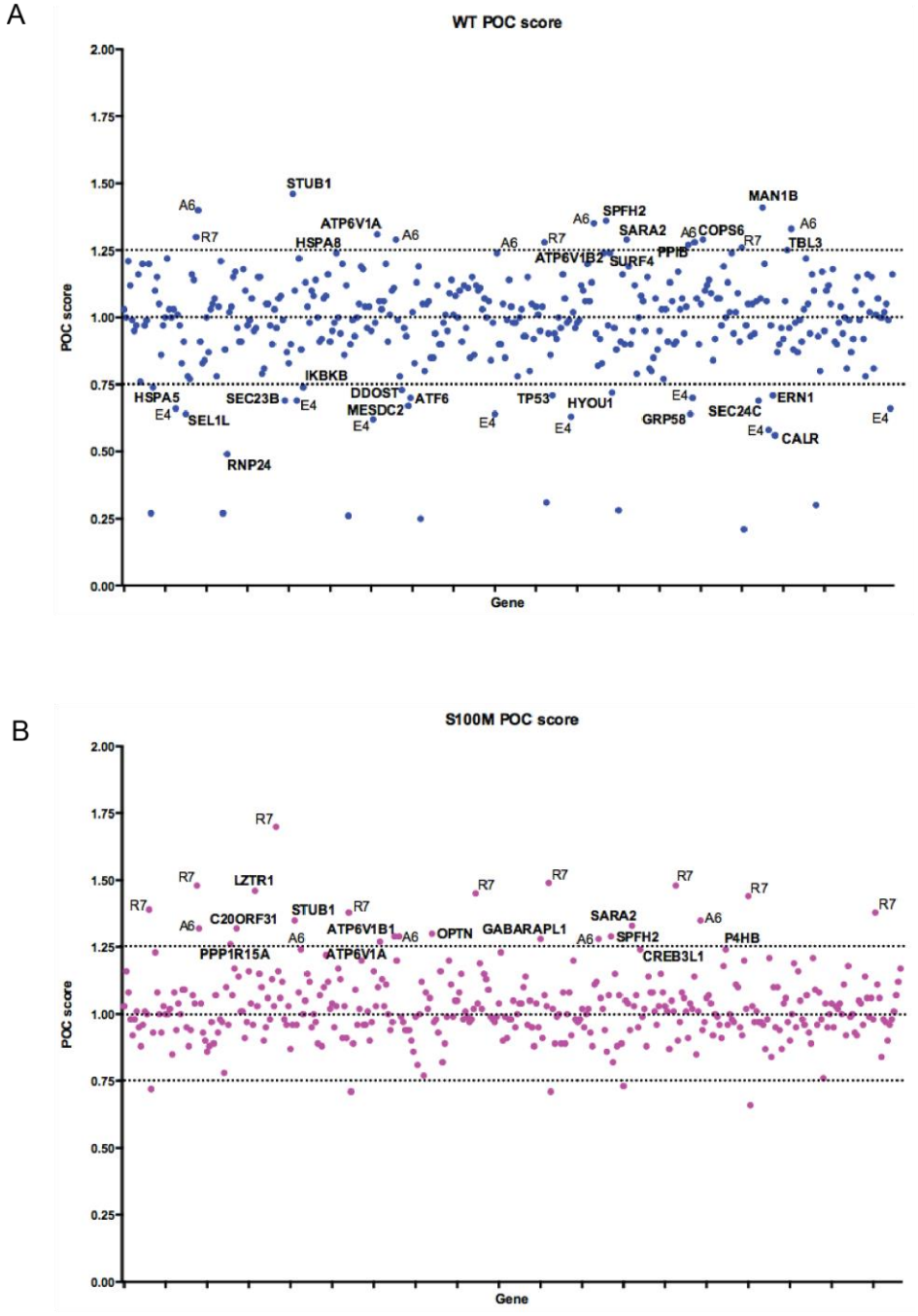

Figure 4.6 POC scores for candidate genes and potential hits for DLD-1 WT or S100M RET expressing cells

POC scores for all candidate genes have been plotted for DLD-1 cells expressing WT (blue) or S100M (pink) RET. Candidates considered hits have been annotated, while control genes have been coded as follows: A6 – ATP6V0C; R7 – RAB7A; E4 – Erp44. RET has not been labelled; it accounts for every non-annotated point below the 0.75 threshold.

The hits identified from the HTS screen can be divided into four groups: those that negatively regulate both WT and S100M RET surface expression (i.e. knockdown boosts cell surface levels), those that negatively regulate either WT or S100M RET surface expression and those that are required for WT RET surface expression (i.e.

knockdown reduces cell surface levels). The significance of the hits in this latter category (required for WT RET surface expression) cannot be determined for S100M RET due to the almost complete lack of the receptor at the cell surface.

4.5 Dissection of factors involved in WT and S100M RET surface expression

The siRNA targets and resulting POC scores for the identified 30 hits have been listed in Table 4.1 (a full list of all siRNA targets and resulting POC scores can be found in the appendix).

Gene silencing increases WT & S100M S.E		
	WT POC	S100M POC
STUB1	1.46	1.35
ATP6V0C	1.4	1.32
RAB7A	1.26	1.44
ATP6V1A	1.31	1.27
SARA2	1.29	1.33
SPFH2	1.36	1.29

Gene silencing increases S100M S.E only		
	WT POC	S100M POC
OPTN	1.06	1.3
GABARAPL1	1.04	1.28
PPP1R15A	1.02	1.26
EDEM2	1.17	1.32
LZTR1	0.95	1.46
ATP6V1B1	1.1	1.29

Gene silencing increases WT S.E only		
	WT POC	S100M POC
PPIB	1.27	1.14
COPS6	1.29	1.07
MAN1B1	1.41	1.21
TBL3	1.25	1.19

Gene silencing reduces WT S.E only		
	WT POC	S100M POC
HSPA5	0.74	0.93
SEL1L	0.64	0.95
RNP24	0.49	0.96
SEC23B	0.69	0.96
IKBKB	0.74	1.05
DDOST	0.73	0.94
MESDC2	0.67	0.9
ATF6	0.7	0.86
P53	0.71	0.99
HYOU1	0.72	0.88
GRP58	0.64	0.85
SEC24C	0.69	0.87
CALR	0.56	0.87
ERN1	0.71	0.94

Table 4.1 Hits from the HTS siRNA screen satisfying significance criteria

A list of genes silenced that gave a POC value higher than 1.25 or lower than 0.75. Targets are divided into those that increase WT and S100M RET surface expression, those that increase either WT or S100M RET surface expression, and those that reduce WT RET surface expression. S.E = surface expression.

To verify hits obtained from an HTS siRNA screen, it is often advised to deconvolute the SMARTpooled siRNAs and silence the selected genes with four individual siRNAs, rather than a pool. Only those genes whose knockdown elicits the same effect with three or more single siRNAs are then taken forward, eliminating those that may have off-target effects. This method is effective when

attempting to reduce the number of hits and only investigate those with a higher level on confidence. However, it may also result in the loss of genuine hits that have a less significant effect, which is especially undesirable when the hit list taken forward for validation is already relatively small or the definition of a hit (+/-25% POC) is not profoundly different from the norm. For these reasons, I have chosen not to deconvolute the siRNAs. Instead, I have pooled the targets into pathways, highlighting cellular mechanisms that appear to influence WT and S100M RET cell surface levels (Table 4.2).

Candidate loss resulting in WT & S100M increase		
ERAD/Proteasomal degradation	Endocytosis/Organelle acidification/Lysosomal degradation	ER-Golgi transport
STUB1/CHIP SPFH2	ATP6V0C ATP6V1A RAB7A	SPFH2

Candidate loss resulting in S100M increase only			
ERAD	Endocytosis/Organelle acidification/Lysosomal degradation	Autophagy	Transcription/Translation
EDEM2	ATP6V1B1	OPTN GABARAPL1	LZTR1 PP1R15A

Candidate loss resulting in WT increase only		
Folding/ER quality control	Proteasomal degradation	Regulatory roles
PPIB MAN1B	COPS6	TBL3

Candidate loss resulting in WT reduction only		
Folding/ERAD/UPR	ER-Golgi transport	Miscellaneous
HSPA5 SEL1L DDOST MESDC2 ATF6 HYOU1 GRP58 CALR ERN1	RNP24 SEC23B SEC24C	IKBKB P53

Table 4.2 Clustering of 30 hits identified from primary siRNA screen into cellular processes
Hits identified as increasing or reducing WT or S100M RET levels (or both) have been divided into broad cellular processes for future validation and investigations.

Preliminary validation would then be carried out with chemical inhibitors that target a particular pathway, or repeated siRNA experiments. Three key components of the eukaryotic degradation system (proteasomal, lysosomal and autophagosomal degradation) all appear to significantly influence both WT and S100M RET cell

surface levels. The control targets (RAB7A, V-ATPase, ERp44 and RET) all influenced WT and S100M RET surface levels as predicted, which allows a higher degree of confidence regarding the hits observed.

4.5.1 siRNA targets negatively influencing both WT and S100M RET cell surface levels

Analysis of hits from the siRNA screen suggested the targeting of two distinct pathways can increase cell surface levels of both WT and S100M RET protein: ER-associated proteasomal degradation (ERAD) (defined by components STUB1 and SPFH2) and receptor internalisation and lysosomal degradation (defined by components RAB7A, ATP6V0C and ATP6V1A). These components are discussed in more detail below.

4.5.1.1 ER-associated proteasomal degradation

The quality control system of the ER targets misfolded proteins for degradation, a process commonly referred to as ERAD. The folding and chaperone systems of the ER will persist in protein folding for a finite time, before subsequent extraction from the pathway and disposal takes over (Hebert et al., 2010). The intrinsically slow folding nature of WT RET and the known misfolding properties of S100M HSCR RET make this pathway a predictable regulator of RET degradation.

The STUB1 gene encodes Carboxyl terminus of Hsc70 Interacting Protein (CHIP), an E3 ligase that regulates protein quality control by targeting misfolded proteins for degradation (Matsumura et al., 2013). The protein contains three tetratricopeptide repeats (TPR), a structural motif that mediates protein-protein interactions, and a catalytic U-box domain required for ubiquitination (Ballinger et al., 1999, Jiang et al., 2001). CHIP binds to the C-terminus of Hsp/c70 (70kDa heat shock protein/70kDa heat shock cognate) and facilitates the polyubiquitination of misfolded client proteins, resulting in their degradation via the proteasome (Jiang et al., 2001, Matsumura et al., 2013).

Heat shock proteins Hsp70 and Hsp90 have been found to regulate protein folding and degradation by binding to proteins – such as folding chaperone HOP and E3

ligase CHIP – that contain TPR motifs (Liu et al., 1999, Russell et al., 1999). Binding occurs via their highly conserved C-terminal EEVD sequence and is regulated by phosphorylation of this region (Muller et al., 2013). Several papers demonstrate that antagonising the client protein-Hsp90 interaction – and thus inhibiting assisted protein folding – results in CHIP-dependent degradation of Hsp90 client proteins (Krishnamoorthy et al., 2013, Connell et al., 2001, Zhou et al., 2003). RET was recently shown to be an Hsp90 client protein, so the involvement of CHIP in receptor degradation is very possible (Alfano et al., 2010). CHIP has also been implicated as a tumour suppressor due to its role in the degradation of several oncogenic proteins, including p53, the Met receptor and SRC-3 (Muller et al., 2008, Jang et al., 2011, Kajiro et al., 2009b). The role of CHIP in RET degradation could be very interesting, as it could regulate the levels of oncogenic RET and target misfolded HSCR RET for degradation.

CHIP knockdown resulted in an increase in both WT and S100M RET cell surface levels, suggesting that both forms of the receptor are targeted for ERAD via CHIP polyubiquitination (Murata et al., 2001). Notably, Hsp70 (HSPA1A) and Hsc70 (HSPA8) were both included in the screen and although they were not identified as hits, their knockdown did result in increased RET levels (HSPA1A: WT +15%, S100M +14%; HSPA8: WT 24%, S100M +17%) of WT and S100M RET surface expression. This further implicates CHIP in RET degradation, as the loss of Hsp/c70 would result in impaired CHIP ubiquitination and a decrease in RET degradation. However, the knockdown of both Hsp90 (HSP90AA1/HSPCA) and Hsp90's ER-localised paralog HSP90B1 had no effect on WT or S100M RET surface levels. Firstly, the efficiency of these particular knockdowns should be checked to confirm the effect of each and check for any disparities between the siRNAs. Also, the genes HSP90AA2 and HSP90AB1, coding for Hsp90-α_2 and Hsp90-β were not included in the screen and should be examined.

SPFH2 (also known as Erlin-2) is an ER-membrane protein residing within the ER lumen that contains the stomatin/prohibitin/flotillin/HflK/C (SPFH) domain. This domain anchors proteins to lipid membranes through associations with N-terminal hydrophobic regions (Matsumura et al., 2013). SPFH2 is a prohibitin family member that defines lipid raft regions within the ER membrane and has been

shown to mediate the ERAD of inositol 1,4,5-triphosphate (IP3) receptors (Xu et al., 2008, Scheffner et al., 1995). Other substrates are likely and if this hit is correct, it would suggests that SPFH2 plays a key role in the ERAD of RET and may act as a degradation target recognition receptor.

4.5.1.2 Endocytosis & lysosomal degradation

Receptor internalisation by endocytosis can engage different intracellular sorting pathways, leading to the cargo being recycled back to the plasma membrane or degraded via the lysosome. A number of protein components operating within the lysosome have been identified. ATP6V0C and ATP6V1A both encode components of the ATP-dependent protein pump vacuolar (H^+)-ATPase (V-ATPase), an enzyme that mediates the organelle acidification required for processes such as receptor-mediated endocytosis and protein sorting (Jiang et al., 2001). ATP6V0C is one of six subunits that make up the membrane bound V_0 domain required for protein translocation, while ATP6V1A is one of the eight subunits that compose the V_1 domain responsible for the ATPase activity. ATP6V1A has been proposed to be responsible for directing assembly of the complex and targeting the enzyme to the correct cellular location (Ballinger et al., 1999). Genes coding for other subunits were included in the screen (ATP6V0A1, ATP6V0B, ATP6V0D1, ATP6V1B1, ATP6V1B2, ATP6V1D, ATP6V1F) but their siRNA knockdowns did not result in a significant increase in WT or S100M RET knockdown. It is worth noting that this could be due to the efficiency of the siRNA.

Due to the role of V-ATPase in Golgi acidification, it was originally hypothesised (as mentioned in chapter 3) that a loss of V-ATPase activity would result in lower surface expression levels of WT RET through the prevention of RET maturation. As the siRNA knockdown resulted in increased levels of both WT and S100M RET, it is thought that this has been caused by one of the other many roles V-ATPase plays within the cell. As well as facilitating endocytosis, V-ATPases are found within the acidified sorting endosomes that are required for receptor recycling; within multivesicular bodies (MVBs) required for endosomal transport; and within the lysosomes to allow degradation to occur (Muller et al., 2013, Liu et al., 1999, Russell et al., 1999). Therefore the observed increase in cell surface levels could

be due to an inhibition of endocytosis or lysosomal degradation. This could be examined in the future using chemical inhibitors against both pathways and preliminary investigations into the inhibition of endocytosis itself are discussed later on.

RAB7A encodes the Rab7 protein: a small GTPase associated with the late endosomes and lysosomes. Several Rab GTPases are involved in this pathway, with Rab5 found on the early endosomes before being replaced by Rab7 on matured late endosomes. This Rab family member plays important roles in both endosomal maturation and transport from the late endosome to the lysosome (Gautreau et al., 2014). Rab7 has been shown to regulate the lysosomal degradation of the EGF:EGFR complex, therefore suggesting a possible role in the regulation of RTK degradation that could encompass RET (Connell et al., 2001).

4.5.2 siRNA targets negatively influencing WT RET cell surface levels only

Components of two main cellular pathways were identified from the siRNA screen as possible negative regulators of WT RET surface expression: protein folding and ER quality control (defined by components MAN1B1, PPIB), and proteasomal degradation (defined by the component COPS6). MAN1B1, also known as ERManI, is a class 1 mannosyl-oligosaccharide α-1,2-mannosidase. Like other class 1 α-mannosidases, MAN1B1 is a member of the glycosyl hydrolase family 47 (GH47) and has an $(\alpha\alpha)_7$ barrel structure. Other members of the GH47 also appear as hits in the screen and are discussed later. MAN1B1 is involved in both the maturation of N-glycans in protein folding and secretion as well as contributing to the disposal of misfolded glycoproteins by ERAD. Specifically, MAN1B1 removes the α-1,2-linked mannose groups from Asp-linked oligosaccharides such as $Man_9GlcNAC_2$ on glycoproteins in the ER. Glycoproteins that fail to fold have an increased amount of α-1,2-linked mannose groups removed, targeting these proteins for ERAD (Avezov et al., 2008). MAN1B1 represents a crucial point in the protein-folding pathway: glycoproteins targeted by MAN1B1 are subsequently targeted for ERAD, while those that are not trimmed can continue within the folding/export process. It has also been identified that MAN1B1 can reside within the Golgi apparatus, facilitating the retrieval of ERAD substrates back to the ER (Pan et al., 2013).

PPIB encodes the protein Cyclophilin B (CypB), a member of the cyclophilin chaperone family that increase the rate at which proteins fold through their peptidyl-prolyl cis-trans isomerase (PPIase) activity. The protein is thought to protect cells from ER stress and has been shown to interact with the ER stress regulator BiP (also known as GRP78) (Kim et al., 2008). As the purpose of this chaperone is to increase the speed at which client proteins fold, it is interesting that it appears to negatively regulate the export of WT RET. It may therefore work indirectly to assist the folding of an intermediary RET component. It has been previously reported that CypB influences the activity of PDI, and it is thought that the two chaperones cooperate with each other to promote protein folding (Horibe et al., 2002). Therefore, the silencing of PPIB may negatively affect PDI activity.

4.5.3 siRNA targets that negatively influence S100M RET cell surface levels only

There are two cellular pathways that appear to selectively impact on the cell surface levels of S100M RET alone: ERAD (defined by the component EDEM2) and aggresome-based autophagy (OPTN, GABARAPL1). ER degradation-enhancing α-mannosidase-like protein (EDEM)2 is one of three (EDEM1-3) lectins involved in the targeting of glycoproteins for ERAD (Mast et al., 2005, Hosokawa et al., 2001, Olivari et al., 2005). The exact role of these ER-localised glycosyl hydrolase 47 (GH47) family proteins is unclear, but their transcription is activated under conditions of ER stress and their overexpression accelerates the targeting of misfolded glycoproteins for ERAD (Hosokawa et al., 2001, Mast et al., 2005). Unlike the related MAN1B1, EDEMs were first believed to have no catalytic activity, but they retained a carbohydrate-recognition function involved in recognition of misfolded glycoproteins (Aebi et al., 2010). However, more recent data show that EDEM overexpression enhances de-mannosylation of misfolded proteins and that EDEMs possess all catalytic residues required for enzymatic activity in 1,2-mannosidases (Hosokawa et al., 2010, Hirao et al., 2006). The activation of EDEM proteins is thought to accelerate N-glycan removal and promote ERAD. They may have distinct functions and specific client proteins, as the knockdown of EDEM1 and EDEM3 had no effect on WT or S100M RET cell surface levels. The finding

that different GH47 family members appear as hits for WT (MAN1B1) and S100M (EDEM2) RET appears to implicate differential glycosylation between the two species, which may be of potential importance for restoring maturation of HSCR RET mutations.

The second pathway implicated in negatively influencing S100M RET levels is the aggresome-autophagy pathway. This recently discovered pathway selectively targets protein aggregates or damaged organelles for clearance in cells (Lamark and Johansen, 2012). Two key components within the pathway are striking hits in the siRNA screen. One is an LC3-like homologue, GABARAPL1 (GABA(A)-receptor associated protein like 1), an autophagy modifier that is located on the autophagosomal membrane. The second is Optineurin (OPTN), an autophagy receptor that binds to both the cargo protein and an autophagy modifier such as GABARAPL1 (Chakrama et al., 2010, Wild et al., 2011). The five GABARAP family members – GABARAP, GABARAPL1, MAP-LC3 (light chain 3 of microtubule associated protein), GATE-16 (golgi-associated ATPase enhancer of 16 kDa or GABARAPL2) and Atg8 – are implicated in protein and vesicle transport, as well as the formation of the autophagosome (Longatti and Tooze, 2009). These Atg8 family proteins are involved in the final step of autophagy: the formation of the autophagosome itself, through lipidation of the cytosolic proteins. OPTN is a ubiquitin-binding autophagy receptor localised in LC3-positive (an Atg 8 family member) vesicles. The receptor is phosphorylated by Tank-binding kinase 1 (TBK1), a modification that is required for OPTN to be able to bind to autophagy modifiers (Wild et al., 2011, Korac et al., 2013). TBK1 is activated by Gram-negative bacteria and OPTN has been shown to target *Salmonella enterica* for degradation via the autophagosome (Wild et al., 2011). Aside from this role in innate immunity, OPTN has been found to bind to aggregated proteins – through its C-terminal coiled-coil domain – and target them to the autophagy-lysosome pathway (Korac et al., 2013). Thus, the siRNA screen has identified a potentially surprising link between S100M RET and an aggresome-autophagy pathway not previously connected.

4.5.4 siRNA targets that positively influence WT RET cell surface levels

Unsurprisingly, the knockdown factors involved in ER to Golgi transport (RNP24, SEC23B, SEC24C) resulted in a reduction in WT RET cell surface levels. Perhaps also unsurprising is the important role a number of folding chaperones and ER quality control factors (HSPA5 (BiP), SEL1L, DDOST, MESDC2, ATF6, HYOU1, GRP58, CALR, ERN1) play in successful WT RET export. These initial findings do however start to build a detailed picture of the specific factors required for RET export. Not only would it be interesting to investigate whether these factors are RET or general RTK specific, but it could also be used in the development of future treatments of cancers caused by RET overexpression.

It is notable that a number of genes included in the screen did not have the expected effect on WT or S100M RET surface expression. For example, ERGIC-53 (Endoplasmic Reticulum-Golgi Intermediate Compartment Protein-53, also known as LMAN1), a mannose-specific lectin responsible for the transport of glycoproteins from the ER to the ERGIC (Hauri et al., 2000). There are other lectins involved in the process, which indicates a level of specificity within the pathway (Aebi et al., 2010). A future experiment examining the effect of each of these lectins on WT RET cell surface levels could give an indication of the particular protein involved. Silencing of the EDEM1-associated disulphide reductase ERdj5 (gene name DNAJC10) also elicited no effect, despite the protein being a member of the ERAD complex that recognises and unfolds ERAD substrates (Ushioda et al., 2008). Again, this gives an indication of substrate specificity within the pathway.

4.6 Preliminary validation of factors identified to be involved in RET surface expression

4.6.1 Validation of hits involved in RET degradation using immunofluorescence

To confirm that hits identified in the immunofluorescence-based assay were true positives, a subset – or pathways containing those chosen – that could be directly targeted by small molecule chemical inhibitors were investigated. These included

chemical inhibition of endocytosis (involving hits such as V-ATPase and Rab7), proteasomal degradation (COPS6, SPFH2, CHIP), and TBK1 activity (OPTN). For TBK1 inhibition, Professor Philip Cohen kindly donated a highly selective TBK1 inhibitor with a control inhibitor known to inhibit the same off-targets (Clark et al., 2011, Clark et al., 2012). Pitstop2 was used to inhibit endocytosis (von Kleist et al., 2011), while epoxomicin was used to inhibit proteasomal degradation (Sin et al., 1999).

To confirm that these chemical inhibitors were restoring S100M RET cell surface expression, cell surface levels were examined using immunofluorescence. The experiment was also carried out in a 96-well plate format and the cells fixed and stained with the 1D9 anti-RET antibody. DLD-1 cell surface levels of WT and S100M RET were stained for immunofluorescence. 4-PBA was used as a control, as it was already known that this chemical chaperone can increase RET cell surface levels. The mean channel 2 intensity values were normalised against the control (i.e. no inhibitor), with each condition tested in triplicate wells, to obtain a POC value (Figure 4.7). Ordinary two-way ANOVA statistical analysis was carried out on the data. This test was chosen because there were two variables: a group of chemical inhibitors and two different forms of RET (WT and S100M). Statistical significance has been displayed on the graphs, between the non-induced (N) and induced (I) samples or the induced and the inhibitor samples. Non-significant results have a P value of >0.05, while significant results are as follows: * P<0.05; ** P<0.01; *** P<0.001; **** P<0.0001.

The results show that the chemical inhibitors chosen all increase S100M RET surface expression (and that of WT RET), excepting the control TBK1 off-target inhibitor. This confirms that the increased surface expression caused by the TBK1 inhibitor is not due to the known off target effects. All inhibitors (excepting the off-target TBK1 control inhibitor) also caused an increase in intracellular (+ Triton-X100) RET levels. This is understandable in the cases of 4-PBA (increased RET folding and export), epoxomicin (reduced proteasomal RET degradation) and the TBK1 inhibitor (reduced autophagosomal RET degradation). Inhibition of endocytosis with Pitstop2 also resulted in increased intracellular levels, which may be due to a reduction in lysosomal degradation of the cell surface receptor.

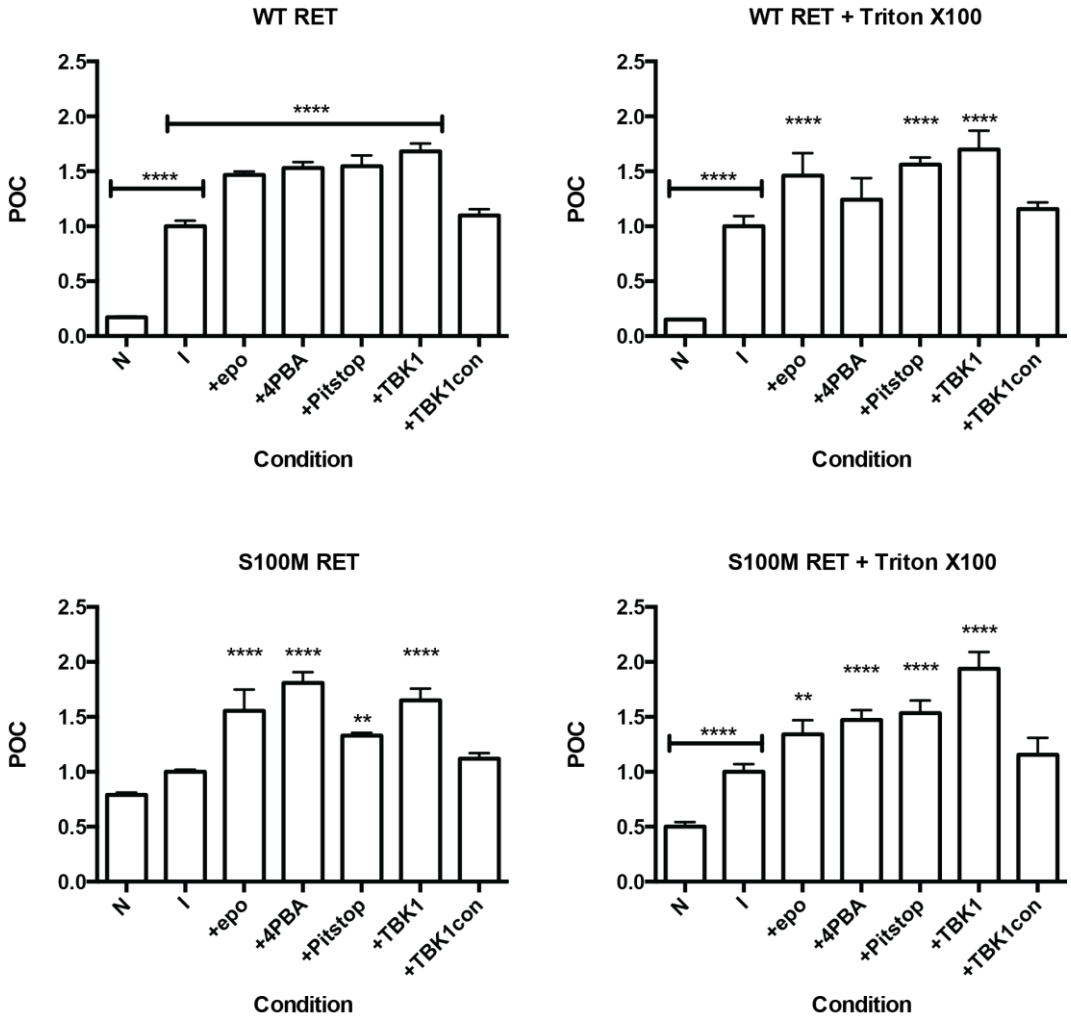

Figure 4.7 POC values for WT and S100M RET surface expression in the presence of selected chemical inhibitors
DLD-1 cells stably expressing WT or S100M RET were incubated with chemical inhibitors for 24 h before fixing and staining. Mean channel 2 fluorescence intensity values were normalised against control (I) to obtain a POC value. Standard deviation error bars are calculated from triplicate values. Two-way ANOVA statistical analysis was carried out, with statistical significance indicated between control (I) and each condition. Key: N – no RET expression; I – no inhibitor control; epo – epoxomicin; 4PBA – 4-phenylbutyrate; Pitstop – Pitstop2; TBK1 – TBK1 inhibitor; TBK1con – TBK1 control inhibitor.

4.6.2 Investigation of hits involved in RET degradation by immuno-blotting

Having confirmed that the chemical inhibitors could increase WT and S100M RET surface levels, it was necessary to determine whether they could restore S100M RET signalling. This was determined by western blot analysis of DLD-1 WT and S100M RET expressing cell lysates for phosphorylated tyrosine (referred to as pTyr-pan) and ERK1/2 (pERK1/2). As discussed in chapter 3, these are known

reliable surrogates for RET activation and signalling. Pilot experiments have investigated the effect of three inhibitors: the TBK1 inhibitor, the TBK1 off-target control inhibitor and 17-AAG. 17-AAG was used as a known potent Hsp90 inhibitor, in order to potentially upregulate CHIP activity. Further work is required to determine the effect of endocytosis or proteasomal inhibition on S100M RET activity.

DLD-1 cells stably expressing WT or S100M RET were incubated with the inhibitors overnight, before lysis and sonication in sample buffer. Activation of TBK1 leads to direct phosphorylation of the autophagy receptor OPTN. This modification leads to enhanced interaction of OPTN with the family of mammalian Atg8 proteins, which are ubiquitin-like and essential for autophagy. Inhibition of TBK1, which has been shown to block OPTN function, resulted in an overall increase in RET levels (Figure 4.8a&b). This increase was more prominent in the case of S100M RET and was not observed when the cells were incubated with the TBK1 off-target control inhibitor. While cell surface levels of S100M RET are seen to increase, there is no general increase in mature RET levels. Overall pTyr-pan and pERK1/2 levels were seen to increase for WT RET in the presence of GDNF and GFRα1. Again, this increase was not visible for S100M RET in the presence the TBK1 inhibitor – while a pTyr-pan band is observed when cells were incubated with TBK1 inhibitor, this background may be due to the much higher RET expression levels.

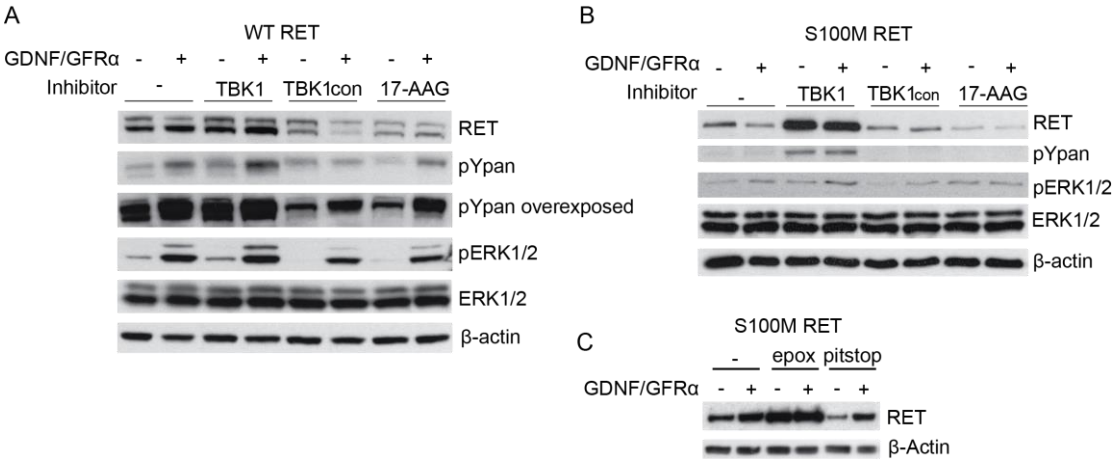

Figure 4.8 WT and S100M RET levels and activation in the presence of chemical inhibitors

(A) Western blot analysis of DLD-1 cells stably expressing WT RET in the presence of the TBK1 inhibitor, TBK1 control inhibitor or 17-AAG for 24 h. Cells are incubated with recombinant

GDNF and GFRα for 30 minutes before lysis. **(B)** Repeated western blot analysis of DLD-1 cells stably expressing S100M RET. **(C)** Western blot analysis of DLD-1 cells stably expressing S100M RET in the presence of epoxomicin or Pitstop2 for 24 h.

Incubation with 17-AAG appears to result in a reduction in overall RET levels for both WT and S100M RET as was hypothesised (Figure 4.8a&b). 17-AAG inhibits Hsp90, thus potentially resulting in an increase in CHIP activity, so a greater amount of RET would be targeted for proteasomal degradation. This result provides preliminary validation of the implication of CHIP in RET degradation. None of the inhibitors (TBK1, TBK1 control, 17-AAG, epoxomicin or Pitstop2) resulted in S100M RET maturation (Figure 4.8), despite restoring surface expression (Figure 4.7).

While there is a degree of separation between the chemical inhibitors used and the hits identified in the screen, this result does further implicate the involvement of both autophagy and ERAD in the degradation of the RET receptor. These data also suggest that some pathways identified by the screen do indeed increase levels of WT and S100M RET at the cell surface but, for S100M RET, this does not result in the restoration of RET signalling. This may be because the increased RET levels are mostly immature forms that are not functional and cannot bind ligand. It points toward the need to implement a secondary screen to test for the restoration of ERK1/2 phosphorylation using hits from the primary immunofluorescence screen.

The inhibition of Hsp90 using 17-AAG has partially validated the role of ERAD in RET degradation, but a more specific experiment is required to look closer at the role of CHIP itself. In order to further examine this, DLD-1 cells were transiently transfected with WT and dominant negative CHIP and Ube2D1 (UbcH5α). A mutation within the U-box of CHIP (P269A) has been reported to result in a dominant negative version of the protein, by eliminating the E3 ligase activity (Matsumura et al., 2013). Ube2D1 is an E2 enzyme that has been shown to specifically interact with CHIP, while the dominant negative mutation (C85A) eliminates the enzyme's ability to form the thioester complex required for protein ubiquitination (Scheffner et al., 1995, Xu et al., 2008).

All constructs appear to express, with an optimal transfection reagent:DNA construct ratio of 2:1 for CHIP WT and P269A (Figure 4.14). The antibody used to detect Ube2D1 also detects Ube2D2 and Ube2D3, which are of almost identical molecular weights (16.6kDa, 16.7kDa and 16.7kDa respectively). As there are two bands present at approximately 17kDa (Figure 4.9), it can only be assumed at this point that the upper band is Ube2D1 as it appears with increasing transfection ratios. This needs to be repeated with a different Ube2D1 antibody, or analysed by mass spectrometry to be sure of the band identity. Future experiments are required to investigate the consequence of this overexpression on both WT and S100M RET maturation and signalling.

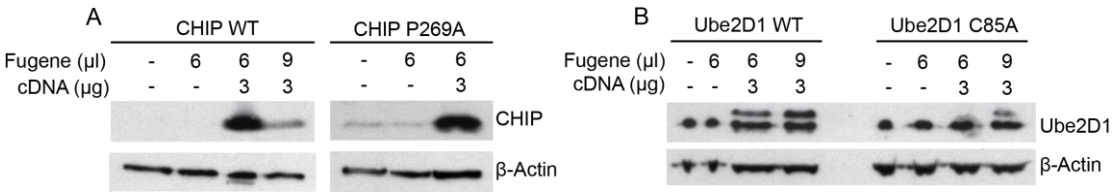

Figure 4.9 Transient overexpression of CHIP and Ube2D1 in DLD-1 cells

(A) DLD-1 cells were transiently transfected with WT or P269A CHIP cDNA using the FuGENE transfection reagent, before lysis and immuno-blotting with anti-CHIP and anti-β-Actin antibodies. **(B)** DLD-1 cells were transiently transfected with WT or C85A Ube2D1 cDNA using the FuGENE transfection reagent, before lysis and immuno-blotting with anti-Ube2D1 and anti-β-Actin antibodies.

In conclusion, inhibition of proteasomal, lysosomal and autophagosomal degradation appears to result in restored S100M RET cell surface expression. Preliminary investigations show that the inhibition of autophagosomal degradation using a TBK1 inhibitor does not restore S100M RET signalling capabilities or maturation. While this needs to be investigated further in the other pathways, it suggests that protein that has already been targeted for degradation is no longer functional.

It has previously been shown that the recombinant S100M RET ectodomain, as a result of the double cysteine mutation facilitating its secretion into the cell medium, can bind to ligand and co-receptor as efficiently as WT RET (Kjaer et al., 2010). However, here we show that immature S100M RET in a full-length context at the cell membrane is not functional at the cell surface. This may be for two reasons. Firstly, protein that has been targeted for degradation may have been modified in

some way that makes it unable to bind to its bipartite ligand or signal. Secondly, the fact that the 'rescued' S100M RET is not fully mature implies that it has not travelled through the Golgi apparatus. This could suggest that the complex N-linked glycosylation received in the Golgi may be necessary for either bipartite ligand recognition or signal transduction. It has been previously shown that inhibition of RET maturation – via inhibition of Golgi acidification – does not prevent surface expression, but it was not examined as to whether that protein could function at the cell surface (Hirata et al., 2010). Work carried out in the laboratory has identified hotspots on the RET ectodomain that potentially implicate glycosylation sites in bipartite ligand binding (Goodman et al., 2014, in press). Therefore, future efforts into the restoration of S100M RET signalling should investigate the requirement for complex N-linked glycosylation in RET signalling and the possibility of 'rescuing' S100M RET before it is targeted for degradation. Alternatively, a greater emphasis should be placed on increasing mature RET levels by investigating components influencing proper glycosylation and disulphide formation of full-length RET.

4.7 Future efforts: monitoring RET activation

It is now clear that restored S100M RET cell surface expression does not correlate with restored signalling. Therefore, a secondary signalling screen is required to analyse the positive hits from the primary immunofluorescence screen. The signalling screen could use the RET activation surrogates such as RET auto-phosphorylation or ERK1/2 phosphorylation, which can be readily monitored by immuno-blotting. However, this method is only suited at present for low to medium-throughput screening.

For this reason, I investigated the possibility of monitoring RET activation via immunofluorescence. DLD-1 cells stably expressing WT or S100M RET were incubated with recombinant GDNF and GFRα1 for 30 minutes before fixing and staining with anti-RET, -phospho-RET (pTyr1062), -pTyr-pan and -pERK1/2. The average channel-2 fluorescence intensity values were normalised against the average fluorescence intensity of the non-induced control; WT and S100M RET values were normalised separately, as were those from separate antibodies. As seen in Figure 4.10, both intracellular and surface WT RET levels increase upon

induction of RET expression as expected, followed by a drop when activated by the recombinant ligand and co-receptor. This drop is most likely a direct consequence of ligand-induced receptor internalisation. To confirm this, repeated experiments in the presence of the endocytosis inhibitor Pitstop2 are needed. The increase in S100M RET surface and intracellular levels was far less prominent, as expected.

A large increase in pTyr1062 intensity was observed when WT RET expression was induced and once again when activated. This increase may be due to background RET staining, as pTyr1062 intensity also increased for S100M RET when incubated with ligand and co-receptor. However, WT RET levels drop following RET activation while pTyr1062 levels rise, suggesting that it is specific to RET activation and could potentially be used as a method for monitoring RET activation.

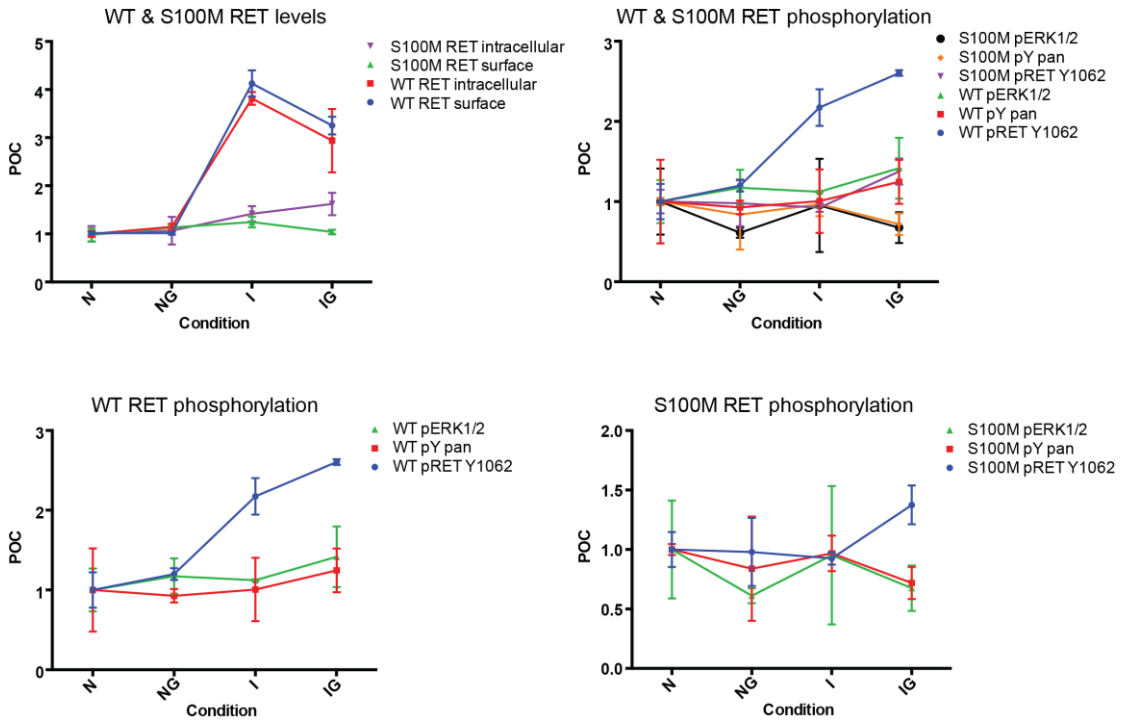

Figure 4.10 Using immunofluorescence to monitor WT and S100M RET levels and activation status
DLD-1 cells stably expressing WT or S100M RET were activated with bipartite ligand for 30 min before fixing (PFA), permeabilisation (Triton-X100) and staining. Average channel 2 fluorescence intensity values were normalised against non-induced controls for separate cell lines and primary antibodies. Key: N – non-induced; NG – non-induced + GDNF/GFRα; I – induced (+doxycycline); IG – induced + GDNF/GFRα.

While the intensity increase for pTyr-pan and pERK1/2 is much less obvious, the rise appears more specific to activated WT RET rather than induced WT RET expression. This rise in pTyr-pan and pERK1/2 intensity is also not observed in DLD-1 S100M RET cells that have been incubated with ligand and co-receptor. With optimisation, it is possible that this method could be used to monitor RET phosphorylation and identify either siRNA knockdowns or compounds that restore S100M RET signalling capabilities.

pERK1/2 levels can increase when the ER is under stress (Arai et al., 2004), which could be the case when S100M RET expression is induced at the same time as other conditions within the DLD-1 cell are altered. It is therefore crucial that the pERK1/2 intensity increase is specific for induced + GDNF/GFRα, rather than the induced expression alone. Using either pTyr-pan or pTyr1062 as an alternative antibody alongside pERK1/2 could control for this. Future optimisation could involve the testing of other phospho-RET antibodies, such as pTyr905.

4.8 Conclusion

The aim of this chapter was to develop an immunofluorescence cell-based assay that could be used to study RET folding, maturation and trafficking to the cell surface. I hoped to identify factors involved in these processes and investigate their contribution towards the development of Hirschsprung's disease or their role as potential tumour suppressors. I successfully set up and carried out a high throughput biased siRNA screen that has identified novel factors and pathways that potentially regulate both WT and S100M RET cell surface expression levels. S100M RET cell surface expression can be restored via the siRNA knockdown of factors involved in folding, export and degradation. Aggrephagy, lysosomal degradation and ERAD all appear to play a role in RET degradation, but preliminary validation of a small number of positive hits from the primary screen suggest that protein rescued from degradation is no longer functional, underlining the need for a secondary screen on all positive primary screen hits to identify those that restore a GDNF-GFRα1 mediated RET signalling response.

4.8.1 Optineurin & macroautophagy

Optineurin and GABARAPL1 were both identified as negative regulators of S100M RET surface expression. The observation that both knockdowns were specific to S100M RET suggests that the mutated receptors are misfolded or improperly glycosylated and targeted to the autophagosome. It is important to note that the autophagy pathway assembles within the cytosol (Wong and Cuervo, 2010), arguing that misfolded S100M must be translocated from the ER back into the cytosol in order to engage the aggresome-autophagy pathway. This process may occur in a similar sequence to E3 ligase ubiquitination and subsequent proteasomal degradation. The inhibition of TBK1 results in both increased cell surface expression and increased overall protein levels, but does not restore S100M RET maturation or downstream signalling (measured by pTyr-pan and pERK1/2 levels). This needs to be repeated with OPTN siRNA to be sure of the effect, but suggests that the inhibition of OPTN-related autophagy will not restore S100M RET signalling.

While the inhibition of aggrephagy may not be sufficient in rescuing S100M RET function, the identification of OPTN as a hit suggests a novel role for this pathway. Future investigations are required to elucidate whether this degradative mechanism is specific to RET – due to the misfolding nature of the protein – or to RTKs in general. So far, optineurin has been implicated in the autophagy of *Salmonella* and aggregated proteins (Wild et al., 2011, Korac et al., 2013). It would therefore be interesting to see whether all HSCR mutant forms of RET are targeted, or even a portion of the WT protein (as TBK1 inhibition did increase cell surface levels of WT RET when tested via immunofluorescence). It would be interesting to examine the difference between the targeting of kinetically compromised HSCR mutants (represented by S100M RET) and the more severe thermodynamically compromised HSCR mutants (such as G93S RET). To test this, a DLD-1 cell line stably expressing G93S RET would need to be created, with total cell levels of S100M or G93S measured via immuno-blotting before and after OPTN siRNA knockdown.

4.8.2 Possible ER exit routes for misfolded RET

While the possible role of aggrephagy in RET degradation has been discussed, one potential obstacle is the subcellular location of RET when it is targeted for degradation. Aggrephagy operates within the cytosol, whereas ERAD pathways – whose inhibition leads to increased cell surface export of WT and S100M RET – function within the ER, using retrotranslocation to membrane-bound or cytosolic ubiquitin ligases (Olzmann et al., 2013). Retrotranslocation of RET for proteasomal degradation could potentially expose its transmembrane (TM) domain. Little is known about how such membrane proteins are exported out of the ER for degradation. Considering that cell surface RET will require an intact TM region, there are currently two models by which this could occur: ER associated autophagy (ERAA) and autophagy-independent EDEMosomes (Bernales et al., 2007, Zuber et al., 2007).

Several misfolded proteins are known to be degraded by macroautophagy, such as the androgen receptor and α–synuclein (Webb et al., Pandey et al.). ERAA has been shown to involve the engulfment of the ER (as ERAA autophagosomes are derived in part from the ER membrane), which could in turn result in the degradation of damaged proteins within that portion of the ER (Bernales et al., 2007). ERAA can be activated by the UPR, with specific emphasis on the Ire1 branch (Ogata et al., 2006). Interestingly, the knockdown of Ire1 (a.k.a ERN1) in the siRNA screen resulted in reduced cell surface levels of WT RET. This suggests that Ire1 may have an alternative role in the case of RET.

Separate to ERAA, ERAD regulators – such as the EDEM proteins – are cleared from the ER to prevent excessive protein degradation and allow protein folding to occur. They are released via COPII-independent vesicles that travel to the lysosome to target the chaperones for degradation (Zuber et al., 2007). These vesicles – termed EDEMosomes – are distinct from the autophagosome: ERAD-associated vesicle membranes contain the noncovalently bound LC3-I (Cali et al., 2008), while autophagosome membranes contain covalently bound (lipidated) LC3-II (Kabeya et al., 2000). The transmembrane protein SEL1L (involved in the dislocation of misfolded proteins) has been implicated as the ERAD tuning receptor,

interacting with both cytosolic LC3-I and ER-localised EDEM1 and OS-9 (Bernasconi et al., 2012). These interactions ensure that the GH47 family members are sequestered into EDEMosomes and transported for degradation. The identification of this process brings about the possibility that misfolded EDEM substrates could also be carried within the EDEMosomes and targeted for degradation. While EDEM1 and OS-9 were two GH47 family members that were not identified as hits within the siRNA screen, MAN1B1 has also been implicated in the process (Bernasconi et al., 2012). MAN1B1 appears to negatively regulate cell surface levels of WT RET, and this possible mechanism behind that regulation should be investigated in future experiments. EDEM2 (identified in this thesis as a negative regulator of S100M RET export) has not yet been found to localise to the EDEMosome, and this could also be examined in future studies.

4.8.3 CHIP & ER-associated degradation

Data presented in this chapter suggests both WT and S100M RET are targeted for ERAD via the E3 ligase CHIP. Overexpression of CHIP, Ube2D1 and dominant negative versions of both in DLD-1 cells stably expressing WT or S100M RET will help to confirm this. At that point, S100M RET maturation and signalling capabilities can also be tested, although it appears unlikely that CHIP inhibition will be sufficient to restore function. At the point of CHIP recognition, the protein has already been extradited from the ER and may have been unfolded in the process. CHIP has been implicated as a regulator of oncogenic pathways and has been found to target several kinases – including Akt, ErbB2 and EGFR – for degradation (Zhou et al., 2003, Kajiro et al., 2009a, Su et al., 2011). Therefore, RET may be targeted for degradation by CHIP due to the intrinsically slow folding trajectory of WT RET activating ERAD. This point comes back to the question of RET evolution raised in chapter 3: have unpaired cysteine residues been introduced into the receptor to slow down folding and prevent oncogenic levels at the cell surface? Once CHIP's involvement in RET degradation has been confirmed using the overexpression constructs, it would be interesting to examine the effect of CHIP knockdown on the growth of RET-dependent cancer cells – such as luminal breast cancer cells.

4.8.4 Future efforts: validation of hits involved in RET folding & glycosylation

MAN1B1 and EDEM2 were identified as factors that negatively regulate cell surface expression levels of WT and S100M RET, respectively (Table 4.3). Firstly, validation of these hits via siRNA knockdown and chemical inhibition (using Kifunensine (Weng and Spiro, 1996)) is required to confirm their involvement in RET quality control. It is interesting that WT and S100M RET appear to be selectively targeted for ERAD by different ER-mannosidases. EDEM1/2/3 gene transcription is upregulated during ER stress (Olivari et al., 2005, Molinari et al., 2003), which could explain why EDEM2 is only associated with S100M RET: EDEM2 levels are not high during WT RET expression and so the knockdown does not elicit a noticeable effect.

It appears that S100M RET protein that has already been targeted for degradation cannot signal, even if it is directed to the cell surface. This observation is coupled with the fact that the 'rescued' protein is also not fully mature. Therefore, the receptor is reaching the cell surface without travelling through the Golgi to become fully glycosylated. Analysis of the human RET amino acid sequence using ExPASY's NetNGlyc prediction server results in the high-confidence prediction of nine N-linked glycosylation sites (Gupta et al., 2004). While N-glycans are first added to the glycoprotein in the ER, processing often occurs in the Golgi (Stanley, 2011). It may be that the complex N-linked glycosylation received in the Golgi is required for ligand and co-receptor binding. The NetOGlyc prediction server also finds four possible O-linked glycosylation sites within the sequence (although information on O-linked glycosylation consensus sequences is far less established). O-linked carbohydrates are attached to the amino acids serine or threonine. O-linked glycosylation is carried out by the enzyme N-acetylgalactosamine (GalNAc) transferase, while N-linked glycosylation requires a host of enzymes that are localised to different portions of the Golgi. Mannosidases found within the *cis* cisterna first remove mannose residues; GlcNAc (N-acetylglucosamine) transferase I and Mannosidase II are found in the medial cisterna, mediating the process of complex N-glycan synthesis; Gal (galactose) transferase is found in the *trans* Golgi network and add galactose to the carbohydrate complexes (Stanley, 2011).

Future studies involving the knockdown of enzymes mentioned above could build a more elaborate picture of the glycosylation process the RET receptor goes through when in the Golgi. The existence of WT RET as two species detectable via western blot analysis allows us to identify those involved in the creation of the mature form. Once the enzymes involved have been established, investigations into WT RET cell surface expression and signalling capabilities should give an indications of whether the Golgi-localised complex glycosylation is necessary for ligand and co-receptor binding or signal transduction. While previous studies have suggested that glycosylation is not necessary (Kjær and Ibanez, 2003a), recent work has identified several glycosylation sites within the RET ECD as 'hot-spots' for ligand and co-receptor binding (Goodman et al., 2014, In press).

Inhibition of ERAD could help to determine how much of both WT and S100M RET are targeted by members of the GH74 family within the quality control pathway. Kifunensine, an alkaloid compound, is used to suppress ERAD by inhibiting ER-associated mannosidase activity (Tokunaga et al., 2000). This experiment would also assist in the validation of the EDEM2 and MAN1B1 members of GH74 family.

4.8.5 WT RET folding

Several chaperones have been identified as being required for optimal WT RET export, with crucial players such as calreticulin and BiP in the list adding confidence to others identified. As the screen was comprised of a large number of chaperones, some of which do not appear to be involved in RET folding, a more specific picture of RET export can be created through validation of these hits. Following on from repeated siRNA experiments, it would then be interesting to investigate whether the chaperones identified are also involved in the folding of another RTK, such as EGFR. It would also be possible to overexpress the chaperones in a RET-dependent cancer cell line and investigate their effect on cell growth and differentiation. Identifying ways to control oncogenic RET cell surface expression could have implications in future cancer treatments.

4.8.6 Hypothetical model for future validation

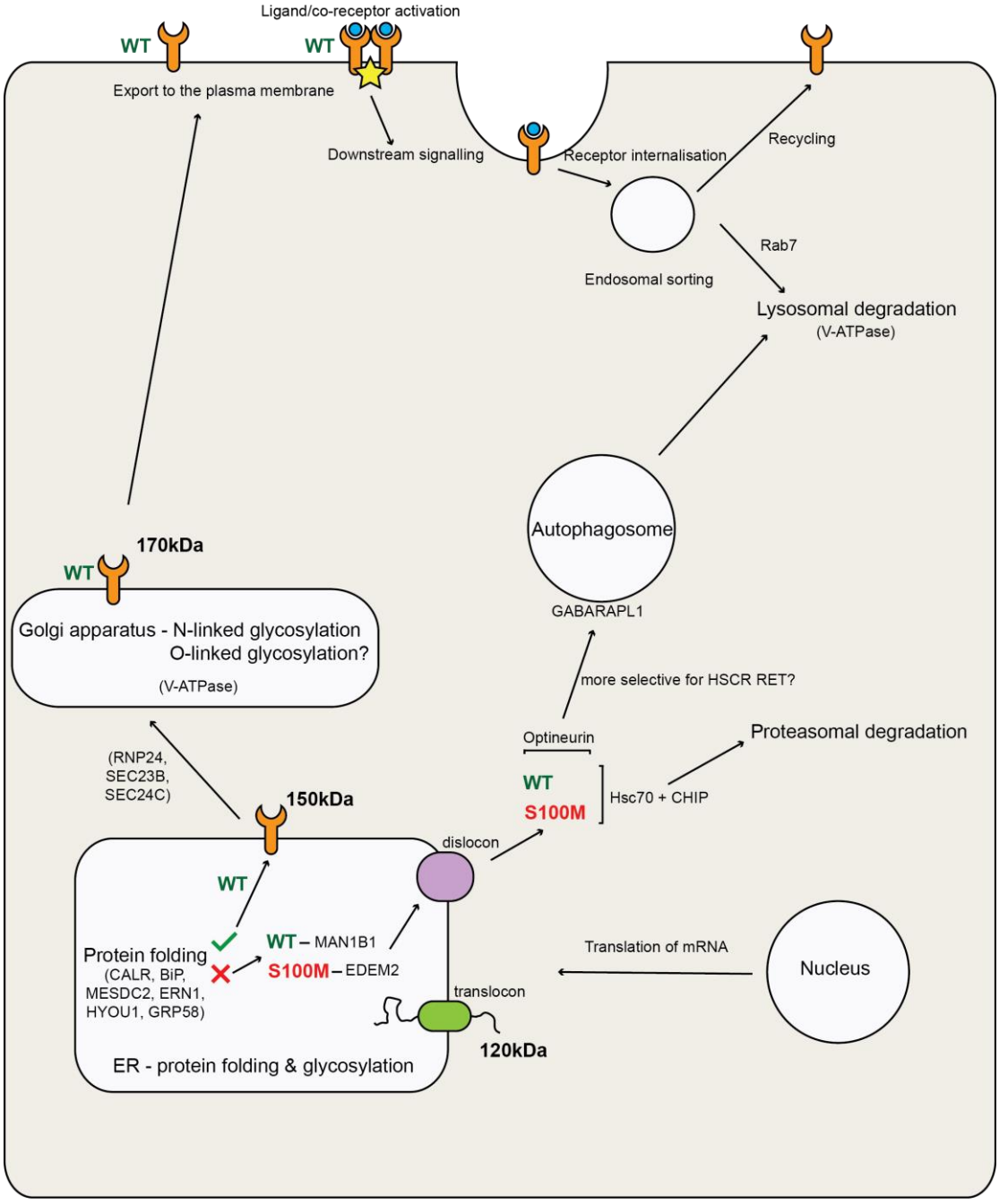

Figure 4.11 Model of RET trafficking for future validation and investigations

Schematic model of WT and S100M trafficking through the cell, with implicated pathways and factors highlighted.

Chapter 5. Structural analysis of distinct ATP-competitive chemical inhibitor scaffolds bound to the RET tyrosine kinase

5.1 Introduction

This chapter describes the preparation, crystallisation and structure determination of nine distinct chemical inhibitors bound to the RET tyrosine kinase domain (RET KD). All compounds are ATP-competitive and bind within the RET nucleotide-binding pocket. Also presented is the structure of ADP bound to RET KD. Several related crystal forms were identified during this study. Solution IC_{50} data from collaborators is presented for the chemical inhibitors together with thermodynamic analysis using differential scanning fluorimetry. Comparisons between the solution and crystal data suggest ways to improve the inhibitors and rationalise their potencies leading to an improved 3D pharmacophore for the RET tyrosine kinase ATP-binding cleft. Key components of the kinase nucleotide-binding pocket are highlighted in Figure 5.1.

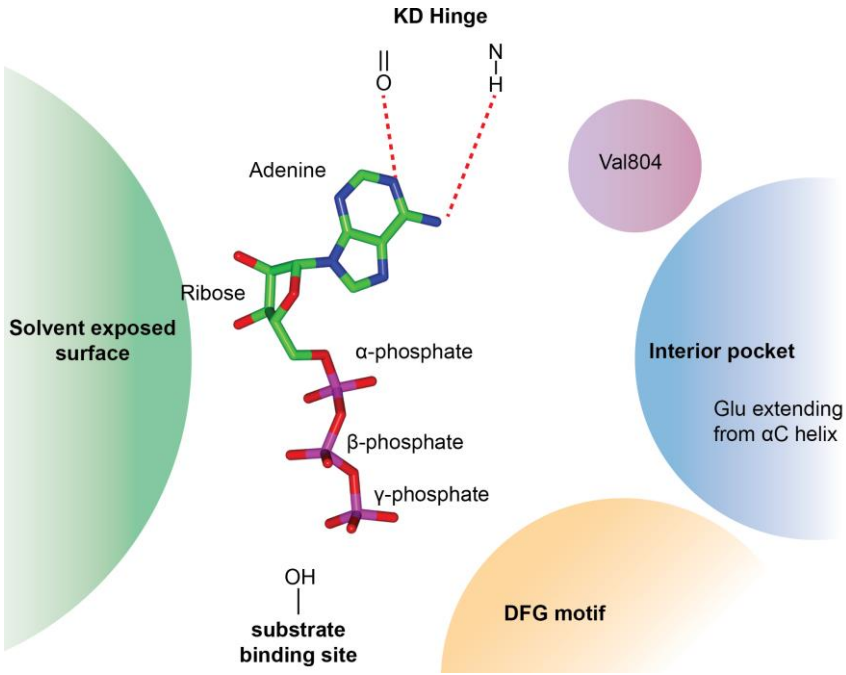

Figure 5.1 Schematic of ATP within the kinase nucleotide-binding pocket

The structure of ATP (N – blue, C – green, O – red, P – magenta) annotated, with key areas within the pocket annotated.

Published data from laboratory has presented the structures of the RET KD bound to AMP and AMPPNP (with only the adenosine visible). In the AMP structure, the gly-rich loop (GRL) is in a ‘closed’ conformation, and this was thought to preclude ATP binding. The AMPPNP structure contains the GRL in two alternative conformations, with an ‘open’ as well as closed arrangement. I present the structure of the RET KD bound to ADP. The predicted position of the gamma phosphate differs from that seen in related RTKs, such as the FGFR or Src.

Current FDA-approved drugs, for RET-dependent metastatic thyroid cancer, suffer from off-target dose-dependent toxicity and a lack of specificity. I therefore hoped that the characterisation of the binding modes of several different scaffolds would provide further insight into their molecular interactions and contribute to the design of a second generation of more RET-specific chemical inhibitors. The structures solved identify five binding modes that have similarities and differences that are defined by specific interactions between the inhibitor and residues within the nucleotide-binding pocket (annotated in Figure 5.2). These observations have been combined with biochemical data investigating the binding and thermal stabilising properties of each inhibitor towards the RET KD, in order to design an improved RET pharmacophore.

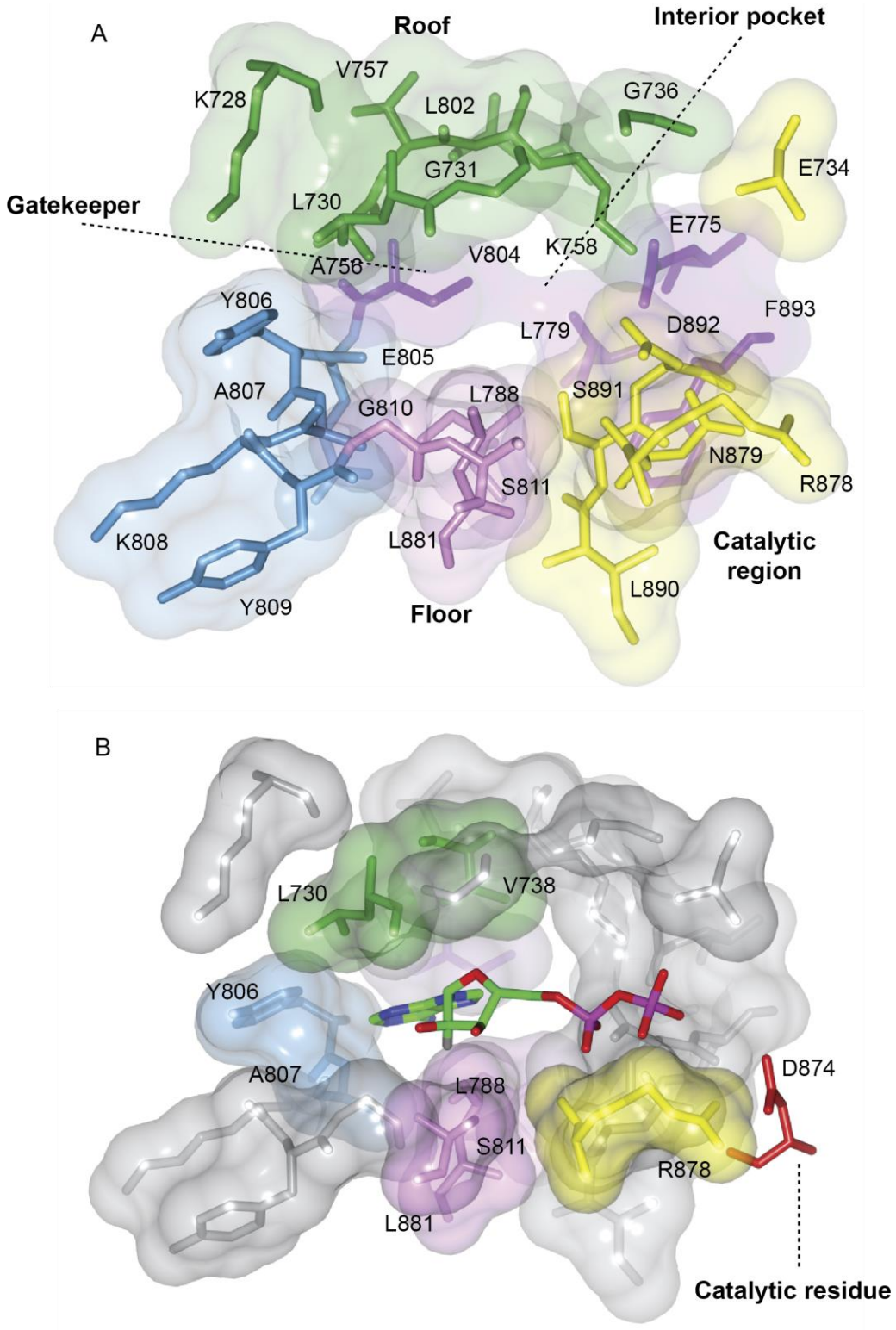

Figure 5.2 The RET nucleotide-binding pocket

(A) View of the RET nucleotide-binding pocket with the side chains of residues with the pocket shown (Hinge – light blue, interior pocket - purple, catalytic region - yellow, roof - green, floor - pink.) **(B)** ADP bound within the pocket, with residues within 4 Å of the ligand highlighted. Among those annotated are the catalytic residue D874 and gatekeeper residue V804.

The McDonald laboratory has previously determined structures for the RET tyrosine kinase domain bound to a variety of chemical inhibitors including Vandetanib, as well as adenosine (Knowles et al., 2006, Mologni et al., 2010, Plaza-Menacho et al., 2014). A structure of the M918T oncogenic RET mutant has also recently been determined. The crystal form used in these studies is amenable to co-crystallisation or soaking of a variety of ATP-competitive inhibitors. Academic collaborations with several different medicinal chemistry groups at the Paterson Institute (UK), Arizona (USA), Uppsala (Sweden) and Harvard (USA) have provided us with various different compound scaffolds that all potently inhibit RET kinase activity. These compounds can be broadly classified into type I inhibitors (*DFG-in*) and type II (*DFG-out*). I therefore initiated experiments to structurally characterise several different scaffolds to define their contacts with RET, their mode of action, potency and structure-activity relationships (SAR). Our goal was to understand the available inhibitor SAR, provide ideas for new improved inhibitors, define a better pharmacophore for RET inhibition and link this to solution-based kinase stability and cellular data on RET inhibition. Previous structural studies on other enzyme-inhibitor targets have found novel inhibitor binding modes that were subsequently exploited chemically (Walker et al., 2000, Hutton et al., 2014). Also, the crystal structure of the heterocyclic scaffolds within the kinase nucleotide cleft is still required to define the inhibitor orientation.

5.2 RET chemical inhibitors: identifying distinct scaffolds

The inhibitors used in this chapter were provided by several groups, with details of each inhibitor and its origin in Table 5.1. Prior to this thesis, the RET KD had been crystallised with the inhibitors Sunitinib (Sutent®), PP1, Vandetanib and three indolin-2-one compounds (referred to as X2K, X2L and X2M). This chapter presents the structure of the RET KD bound to a further nine. Within this set of inhibitors, there are five distinct chemical scaffolds that have been detailed below.

Scaffold	Chemical name	Inhibitor	Collaborator	Reference
1	Pyrimido [4,5-b][1,4]-benzodiazepine	I-1	Dr. Nathanael Gray, Harvard Medical School	Miduturu et al., 2011
		I-5	Dr. Nathanael Gray, Harvard Medical School	
		I-6	Dr. Nathanael Gray, Harvard Medical School	
		I-7	Dr. Nathanael Gray, Harvard Medical School	
		I-8	Dr. Nathanael Gray, Harvard Medical School	
		I-9	Dr. Nathanael Gray, Harvard Medical School	
		I-10	Dr. Nathanael Gray, Harvard Medical School	
2	Pyrazolopyrimidine	I-4	Professor Morten Grötli, University of Gothenberg	Diner et al., 2012
		PP242	Commercially available - Selleck	Feldman et al., 2009
4	4-anilinoquinazoline	I-3	Dr. Allan Jordan, Patterson Institute for Cancer Research	
5	Phenyl-benzimidazole	BMS-536924	Commercially available - Selleck	Wittman et al., 2005
		Pz-1	Dr. Hong-Yu Li, University of Arizona	

Table 5.1 Inhibitors and collaborators

The nine RET KD-inhibitor structures described in this chapter cluster into five distinct chemical scaffolds. I-1, I-7, I-8, I-9 and I-10 contain the pyrimido [4,5-b][1,4]-benzodiazepine scaffold, referred to as scaffold 1 (S1) (Figure 5.3), were received from Professor Gray's laboratory at Harvard (Miduturu et al., 2011). The scaffold was identified as an inhibitor of several kinases during the high-throughput kinase profiling of 353 kinases. The core benzodiazepine heterocycle (a benzene ring fused to a diazepine ring) has been used to target the central nervous system, producing an array of anti-anxiety drugs (Olkkola and Ahonen, 2008). The benzodiazepine scaffold has also been used in the inhibition of p38 MAPK and the Parkinson's disease kinase LRRK2 (Ghori et al., 2010, Deng et al., 2011).

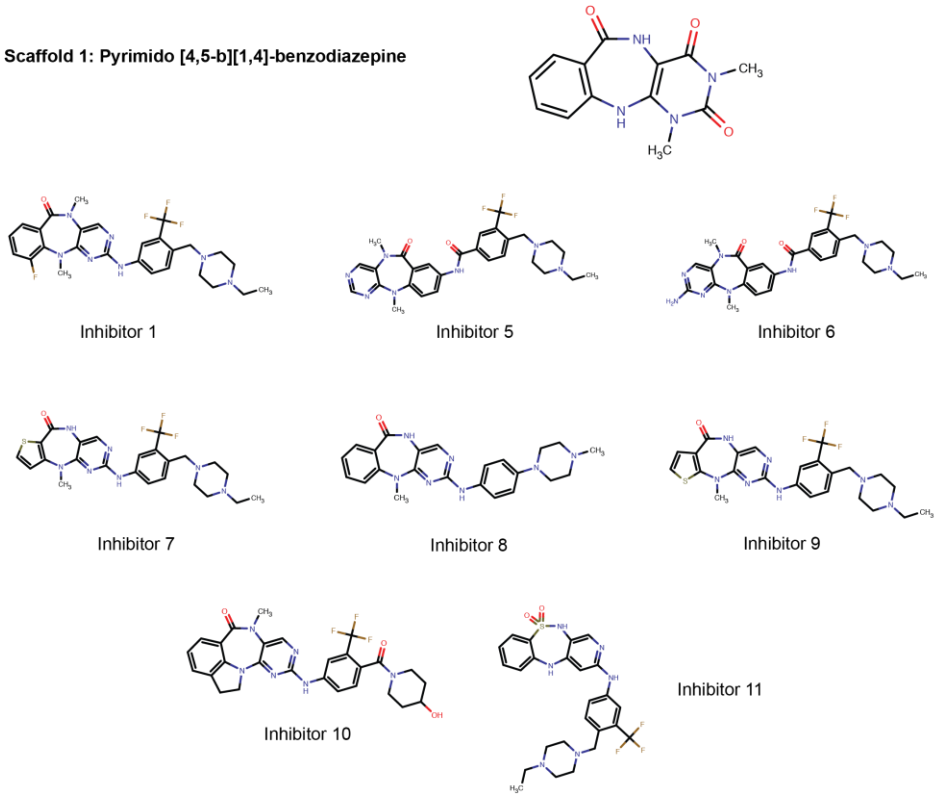

Figure 5.3 S1 inhibitors based on pyrimido [4,5-b][1,4]-benzodiazepine

The chemical structure of S1 is shown, along with each of the inhibitors in this thesis (I-1,I- 7,I-8,I- 9 and I-10) that are based on this scaffold.

As seen in Figure 5.3, these related inhibitors differ, with all of them containing the core heterocyclic ring structure – that is reportedly 'boat' conformer – followed by an additional benzene ring. IC_{50} data from our collaborators defines the main off-targets of these particular inhibitors as ERK5, AURKA and AURKB, LRRK2 and NUAK1. As AURKA (Aurora kinase A) inhibition leads to mitotic arrest in a large number of cases (Gorgun et al., 2010, Zhou et al., 2013), it would be important to attempt to "dial out" this effect if possible using the structural data to steer a further round of scaffold modification. Our main focus was therefore to compare the S1 type inhibitors bound to RET KD with IC_{50} data from our collaborators and thermal shift assay data detailed below, to identify key substituents required for RET specificity.

PP1, I-4 and PP242 were based on scaffold 2 (S2): pyrazolopyrimidine, a heterocyclic compound with a molecular formula of $C_6H_5N_3$ (Figure 5.4). Pyrazolopyrimidines are also a class of sedative drugs, with many examples of

their use targeting kinases (Antonelli et al., 2011, Peat et al., 2004, Carlomagno et al., 2002b).

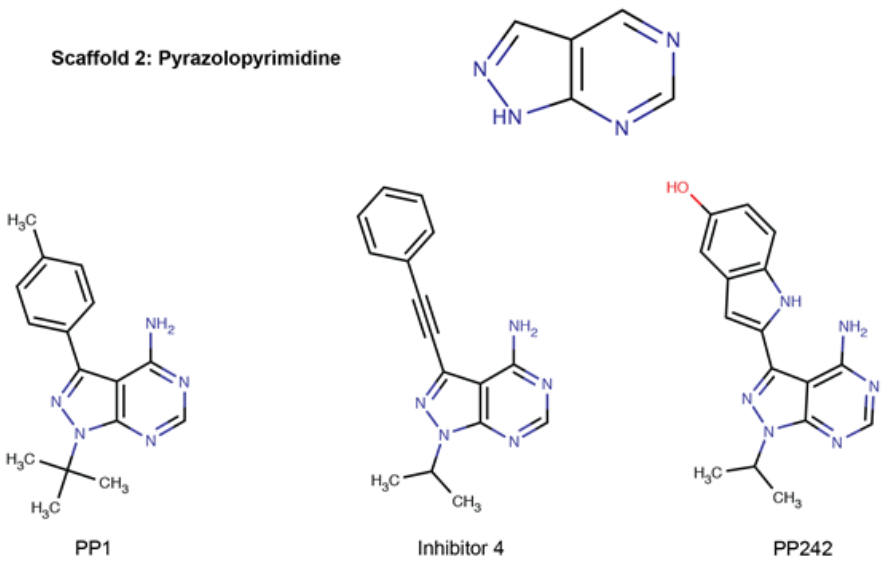

5.4 S2 inhibitors are based on the pyrazolopyrimidine scaffold

Chemical structures of S2, PP1, I-4 and PP242 are shown.

PP1 was originally identified as a Src inhibitor (Hanke et al., 1996), and was then shown to inhibit the growth of human papillary thyroid carcinoma cell lines containing the RET/PTC fusion oncogene, and target MEN2A and B oncogenic forms of the receptor (Carlomagno et al., 2002b). The structure of RET KD bound to PP1 has already been elucidated (PDB code 2IVV) and has shown that this S2 ring system mimics the adenosine position of ATP, forming hydrogen bonds with the main chain atoms of Glu805 and Ala807 of the RET KD hinge region. PP242 was originally identified as an inhibitor of mTOR (mammalian Target Of Rapamycin), which resulted in the inhibition of Akt phosphorylation (Feldman et al., 2009). Further investigation found that PP242 displayed potent cellular activity against RET and JAK family kinases (Liu et al., 2012). The benzene ring is predicted to extend into the interior pocket (defined in Figure 5.1). I-4 is one of a series of pyrazolopyrimidine compounds designed specifically to target RET kinase activity (Diner et al., 2012). I-4 was found to inhibit GFNF-induced RET activation of ERK1/2 in MC-7 breast cancer cells at a concentration of 100 nM. I-4 and PP242 were anticipated to bind in a similar way to PP1, but the longer linker and added substituents on each compound could push further into the back of the RET ATP pocket up to and including residue Glu775.

Sunitinib and the compounds X2K, X2L and X2M all contain a 2-oxo-1H-indolinone core scaffold (S3) (Figure 5.5). Indolinones are a popular scaffold for kinase inhibition, with a number of inhibitors designed for kinases such as VEGFR, FGFR, PGFR and RET (Prakash and Raja, 2012). Sunitinib itself is marketed as Sutent® and is FDA-approved for the treatment of kidney cancer, pancreatic neuroendocrine tumours and gastrointestinal stromal tumours (GIST). Interestingly, Sunitinib was found to preferentially inhibit the non-phosphorylated *DFG-out* conformation of the RTK c-KIT (Gajiwala et al., 2009), while there appeared to be no preference between non- and phosphorylated RET KD (Dr Kerry Goodman, unpublished). The crystal structures of RET KD bound to each of these compounds has been elucidated: Sunitinib:RET KD was solved by Kerry Goodman and is currently unpublished; X2K, X2L and X2M structures can be found under the PDB codes 2X2K, 2X2L and 2X2M respectively (Mologni et al., 2010).

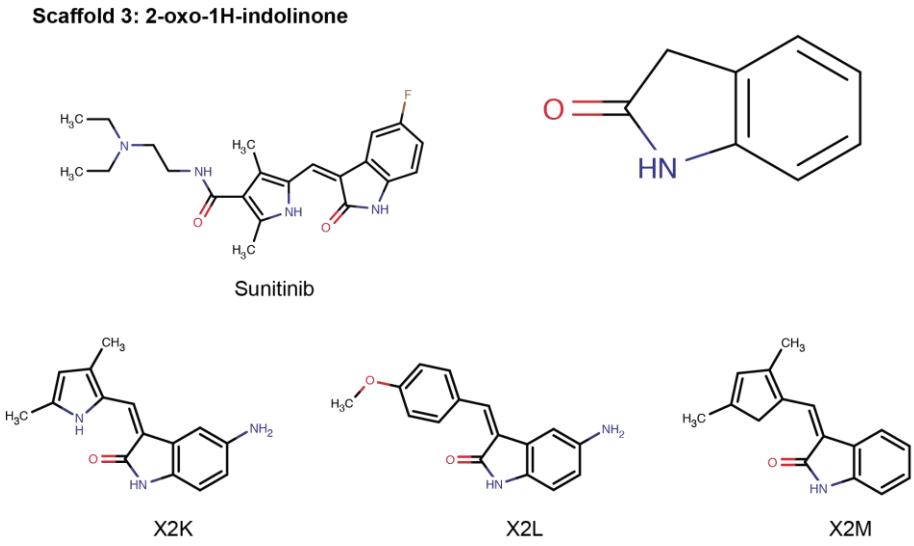

Figure 5.5 S3 inhibitors are based on 2-oxo-1H-indolinone scaffold

Chemical structures of S3, sunitinib, X2K, X2L and X2M are shown

Vandetanib (marketed under its trade name Caprelsa) and I-3 are based on the 4-anilinoquinazoline compound, referred to as scaffold 4 (S4) (Figure 5.6). This scaffold has been successfully used to inhibit several kinases, and has been reported to inhibit EGFR (Zhao et al., 2013). Vandetanib is FDA approved to treat medullary thyroid carcinoma and inhibits RET, but also targets the EGFR and VEGFR kinases (Carlomagno et al., 2002a, Thornton et al., 2012). I-3 was

synthesised by our collaborator at the Paterson Institute (Table 5.1) and was predicted to bind in a similar mode to Vandetanib, but could use the additional hydroxyl group to reach into the back pocket towards Glu775.

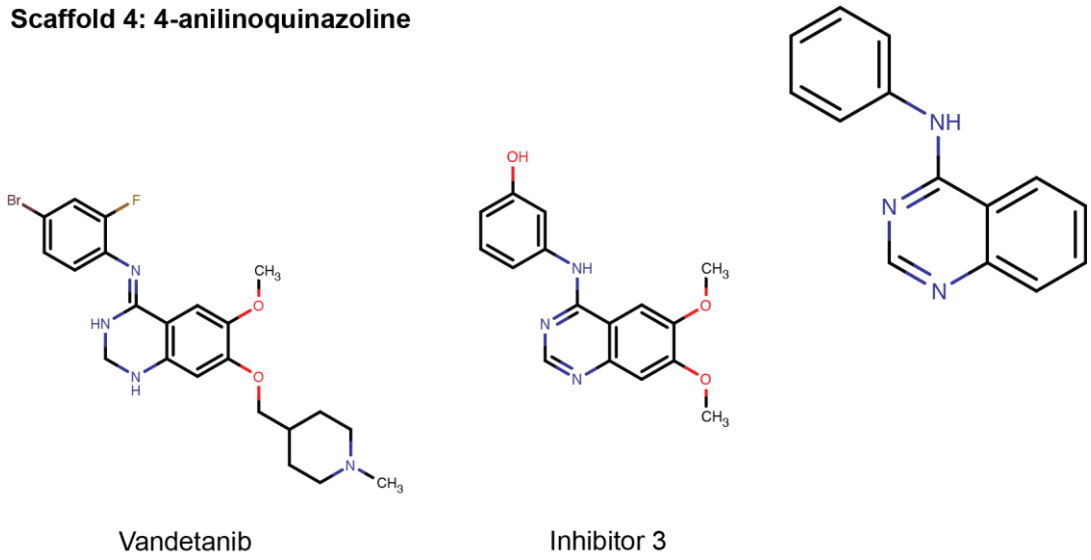

Vandetanib Inhibitor 3

Figure 5.6 S4 inhibitors are based on the 4-anilinoquinazoline scaffold

Chemical structures of the scaffold, Vandetanib and I-3 are shown

Pz-1 and BMS-536924 are known in this thesis as scaffold 5 (S5) inhibitors, due to the presence of a phenyl-benzimidazole ring in both (Figure 5.7). BMS-536924 is a commercially available IGFR inhibitor (Wittman et al., 2005), while Pz-1 has been designed by collaborators in Arizona to target RET as a *DFG-out* inhibitor (the structure of Pz-1 is currently confidential). As mentioned in the thesis introduction, the conserved DFG motif must be in the active *DFG-in* conformation in order for the aspartate to coordinate magnesium binding. Type II inhibitors force this motif into a catalytically incompetent *DFG-out* conformation (Liu and Gray, 2006). The scaffolds are presented together in Figure 5.8.

Scaffold 5: Phenyl-benzimidazole

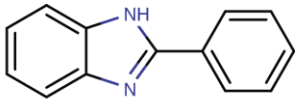

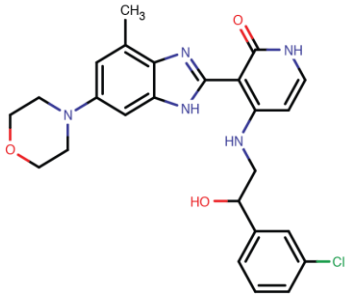

BMS-536924

Figure 5.7 S5 inhibitor based on the phenyl-benzimidazole scaffold

Chemical structures of S5 and BMS-536924 are shown. The chemical structure of Pz-1 is currently confidential.

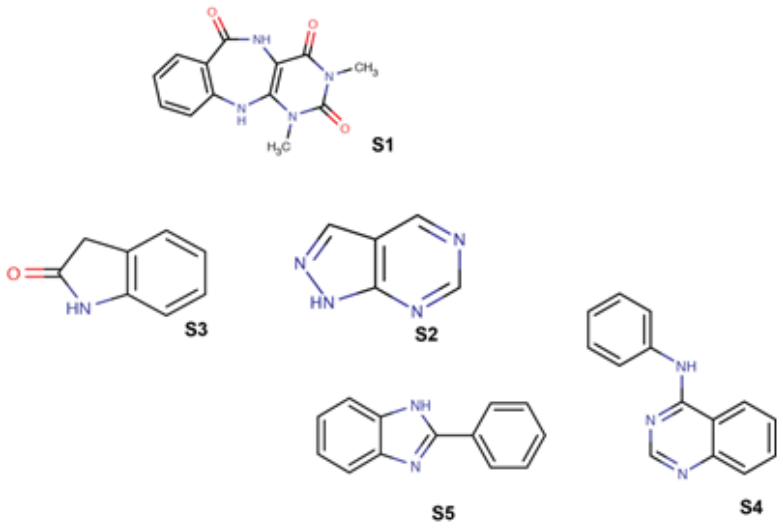

Figure 5.8 Scaffolds 1-5

5.3 RET KD production

5.3.1 Sequence alignment of RET intracellular domains

Alignment of the RET intracellular domain (RET-ICD) amino acid sequences from mammalian and lower vertebrate species (Figure 5.9) shows very high sequence conservation throughout. The most divergence is observed within the glycine and

serine rich kinase insert of the KD, which has been removed from the RET KD used for structural studies.

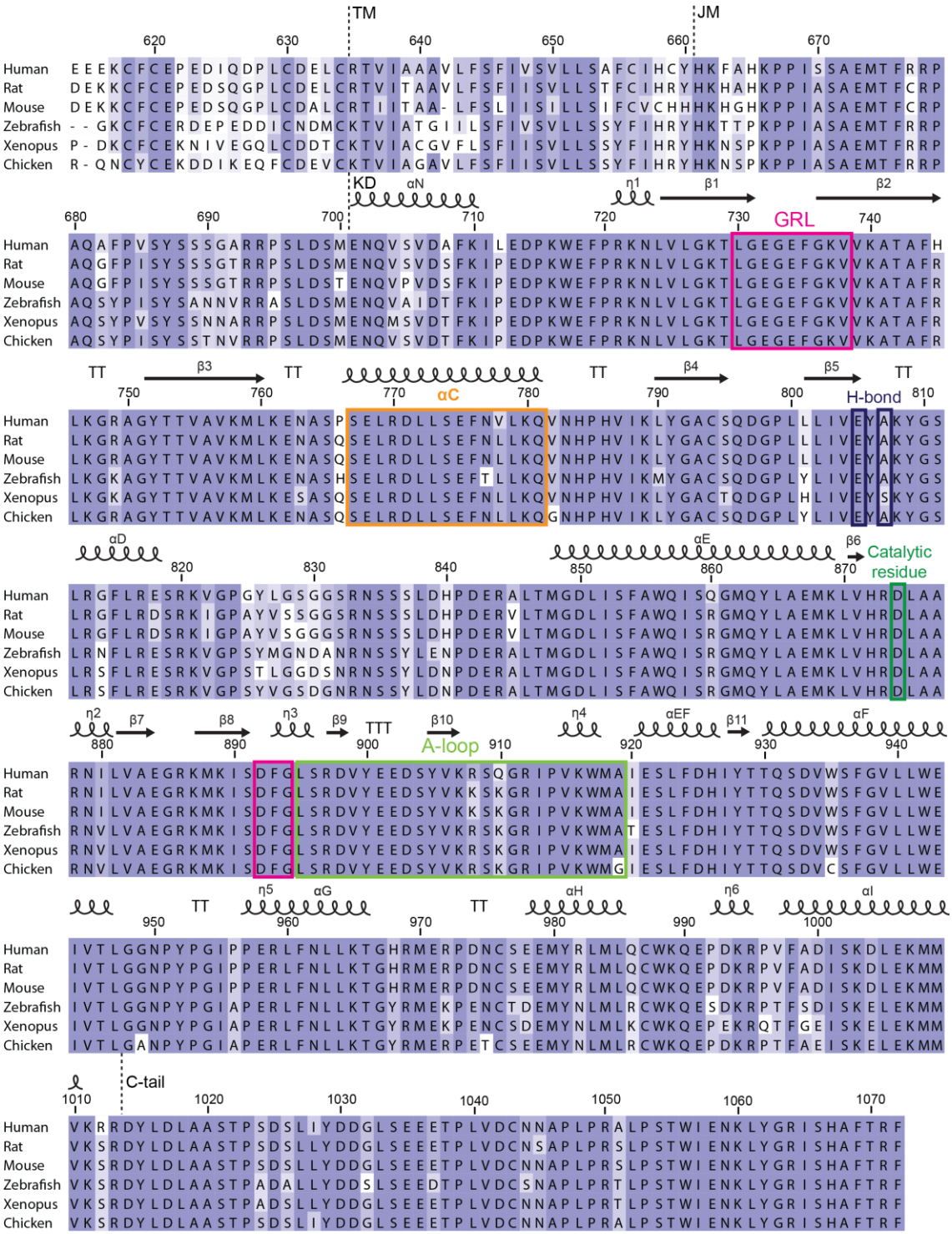

Figure 5.9 Alignment of vertebrate RET-ICD amino acid sequences

Jalview alignment of three higher (human, rat and mouse) and three lower (Xenopus, chicken and zebrafish) vertebrate RET-ICDs. Completely conserved residues are purple, with similarity correlating to the shade of purple. Secondary structural elements and domain boundaries are

annotated above the sequence, as observed in the RET KD crystal structure. Key structural elements are highlighted. Alignment carried out using TCoffee.

5.3.2 RET KD protein expression and purification

A detailed protocol had been previously developed in the laboratory for the expression of human recombinant RET KD in insect cells using baculovirus technology. Yields of approximately 1-2 mg/litre from Hi5 or Sf9 cells were routinely obtained. The baculovirus construct used throughout made use of a codon-optimised (for insect cell expression) synthetic gene for hRET KD, spanning residues 705-1013, removing the highly flexible kinase insert (residues 827-840). The protein was produced with an N-terminal glutathione S-transferase (GST) affinity tag and a 3C protease site within a connecting linker. Purified RET KD produced in insect cells is not phosphorylated, so generating a fully active phosphorylated RET (pRET) required the addition of ATP and magnesium to trigger *trans*-phosphorylation. *Trans*-phosphorylation was performed while RET KD was still attached to the glutathione resin upon addition of 5 mM ATP and 10 mM $MgCl_2$ for 6 hours at 4°C. The ATP and $MgCl_2$ were then removed by washing of the resin, before adding 3C protease. The protein eluate was judged pure by SDS-PAGE (Figure 5.10a), and was known to crystallise without further purification. To readily visualise whether the RET KD was phosphorylated, the molecular weight of RET KD was compared to of pRET KD using SDS-PAGE (Figure 5.10b), with the more acidic pRET KD migrating slower. Previous work in the lab using Western blot analysis with anti-phospho-Tyrosine antibodies has shown RET to be fully phosphorylated under these conditions.

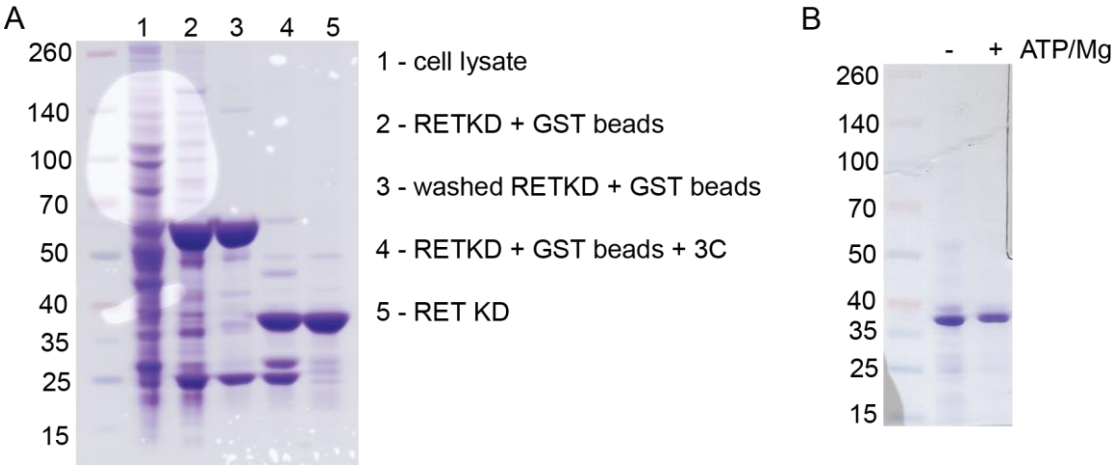

Figure 5.10 RET KD expression, purification and phosphorylation

(A) SDS-PAGE analysis of RET KD expression and purification. **(B)** SDS-PAGE analysis of RET KD phosphorylation, indicated by a slight upwards shift in protein band location.

5.4 Biochemical analysis of inhibitor potency

5.4.1 Examining RET inhibitor potency using differential scanning fluorimetry

Monitoring the thermal stability of a protein kinase in the presence of a range of chemical inhibitors is becoming a facile method for examining inhibitor potency. The process, known as differential scanning fluorimetry (DSF), utilises a fluorescent dye to track the thermal unfolding of a protein. The dyes used are more fluorescent in nonpolar environments, such as those accessible in the hydrophobic regions of unfolded proteins, when compared to the aqueous solution of stable protein. SYPRO orange is the fluorescent dye used in this thesis to examine RET KD stability, and was chosen because of its high signal-to-noise ratio and high excitation wavelength. A high excitation wavelength reduces the risk of the aromatic inhibitors interfering with the fluorescent signal and distorting the unfolding curve detected. This method identifies shifts in protein thermal stability and is known as the thermal shift assay (TSA) (Niesen et al., 2007, Vedadi et al., 2006).

In order to determine the melting temperature of a protein (T_m), the fluorescence intensity is plotted as a function of temperature. This generates a two-state transition sigmoidal curve, from which the inflection point (T_m) can be calculated using the Boltzmann equation in GraphPad Prism (R^2 values of > 0.99). In order to

examine the influences different inhibitors have on RET KD stability, the shift in T_m (ΔT_m) has been plotted and examined (Niesen et al., 2007).

A pilot TSA trial was carried out with RET KD protein at increasing concentrations in the absence of any inhibitor (Figure 5.11a). A prominent increase in fluorescence intensity could be observed as the temperature was increased from 25°C to 90°C. While the fluorescence intensity signal was amplified at a higher protein concentration of 0.4 mg/ml, 0.05 mg/ml was chosen for future assays, due to the feasibility of testing a large array of inhibitors at a sufficient (n=3) number of replicates and concentrations. As seen in Figure 5.11b, a large increase in fluorescence intensity – with a clear curve that could be used for calculating the T_m – can be observed at 0.05 mg/ml when the data is isolated.

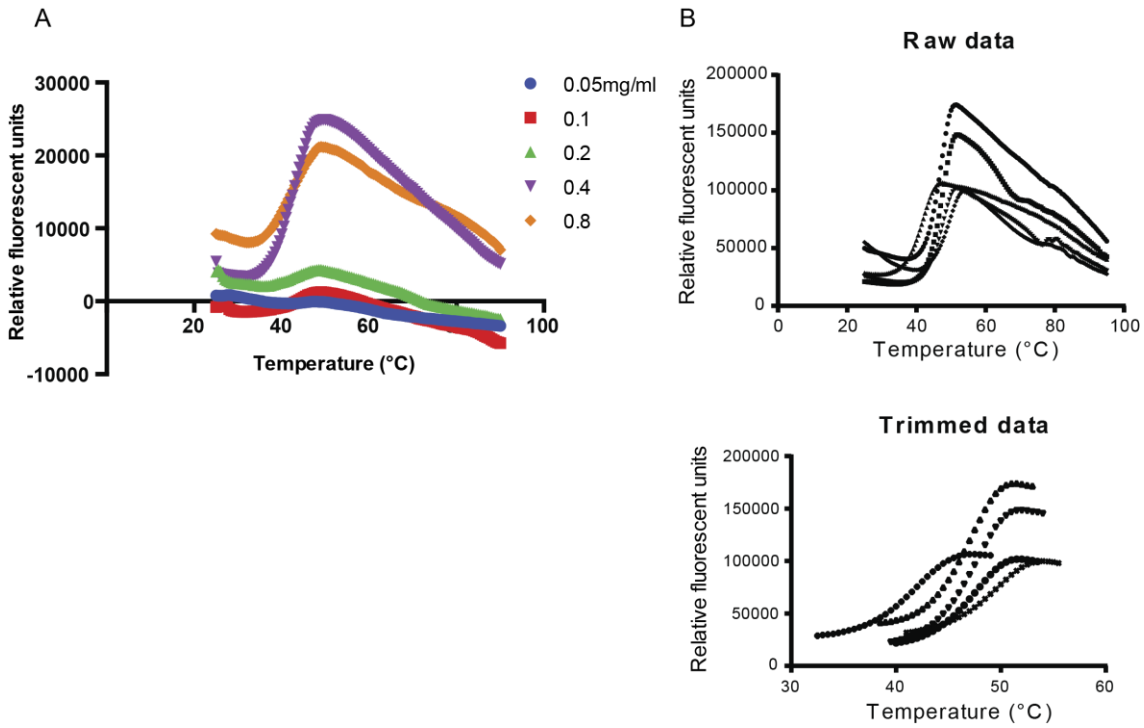

Figure 5.11 Pilot TSA analysis of RET KD protein alone

(A) The fluorescent properties of SYPRO Orange dye binding to RET KD protein was recorded at increasing concentrations of protein. **(B)** Example of raw and trimmed data curves with a protein concentration of 0.05 mg/ml. Data presented in (A) and (B) are from separate experiments.

Pilot experiments showed that RET KD thermal stability could be examined using the TSA. Therefore, the protein stability was probed by TSA after addition of the

inhibitor at a concentration of 1 μM. Although the protein was prepared and purified in a phosphorylated state, ATP and $MgCl_2$ (at 5 mM and 10 mM respectively) were added to RET KD as a separate control. After an incubation of 2 hours at 4°C, the SYPRO Orange dye was diluted 1:100 in purification buffer and added to each protein sample at a ratio of 1:20. The TSA was then carried out using a Real-Time PCR instrument, increasing the temperature of the rtPCR plate containing the protein from 25°C to 90°C over a period of 2 hours. For these particular experiments, RET KD was purified in HEPES buffer rather than Tris, as HEPES buffer can remain at a stable pH over the range of temperature involved.

The Relative Fluorescence Units (RFU) were plotted against the temperature, with the sigmoidal curve truncated at the bottom and top of the 1st slope in the two-state transition, defining the minimum and maximum intensities (Figure 5.11b). The T_m of RET KD in the presence of ATP or inhibitor was calculated using the Boltzmann equation and subtracted from the T_m of the RET KD alone, creating a ΔT_m (Figure 5.12a). In order to visualise these data, the RET KD ΔT_m values have also been plotted as individual scaffolds (Figure 5.12b).

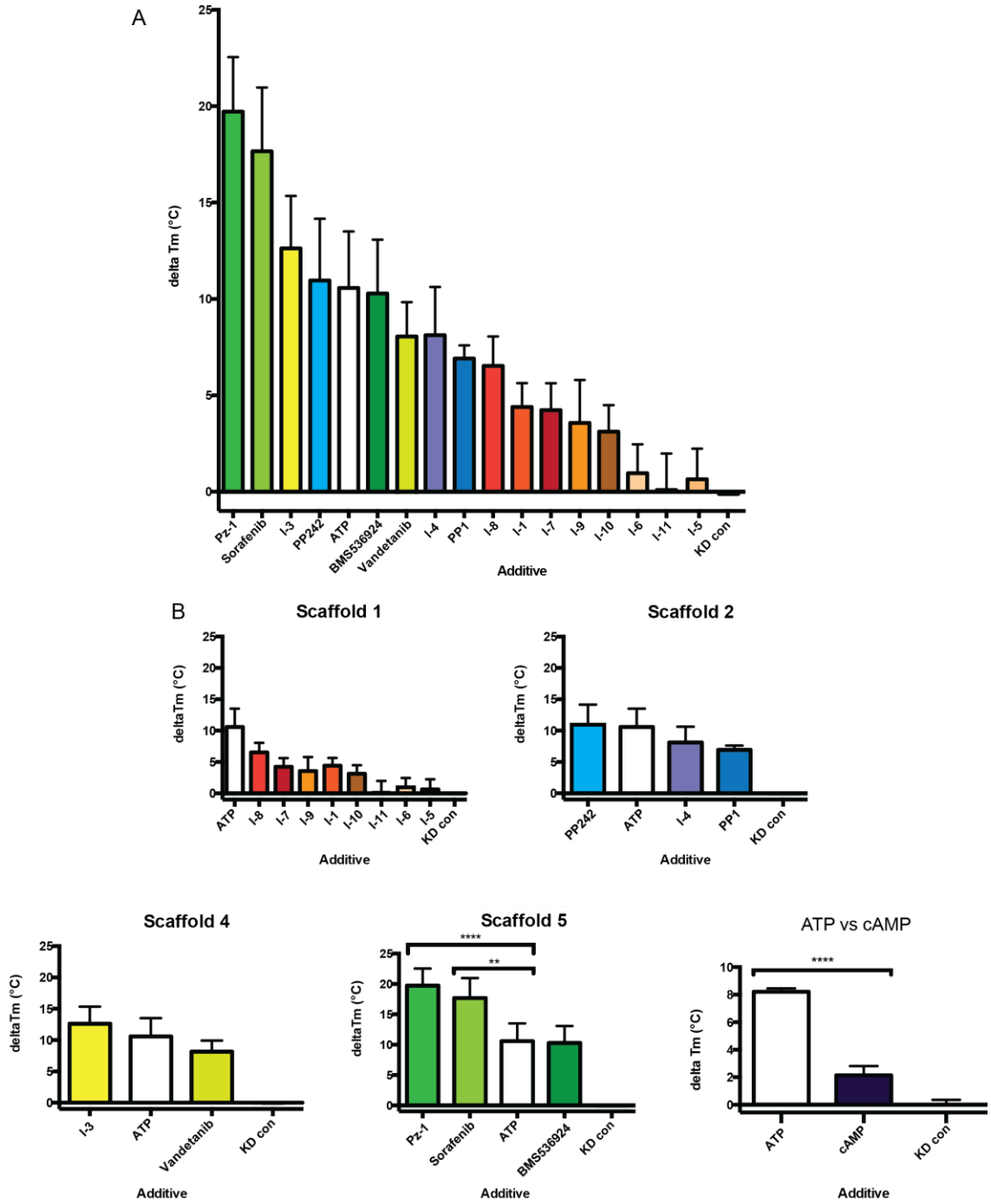

Figure 5.12 TSA analysis of the RET KD in the presence of ATP or inhibitors

(A) The shift in thermal stability (ΔT_m) of RET KD when incubated with ATP or each inhibitor. ΔT_m is calculated by subtracting the T_m of the RET KD alone (KD con) from each individual T_m. Standard deviation (S.D) bars are shown from n=3 experiments. Each experiment contained four repeats of each condition. Data was analysed in Prism. **(B)** ΔT_m of RET KD in the presence of each additive divided into scaffolds 1, 2, 4 and 5. Conditions with ΔT_m values that are significantly higher than ATP (one-way ANOVA, P<0.005) are highlighted. All inhibitors excepting 1, 7, 9 and 10 gave ΔT_m values significantly higher than the KD alone control (one-way ANOVA, P<0.005).

Surprisingly, adding ATP and magnesium to RET KD caused a large shift in thermal stability (Figure 5.12a). As the ATP within the active site will have been hydrolysed to ADP or AMP during protein purification, this suggests that the RET KD has a higher affinity for ATP than ADP or AMP, resulting in an exchange of ligand and an increase in thermal stability. Future investigations should include ADP and AMP in the assay. Thermal stability is significantly higher in the presence of ATP than with cyclic AMP (cAMP) (Figure 5.12b); cAMP was tested in the assay due to its reported presence within the RET nucleotide-binding pocket in unsuccessful RET KD-compound crystallisation trials. The higher stability induced by ATP may be due to a higher affinity towards RET KD or the fact that ATP bound within the pocket will stabilise the C-spine. A lack of thermal shift can suggest one of two things: the inhibitor has not bound to the kinase, or the inhibitor has not affected the stability of the protein.

S1 inhibitors all induced a thermal shift less than that of ATP and only I-8 gave an increase in thermal stability significantly higher than the KD alone control (Figure 5.12). Statistical analysis was carried out using the ordinary one-way ANOVA statistical test, in order to make multiple comparisons between the datasets. The observation that most S1 inhibitors do not induce a significant ΔT_m contradicts the assumption that a lack of positive ΔT_m indicates a lack of binding, as I-7, I-9 and I-10 were also captured in crystal forms bound to the RET KD. It does however give some indication of whether a complex should be taken forward for crystallisation trials, as I-5, I-6 and I-11 have the lowest ΔT_m and could not be captured within the active site and were unable to displace the cAMP that is presumed endogenous, co-purifying with the RET KD from insect cells. Reasons behind the lack of binding of I-5, I-6 and I-11 will be discussed later in this chapter when RET KD-Inhibitor structures have been presented. As the S1 inhibitor giving the largest effect, I-8 is also the only compound from those tested that does not contain a trifluoromethyl group at the end, suggesting that its presence may hinder binding. I-10 was the least effective at inducing a thermal shift from those captured within the active site, which may be due to the extra five-membered ring within the heterocyclic core.

S2 inhibitors appear more effective at inducing a shift in thermal stability than S1, with ΔT_m values closer to that of ATP and all compounds found to be significantly

different to the KD alone (Figure 5.12). This may be due to the fact that the pyrazolopyrimidine scaffold is very similar to the core adenosine structure of ATP, but with bulky substituents extending from the N1 position. I-4 induces a higher thermal shift than PP1, with the main difference between the two inhibitors being the extended triple bond between the pyrazolopyrimidine scaffold and the benzene ring in I-4, which should extend further back into the interior pocket. PP242 appears to be the most effective out of the S2 inhibitors, inducing the highest ΔT_m. Again, based on the structure of this compound, it may extend further into the interior pocket. This may be causing an increase in RET KD stability and also may be – if interacting with residues in the αC-helix – inducing a slight change in the conformation of the αN helix.

Attempts to monitor the ΔT_m of RET KD in the presence of Sunitinib were unsuccessful, despite using the protocol (identical to that of the other inhibitors) for incubating RET KD with sunitinib defined by Dr Kerry Goodman during crystallisation. This may be due to the auto-fluorescent properties of Sunitinib interfering with the measurements. X2K, X2L and X2M were not included in the assay as they were not available at the time of the experiment. Future investigations should include these inhibitors.

S4 inhibitors, I-3 and Vandetanib, had a substantial effect on the thermal stability compared to the KD alone (Figure 5.12). The higher ΔT_m of RET KD-I-3 could be due to several key differences between the two inhibitors. Firstly, I-3 contains a phenol group that could potentially push into the back of the ATP pocket and interact with Glu775 or the water molecule that is often seen close to this key αC-helix residue; as opposed to the benzene ring with a fluoride and bromine attached. Alternatively, this higher stability could be due to the lack of a hydrogenated pyridine group at the other end of the compound. Within the RET KD-Vandetanib structure (PDB code 2IVU), this substituent – often added to improve solubility – forms hydrogen bonds with a water molecule and sits slightly outside of the pocket – as seen for the trifluoromethyl groups of the less effective S1 inhibitors.

Sorafenib was included in the S5 inhibitors, along with Pz-1 and BMS-536924. Sorafenib is a *DFG-out* compound and has a rather similar structure to the S5

inhibitors (Figure 5.13). All three compounds have an extended shape and are composed of multiple ring systems. The RET KD thermal stability was increased by a remarkable amount when incubated with Sorafenib, which is indicative of a conformational change within the protein (Figure 5.12). Pz-1 induced a thermal shift of almost 20°C, suggesting that it too induces a conformational change similar – if not equal – to Sorafenib and is also likely to be a type II inhibitor stabilising a *DFG-out* conformer. These two inhibitors were the only compounds to induce a ΔT_m significantly higher than that of RET KD-ATP. This suggests that TSA is a facile and quick method to distinguish between *DFG-in* and *DFG-out* inhibitors in solution.

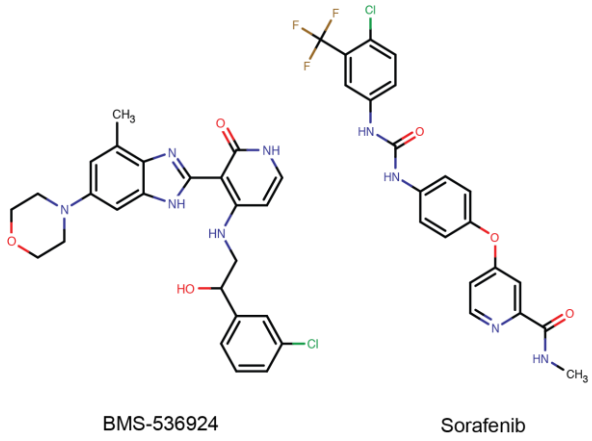

Figure 5.13 Comparisons of the BMS-536924 (S5) and Sorafenib chemical structures

5.4.2 Inhibitory effects of each compound on RET tyrosine kinase activity

The inhibitory activity of each compound is measured using the maximal inhibitory concentration (IC_{50}) value against a particular target. I have collated data both from published work and collaborators for each of the inhibitors in S1, 2, 4 and 5. Table 5.2 shows IC_{50} values for each S1 compound against RET, V804L RET (oncogenic gatekeeper mutant) and known off-target kinases, along with data on PP242 and BMS-536924. These data are displayed together as the same collaborator contributed them: Dr. Nathanael Gray, Harvard Medical School. Table 5.3 shows IC_{50} values for I-4 and PP1 (S2), Vandetanib (S3), and Sorafenib and Pz-1 (S5) against RET and the V804M mutant. These data are collated from published work, with references provided.

Harvard collaborators

	Target IC50 (nM)					
Inhibitor	**RET**	**RET (V804L)**	**AURKA**	**AURKB**	**LRRK2 (G2019S)**	**NUAK1**
1	107	47.1	10.3	231	15.3	96.3
5	>10000	>10000	>10000	>10000		
6	>10000	>10000	>10000	>10000		
7	207	127	28.1	378	5.47	
8	36.4	10.1	7.17	25.9	14	27.2
9	239	159	34.1	806		
10	668	382	12	182		
11	>10000	>10000	>10000	>10000		
PP242	2.84	394	3540	3150		
BMS-536924	6.77	2.24	312	639		

Table 5.2 *In vitro* IC_{50} data for S1 compounds, PP242 and BMS-536924 against RET and off target kinase

IC_{50} data obtained from our collaborators (Dr Nathanael Gray, Harvard Medical School) investigating the ability of each S1 compound to inhibit RET, the gatekeeper mutant of RET (V804L), and their main off targets: AURKA, AURKB, LRRK2 (G2019S) and NUAK1.

In the case of S1 compounds, the ΔT_m of the RET KD bound to each correlates with the inhibitory activity (Table 5.2). The most effective inhibitor (I-8) also has the lowest IC_{50} value of 36.4 nM against RET, while the ineffective inhibitors (I-5, I-6 and I-11) had IC_{50} values of over 10 μM. One of the current problems with this group of inhibitors is that RET potency tracks AURKA activity: reducing off-target potency also results in a loss of potency towards RET. PP242 is very potent against RET (2.84 nM, Table 5.2), with much lower potencies for the AURKA/B off-target kinases. Interestingly, PP242 and I-4 have very similar potencies toward RET, while PP1 is approximately 10-fold less effective (80 nM, Table 5.3). This also correlates with TSA data (Figure 5.12b), as I-4 induces the lowest shift in thermal stability. This may be due to the fact that both PP242 and I-4 are chemically extended and should push further into the interior pocket of the nucleotide-binding region towards Glu775. It is worth noting that all S2 inhibitors lose potency towards the gatekeeper mutant forms of RET (V804L/M), as the mutation at this position into a bulky residue will occlude access to the interior pocket. Vandetanib also loses potency against the gatekeeper mutant.

Published IC50 data			
	Target IC50 (nM)		
Inhibitor	**RET**	**RET (V804M)**	**Reference**
I-4	8	-	Diner et al., 2014
PP1	80	5000	Carlomagno et al., 2002a & 2004
Vandetanib	100	5000	Carlomagno et al., 2002b & 2004
Sorafenib	5.9	7.9	Plaza-Menacho et al., 2007
Pz-1	<1	<1	Unpublished

Table 5.3 *In vitro* IC_{50} data for inhibitors against WT and V804M RET

Inhibitory activity of I-4, PP1, Vandetanib, Sorafenib and Pz-1 against wild type RET and the gatekeeper mutant V804M. References for the original data are shown.

Interestingly, all S5 compounds (BMS-536924, Pz-1 and Sorafenib) are very potent against both WT and V804L/M RET – again, correlating with TSA data for WT RET. Pz-1 induced the largest shift in thermal stability, and is the most potent inhibitor against RET yet described (data obtained from our collaborator, Dr Hong Yu-Li, University of Arizona). While IC_{50} data collated from different sources should be validated within the laboratory in near future investigations, there is a clear correlation between inhibitor activity against RET and elicited effect on protein thermal stability (Figure 5.14). This correlation has been previously reported in the literature and could prove useful in future high throughput investigations (Fedorov et al., 2007, Slaymaker et al., 2008).

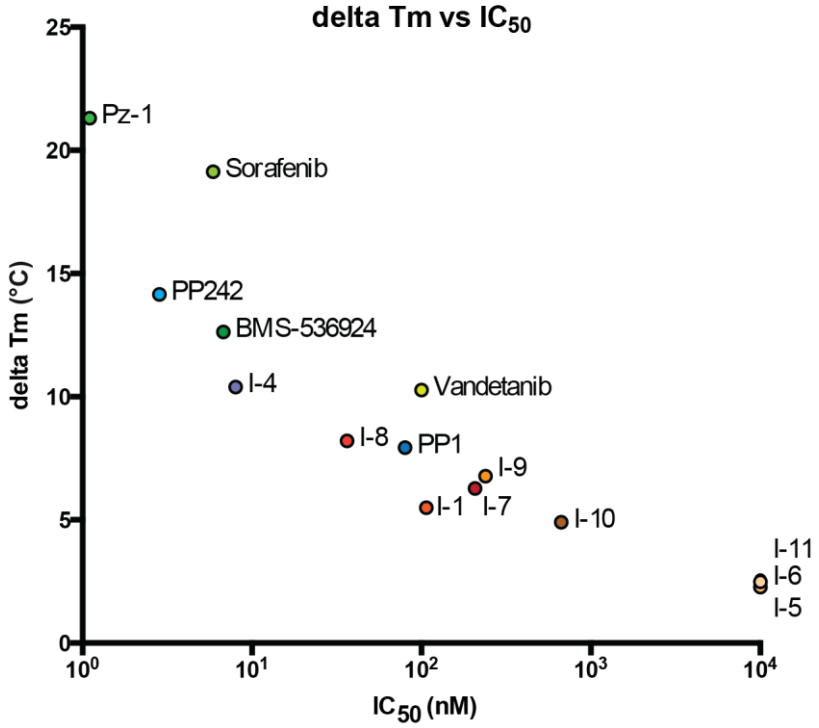

Figure 5.14 Correlation between RET KD IC_{50} values and ΔT_m enhancement after incubation with each inhibitor
Log-transformed IC_{50} values (from nM to µM concentrations) for each inhibitor against RET (x) are plotted against the shift in thermal stability of the RET KD in the presence of each compound (y). There is clear correlation between induced thermal stability and the inhibitor potency. (Correlation coefficient of -0.8995).

5.5 RET KD crystallisation with inhibitors

In order to structurally characterise the binding of each inhibitor to the RET KD, co-crystallisation experiments were carried out. Each inhibitor was dissolved in DMSO and added to purified pRET KD at a 3:1 inhibitor:protein molar ratio in solution. The inhibitor:protein solution was incubated at 4°C for 2 hours to allow binding, before concentrating to 3-5 mg/ml for crystallisation.

RET KD was previously crystallised in the presence of sodium acetate buffer and formate (Knowles et al., 2006), so this condition was used as a starting point for crystallisation by vapour diffusion. The protein-inhibitor complex was plated in 96 well trays with a range of formate concentrations and with MES or acetate buffer at varying pH to identify the optimal crystallisation condition for each compound. The exact crystallisation condition for each inhibitor is detailed in Table 5.4. The crystals

obtained took the form of stacked square plates, with further optimisation leading to thicker single plates (Figure 5.15a).

Scaffold	Ligand	Buffer	Sodium formate (M)	Additive
-	ADP	0.1 M Sodium acetate pH 4.8	3.3	3% (v/v) Ethanol
1	I1	0.1 M MES pH 5.1	3.1	0.2 M Lithium chloride
	I7	0.1 M MES pH 5.8	2.7	3% (w/v) Trimethylamine N-oxide
	I8	0.1 M MES pH 5.9	3.2	
	I9	0.1 M MES pH 5.9	3	0.01 M Cobalt (II) chloride
	I10	0.1 M MES pH 5.9	2.8	
2	I4	0.1 M MES pH 5.2	3	
	I18	0.1 M MES pH 5.5	3.3	
4	I3	0.1M Sodium acetate pH 4.4	3.4	
5	I19	0.1 M MES pH 6.0	3.8	

Table 5.4 Crystallisation conditions for each RET KD:ligand structure

5.5.1 RET KD-inhibitor structure determination

Crystals for each inhibitor ranged between 30 and 120 μm in size and were cryo-protected in perfluoropolyether (PFPE) oil (Hampton Research) before flash-freezing in liquid nitrogen. The crystals were screened at either the Diamond Light Source (DLS) or the European Synchrotron Radiation Facility (ESRF) and data was collected on crystals diffracting to at least 2.6 Å (example diffraction shown in Figure 5.15b). Data collection statistics for each inhibitor can be found in Table 5.5.

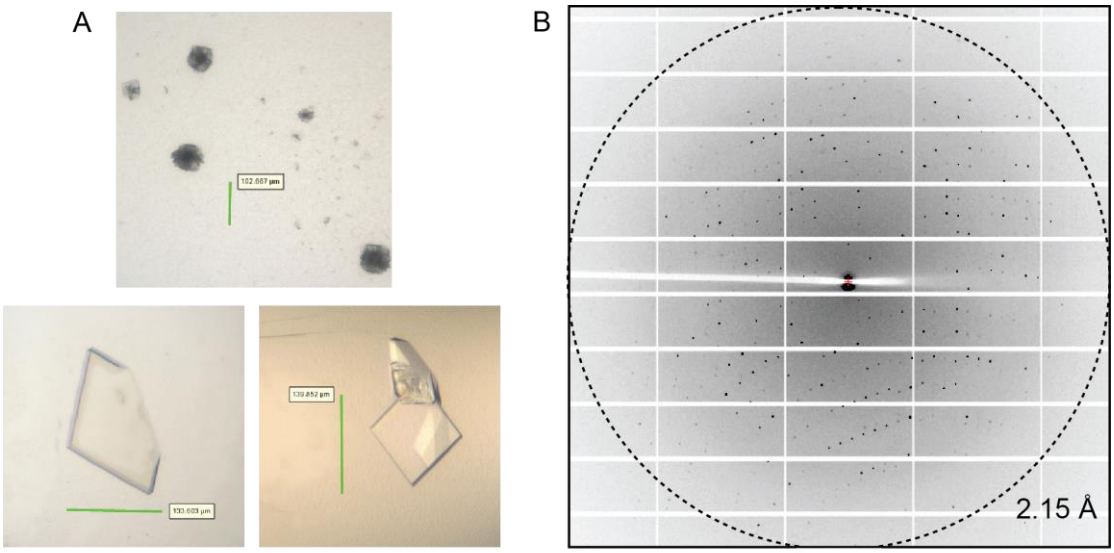

Figure 5.15 Crystallisation and structural determination of RET KD-inhibitor complexes

(A) Stacked crystal plates were grown in acetate/formate conditions (top), before optimisation into single plates grown in formate with MES or acetate buffer (bottom). **(B)** Example of diffraction images collected at a resolution of 2.15 Å that were used in structure determination.

	RETKD:ADP	RETKD:I1	RETKD:I7	RETKD:I8	RETKD:I9
X-ray source	DLS	DLS	DLS	DLS	DLS
Wavelength / Å	0.97	0.92	0.98	0.92	0.98
Space group	C2(C121)	C2(C121)	C2(C121)	C2(C121)	C2(C121)
Unit cell dimensions					
a, b, c / Å	72.85, 69.43, 78.92	73.19, 69.89, 79.42	73.09, 69.76, 79.20	72.97, 70.68, 79.26	72.7, 69.73, 79.28
α, β, γ / °	90.00, 102.13, 90.00	90.00, 102.89, 90.00	90.00, 103.14, 90.00	90.00, 102.24, 90.00	90.00, 103.18, 90.00
Resolution / Å	35.28 - 2.21	77.42 - 2.00	49.82 - 1.95	16.88 - 2.65	39.03 - 1.70
(Outer resolution shell) / Å	(2.27 - 2.21)	(2.05 - 2.00)	(2.00 - 1.95)	(2.72 - 2.65)	(1.74 - 1.70)
No. of unique reflections	19032	25956	27785	11338	40841
Redundancy	2.9 (2.6)	3.0 (3.0)	2.5 (2.5)	3.5 (3.6)	3.0 (2.0)
Completeness / %	98.2 (95.9)	98.2 (97.8)	98.1 (97.5)	98.4 (99.2)	96.3 (73.5)
CC(1/2) (outer shell)	0.596	0.558	0.573	0.493	0.52
I/σ	1.8	1.1	1.4	1.2	1.1
Rmerge / %	8.6 (66.6)	12.4 (87.1)	5.5 (68.1)	17 (89.7)	4.2 (75.4)
Rp.i.m / %	5.9 (50.1)	8.3 (58.2)	4.2 (51.2)	10.7 (64.9)	2.8 (60.9)

	RETKD:I10	RETKD:I4	RETKD:PP242	RETKD:I3	RETKD:BMS-536924
X-ray source	DLS	DLS	DLS	DLS	DLS
Wavelength / Å	0.98	0.92	0.92	0.98	0.98
Space group	C2(C121)	C2(C121)	C2(C121)	C2(C121)	P4(P41212)
Unit cell dimensions					
a, b, c / Å	72.87, 69.56, 79.28	73.2, 70.28, 79.53	72.75, 71.31, 79.85	73.85, 70.22, 158.78	50.23, 50.23, 236.81
α, β, γ / °	90.00, 102.92, 90.00	90.00, 102.86, 90.00	90.00, 102.71, 90.00	90.00, 102.91, 90.00	90.00, 90.00, 90.00
Resolution / Å	49.70 - 1.80	39.36 - 2.60	50.30 - 2.26	51.56 - 2.45	50.23 - 2.3
(Outer resolution shell) / Å	(1.85 - 1.80)	(2.67 - 2.6)	(2.32 - 2.26)	(2.51 - 2.45)	(2.36 - 2.30)
No. of unique reflections	35417	48525	17865	15057	14470
Redundancy	3.0 (.2.6)	4.0 (4.1)	2.9 (3.0)	6.8 (6.7)	7.5 (7.6)
Completeness / %	98.9 (93.8)	99.0 (96.3)	95.5 (91.0)	99.7 (98.6)	100.0 (100.0)
CC(1/2)	0.581	0.641	0.712	0.551	0.619
I/σ	1.5	1.3	2	0.9	1.9
Rmerge / %	5.4 (67.9)	10.5 (91.3)	8.6 (54.1)	12.7 (72.3)	9.5 (112.1)
Rp.i.m / %	3.7 (49.6)	5.8 (66.3)	6.1 (37.3)	14.8 (65.5)	3.7 (43.0)

Table 5.5 Data collection statistics for each RET KD-ligand dataset

5.5.2 Data processing, structure solution and refinement

I processed the data and refined the structures for all inhibitors except 9 and 10, which were processed by Dr Andrew Purkiss. The datasets were processed using the program Xia2 (Winter et al., 2013), using option “3daii” which utilises software programs XDS for indexing and integration (Kabsch, 2010), XSCALE for scaling and Aimless for merging (Evans and Murshudov, 2013). The datasets with the same cell dimensions (all except I-3 and BMS-536924) were processed with a consistent R_{free} set copied from the first dataset (I-1). Xia2 confirmed the spacegroup for each inhibitor using the program POINTLESS (Evans, 2006), with the majority being monoclinic C2, but a tetragonal cell space group $P4_32_12$ was found for BMS-536924. Cell content analysis using the Matthews coefficient program in CCP4 indicated the number of molecules in the asymmetric unit (one molecule for all inhibitor structures except I-3, in which there were two molecules) (Matthews, 1968, Kantardjieff and Rupp, 2003). Each structure was solved by molecular replacement with PHASER (McCoy et al., 2007), using the pRET KD-adenosine structure with the GRL and vector-derived N-terminal helix removed, to reduce initial model bias. Each structure was refined using Phenix.refine and model building was carried out in COOT (Emsley and Cowtan, 2004). Initial refinement was carried out for approximately four rounds, before TLS (translation, libration, screw rotation) groups were added (N-terminal helix 700-712; N-lobe 716-808; C-lobe 809-1013) to refinement. These groups allowed separate correlated motions of each defined subdomain, within the RET KD, to be modelled via temperature factors. The inhibitors were fitted into positive density after several rounds of refinement, to ensure optimal positive density within the active site after the kinase domain structure itself had been modelled. Final refinement statistics for each inhibitor can be found in Tables 5.6, with the electron density surrounding each ligand shown later.

	RETK:ADP	RETKD:I1	RETKD:I7	RETKD:I8	RETKD:I9
Resolution / Å	35.277 - 2.21	77.42 - 2.00	49.82 - 1.95	16.88 - 2.65	39.03 - 1.70
(Outer resolution shell) / Å	(2.27 - 2.21)	(2.05 - 2.00)	(2.00 - 1.95)	(2.72 - 2.65)	(1.74 - 1.70)
Completeness / %	98.2 (95.9)	98.2 (97.8)	98.1 (97.5)	98.4 (99.2)	96.3 (73.5)
No. of unique reflections	19032	25956	27785	11338	40841
Rwork / %	17.23 (33.67)	18.76 (27.4)	17.07 (26.26)	20.39 (30.06)	18.67 (35.49)
Rfree / %	23.11 (40.97)	22.96(34.03)	21.06 (28.07)	23.31 (33.00)	21.42 (40.92)
Total protein atoms	2204	2276	2274	2241	2232
Total ligand atoms	39	39	29	32	36
Total solvent atoms	93	153	110	74	25
Wilson B factor	36.00	29.52	33.52	37.94	28.66
B-factor (Å2)					
Protein	35.87	34.04	38.87	43.02	34.17
Ligand	88.6	41.87	36.62	36.95	36.44
Water	46.25	44.13	50.45	38.55	43.54
Ramachandran Plot / %					
Favoured	97.57	98.64	98.32	97.91	98.29
Allowed	2.43	1.36	1.68	2.09	1.37
Outliers	0	0	0	0	0.34
RMSD from ideal values					
Bonds / Å	0.013	0.006	0.014	0.002	0.007
Angles / °	1.326	0.913	1.528	0.625	1.183
No. of TLS groups	3	3	3	3	3

	RETKD:I10	RETKD:I4	RETKD:PP242	RETKD:I3	RETKD:BMS-536924
Resolution / Å	49.70 - 1.80	39.36 - 2.60	50.30 - 2.26	51.56 - 2.45	50.23 - 2.3
(Outer resolution shell) / Å	(1.85 - 1.80)	(2.67 - 2.6)	(2.32 - 2.26)	(2.51 - 2.45)	(2.36 - 2.30)
Completeness / %	98.9 (93.8)	99.0 (96.3)	95.5 (91.0)	99.7 (98.6)	100.0 (100.0)
No. of unique reflections	35417	48525	17865	15057	14470
Rwork / %	19.15 (26.14)	22.36 (37.36)	18.23 (26.22)	25.09 (31.27)	19.76 (25.28)
Rfree / %	21.62 (30.35)	24.08 (37.47)	23.56 (32.29)	28.49 (40.68)	24.46 (32.71)
Total protein atoms	2193	2129	2206	2156 (mol A)	2135
Total ligand atoms	59 (2 conformations)	21	23	24	34
Total solvent atoms	36	43	128	28	49
Wilson B factor	26.43	55.35	36.06	38.39	44.04
B-factor (Å2)					
Protein	31.46	60.42	39.2	45.7 (mol A)	48.59
Ligand	44.9	53.05	34.18	35.47 (mol A)	84.78
Water	30.27	57.75	44.41	29.95	55.23
Ramachandran Plot / %					
Favoured	98.23	94.74	97.21	96.36	98.6
Allowed	1.41	4.91	2.79	3.1	1.4
Outliers	0.35	0.35	0	0.55	0
RMSD from ideal values					
Bonds / Å	0.008	0.002	0.003	0.003	0.002
Angles / °	1.213	0.73	0.927	0.732	0.624
No. of TLS groups	3	3	3	3	3

Table 5.6 Refinement statistics for each of the RET KD-ligand datasets

5.6 Overall description of the RET kinase-inhibitor structures

All of the structures presented in this thesis show the same overall arrangement of N- and C-lobes: the smaller N-lobe consisting of a β–sheet comprised of five anti-parallel β-strands (β1-5) with the αC helix between strands β3 and β4 (within the amino acid sequence), the flexible GRL lining the top of the active site, and a larger helical C-lobe (Figure 5.16).

RET KD also has an N-terminal helix called αN, which contains five vector-derived residues (GPLSL) and 6 *de novo* residues (SVDAFK). The vector derived residues are not similar to those found in full-length RET, so it is unclear as to whether this helix is present in full-length RET. The linker (I711 to P715) connecting the αN-helix to the KD is often disordered.

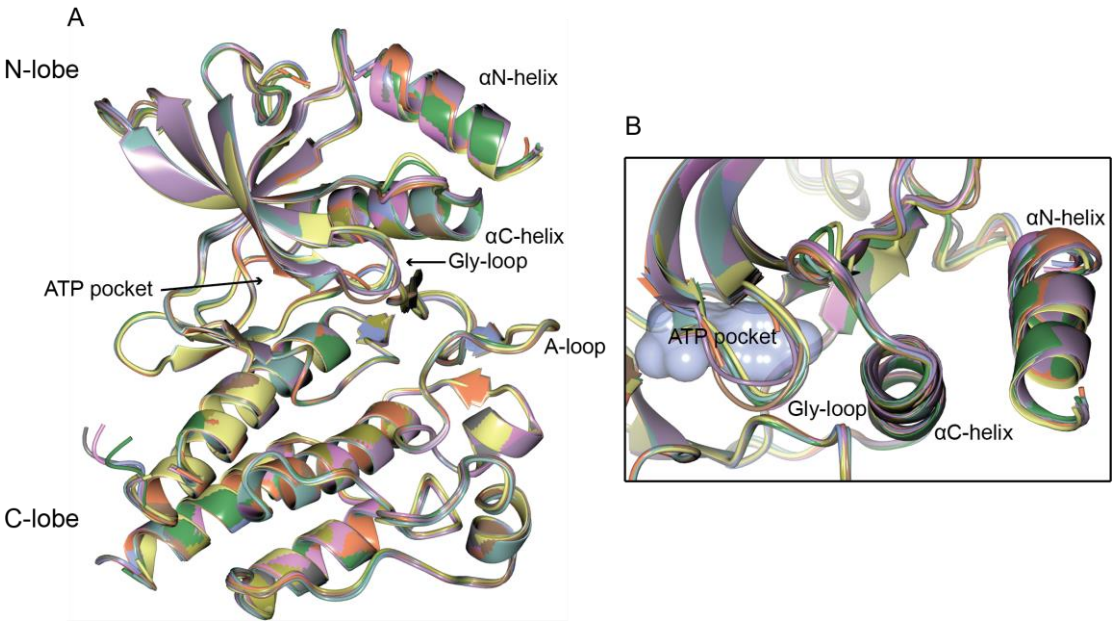

Figure 5.16 Superposition of KD structures solved in this thesis

(A) Ribbon view of aligned RET KD structures solved in this thesis. I-1 – ice blue; I-3 – light brown; I-4 – sea green; I-7 – gold; I-8 – coral; I-9 – grey; I-10 – pink; PP242 – lilac; BMS-536924 – lemon; ADP – lawn green. **(B)** Side view of the RET KD, highlighting the positions of the αN-helix, αC-helix, the Gly-loop and the ATP pocket (surface view of PP1 inhibitor (PDB code 2IVV)).

The main difference between the structures maps to the GRL, already known to be highly flexible and found on top of the nucleotide-binding pocket. While the majority of the structures contained a “closed” GRL conformation (including RET KD-ADP),

RET KD-I-3 had a more open conformer (approximately 1.25 Å above RET KD-ADP, as measured between the backbones of Glu734 in each structure) and the RET KD-PP242 GRL was found to be even further open (approximately 4 Å at the widest point, again between the backbones of Glu734) (Figure 5.17a). The loop preceding the αC helix also has a different conformer depending on the inhibitor bound (Figure 5.17c). In the RET KD-PP242 structure, the Phe735 in the GRL has a different side chain rotamer, pointing away from the nucleotide-binding pocket, while all other structures show this residue pointing towards the pocket. This shift in rotamer may be due to the relative position of Lys758, which has also shifted to point towards the GRL, thus breaking the conserved salt bridge between itself and Glu775. While not as notable, the position of Lys758 appears to be coupled to the position of Phe735 for all structures. A change in the rotation along the Cα-Cβ axis of Lys758 (either towards or away from the GRL) induces a relative shift in the position of Phe735 (Figure 5.17b). It is also possible that the Phe735 is positioning Lys758 into an active conformer, rather than the opposite.

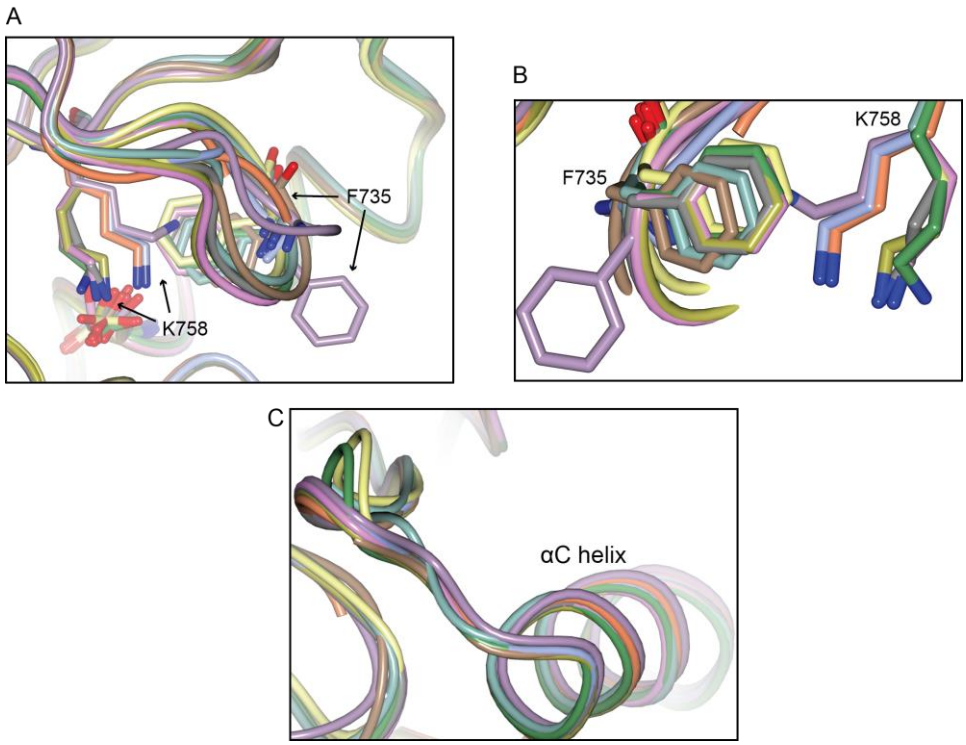

Figure 5.17 Comparisons of Phe735 and Lys758 side chain positions

(A) Close-up view of aligned RET KD structures solved in this thesis, with side chain positions of Phe735 and Lys758 highlighted. I-1 – ice blue; I-3 – light brown; I-4 – sea green; I7 – gold; I-8 – coral; I-9 – grey; I-10 – pink; PP242 – lilac; BMS-536924 – lemon; ADP – lawn green. **(B)**

Alternate view of aligned structures with side chain positions of Phe735 and Lys758 highlighted. **(C)** Differences in the loop formation preceding the αC helix.

5.7 Overall description of the RET kinase-ADP complex

During protein purification and crystallisation, I attempted to crystallise the RET KD with Sorafenib, as the *DFG-out* form of RET has not been captured thus far. The process was identical to that with other inhibitors, in that the KD was incubated with ATP and magnesium before washing and cleavage from the GST resin. After incubation with Sorafenib at 3:1 molar excess and concentration to approximately 3 mg/ml, crystallisation trays were set up with the original formate/acetate conditions. Crystals were produced (Figure 5.18a), cryo-protected in PFPE oil and flash frozen. Data was collected at Diamond Light Source, in the usual C2 space group and diffraction to 2.1 Å was observed (Figure 5.18b).

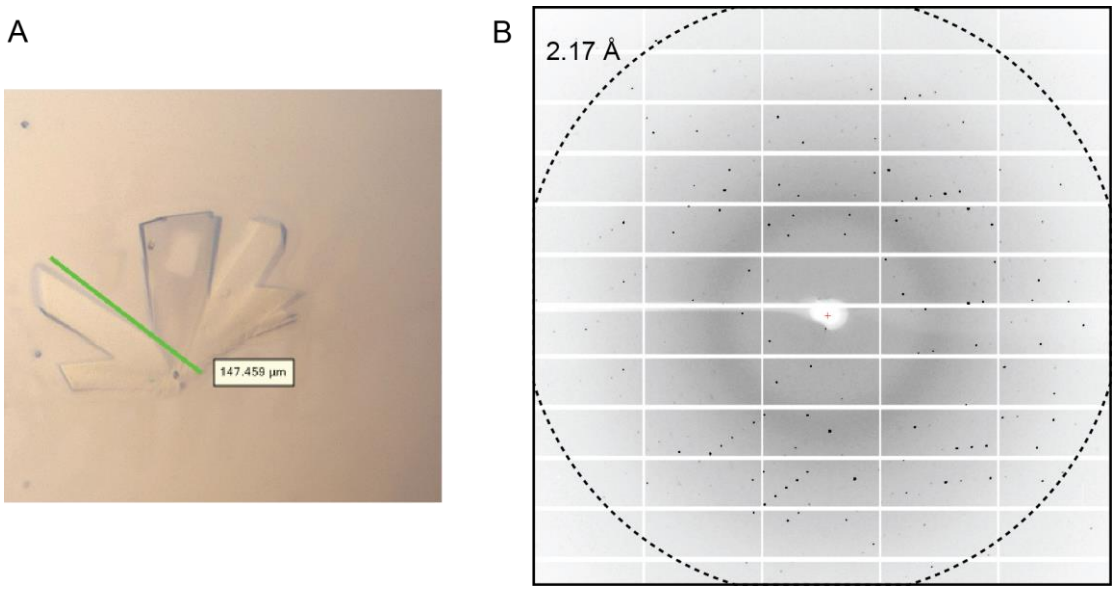

Figure 5.18 Crystallisation and data collection of the RET KD-ADP complex

(A) Crystal plates obtained in formate/acetate condition, believed at this point to be the RET KD-Sorafenib complex. **(B)** Example of diffraction images collected at a resolution of 2.1 Å that were used in structure determination.

However, after processing and initial refinement, the density within the nucleotide-binding pocket clearly did not correspond with the structure of Sorafenib. ATP was placed within the density, before being replaced with ADP due to poorly defined density surrounding the γ-phosphate. It is possible that the crystal contains multiple

occupancies of ATP and ADP, as the ATP is hydrolysed to ADP. Crystals from the same drop were taken to the synchrotron again after one month, resulting in the collection of a 2.1 Å dataset. In this particular crystal, only adenosine was found within the nucleotide-binding pocket, which validated the presence of ADP within the original crystal and confirmed its susceptibility to hydrolysis.

ADP extends across the right side of the pocket, with the GRL in the closed position (Figure 5.19a). This is surprising, as the closed conformation has been suggested to sterically block ATP from accessing the pocket and binding within it. This was based on comparisons to the related FGFR kinase structure bound to ATP/Mg^{2+}, where the phosphates interact with residues within the GRL (Figure 5.20a). It is notable that no magnesium is present with ADP in the pocket. However, not all solvent will be visible at a resolution of 2.1 Å, so the presence – or lack of – a magnesium ion within the pocket could only be confirmed with a higher resolution dataset or a potential substitution with manganese. The nucleotide extends across the catalytic region of the pocket towards the catalytic residue Asp874 (Figure 5.19d), and the γ-phosphate would be positioned close to where the incoming tyrosine nucleophile would be expected. The adenosine forms hydrogen bond with the main chain of both Glu805 and Ala807 in the KD hinge.

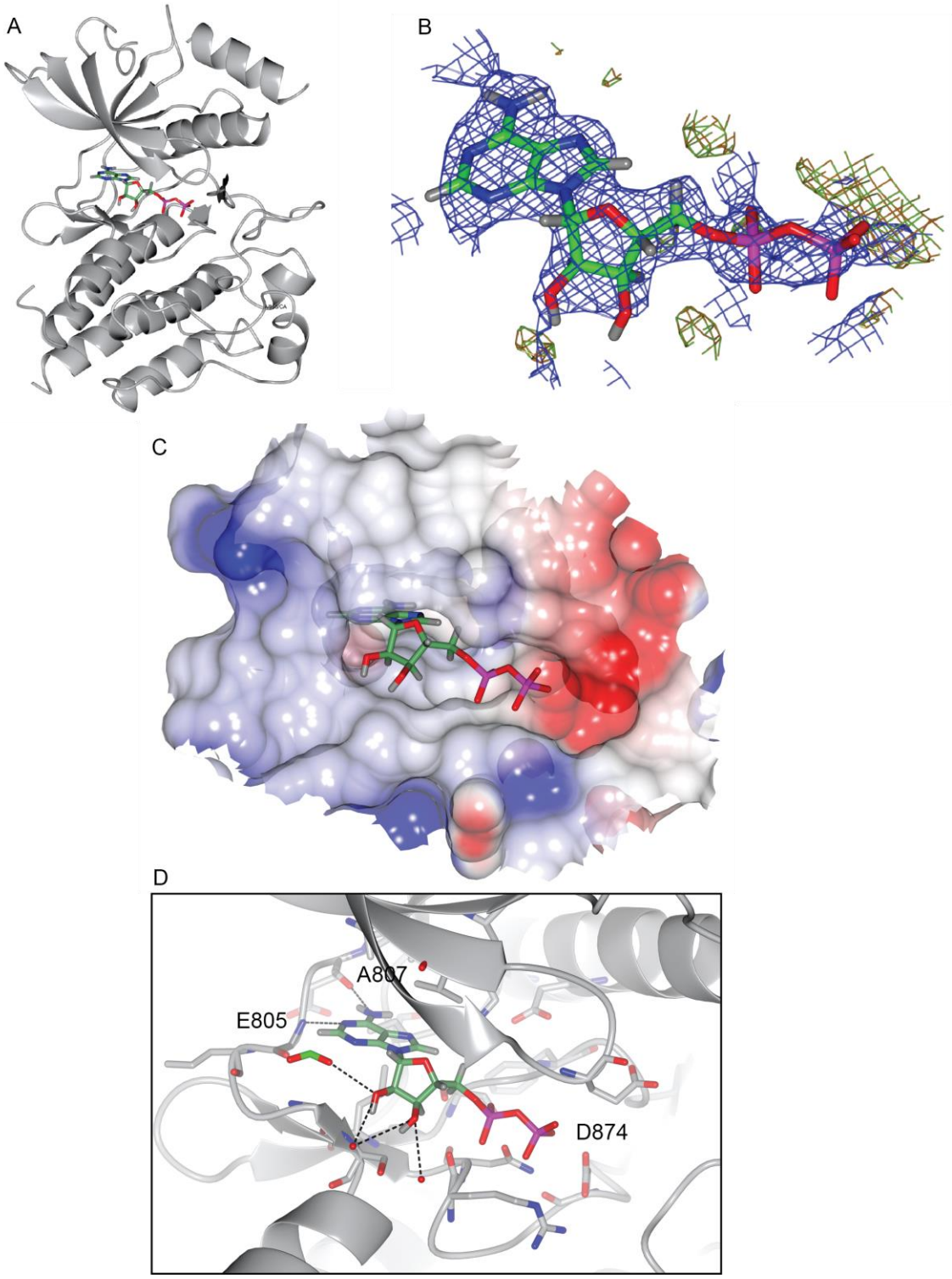

Figure 5.19 Structural characterisation of the RET KD-ADP complex

(A) Ribbon view of RET KD (light grey) with ADP bound to the nucleotide-binding pocket. **(B)** Difference (blue), positive (green) and negative (red) density maps surrounding ADP. **(C)** Electrostatic surface view of the ATP pocket with ADP sat within it. **(D)** Close-up of ADP within the nucleotide-binding pocket of RET (light grey). Key residues within the pocket have side chains visible (grey), with dotted lines indicating hydrogen bonds between ADP and side chains (dark grey) or solvent (red). ADP key: carbon – lawn green; nitrogen – blue; oxygen – red; phosphorus – purple.

It is possible that two distinct ATP binding modes exist: that captured in this particular RET KD-ADP complex and that of the canonical RTK GRL + ATP. Further validation of this RET KD-ADP structure is required. It was previously reported that the closed GRL conformation of RET involves the tethering of three residues – Glu734, Arg912 and Asp771 – through hydrogen bonds (Plaza-Menacho et al., 2014). Therefore, future investigations could examine the affinity of ATP towards both the wild type and mutant RET KD, or crystallisation of ATP (or a non-hydrolysable analogue) within the mutant RET KD could be attempted.

As seen in Table 5.6, the B-factor for ADP is currently much higher than the protein or solvent. When examining the individual atom B-factors, it became apparent that the α- and β-phosphates had B-factors double that of the rest of the molecule, with the ribose slightly higher than the adenine ring. This may be due to low occupancy of the α- and β-phosphates. Further refinement is required, reducing the occupancy of the phosphates, to determine the optimal ligand and position. This RET KD:ADP conformation may contain a collapsed GRL, influenced by the presence of the αN helix. Importantly, there are currently no main chain hydrogen bonds to the ADP phosphates, and Lys758 and Asp892 are too far away to contribute to the alignment of the ligand. Given their invariance in all RTKs, it would seem they should have a similar role in the binding of ADP to RET. A major difference when compared to other RTK:ATP structures is the current C4'-C5' torsion angle of the ribose (Figure 5.20a). Structures of ADP (or ACP) within EphrinB2, ALK (anaplastic lymphoma kinase) or FGFR display a distinctly different torsion angle that directs the phosphates back under the GRL towards the catalytically conserved Lysine residue. In the case of EphrinB2 and FGFR, the phosphates are interacting with both the Lysine and the GRL, and magnesium ions are present - elements thought to be required for the catalytic mechanism of a kinase (Hubbard, 1997).

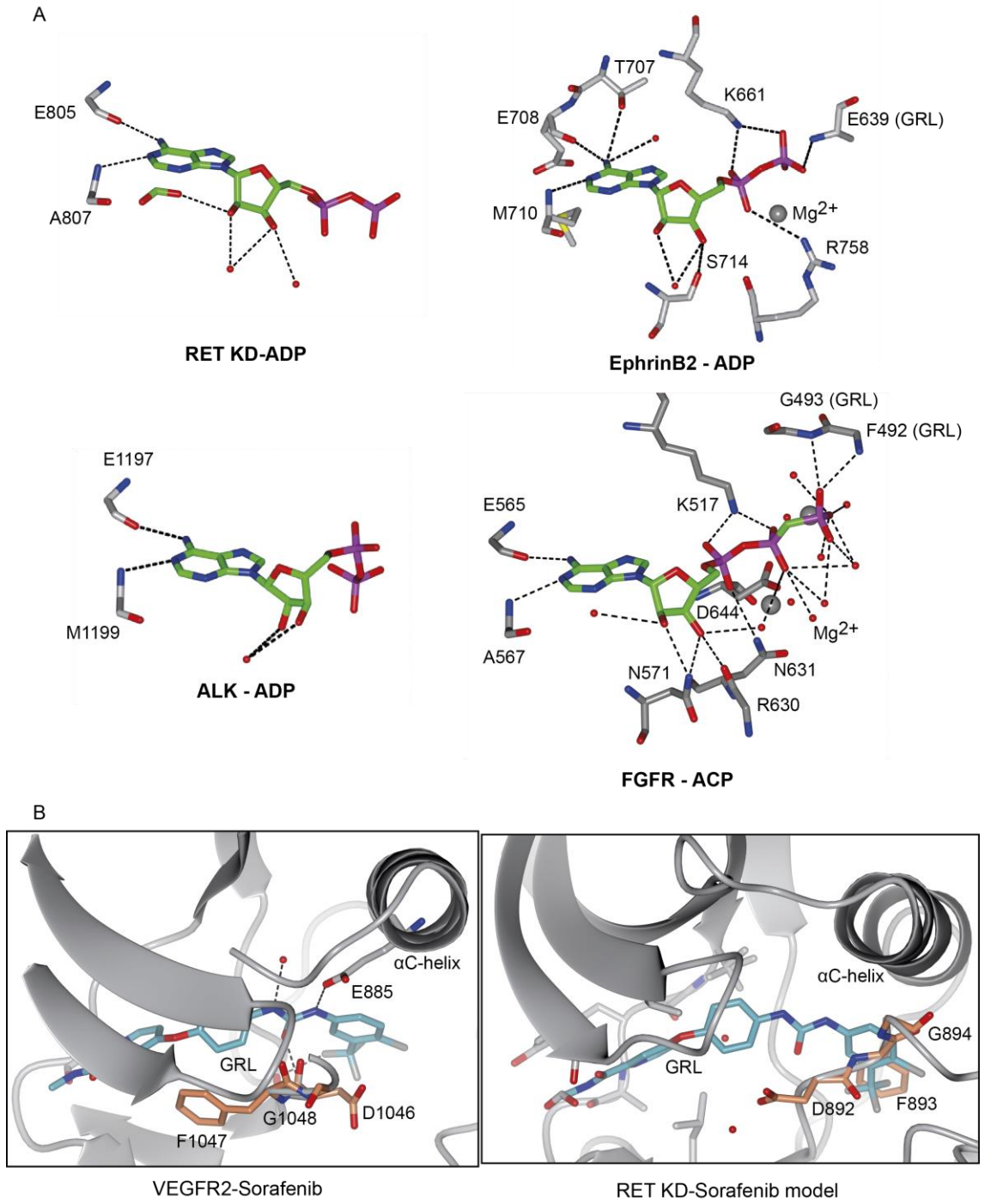

Figure 5.20 Comparisons of nucleotide binding and DFG conformation

(A) Comparisons of RTK-ADP binding. Key hydrogen bonds between ADP or ACP (Carbon - green; nitrogen - blue; oxygen - red; phosphorous - purple) and relevant regions of amino acids in RET KD, EphrinB2 (PDB code 2HEN), ALK (PDB code 3LCT) and FGFR (PDB code 2PVF). Magnesium ions are represented as grey spheres and solvent is represented as red spheres. Residues in the GRL are annotated as such. Hydrogen bonds not annotated: EphrinB2 magnesium forms hydrogen bonds with R758; FGFR magnesium forms hydrogen bonds with N631 and secondary phosphate. **(B)** The *DFG-out* conformation of VEGFR-2 bound to type II inhibitor Sorafenib (PDB code 4ASD) and the *DFG-in* conformation of RET (PDB code 2IVV) with Sorafenib from 4ASD modelled into the structure. The DFG motif (coral) is annotated.

It is unclear as to how ATP (hydrolysed to ADP) came to be present within the pocket, since the protein was washed after phosphorylation. It is possible that some residual ATP was still in the solution at the time of crystallisation. This crystal form has proved very useful in crystallising *DFG-in* type I compounds. However, despite many efforts it appears *DFG-out* type II inhibitors cannot be captured in the current crystal lattice. One explanation may be the presence of the vector-derived αN-helix (required for crystallisation of a *DFG-in* structure). Based on the structure of VEGFR2 bound to Sorafenib (Figure 5.20b), it is highly probable that the inhibitor will extend far into the back pocket in order to push out the DFG motif. As the vector-derived helix can be found behind the αC helix, its position may prevent the required conformational change from occurring - in RET's *DFG-in* conformation, Sorafenib would clash with Phe893. In solution, Sorafenib can bind (hence the large RET KD ΔT_m), but the position of the vector-derived helix within the crystal lattice may force the protein into its original conformation. This could eject Sorafenib from the nucleotide pocket, allowing ATP to re-bind in its place.

5.8 Structural characterisation of RET KD with S1 inhibitors

The RET KD was crystallised with five S1 inhibitors (as seen in Figure 5.1): I-1 (2.00 Å), I-7 (1.95 Å), I-8 (2.65 Å), I-9 (1.70 Å) and I-10 (1.80 Å). Crystals were also generated in the presence of Inhibitors I-6 and I-11, but compounds were not found within the active site (the monophospho-nucleotide cAMP was present in its place) and Tyr905 was phosphorylated. This is consistent with TSA data (Figure 5.12) data and will be discussed further in the next section.

All S1 inhibitor-bound structures have a closed GRL, with Phe735 folding back towards I-7, I-9 and I-10 (Figure 5.21). This may be the case for I-1 and I-8 also, but unfortunately the electron density for these two structures does not define the complete GRL. The scaffold occupies the one side of the nucleotide pocket towards the KD hinge, forming a hydrogen bond with the main chain of Ala807, with none of the inhibitors extending into the interior pocket (as seen for S2, S4 and *DFG-out* inhibitors). The non-planar 3D shape of the benzodiazepine scaffold can be seen to fold over the floor (Leu881 and Gly810) of the nucleotide cleft, forming

hydrophobic contacts with those residues and those in the ceiling – Val738, Ala756 and Leu730 (Figure 5.21d). I-10 is the only S1 inhibitor to contain an additional five-membered ring underneath the benzodiazepine scaffold. This ring appears to induce strain within the central ring system and shift the position of the benzyl ring. This appears to have no positive effect on inhibitor-residue interactions and results in a slightly lower RET KD thermal stability (seen earlier in Figure 5.12). Therefore, S1 may be more effective as a RET inhibitor without this five-membered ring.

The trifluoromethyl group found at the end of all S1 inhibitors – except for I-8 – appears to be flexible, as this portion of each inhibitor appears in different positions (Figure 5.21). I-8 induced the largest increase in RET KD thermal stability and lacks this group, suggesting that it hinders inhibitor binding. As an alternative, this portion of the S1 inhibitors could have a hydrogen bond acceptor – such as a carboxyl (COH) group – to interact with the Lys808 carbonyl group.

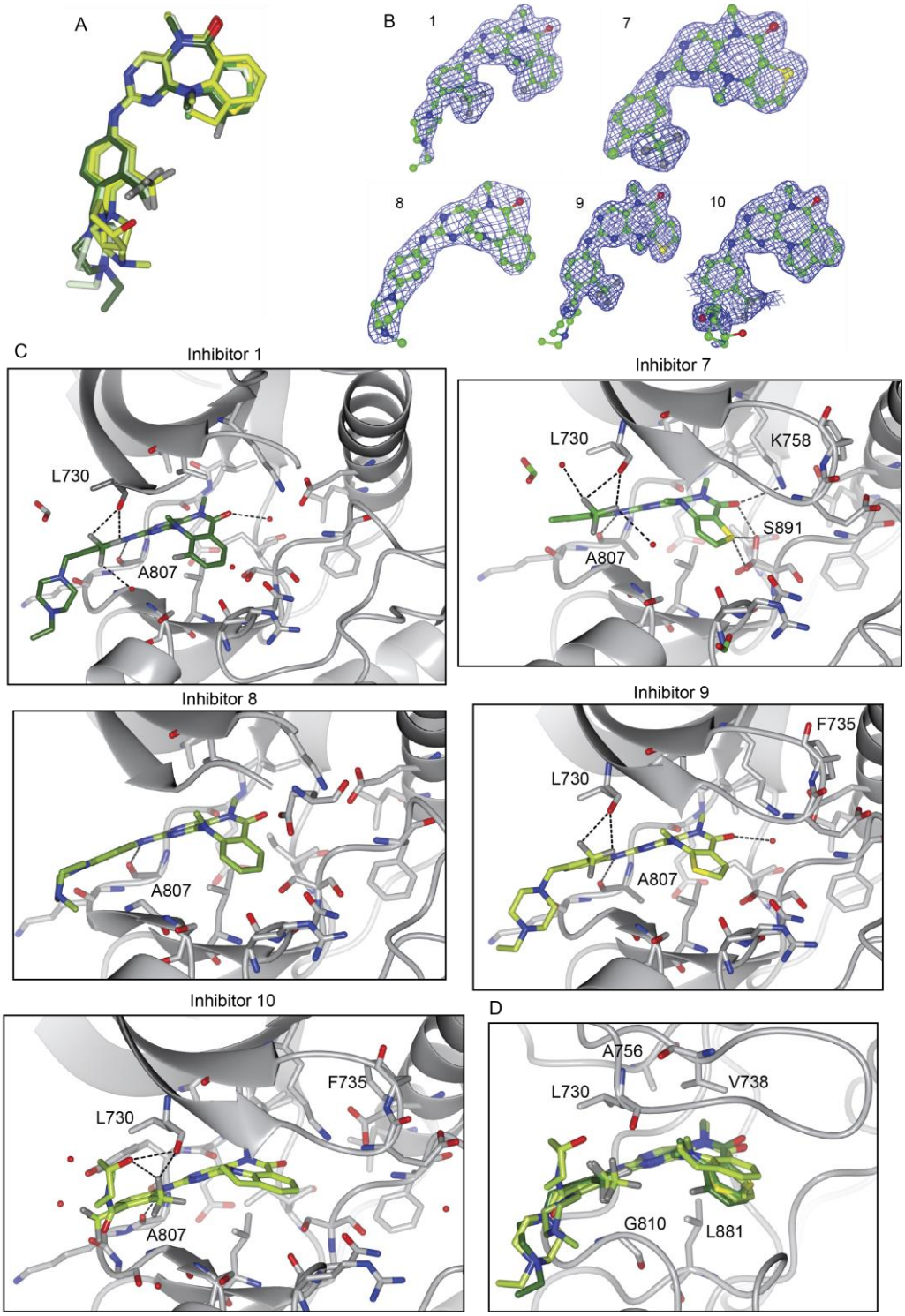

Figure 5.21 Structural characterisation of RET KD bound to S1 inhibitors

(A) Superposition of Inhibitors 1, 7, 8, 9 and 10, highlighting their related binding modes. I-1 – dark green; I-7 – lawn green; I-8 – lime green; I-9 – pale green; I-10 – yellow green. **(B)** Electron density (blue) surrounding each of the S1 inhibitors. Inhibitor number indicated for each image. **(C)** Close-up of each inhibitor within the nucleotide-binding pocket of RET. Key residues within the pocket have side chains visible (grey), with dotted lines indicating hydrogen bonds between the inhibitor (green) and side chains or solvent (red). **(D)** Superimposed inhibitors (green) within the nucleotide-binding pocket (grey ribbon), with Van der Waals contacts annotated.

5.8.1 Crystallisation of RET KD with S1 inhibitors 6 and 11

As the core scaffold within I-6 and I-11 is the same as that of other S1 inhibitors, the poor potencies and almost no increase in RET KD thermal stability indicates specific atoms within the scaffold may hinder RET-binding. For I-6, this may be due to the close proximity of the primary amine on the piperidine ring to Arg878 – clashing with this residue could prevent the inhibitor from being tolerated within the active site. The benzodiazepine system has been flipped – when compared to the other S1 inhibitors – so that the R7 carboxyl group would be directed towards the RET KD hinge (based on a model seen in Figure 5.22a). By doing so, the carbonyl interacting with a water molecule between the other S1 inhibitors and Glu775 is removed. As this water molecule appears relatively conserved within the structures, the bridge that it creates between the inhibitor and the back of the nucleotide-binding pocket may be important for inhibitor binding. I-6 also has an amide linker between the benzodiazepine system and the benzyl ring, which is not present for other S1 inhibitors. While the –NH group is likely to form a hydrogen bond with the RET KD hinge, the presence of an extra carboxyl group may hinder the inhibitor's ability to bind.

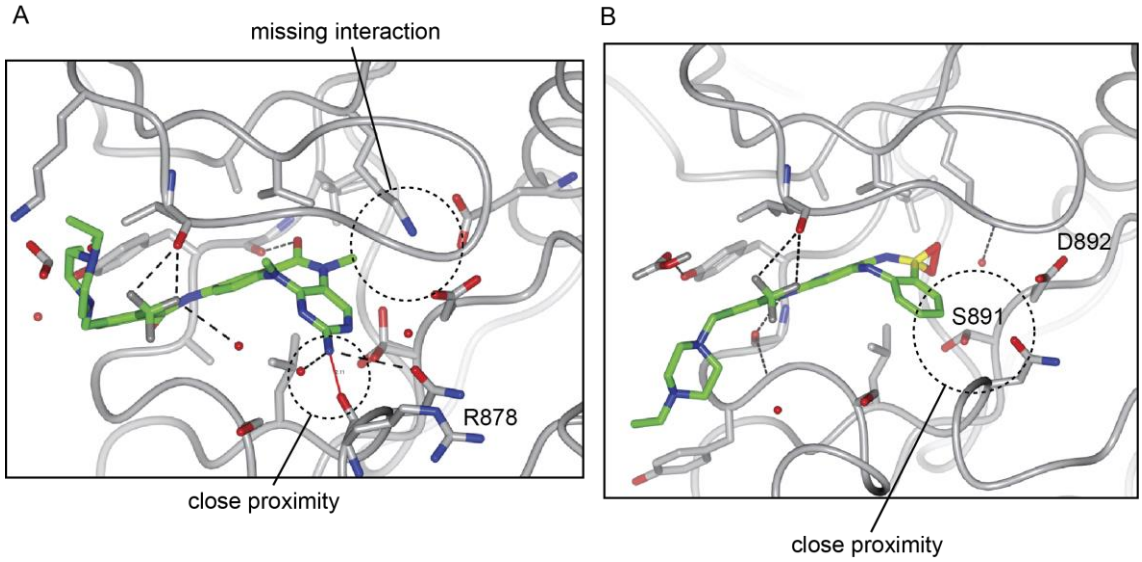

Figure 5.22 Modelling of the poor-affinity I-6 & 11 in the RET nucleotide-binding pocket
(A) Model of I-6 (green) fitted into the nucleotide-binding pocket of the RET KD (spaghetti view, grey), using the RET KD-I-7 PDB and superposition of I-6 with I-7. **(B)** Model of I-11 (green) fitted into the nucleotide-binding pocket of the RET KD (spaghetti view, grey), using the RET KD-I-9 PDB and superposition of I-11 with I-9.

While these observations are simply based on a model, I-5 – with which crystallisation has not been attempted – also contains the flipped benzodiazepine system and amide linker. This inhibitor (seen earlier in Figure 5.3) did not cause an increase in RET KD stability (Figure 5.12), suggesting that its ability to bind to RET KD is similar to that of I-6. This suggests that the points mentioned are in some way responsible for the lack of inhibitor potency and should be avoided in future designs. For I-11, the sulphoxide group on the benzodiazepine ring was intended to interact with the RET gatekeeper residue Val804 and was a hopeful compound for RET inhibition, due to data from collaborators showing that it did not inhibit the Aurora kinases AURKA and AURKB (the main off-targets). However, the sulphoxide group on the benzodiazepine group is very close to Lys758 and Asp892, which could also result in clashing and a prevention of inhibitor binding (Figure 5.22b).

5.9 Structural characterisation of RET KD with S2 inhibitors

The crystal structures of RET KD bound to I-4 and PP242 were obtained at resolutions of 2.6 Å and 2.26 Å, respectively. The binding mode observed for I-4 and PP242 is very similar to that found in the already crystallised RET KD-PP1 structure (PDB code 2IVV). The main pyrazolopyrimidine scaffold takes the position of the adenosine ring, with the extended rings shown in Figure 5.23a pushing into the interior pocket (Figure 5.23c). The left side of the pyrazolopyrimidine scaffold interacts with the kinase hinge, forming a hydrogen bond with the main chain of Glu805. This bond is highlighted in Figure 5.23 for PP242 and PP1, and is most likely present in I-4 but has not been indicated due to the slightly extended distance of 3.12 Å.

Electron density along the extended carbon bond in I-4, between the pyrazolopyrimidine scaffold and the benzene ring was very prominent, but weakened around the benzene ring itself, suggesting that the ring rotates within the interior pocket (Figure 5.23b). Unfortunately, the data was not of a high enough quality to define Lys758 or Glu775 – two important residues when examining inhibitors that extend into the interior pocket. While writing, datasets have been collected for the RET KD bound three other S2 inhibitors synthesised by the same

collaborator. The higher resolution obtained will hopefully help to define the position of these residue side chains. It is likely that I-4 also forms hydrogen bonds with the main chain of Glu805, as seen for the other two S2 inhibitors. Again, refinement of the new S2 inhibitor datasets will hopefully help to confirm this.

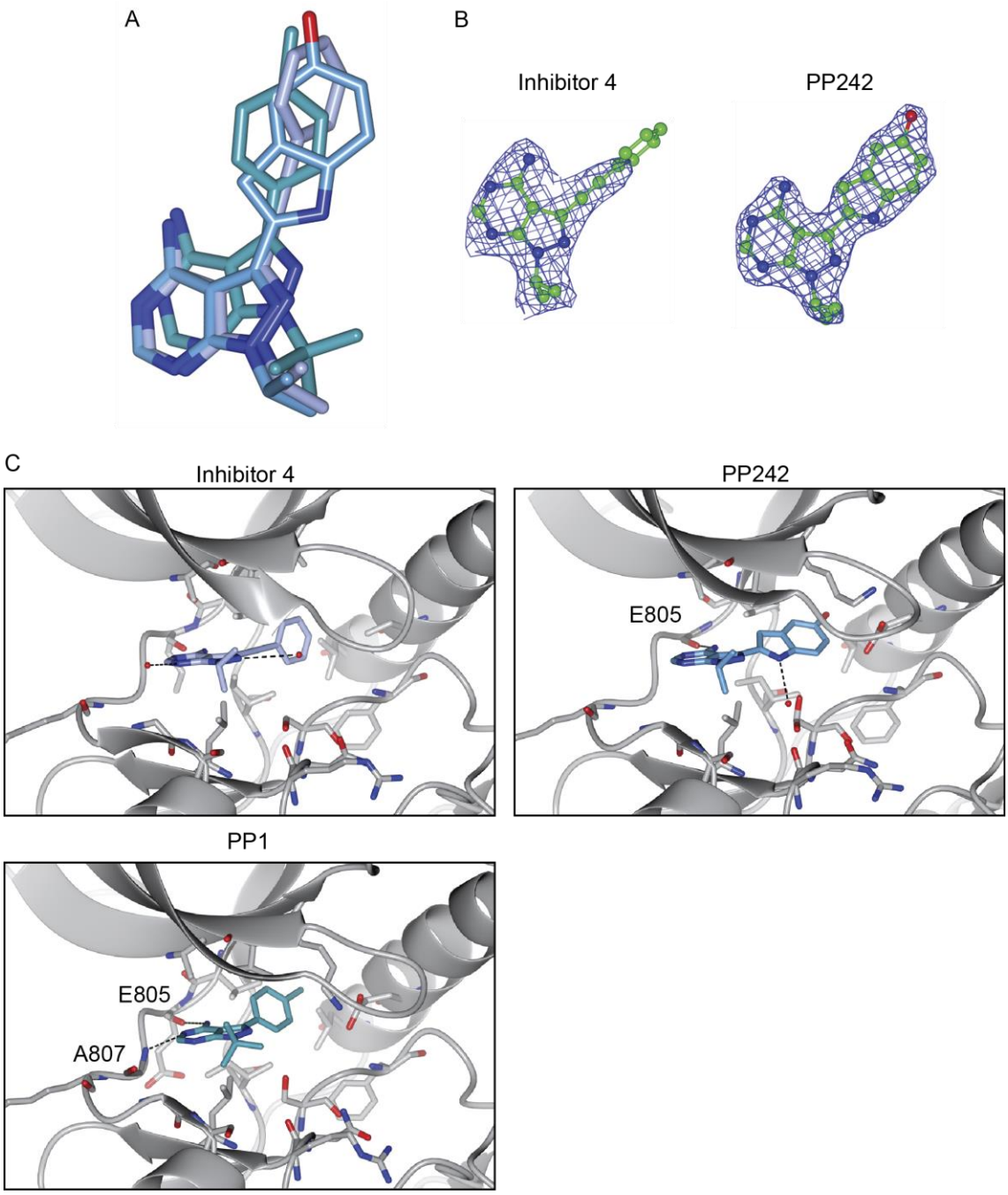

Figure 5.23 Structural characterisation of RET KD bound to S2 inhibitors

(A) Superimposition of I-4 (pale blue), PP242 (blue) and PP1 (cyan). **(B)** Difference electron density (blue) surrounding I-4 and 18, at a sigma level of 1.0. **(C)** Close-up of each inhibitor within the nucleotide-binding pocket of RET. Key residues within the pocket have side chains visible (grey), with dotted lines indicating hydrogen bonds between the inhibitor (green) and side chains (dark grey) or solvent (red). Hydrogen-bonding residues are annotated.

PP242 hydrogen bonds with the main chain of Glu805 and extends even further into the back pocket, with a phenol ring pointing towards Glu775. As mentioned earlier, the extension of this inhibitor actually displaces Lys758, disrupting the conserved salt bridge that forms between this residue and Glu775. Neither I-4 nor 18 appear to hydrogen bond with the main chain of Ala807 within the KD hinge, as seen with PP1.

5.10 Analysis of pre-solved structures of RET KD with S3 inhibitors

Dr Kerry Goodman previously solved the structure of the RET KD bound to Sunitinib in the McDonald Laboratory, while the structures of the RET KD bound to X2K, X2L and X2M were published in 2010. As shown in Figure 5.24, the inhibitors engage both Glu805 and Ala807 in the KD hinge. A noticeable difference between X2K, X2L and X2M is the lack of an amide group on X2M. It appears that this particular amide group in X2K and X2L hydrogen bonds with Asp892 (the first residue of the conserved DFG motif), an interaction that is lost when X2M is bound (Figure 5.24). Instead, Ser891 hydrogen bonds with a water molecule commonly found between an inhibitor at Glu775.

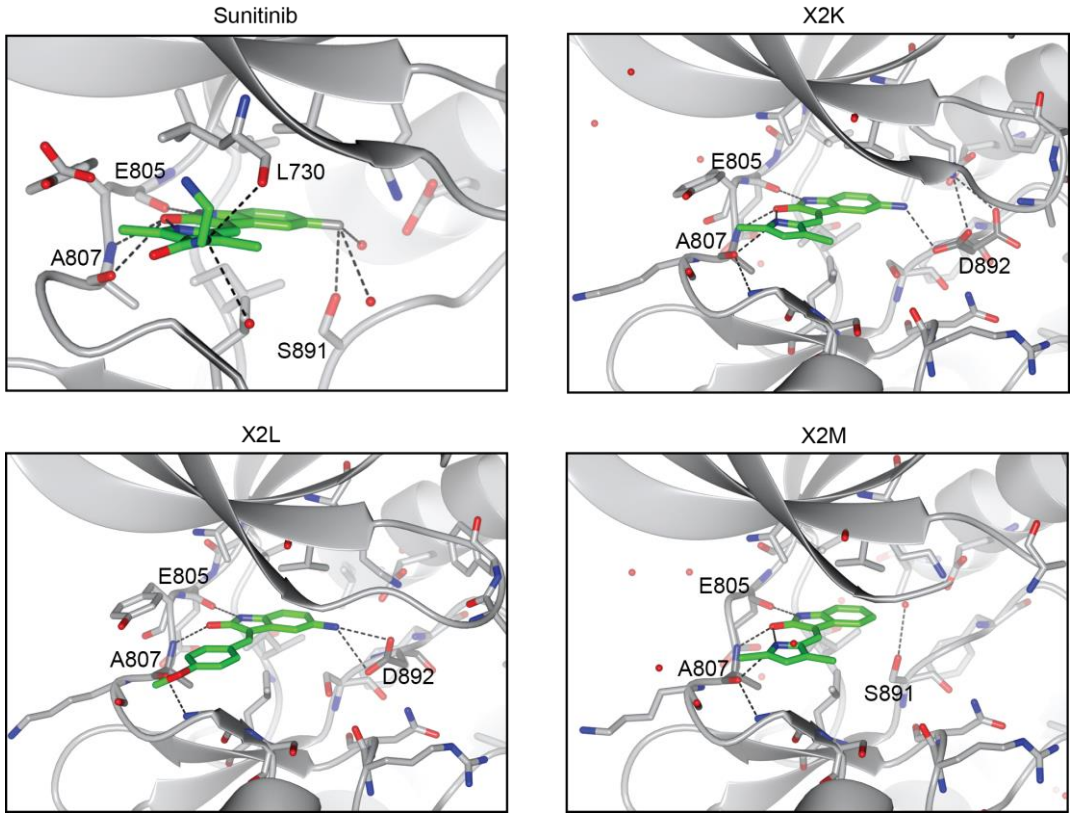

Figure 5.24 Structural characterisation of RET KD bound to S3 inhibitors

Close-up of each inhibitor (green) within the nucleotide-binding pocket of RET (grey ribbon). Key residues within the pocket have side chains visible (grey), with dotted lines indicating hydrogen bonds between the inhibitor and side chains (dark grey) or solvent (red). Hydrogen-bonding residues are annotated.

5.11 Structural characterisation of RET KD with S4 inhibitor

The RET KD-I-3 dataset (collected at a resolution of 2.45 Å) was found to be in the C2 space group, but with an extended c edge (doubled from 79.9 Å to 158.7 Å), allowing for two molecules within the asymmetric unit instead of the usual single dimer (converting the crystallographic dimer into a non-crystallographic one). The dataset was found to contain pseudo-translational non-crystallographic symmetry and was twinned (as reported using Xtriage). As a result, the Wilson B factor and $R_{work}/_{free}$ values reported in Table 5.6 are less reliable, as the values obtained from twinned data are not directly comparable to that of untwinned data. The inhibitor binding may have caused this twinning (especially as a large ΔT_m was observed, indicating there may have been some conformational change), but it also may have occurred during crystal cooling.

Structural comparisons of RET KD-I-3 and RET KD-Vandetanib highlight several differences within the ATP pocket (Figure 5.25). While Vandetanib hydrogen bonds with the KD hinge, it has not been indicated in Figure 5.25 due to the slightly extended bond distance (Knowles et al., 2006). I-3 is found to hydrogen bond with Glu775 in the αC helix. This is the only inhibitor found to extend far enough back to make this connection. Unfortunately, the side chain of Lys758 is disordered, so it is unclear as to what effect this interaction has on the position of the residue. It is possible that the disruption of the ion-pair between Glu775 and Lys758 by I-3 has led to the disorder of the lysine.

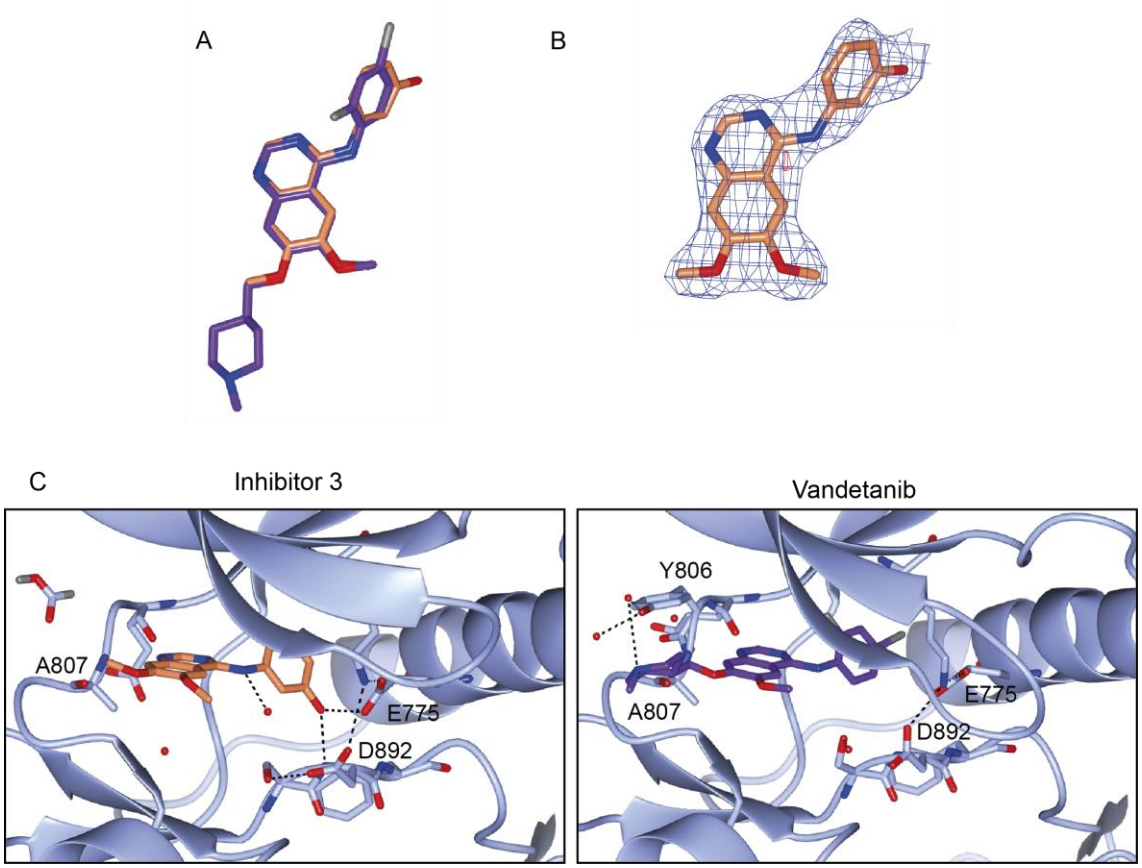

Figure 5.25 Structural characterisation of the RET KD bound to S4 inhibitors

(A) Superimposition of I-3 (light coral) and Vandetanib (purple). **(B)** Difference electron density (blue) surrounding I-3 ligand. Sigma = 1.0. **(C)** Close-up of each inhibitor within the nucleotide-binding pocket of RET. Key residues within the pocket have side chains visible (grey), with dotted lines indicating hydrogen bonds between the inhibitor and side chains (dark grey) or solvent (red). Hydrogen-bonding residues are annotated.

5.12 Structural characterisation of RET KD with S5 inhibitor

Based on the earlier TSA data (Figure 5.12), BMS-536924 was believed to be a type II inhibitor, due to the fact that the shift in RET KD stability in the presence of the compound was very similar to that of *DFG-out* compound Sorafenib. The scaffold adopted by BMS-536924 is also similar to another *DFG-out* compound designed by our collaborators in Arizona: Pz-1 (structure not shown). Efforts to crystallise the RET KD with both Sorafenib and Pz-1 have been unsuccessful so far, while BMS-536924 was captured within the nucleotide-binding pocket.

The structure of RET KD bound to BMS-536924 was obtained at a resolution of 2.3 Å. While the majority of RET KD datasets have been collected in the monoclinic C2 space group, the dataset for RET KD bound to BMS-536924 was collected in the tetragonal $P4_32_12$. As seen in Table 5.6, the ligand B-factor is rather high, indicating that further refinement is required – possibly with reduced occupancy on portions of the ligand – to be sure of the ligand geometry. The different space group suggests slightly altered packing of the protein molecules within the crystal lattice, which may have been induced by BMS-536924 binding. Instead of adopting a *DGF-out* binding mechanism, the inhibitor appears to fold around to the otherwise unoccupied catalytic region of the pocket (Figure 5.26).

Electron density surrounding the final aromatic ring of BMS-536924 is particularly weak, and further refinement may be required to be completely confident of its position. While this S5 inhibitor may be presenting a subtly different binding mode, it is also possible that its position has been affected by the presence of the vector-derived αN-helix required for RET KD crystallisation. As mentioned previously, this helix sits behind the αC-helix that contains the residues lining the back of the ATP pocket, including the DFG motif. It is possible that in solution, BMS-536924 induces a *DFG-out* conformation (consistent with the high shift in RET KD thermal stability) that is prevented within the crystal lattice by the αN-helix. Structures of the RET KD with Sorafenib and Pz-1 may not have been achieved thus far due to their inability to bind within the pocket in a mode other than *DFG-out*. Possible strategies for overcoming this are discussed later in the chapter conclusion.

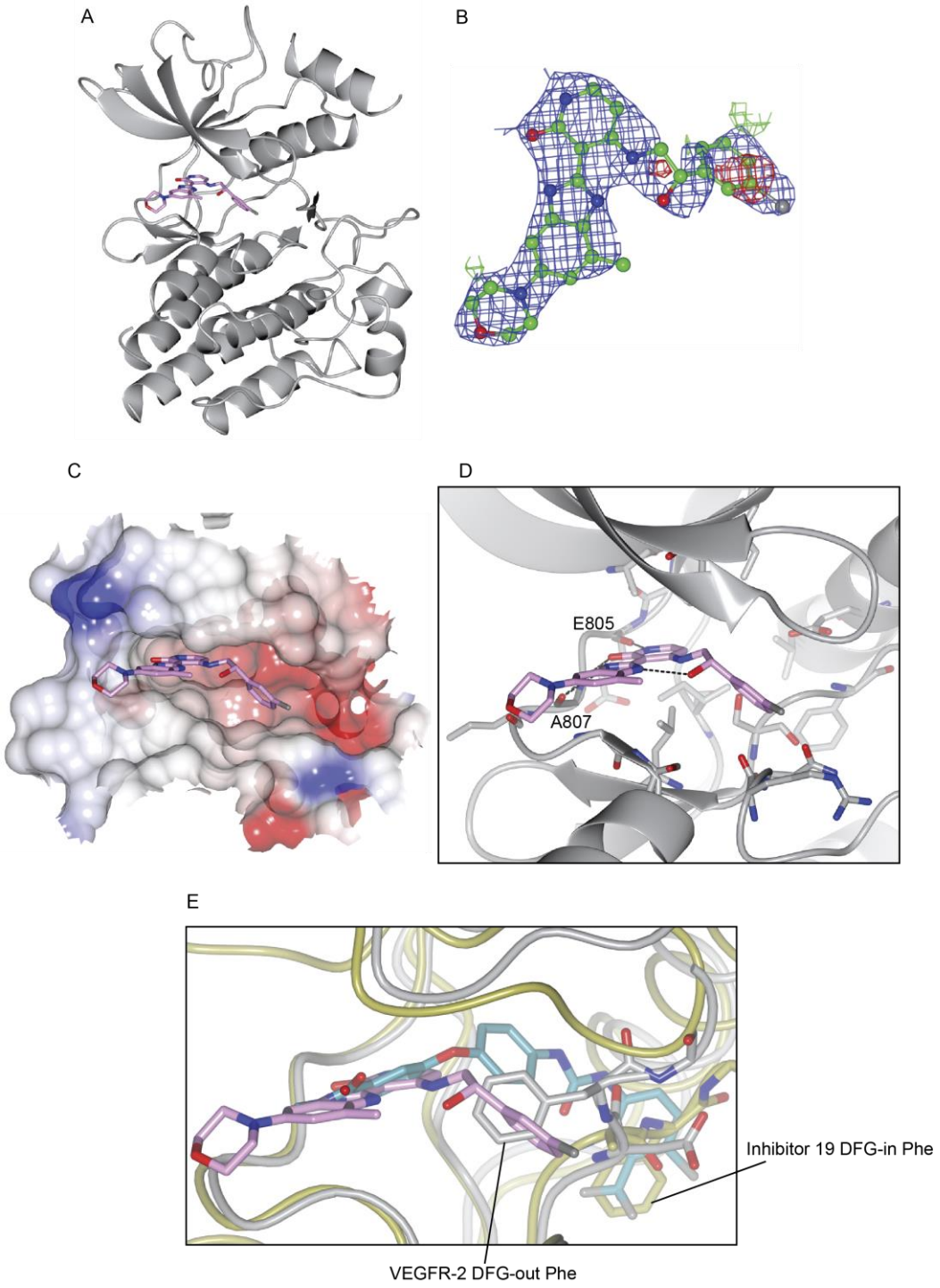

Figure 5.26 Structural characterisation of the RET KD bound to BMS-536924

(A) Ribbon view of the RET KD (grey) with BMS-536924 (pink) within the ATP pocket. **(B)** Electron density (blue) and difference density (red/green) around BMS-536924, Sigma = 0.8. **(C)** Electrostatic surface view of the RET ATP pocket with BMS-536924 (pink). **(D)** Close-up of BMS-536924 within the nucleotide-binding pocket of RET. Key residues within the pocket have side chains visible (grey), with dotted lines indicating hydrogen bonds between the inhibitor and side chains (dark grey). **(E)** Comparison of BMS-536924 (pink) binding in the RET (gold) ATP pocket with Sorafenib (light blue) binding into the VEGFR-2 (gold, PDB code 4ASD) ATP pocket. BMS-536924 clashes with the DFG motif of VEGFR-2, while Sorafenib clashes with the DFG motif of RET.

5.13 Development of an updated RET inhibitor pharmacophore

As discussed in the introduction, there are several RET inhibitors currently being used to treat thyroid cancer but their multi-target effects are less than optimal. Due to the conserved nature of the tyrosine kinase nucleotide-binding pocket, a great deal of inhibitors lack specificity. Therefore, structure-activity relationship (SAR) data is collated and analysed to ensure that future generation inhibitors focus on what are believed to be the most important characteristics.

A pharmacophore is a description of structural features that are deemed necessary for target-protein binding. Once developed, current databases – such as the Kinase KnowledgeBase database (Eidogen-Sertanty Inc.) – can be searched for existing inhibitors that contain those particular atoms in a specific geometry. There are several sources of information that can be used to create a pharmacophore. Firstly, X-ray derived structures provide information on hydrogen bonding opportunities. While the hydrophobicity of the protein primarily defines the region of inhibitor-protein binding, hydrogen bonds within the region lead to binding specificity. Structures provide information on the geometry on the inhibitor itself, an important feature that is used in rational drug design to select compounds that meet particular geometric criteria. X-ray structures also allow us to create a picture of the active site itself, identifying key residues in inhibitor binding and highlighting regions of inhibitor interaction (for example, the hydrophobic interior pocket of the nucleotide-binding region). This information can be combined with biochemical data reporting the *in vitro* and *in vivo* effects of the compounds against particular targets (Yang, 2010). In 2011, Shih et al. published a RET pharmacophore model. In this model, inhibitors should contain one hydrogen bond acceptor, one hydrogen bond donor, one hydrophobic and one aromatic ring. They compared the SAR information on 76 inhibitors from the Kinase KnowledgeBase database and used the 3D-QSAR Pharmacophore Generation technology to create computational pharmacophore hypothesis models. The inhibitors presented in this thesis adhere to this optimal pharmacophore model, but still differ greatly in terms of potency. In order to understand these differences, the areas of the RET nucleotide-binding pocket targeted by each inhibitor were examined.

In this thesis, information from the X-ray derived structures of 15 compounds (I-1, I-3, I-4, I-7, I-8, I-9, I-10, PP242, BMS-356924, PP1, Vandetanib, Sunitinib, X2K, X2L, X2M) was combined to highlight key residues (those that may be necessary for inhibitor binding) and identify differences between scaffold binding modes (Figure 5.27). Key residues within the ATP pocket were defined as those within 4 Å of each inhibitor (Figure 5.27a); the number of possible interactions (within 4 Å) that residue could make with each inhibitor were then counted and entered into the cluster analysis program Cluto (http://www.cs.umn.edu/~cluto). Clustering algorithms allow datasets to be divided into meaningful groups, so that similarity within a group is maximised and the similarity between different groups is minimised. Initially, a heat map was generated, highlighting areas within the pocket that had a high and low prevalence of inhibitor interaction (Figure 5.27b). Following this, the datasets were reanalysed with the request of separating into five clusters: one for each inhibitor scaffold (Figure 5.27c). Analysis was carried out using the “vcluster” clustering program within Cluto, which uses a “repeated bisection” algorithm. The algorithm first splits the data into two groups, and then a further two – this process is continued until the number of defined clusters (five, in this case) is reached.

Figure 5.27b highlights residues that are consistently involved in ligand binding, irrelevant of the scaffold – such as Leu881 in the floor of the pocket or Leu730 in the roof – while enabling comparison between the scaffolds themselves. Val804 and Glu775 in the back pocket region are interacting with both S2 (I-4, PP242 and PP1) and S4 (I-3 and Vandetanib) compounds, while appearing less involved in S1, S3 and S5 binding. As shown in Figure 5.27c, S1 inhibitors I-7, I-8 and I-9 were clustered together, as were S2 inhibitors PP1 and I-4, and S3 inhibitors Sunitinib, X2K, X2L and X2M. The divergence between S4 and 5 inhibitors may indicate subtle differences between the inhibitors, or the dataset may need to be built upon to ensure correct clustering. For future development, this information will be combined with hydrogen bonds, TSA data, IC_{50} data from each collaborator and known off-targets.

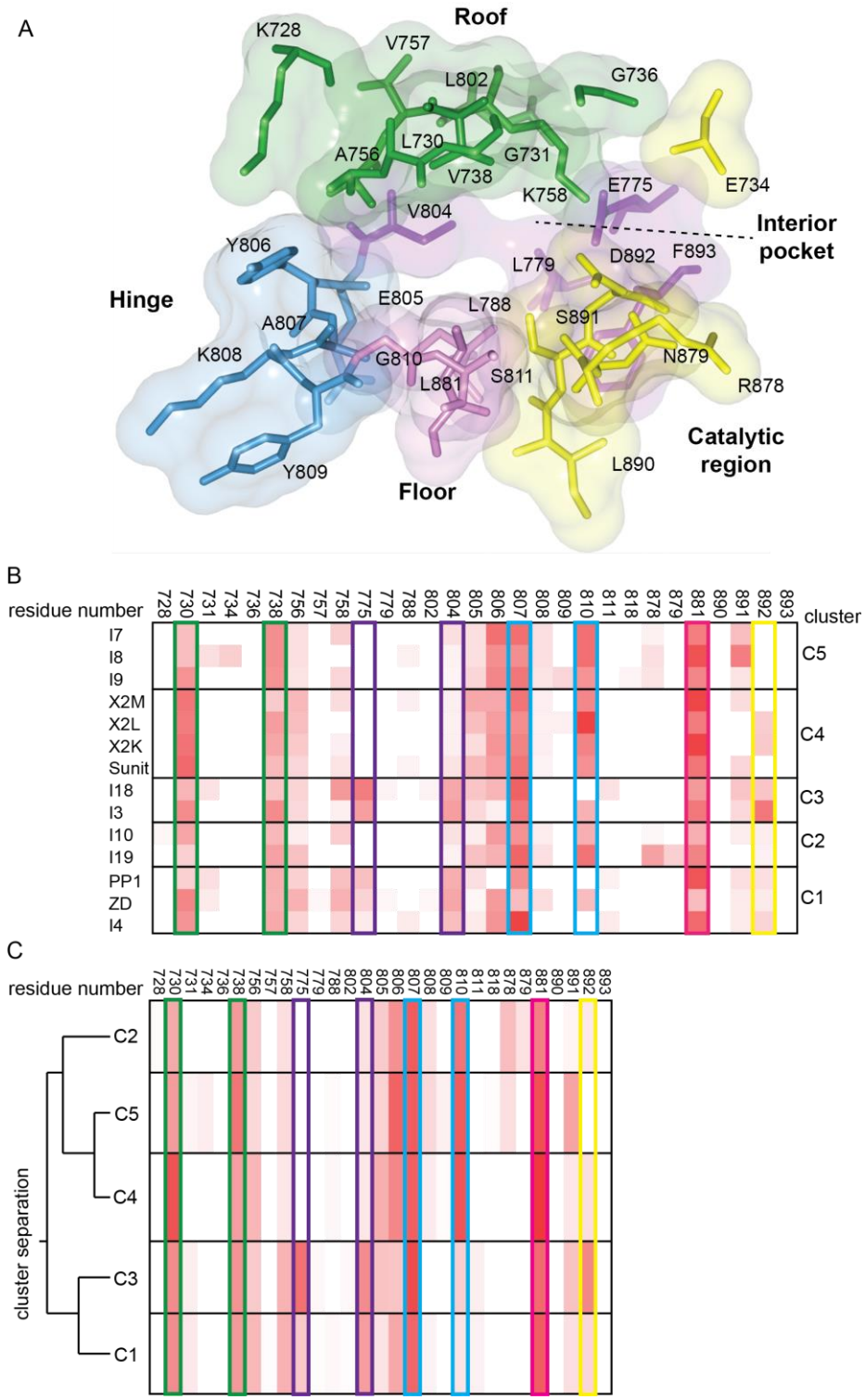

Figure 5.27 Towards a better RET pharmacophore

(A) View of the RET nucleotide-binding pocket with the side chains of the key residues (Hinge – light blue, back pocket - purple, right side - yellow, roof - green, floor - pink.) **(B)** Heat map displaying the number of possible interactions each inhibitor can make with each key residue (Red – high prevalence, white – low prevalence). **(C)** Heat map with separations of inhibitors into five clusters, based on the repeated bisection clustering algorithm carried out by the vcluster Cluto program. The tree indicated similarity between the clusters: those separating early are furthest apart.

5.14 Conclusions

In this chapter I have presented the crystal structures of the RET KD bound to nine compounds that have been developed for RET or similar RTK inhibition. I have collated this data with the previously solved structures of the RET KD bound to Sunitinib, X2K/L/M, Vandetanib and PP1 and have identified various RET-binding modes based on five distinct compound scaffolds. I have also presented the crystal structure of the RET KD bound to ADP, revealing the unexpected closed conformation of the GRL.

5.14.1 Determining the physiological relevance of the RET KD-ADP structure

Repeated X-ray analysis of older RET KD-ADP crystals lead to the discovery of adenosine within the nucleotide-binding pocket, confirming that ADP is present in the RET KD-ADP structure and suggesting that hydrolysis occurs over time. This structure currently does not appear to contain magnesium – an important element in ATP-KD binding – and future work will need to be carried out in order to identify whether this is a physiologically relevant arrangement of ADP within the active site of RET. Firstly, a higher resolution dataset (under 2 Å) may reveal the presence of magnesium within the active site. The protein could also be crystallised with manganese as a substitute for magnesium, as the Mn2+ ion has a larger ionic radius of 0.9 Å and crystals could be analysed using SAD (single wavelength anomalous dispersion) to determine the presence of manganese within the protein. The structure may be forced into a collapsed GRL conformation influenced by the presence of the αN helix. The phosphates currently do not engage with the GRL and important catalytic residues Lys758 and Asp892 are not involved in the positioning of the ligand, as they are in other kinase-ATP structures. As such, this structure requires further validation.

5.14.2 Examining RET KD stability using TSA

This thesis presents TSA data analysing the effect of various compounds on the thermal stability of the RET KD. Strikingly, the inhibitors believed to target the *DFG-out* conformation of RET induced an extremely large thermal shift of approximately 20 °C. This could be due to the flipped DFG motif pushing against the αN helix and

forcing it into an alternative conformation. A larger array of *DFG-out* inhibitors will confirm whether this technique is effective in identifying this particular binding mode. If so, TSA could be carried out in order to assess whether crystallisation (currently only possible with the RET KD in the *DFG-in* conformation) would be successful.

A large number of the inhibitors did not induce a thermal shift larger than that of ATP/Mg2+. While we know from the crystal structures obtained that the inhibitors can compete with ATP and bind within the nucleotide-binding pocket of RET, TSA should be repeated in the presence of ATP/Mg in all samples. This experiment will confirm that the compounds have indeed taken the place of ATP. It could be argued that the inhibitors that increase thermal stability more than ATP would be the most optimal; but it is currently unclear as to whether the large shift in thermal stability in the presence of Sorafenib and Pz-1 is due to a more stable protein or a conformational shift of the αN helix. To investigate this, the experiments could be repeated with the RET JM-KD recombinant protein that does not contain the vector-derived αN helix.

Current TSA experiments have all been carried out using the WT RET KD. While this is still physiologically relevant, due to the reports of RET overexpression in cancer, it would also be interesting to examine the effects on oncogenic RET KD mutants such as MEN2B M918T. It has been reported that the oncogenic form of the protein is less stable than the WT and has a higher affinity for ATP, therefore compounds may illicit different effects (Plaza-Menacho et al., 2014). At the time of writing, the RET KD M918T expression construct was in production.

5.14.3 Chemical scaffolds targeting RET oncogenic gatekeeper mutations

Missense mutations of the RET gatekeeper residue (Val804) for bulky hydrophobic residues Leu and Met are oncogenic and found in MEN2 disease. These MEN2-associated mutations render several inhibitors – such as PP1 and Vandetanib – ineffective. This is presumably because such inhibitors need access to the interior hydrophobic pocket of the kinase and access would be restricted or blocked by such mutations (Figure 5.28). The mutation of Val804 to the smaller residue glycine actually renders the inhibitors PP1 and Vandetanib more potent (Carlomagno et al.,

2004). S1 inhibitors do not require access to this region, as they sit at the front of the nucleotide-pocket. It would therefore be interesting to assess their activity against RET gatekeeper mutants, raising possibilities for combination therapies. While other inhibitors may be more potent at the start of therapy, S1 inhibitors could be subsequently used to target RET mutations that select for gatekeeper mutant-dependent resistance. Alternatively, S1 and S2 inhibitors could be used in combination therapy.

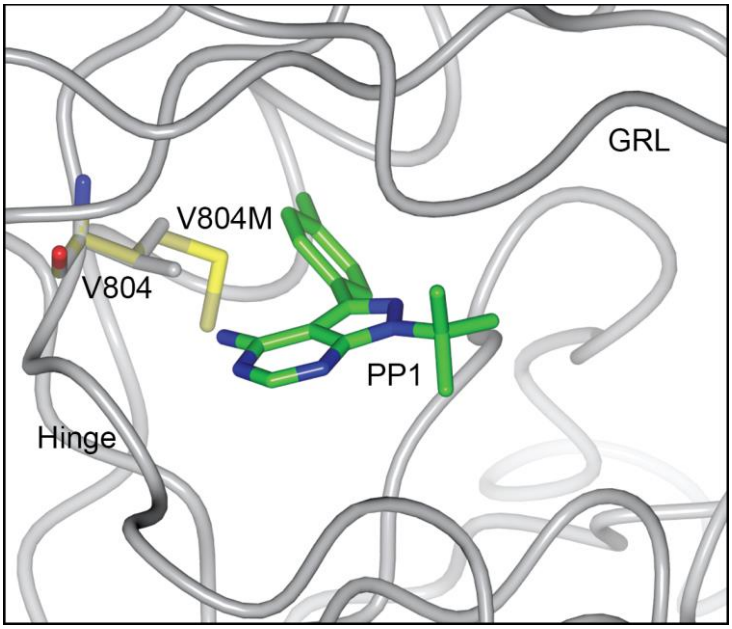

Figure 5.28 Modelling of inhibitor resistance through the RET gatekeeper mutation
Mutation of Val 804 (grey) into Met (gold) or Leu results in reduced access to the hydrophobic back pocket within the nucleotide-binding pocket of RET. This MEN2-associated mutation leads to drug resistance, as many inhibitors (PP1 shown here, green) require access to this pocket.

5.14.4 Towards a surrogate crystallisation platform for *DGF-out* inhibitors against RET

To date, capturing the inactive *DFG-out* conformation of RET in complex with a type II inhibitor has been unsuccessful. It is currently assumed that this is due to the position of the vector-derived αN-helix, preventing any movement in the DFG motif. This conformation of RET is extremely interesting, especially given the potential increase in thermal stability caused by *DFG-out* inhibitors. In order to investigate this further, it may be necessary to crystallise the protein without this αN-helix. There are several strategies for this: RET KD constructs could be

produced with deletions of increasing portions of the αN-helix, in an attempt to find the minimal amount of helix required; an inhibitor could be added during RET KD (without the αN-helix) expression, in an attempt to stabilise the protein; crystallisation of the RET juxtamembrane region (JM) -KD bound to a *DFG-out* inhibitor is currently being attempted within the laboratory, as this does not contain the αN-helix and is known to crystallise. This process will require rescreening for new crystallisation conditions. Other RTKs have been crystallised with Sorafenib, such as VEGFR-2. In the case of VEGFR-2, the structure of the JM-KD in complex with Sorafenib has been elucidated, demonstrating the *DFG-out* conformation (McTigue et al., 2012). As this crystallisation platform now exists, it would be possible to examine the binding mode of inhibitors that are known to target RET and are believed to bind to the *DFG-out* RET conformer. The similarities between the VEGFR-2 and RET nucleotide-binding pocket would allow the confirmation of RET-inhibitor binding modes (i.e. *DFG-in* or *DFG-out*) and provide insight into possible interactions.

5.14.5 RET inhibition vs. mTOR toxicity

It has been reported that mTOR inhibitors can cause MAPK pathway activation, due to a feedback mechanism depending on the S6K-PI3K-Ras pathway (Carracedo et al., 2008). It was shown that chemical inhibition of the MAPK pathway enhanced the anti-tumoral effects of mTOR inhibition *in vitro* and in a mouse model. This suggests the need for either RET inhibitors that do not target mTOR, or combination therapy with MAPK inhibitors. The structure of RET KD-PP242 showed that the inhibitor breaks the conserved salt bridge between Lys758 and Glu775, a structural element required for the catalytic mechanism of the kinase. While this indicates that PP242 is an effective RET inhibitor, its potency against mTOR could be problematic. Recently, a series of inhibitors based on both S2 and Sorafenib structures have been designed to “dial-out” the mTOR inhibition (Dar et al., 2012). They identified – using a *Drosophila* model – that optimal MEN2B treatment would require the inhibition of RET, Src, S6K and Raf, but not mTOR. The novel inhibitors – whose structures suggest a *DFG-out* binding mode – were shown to inhibit tumour growth with far lower levels of toxicity.

Chapter 6. Discussion

In the preceding chapters, I described results from investigations into two poorly understood molecular properties of RET - how it attains a functional native fold appropriate for export and how its enzymatic function can be chemically inhibited. Both properties have relevance to RET-driven disease. Understanding the maturation and export of wild type and HSCR RET raises the possibility of restoring HSCR RET function in cell-lines and potentially in models of HSCR. Defining an improved pharmacophore for RET by comparing a range of crystal structures of chemical scaffolds that all target the RET nucleotide cleft may lead to a new generation of more selective and potent RET inhibitors for the treatment of RET-associated cancers. In the sections below, I have summarised the findings of each chapter and suggested strategies for future investigation.

6.1 Characterisation of RET export and efforts to restore HSCR RET function

6.1.1 Summary of findings

Chapter 3 presented a description of the characterisation of RET maturation and export for both WT and S100M RET, using biochemical and cell-based methods. Previous work implementing a surrogate RET ectodomain secretion assay showed that mild HSCR RET mutations (represented in this thesis by the mutant S100M RET) were not exported to the cell surface (Kjaer et al., 2010). This chapter confirmed and extended these findings, using FACS and immunofluorescence analysis, to convincingly demonstrate that S100M RET accumulates predominantly as an immature intracellular species, presumably retained within the ER. Western blot analysis of the MAPK signalling pathway indicates a loss of ERK1/2 phosphorylation in S100M RET expressing cells in the presence of ligand and co-receptor, suggesting that the absence of the receptor at the cell surface results in a complete loss of ligand-stimulated signalling capabilities.

Kjaer et al. also presented data indicating that restoring proper maturation and export of the mild S100M HSCR mutation - within a RET ECD context - also

restored ligand and co-receptor binding function (Kjaer et al., 2010). Proper maturation was also restored in a full-length S100M HSCR context but the signalling capabilities of this mutant receptor were not examined further. Chapter 3 presents two strategies for successfully restoring S100M RET maturation and export: the deletion of unpaired cysteine residues from CLD1-2 (previously reported in (Kjaer et al., 2010) or alternatively by the addition of chemical chaperones 4-PBA and glycerol. The signalling capability of mature and exported S100M RET under both of these conditions still needs to be fully investigated in the near future.

The chapter presents preliminary investigations into the effect of gene silencing on WT RET export. ERp44 (involved in thiol-mediated ER retention) knockdown leads to a reduction in WT RET cell surface levels, while ATP6V0C (V-ATPase subunit) and RAB7A knockdown lead to an increase in WT RET cell surface levels. Previous reports (using chemical inhibitors) suggested that V-ATPase inhibition affects RET maturation but not cell surface levels (Hirata et al., 2010). Taken together these findings suggest that the role of V-ATPase in endocytosis and the role of both V-ATPase and Rab7 in lysosomal degradation is to negatively regulate the level of WT RET at the plasma membrane.

6.1.2 Implications of chapter 3 and the future investigations

Work within this chapter has confirmed that a mild HSCR mutant RET does not reach the cell surface and cannot therefore activate downstream signalling pathways. Several strategies for increasing cell surface expression levels have been identified, although it is currently unknown as to whether this can translate into a restoration of full downstream signalling capabilities. I have established a system for examining RET export and function outside of an endogenous setting, using robust inducible Flp-In mammalian cell lines. A series of HeLa Flp-In cell lines expressing S100M* RET have been produced during the writing of this thesis, and future investigations should establish the signalling capabilities of WT, S100M and S100M* RET using the HeLa Flp-In system. To do this, Flp-In cells would be incubated with recombinant GDNF-GFRα1 ligand and probed for RET auto-phosphorylation. It should be noted that it is well documented that transfected cell lines expressing RET are notoriously difficult to obtain a robust GDNF-induced

RET activation because of the high level of basal RET autophosphorylation. However, the Flp-In cells overcome this problem and will be a useful tool for researchers working on RET signal transduction. Cells expressing WT, S100M and S100M* RET can also be assessed for downstream pathway activation by western blot analysis, examining the phosphorylation state of ERK1/2, Akt or STAT3 components of discrete signalling pathways. Future work could also examine the hypothesis that acquisition of Cys87 and Cys216 (the two unpaired cysteine residues removed in S100M* RET) in higher vertebrate RET evolved to reduce the level of RET at the cell surface. Mutations within the RET receptor leading to the presence of these two cysteine residues may have occurred randomly, followed by positive selection. The establishment of inducible cell lines expressing both oncogenic (e.g. M918T RET) and WT* RET would allow comparisons to the WT protein and identify differences in the effect of each RET species expression of cell viability, differentiation or proliferation.

6.2 The preliminary identification of factors involved in WT and HSCR RET export and degradation

Chapter 4 described the development and implementation of an immunofluorescence-based gene silencing assay in RET expressing Flp-In cells. The assay was designed to identify factors involved in the folding, export and degradation of the RET receptor. The 300-candidate siRNA screen was carried out on DLD-1 cells expressing both WT and S100M RET, with a total of 30 genes identified as involved in the regulation of WT or S100M RET cell surface expression. Six genes were implicated in the negative regulation of both WT and S100M RET surface levels; four genes were implicated in the negative regulation of WT RET levels; six genes were implicated in the negative regulation of S100M RET levels only; 14 genes were implicated in the positive regulation of WT RET levels alone. These hits were clustered into known cellular pathways; namely, ERAD, endocytosis and lysosomal degradation, autophagy and protein folding and quality control. Due to the way the screen was performed, we cannot comment on whether factors positively influencing WT RET levels also affect S100M RET in the same manner. I discuss below some of the most interesting hits identified, the

specific pathways they are involved in and future validation experiments required for each.

6.2.1 The E3 ligase CHIP as a putative regulator of both WT RET cell surface expression and HSCR RET degradation

E3 ligases are potential negative regulators of many cell surface receptors and individual gene knockdowns for members of this protein family were anticipated. A top hit from screen was the CHIP E3 ligase (also known as STUB1), previously implicated in both the regulation of oncogenic protein expression and the degradation of misfolded proteins (Murata et al., 2001, Zhou et al., 2003). This protein was identified as a hit in both WT and S100M RET siRNA screens as gene knockdown resulted in increased cell surface levels of WT and mutant forms of the receptor. CHIP activity is known to be inhibited by Hsp90, which itself is chemically inhibited by 17-AAG. To validate CHIP indirectly by chemical means, 17-AAG was added to cells resulting in reduced levels of both the WT and S100M RET protein as seen by western blot. This was in agreement with previous reports that Hsp90 inhibition increased levels of CHIP ubiquitination and subsequent proteasomal degradation of the substrate. 17-AAG addition is a common approach to implicate CHIP in the degradation of a protein of interest and has provided preliminary validation of our hit (Stanley, 2011, Muller et al., 2008).

CHIP constructs (both WT and the dominant negative mutant P269A affecting the CHIP U-box) have been produced and preliminarily tested in DLD-1 cells, so future work examining the effect of their overexpression in WT and S100M RET expressing DLD-1 cells would further confirm CHIP's involvement in the degradation of the RET receptor. The fact that CHIP can potentially target both oncogenic and misfolded proteins for degradation suggests this finding may be of particular interest to unravel. WT RET may be targeted for degradation by CHIP due to the slow folding nature of the receptor and its role as an oncoprotein, while S100M RET may lead to activation of the Hsp90/CHIP axis. Future investigations could examine the effect CHIP knockdown has on the viability or proliferation of the inducible cell lines, or such investigations could be carried out in an endogenous cell line – such as the neuroblastoma cell line SK-N-SH (Takahashi and Cooper,

1987). Preliminary antibody tests have confirmed that the cell surface expression levels of RET can be examined in this particular endogenous cell line.

6.2.2 Implicating aggrephagy in the degradation of HSCR RET

The identification of OPTN and GABARAPL1 as hits lead to the hypothesis that S100M RET is targeted for aggrephagy, a specialised type of autophagy that targets aggregated protein or pathogens for lysosomal degradation (Lamark and Johansen, 2012). This hypothesis was strengthened by the observation that the OPTN and GABARAPL1 knockdown selectively increased cell surface expression of S100M RET and had no effect on WT RET levels. Preliminary validation was carried out using a TBK1 inhibitor developed by Professor Philip Cohen (Clark et al., 2011), as TBK1 has been found to co-localise with and phosphorylate OPTN at a unique site, regulating its ability to interact with autophagy modifiers (Korac et al., 2013). Surprisingly, TBK1 inhibition resulted in increased cell surface levels of both WT and S100M RET – something that was not observed in the original screen. siRNAs targeting both TBK1 and OPTN need to be tested in DLD-1 WT and S100M RET cells to examine this further. OPTN silencing in the siRNA screen may not have been 100% efficient. If this was the case, the effect on RET surface levels may only have been apparent for S100M RET due to the higher level of the HSCR protein targeted to this pathway in comparison to WT. Western blot analysis of total protein levels suggests a larger increase in S100M RET levels under TBK1 inhibition in comparison to WT. As such, it is possible that the OPTN-aggrephagy pathway is degrading misfolded protein that has been targeted for degradation and translocated out of the ER into the cytosol. Therefore, a small amount of WT protein could be degraded via this pathway, due to the previously mentioned intrinsically slow folding nature of the receptor. If correct, the connection between a specialised autophagy pathway and the degradation of a poorly folded or misfolded transmembrane receptor could establish a novel degradative pathway. Further investigations would require an inducible DLD-1 cell line expressing a non-rescuable severe HSCR mutant such as G93S. Previous work has shown that HSCR mutants can be divided into two categories: mild-phenotype mutations (such as S100M) that are believed to be targeted for degradation due to slow folding and can be rescued, and severe-phenotype mutations (such as G93S) that are

terminally misfolded and cannot be rescued (Kjaer et al., 2010). One hypothesis from these data is that a larger amount of G93S is targeted for degradation by aggrephagy than S100M RET, which could be directly investigated by OPTN knockdown (or chemical inhibition of TBK1) in each of these three cell lines.

6.2.3 Elucidating a potential RET folding pathway through the identification of specific chaperones

Several positive regulators of WT RET surface expression were identified in the siRNA screen, including HSPA5 (GRP78/BiP), MESDC2, HYOU1, GRP58, CALR and ERN1. The presence of calreticulin (CALR) and BiP in the list of 'hits' provides a level of validation, as both chaperones have been heavily implicated in the folding of glycoproteins (Hebert et al., 1996, Hendershot, 2004). No validation has been carried out on these hits as of yet, with repeated siRNA knockdowns required to confirm the involvement of each chaperone in WT RET folding. If involved, the identification of these factors could create a snapshot of RET folding within the ER before continuing to the Golgi apparatus. Future investigations could involve the knockdown of each chaperone in an endogenous cell line – such as SK-N-SH – and the comparison of the knockdowns in a cell line expressing another RTK, such as EGFR. This would provide an indication of the specificity of the chaperones identified for RET rather than as a more general receptor tyrosine kinase folding mechanism.

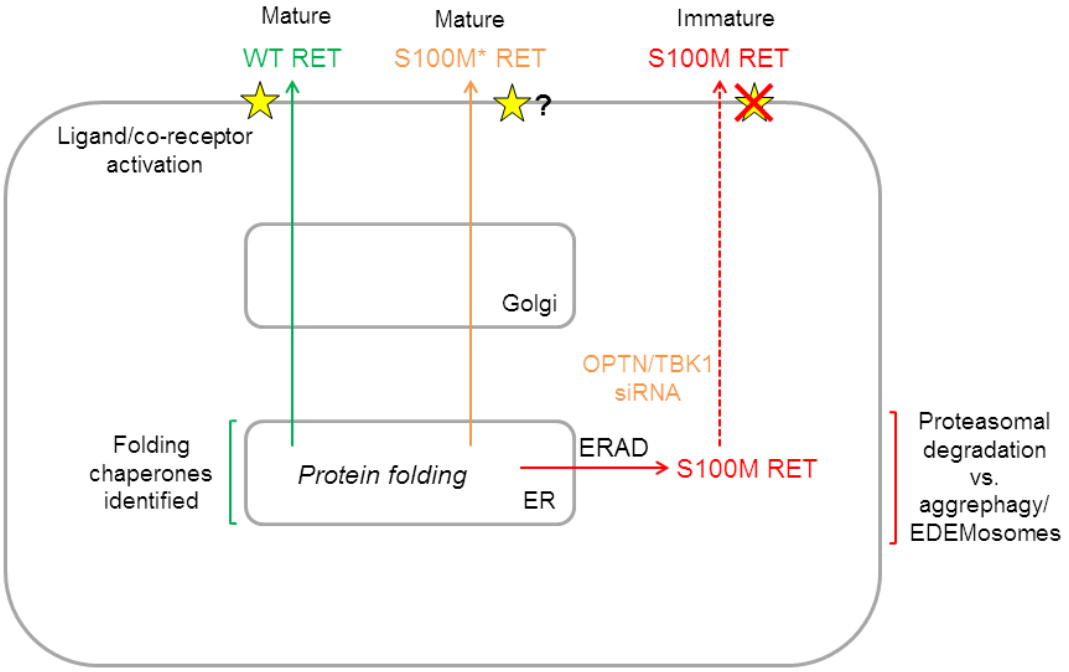

Figure 6.1 Schematic model of WT, S100M* and S100M RET export

WT RET (green) is exported to the cell surface, is fully mature and can activate downstream signalling pathways. Several factors involved in WT RET folding have been identified. S100M* RET (orange) is exported to the cell surface and is fully mature. Future investigations are required in order to establish signalling capabilities. S100M RET (red) is degraded via ERAD, but is exported to the cell surface upon silencing of OPTN or TBK1. Exported protein is not fully glycosylated and cannot activate downstream signalling pathways. Future investigations are required to understand the potential role of EDEMosomes and aggrephagy in S100M RET degradation.

6.2.4 Future investigations: a secondary screen to restore functional signalling for mild RET HSCR mutations

Findings in chapters 3 and 4 have shown that restored S100M RET cell surface expression, by CHIP or OPTN gene knockdown or through TBK1 chemical inhibition, does not appear to enhance the maturation process and therefore is unlikely to have restored functional signalling capability onto S100M HSCR. The increased levels of immature S100M HSCR RET following aggresome inhibition would suggest that this form is present at the cell surface. In the absence of a ligand-induced pERK1/2 signal or S100M RET auto-phosphorylation, I conclude that immature S100M RET is not competent to bind a GDNF-GFRα1 ligand leading to receptor auto-phosphorylation. This leads us to conclude that maturation is the key to restoring functional RET signalling and not simply cell surface localisation. Nevertheless, the siRNA knockdown hits identified in the screen have provided

insights and unexpected leads into new avenues – such as WT RET folding and S100M RET aggrephagy. At the time of writing, a 4000 compound screen has been carried out in collaboration with the HTS facility on DLD-1 cells expressing S100M RET, in an attempt to identify specific compounds that could restore cell surface levels. Preliminary analysis identified 2.9% of the screen as a hit, and further investigations are required to assess their effects on RET signalling. A cross-correlation of target hits from the chemical and genetic screens will provide a robust set of hits to take forwards into a secondary screen for restoration of functional RET signalling.

In considering how to set up a secondary screen, either to run it independently or evaluate genes identified through the immunofluorescence-based screen, the best suited surrogate for functional RET signalling is phospho-ERK1/2. While western blot analysis of ERK1/2 phosphorylation has been used in this thesis, a higher throughput method is required. This could be carried out by immunofluorescence staining of fixed cells with antibodies against phosphorylated RET or members of downstream signalling pathways, as discussed at the end of chapter 4. We are currently in discussions with the HTS facility on the possibility of examining ERK1/2 phosphorylation in fixed cells using our current immunofluorescence assay. Alternatively, intramolecular FRET (fluorescence resonance energy transfer) biosensors could be used to detect phosphorylated ERK and Akt levels in live cells, as developed and optimised by (Komatsu et al., 2011). A combination of this new biosensor technology and the utilisation of the *piggBac* transposase system (Miaczynska et al., 2004) could allow rapid establishment of RET-expressing biosensor cell lines and lead to the identification of compounds or siRNA knockdowns influencing signalling pathways within the cell.

6.2.5 Translating targets found in cell-based models into animal models of Hirschsprung's disease

Throughout this thesis, our experiments have used inducible mammalian cell lines that lack endogenous WT or mutant RET. These allows for the introduction of mutant RET forms into readily transfectable cell-lines. To validate hits required for publication, future investigations would benefit from the use of endogenous WT

RET cell lines, such as the neuroblastoma cell line SK-N-SH. However, there is also an outstanding need for an animal model of Hirschsprung's disease. Especially for validating that functional RET signalling could be restored by gene knockdown or chemical inhibition using the proposed secondary pERK1/2 assay.

Currently mouse models for HSCR use only Ret-null, RET C620R or EDNRB-null, none of which are appropriate in these investigations. The development of new mouse models with specific RET mutations – such as S100M – could be a future possibility. Investigations into endogenous HSCR RET mutants could continue in primary cultures of neural crest cells isolated from mouse model embryos (Yin et al., 2007).

6.3 Towards the development of improved high potency RET inhibitors

Current RET inhibitors that are used in the clinic lack specificity and potency, exhibit hERG activity and have dose-limited toxicities from off-target effects. The case for developing a new generation of inhibitors is well made. Chapter 5 describes the elucidation of crystal structures of the RET tyrosine kinase bound to a variety of *DFG-in* chemical inhibitors with distinct molecular scaffold backbones. These scaffolds appear to interact with distinct but overlapping interaction hot spots within the RET KD nucleotide-binding pocket.

6.3.1 Using differential scanning fluorimetry to examine RET KD-inhibitor binding and stabilisation of protein melting curves

Differential scanning fluorimetry was used to calculate the thermal stability of the RET KD in the presence of each inhibitor, a method that is commonly used to examine enzyme-substrate binding (Niesen et al., 2007). This method is well suited, as it appears to distinguish between *DFG-in* and *DFG-out* inhibitors, due to the large thermal shift induced by *DFG-out* inhibitors Sorafenib and Pz-1. This method could therefore be used to readily characterise newly designed inhibitors and assess whether those inhibitors could be crystallised with the existing RET KD recombinant protein and conditions. The assay has also been used to examine inhibitor selectivity, something that could be examined in the future (Fedorov et al.,

2012). The selected compounds can be incubated with both RET KD and a common off-target (in the case of S1 inhibitors, that could be AURKA) in order to identify the most optimal design of inhibitor. Interestingly, the IC_{50} data provided by our collaborators positively correlated with the thermal shifts observed for the RET KD bound to each of the S1 inhibitors, suggesting that Δ*Tm* (shift in thermal stability) can also give an indication of inhibitor potency. This data is currently statistically insignificant, due to the small differences between each Δ*Tm*, but optimisation (possibly with higher protein concentrations and focussing on S1 inhibitors alone) may overcome this. Going forward, it would be more optimal to calculate IC_{50} values (which could be carried out in RET WT DLD-1 cells) on all inhibitors together rather than collate data from different collaborators performed at different times using different cell lines and protocols.

The arrival of a 20,000-fragment compound screen at the institute also introduces the possibility of a large scale high throughout thermal screen to identify new RET KD inhibitors. Focussing on the identification of ATP-competitive inhibitors (as the crystallisation conditions for this are known), pools of fragments could be added to the RET KD and those inducing a positive thermal shift taken forward for crystallisation trials, either individually or as pools. Structural elucidation of the KD bound to different fragments would encourage the development of new inhibitors, and the information could also be compared to the developing RET pharmacophore. This fragment based drug discovery approach has been used to identify promising compounds against the BRAF kinase, Hsp90 and p38 MAPK (Murray et al., 2012, Carr et al., 2004).

Alternatively, there may be pools of fragments that induce a negative thermal shift, which could give an indication of protein instability (Dai et al., 2014). In the case of oncogenic RET, inducing protein instability could provide an alternate mechanism of inhibition. If this were an objective, the screen would need to be carried out on both WT and oncogenic (e.g. M918T MEN2B) RET, as differences in native stability have been previously reported (Plaza-Menacho et al., 2014).

6.3.2 Structural elucidation of nine RET KD-inhibitor complexes

This thesis has presented the structure of the RET KD bound to nine new inhibitors, at resolutions ranging from 1.8 Å to 2.6 Å. The inhibitors were divided into four scaffolds (S3 currently consists of inhibitors from previously solved structures), with each scaffold exhibiting slightly different binding characteristics within the ATP pocket of the RET KD. S1 inhibitors contain a benzodiazepine scaffold that folds around the hydrophobic floor (Glu810 and Leu881) of the nucleotide pocket and forms hydrogen bonds with the main chain of Ala807 in the KD hinge – it does not extend into the interior pocket. S2 (pyrazolopyrimidine) inhibitors extend much further back, forming hydrogen bonds with the main chain of Glu805 and extending towards Glu775 in the interior pocket. S3 (2-oxo-1H-indolinone) inhibitors appear to hydrogen bond with the main chain of both Ala807 and Glu805, while bonding with a residue in the catalytic region of the pocket also (Ser891 or Asp892). S4 (4-anilinoquinazoline) inhibitors sit in a similar position within the nucleotide pocket, but Vandetanib hydrogen bonds with the main chain of Ala807, while I-3 only hydrogen bonds with Glu775 in the interior pocket – the only inhibitor to make such a connection. BMS-536924 (the phenyl-benzimidazole S5) is found to hydrogen bond with both Ala807 and Glu805 of the KD hinge, while extending over to the catalytic region of the pocket (as defined in chapter 5). The relevance of this binding mode needs further investigations, as the current RET KD recombinant protein cannot be captured in a *DFG-out* conformation, which this inhibitor may induce. The thermal shift assay gives an indication that this inhibitor is *DFG-out*, as incubation with BMS-536924 elicits a positive shift in thermal stability similar to that of Pz-1 and Sorafenib.

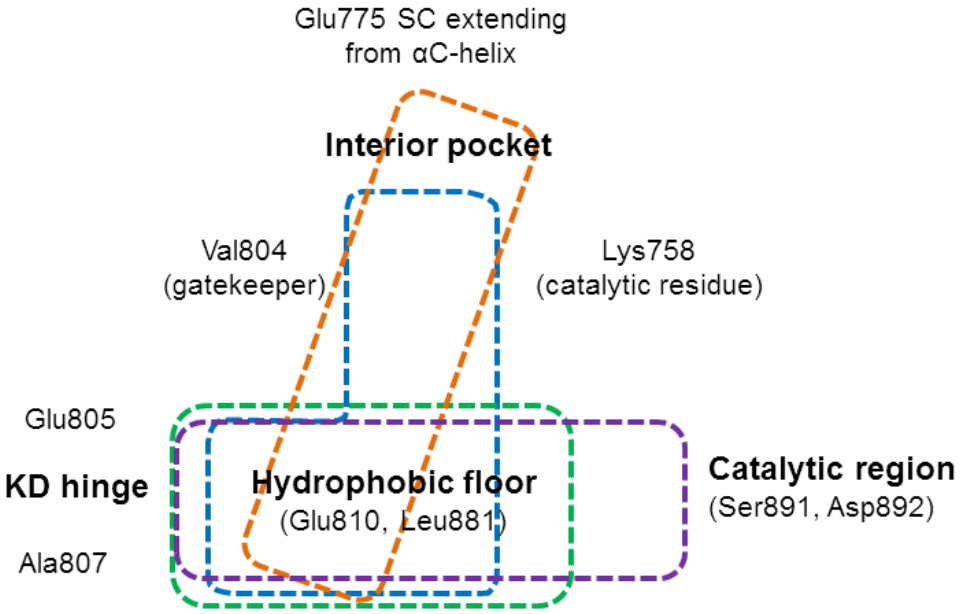

Figure 6.2 Schematic diagram of scaffold positions within the RET nucleotide binding pocket
Schematic of positions of scaffold 1 (green), 2 (blue), 3 (purple) and 4 (orange) within the RET nucleotide binding pocket, with key residues highlighted. The position of scaffold 5 has not been added, due to the requirement of further validation.

During the writing of this thesis, datasets for the RET KD bound to three other S2 inhibitors were collected and require further refinement. Our collaborators have also provided us with other inhibitors. While preliminary comparisons suggest a strong correlation between the induced thermal stability and inhibitor potency (Figure 5.14), there is an urgent need to assemble a comprehensive set of biochemical and cellular IC_{50} values using an identical protocol, reagents and performed by the same person. More detailed comparisons and conclusions could then be drawn, integrating the structural data described here.

6.3.3 Preliminary development of an improved RET pharmacophore

The development of a new RET pharmacophore has begun, through the compilation of information provided from each of the RET KD-inhibitor structures. Inhibitors have been preliminarily clustered based on the number of interactions each residue within the defined ATP-pocket could make with each inhibitor (defined as those within 4 Å). This level of data has already begun to separate scaffolds successfully, with the addition of more data – such as hydrogen bonds within the

hinge, IC_{50} data and Δ*Tm* values – hopefully leading to the optimisation of the database. This database could be greatly built upon if the 20,000 fragment compound screen is carried out with the RET KD. If successful, the database could be used as a reference point for the design of the next generation of RET inhibitors, identifying the most optimal chemical characteristics for potency and specificity.

6.4 Concluding remarks

In this thesis I have sought to progress our understanding of the folding, export and chemical regulation of the RET receptor tyrosine kinase. I have provided a strategy for examining the molecular mechanisms of WT, HSCR and oncogenic RET export, and have identified factors that may be responsible for the regulation of both pathogenic forms of the receptor. I have also presented the crystal structure of the RET KD bound to a range of ATP-competitive inhibitors; with the objective of progressing the development of a new generation of more specific and potent RET inhibitors. I hope that the work presented in this thesis will further our understanding of Hirschsprung's disease and lead to improved RET-associated cancer treatments in the future.

Chapter 7. Appendix

7.1 siRNA screen plates 1-4 layout

Well allocation for all screen siRNA candidates in plates 1-4 with gene name and NCBI reference sequence code.

Plate	Well	Target Symbol	Target ID
1	A01	OTP	NA
1	A02	P4HB	NM_000918
1	A03	DPM1	NM_003859
1	A04	FKBP4	NM_002014
1	A05	IBTK	NM_015525
1	A06	AP1GBP1	NM_007247
1	A07	BRCA1	NM_007298
1	A08	MBTPS2	NM_015884
1	A09	TXNDC4	NM_015051
1	A10	ATP6V0A1	NM_005177
1	A11	GABARAPL2	NM_007285
1	A12	CUL3	NM_003590
1	B01	RAB7A	NM_004637
1	B02	RET	NM_020630
1	B03	HSPA5	NM_005347
1	B04	FBXO23	NM_001006616
1	B05	VPS13D	NM_018156
1	B06	C14ORF100	NM_001098625
1	B07	HERPUD1	NM_001010990
1	B08	ANAPC4	NM_013367
1	B09	CUL1	NM_003592
1	B10	ATG5	NM_004849
1	B11	PDCD6	NM_013232
1	B12	PDIR	NM_006810
1	C01	RF	NA
1	C02	ERP44	NM_015051
1	C03	C2ORF30	NM_015701
1	C04	DNAJA2	NM_005880
1	C05	UFD1L	NM_001035247
1	C06	EIF2B3	NM_020365
1	C07	SEL1L	NM_005065
1	C08	DERL2	NM_016041
1	C09	IKBKG	NM_001099856
1	C10	LMAN1	NM_005570
1	C11	PLD1	NM_002662
1	C12	RAB7	NM_004637
1	D01	ATP6V0C	NM_001198569
1	D02	ATP6V1C2	NM_001039362
1	D03	SEC31L2	NM_015490
1	D04	DNAJC10	NM_018981
1	D05	CAB45	NM_016176
1	D06	FKBP7	NM_181342
1	D07	HSPCA	NM_005348
1	D08	NA	NA
1	D09	DDHD2	NM_015214
1	D10	EPS15	NM_001981
1	D11	ATG16L1	NM_017974
1	D12	DNAJA1	NM_001539
1	E01	RET	NM_020630
1	E02	RF	NA
1	E03	RNP24	NM_006815
1	E04	PPP1R15A	NM_014330
1	E05	KLHDC5	NM_020782
1	E06	PTX1	NM_016570
1	E07	C20ORF31	NM_018217
1	E08	NSFL1C	NM_016143
1	E09	ANAPC5	NM_016237
1	E10	C12ORF8	NM_001034025
1	E11	NOS1	NM_000620
1	E12	HDAC6	NM_006044
1	F01	P4HB	NM_000918
1	F02	OTP	NA
1	F03	HSPCB	NM_007355
1	F04	LZTR1	NM_006767
1	F05	DERL3	NM_198440
1	F06	GGA1	NM_001001561
1	F07	KDELR3	NM_016657
1	F08	XBP1	NM_005080
1	F09	TIMP3	NM_000362
1	F10	FLJ23322	NM_001102371
1	F11	RBX1	NM_014248
1	F12	ATP6V1D	NM_015994
1	G01	ATP6V1C2	NM_001039362
1	G02	RAB7A	NM_004637
1	G03	AHSA1	NM_012111
1	G04	PPM1A	NM_021003
1	G05	SEC23A	NM_006364
1	G06	ADNP	NM_015339
1	G07	SEC23B	NM_032986
1	G08	APG4A	NM_178270
1	G09	DNAJC3	NM_006260
1	G10	AXIN1	NM_003502
1	G11	STUB1	NM_005861
1	G12	GGA2	NM_015044
1	H01	ERP44	NM_015051
1	H02	ATP6V0C	NM_001198569
1	H03	PLDN	NM_012388
1	H04	IKBKB	NM_001556
1	H05	RABAC1	NM_006423
1	H06	BET1	NM_005868
1	H07	CBLL1	NM_024814
1	H08	GRB10	NM_001001549
1	H09	HSPB1	NM_001540
1	H10	AGR2	NM_006408
1	H11	CREB3	NM_006368
1	H12	BAG1	NM_004323

Table 7.1 Plate 1 siRNA candidate well allocation

Plate	Well	Target Symbol	Target ID
2	A01	OTP	NA
2	A02	P4HB	NM_000918
2	A03	SPFH1	NM_001100626
2	A04	ATE1	NM_007041
2	A05	FBXL15	NM_024326
2	A06	CUL2	NM_003591
2	A07	GOSR2	NM_054022
2	A08	HSPA8	NM_006597
2	A09	CBL	NM_005188
2	A10	TEBP	NM_006601
2	A11	CDKN1B	NM_004064
2	A12	EIF2B1	NM_001414
2	B01	RAB7A	NM_004637
2	B02	RET	NM_020630
2	B03	COPS7A	NM_016319
2	B04	MAPK14	NM_139013
2	B05	BAG2	NM_004282
2	B06	HBS1L	NM_006620
2	B07	MAN2A1	NM_002372
2	B08	ETEA	NM_014613
2	B09	GOLPH3	NM_022130
2	B10	SKP1A,SKP1	NM_170679
2	B11	KIAA1181	NM_001031711
2	B12	CRBN	NM_016302
2	C01	RF	NA
2	C02	ERP44	NM_015051
2	C03	TUSC2	NM_007275
2	C04	ATP6V1A	NM_001690
2	C05	STAM2	NM_005843
2	C06	EIF2B4	NM_172195
2	C07	GCS1	NM_006302
2	C08	AUP1	NM_181575
2	C09	FANCL	NM_018062
2	C10	RNF103	NM_005667
2	C11	ATP6V1B1	NM_001692
2	C12	SIP	NM_001007214
2	D01	ATP6V0C	NM_001198569
2	D02	ATP6V1C2	NM_001039362
2	D03	C1ORF22	NM_025191
2	D04	DDOST	NM_005216
2	D05	ATP6V0B	NM_001039457
2	D06	TXNDC12	NM_015913
2	D07	MESDC2	NM_015154
2	D08	ATF6	NM_007348
2	D09	CASQ2	NM_001232
2	D10	ALG5	NM_013338
2	D11	SIL1	NM_022464
2	D12	COPS5	NM_006837

Plate	Well	Target Symbol	Target ID
2	E01	RET	NM_020630
2	E02	RF	NA
2	E03	COPA	NM_004371
2	E04	CDKN2C	NM_001262
2	E05	OPTN	NM_021980
2	E06	GGA3	NM_014001
2	E07	ATG4C	NM_032852
2	E08	DJ971N18.2	NM_021156
2	E09	SDBCAG84	NM_015966
2	E10	BECN1	NM_003766
2	E11	CANX	NM_001024649
2	E12	TRAF2	NM_021138
2	F01	P4HB	NM_000918
2	F02	OTP	NA
2	F03	EPS15L1	NM_021235
2	F04	ATF4	NM_001675
2	F05	ATP6V1F	NM_004231
2	F06	EIF2AK4	NM_001013703
2	F07	ANAPC13	NM_015391
2	F08	NEDD8	NM_006156
2	F09	PRKCSH	NM_002743
2	F10	PCIA1,DDA1	NM_024050
2	F11	ADRM1	NM_175573
2	F12	ATG4D	NM_032885
2	G01	ATP6V1C2	NM_001039362
2	G02	RAB7A	NM_004637
2	G03	MGAT1	NM_002406
2	G04	SELS	NM_018445
2	G05	DNAJB1	NM_006145
2	G06	HSPBP1	NM_012267
2	G07	VHL	NM_000551
2	G08	EDEM1	NM_014674
2	G09	KIDINS220	NM_020738
2	G10	ERN2	NM_033266
2	G11	RAB33A	NM_004794
2	G12	OS-9	NM_001017957
2	H01	ERP44	NM_015051
2	H02	ATP6V0C	NM_001198569
2	H03	DNAJB2	NM_001039550
2	H04	EDNRB	NM_000115
2	H05	KDELR2	NM_001100603
2	H06	STAM	NM_003473
2	H07	TXN	NM_003329
2	H08	DYT1	NM_000113
2	H09	GOLGA1	NM_002077
2	H10	DERL1	NM_024295
2	H11	MAP2K5	NM_002757
2	H12	PREB	NM_013388

Table 7.2 Plate 2 siRNA candidate well allocation

Plate	Well	Target Symbol	Target ID
3	A01	OTP	NA
3	A02	P4HB	NM_000918
3	A03	BARD1	NM_000465
3	A04	COPS4	NM_016129
3	A05	SEC31L1	NM_014933
3	A06	VDP,USO1	NM_003715
3	A07	SEC24B	NM_001042734
3	A08	FLJ32115	NM_152321
3	A09	GABARAPL1	NM_031412
3	A10	CUL4A	NM_003589
3	A11	TXNDC	NM_030755
3	A12	LMAN1L	NM_021819
3	B01	RAB7A	NM_004637
3	B02	RET	NM_020630
3	B03	DET1	NM_017996
3	B04	COPS3	NM_003653
3	B05	TP53	NM_000546
3	B06	FKBP10	NM_021939
3	B07	AKT1	NM_001014431
3	B08	NOSIP	NM_015953
3	B09	RFWD2	NM_001001740
3	B10	CASQ1	NM_001231
3	B11	LAP1B	NM_015602
3	B12	GOLPH3L	NM_018178
3	C01	RF	NA
3	C02	ERP44	NM_015051
3	C03	IKBKE	NM_014002
3	C04	PDIA6	NM_005742
3	C05	ATP6V1C2	NM_144583
3	C06	UBXD2	NM_014607
3	C07	HSPD1	NM_002156
3	C08	SUMF1	NM_182760
3	C09	COPS7B	NM_022730
3	C10	ATG3	NM_022488
3	C11	EIF2A	NM_032025
3	C12	VPRBP	NM_014703
3	D01	ATP6V0C	NM_001198569
3	D02	ATP6V1C2	NM_001039362
3	D03	ARMET	NM_006010
3	D04	ATG12	NM_004707
3	D05	YIPF5	NM_001024947
3	D06	ATP6V1B2	NM_001693
3	D07	SPFH2	NM_001003791
3	D08	UGCG	NM_003358
3	D09	SURF4	NM_033161
3	D10	HYOU1	NM_006389
3	D11	SEC24D	NM_014822
3	D12	NGLY1	NM_018297

Plate	Well	Target Symbol	Target ID
3	E01	RET	NM_020630
3	E02	RF	NA
3	E03	TGOLN2	NM_006464
3	E04	ATG10	NM_031482
3	E05	SARA2	NM_016103
3	E06	RABGEF1	NM_014504
3	E07	ERP70	NM_004911
3	E08	SEC13L1	NM_183352
3	E09	CREB3L1	NM_052854
3	E10	RER1	NM_007033
3	E11	CUL4B	NM_001079872
3	E12	AMFR	NM_001144
3	F01	P4HB	NM_000918
3	F02	OTP	NA
3	F03	ATP6V0D1	NM_004691
3	F04	STX5A	NM_003164
3	F05	SYVN1	NM_032431
3	F06	ZFPL1	NM_006782
3	F07	ATF3	NM_001030287
3	F08	PPM1L	NM_139245
3	F09	BAP1	NM_004656
3	F10	LRPAP1	NM_002337
3	F11	SPRY1	NM_005841
3	F12	ANAPC10	NM_014885
3	G01	ATP6V1C2	NM_001039362
3	G02	RAB7A	NM_004637
3	G03	NOS3	NM_000603
3	G04	VCP	NM_007126
3	G05	SUGT1	NM_006704
3	G06	TRIP15	NM_004236
3	G07	ST5	NM_005418
3	G08	TXNDC10	NM_019022
3	G09	HSBP1	NM_001537
3	G10	HSP90B1	NM_003299
3	G11	PPIB	NM_000942
3	G12	GRP58	NM_005313
3	H01	ERP44	NM_015051
3	H02	ATP6V0C	NM_001198569
3	H03	GOLGA2	NM_004486
3	H04	NIBP	NM_031466
3	H05	UBXD1	NM_025241
3	H06	COPS6	NM_006833
3	H07	ATG4B	NM_013325
3	H08	STIP1	NM_006819
3	H09	TNIP2	NM_024309
3	H10	FEM1B	NM_015322
3	H11	MN1	NM_002430
3	H12	LOC204474	NM_174924

Table 7.3 Plate 3 siRNA candidate well allocation

Plate	Well	Target Symbol	Target ID
4	A01	OTP	NA
4	A02	P4HB	NM_000918
4	A03	HIC2	NM_015094
4	A04	GPS1	NM_004127
4	A05	MAP3K2	NM_006609
4	A06	PPM1D	NM_003620
4	A07	PTEN	NM_000314
4	A08	RAB33B	NM_031296
4	A09	EIF2AK3	NM_004836
4	A10	BCMP11	NM_176813
4	A11	FKBP2	NM_004470
4	A12	YIF1	NM_020470
4	B01	RAB7A	NM_004637
4	B02	RET	NM_020630
4	B03	ATR	NM_001184
4	B04	VCPIP1	NM_025054
4	B05	DDIT3	NM_004083
4	B06	TMEM15	NM_014908
4	B07	PTPN2	NM_002828
4	B08	ANAPC2	NM_013366
4	B09	SEC24C	NM_198597
4	B10	ULK1	NM_003565
4	B11	MAN1B1	NM_016219
4	B12	HIC1	NM_001098202
4	C01	NA	NA
4	C02	ERP44	NM_015051
4	C03	ARIH2	NM_006321
4	C04	ERN1	NM_001433
4	C05	CALR	NM_004343
4	C06	YOD1	NM_018566
4	C07	HGNT-IV-H	NM_013244
4	C08	NPL4	NM_017921
4	C09	DSCR2	NM_003720
4	C10	RNF5	NM_006913
4	C11	TBL3	NM_006453
4	C12	TMED9	NM_017510
4	D01	ATP6V0C	NM_001198569
4	D02	ATP6V1C2	NM_001039362
4	D03	HSF1	NM_005526
4	D04	PARK2	NM_004562
4	D05	HGS	NM_004712
4	D06	P4HB	NM_000918
4	D07	ANKFY1	NM_020740
4	D08	ATP6V0C	NM_001694
4	D09	CNO	NM_018366
4	D10	NF2	NM_181831
4	D11	DCC	NM_005215
4	D12	TXNDC5	NM_030810

Plate	Well	Target Symbol	Target ID
4	E01	RET	NM_020630
4	E02	RF	NA
4	E03	VHLL	NM_001004319
4	E04	SIAH1	NM_003031
4	E05	ANAPC7	NM_016238
4	E06	NF1	NM_000267
4	E07	ATG7	NM_006395
4	E08	ERO1L	NM_014584
4	E09	VPS13A	NM_015186
4	E10	LRBA	NM_006726
4	E11	COPS8	NM_006710
4	E12	UBE2J1	NM_016021
4	F01	P4HB	NM_000918
4	F02	OTP	NA
4	F03	MAP3K3	NM_002401
4	F04	ATG9A	NM_024085
4	F05	DCTN1	NM_004082
4	F06	DOK5L	NM_152721
4	F07	CHUK	NM_001278
4	F08	TMX2	NM_015959
4	F09	HSPA1A	NM_005345
4	F10	HSPA1B	NM_005346
4	F11	NA	NA
4	F12	NA	NA
4	G01	ATP6V1C2	NM_001039362
4	G02	RAB7A	NM_004637
4	G03	GDNF	NM_000514
4	G04	GFRA1	NM_001145453
4	G05	SORL1	NM_003105
4	G06	NA	NA
4	G07	NA	NA
4	G08	NA	NA
4	G09	NA	NA
4	G10	NA	NA
4	G11	NA	NA
4	G12	NA	NA
4	H01	4PBA	
4	H02	4PBA	
4	H03	4PBA	
4	H04	4PBA	
4	H05	4PBA	
4	H06	4PBA	
4	H07	4PBA	
4	H08	4PBA	
4	H09	4PBA	
4	H10	4PBA	
4	H11	4PBA	
4	H12	4PBA	

Table 7.4 Plate 4 siRNA candidate well allocation

7.2 POC scores for all siRNA screen targets

Target Symbol	WT POC score	S100M POC score
OTP	1.03	1.03
P4HB	1	1.16
DPM1	1.21	1.08
FKBP4	1.12	0.98
IBTK	0.99	0.92
AP1GBP1	0.95	0.98
BRCA1	0.97	1.01
MBTPS2	1.16	0.95
TXNDC4	0.76	0.88
ATP6V0A1	1.2	0.96
GABARAPL2	0.97	1.01
CUL3	0.99	1
RAB7A	1.2	1.39
RET	0.27	0.72
HSPA5	0.74	0.93
FBXO23	1.1	1.23
VPS13D	1.15	1.08
C14ORF100	1.05	1
HERPUD1	0.86	0.93
ANAPC4	0.97	1.03
CUL1	1	1
ATG5	1.22	1
PDCD6	1.03	1.02
PDIR	1	0.85
RF	1.03	1.08
ERP44	0.66	0.94
C2ORF30	1.01	1.04
DNAJA2	0.97	1
UFD1L	0.83	1.09
EIF2B3	0.91	1.09
SEL1L	0.64	0.95
DERL2	0.78	0.88
IKBKG	0.77	0.94
LMAN1	1.16	1.07
PLD1	1.14	1.04
RAB7	1.3	1.48
ATP6V0C	1.4	1.32
atp6v1c2	0.91	1.04
SEC31L2	0.83	0.93
DNAJC10	0.84	0.9
CAB45	1	0.86
FKBP7	0.87	0.88
HSPCA	1.03	0.97
NA	1.05	0.89
DDHD2	1.07	1.07
EPS15	0.78	0.93
ATG16L1	1.04	0.98
DNAJA1	1.21	0.97
RET	0.27	0.78
RF	0.88	1.1
RNP24	0.49	0.96
PPP1R15A	1.02	1.26

Target Symbol	WT POC score	S100M POC score
KLHDC5	1.04	1.07
PTX1	1.15	1.17
C20ORF31	1.17	1.32
NSFL1C	0.96	1.14
ANAPC5	0.91	1.01
C12ORF8	0.91	1.01
NOS1	1.18	0.91
HDAC6	1.1	0.97
P4HB	0.97	1.16
OTP	0.99	1.04
HSPCB	1.07	0.96
LZTR1	0.95	1.46
DERL3	0.96	1.03
GGA1	1.15	1.15
KDELR3	1.15	1.1
XBP1	0.79	0.9
TIMP3	0.81	0.95
FLJ23322	1.05	1.06
RBX1	1.05	0.98
ATP6V1D	0.97	1.13
ATP6V1C2	0.9	1.03
RAB7A	1.03	1.7
AHSA1	0.96	1.16
PPM1A	1.07	1.06
SEC23A	1.08	1.12
ADNP	0.99	0.98
SEC23B	0.69	0.96
APG4A	0.87	1.03
DNAJC3	0.83	0.87
AXIN1	0.9	0.96
STUB1	1.46	1.35
GGA2	1.1	0.96
ERP44	0.69	1.08
ATP6V0C	1.22	1.24
PLDN	0.88	1
IKBKB	0.74	1.05
RABAC1	1.13	1.15
BET1	1.04	1.12
CBLL1	0.98	0.95
GRB10	1.1	1
HSPB1	1.08	0.97
AGR2	1.14	0.89
CREB3	1	1.07
BAG1	0.91	0.88
OTP	0.92	1.1
P4HB	1.07	1.22
SPFH1	1.08	1.12
ATE1	1.16	1.02
FBXL15	0.91	1.04
CUL2	0.95	0.95
GOSR2	0.98	1.03
HSPA8	1.24	1.17
CBL	1	1.13
TEBP	0.94	0.91

Table 7.5 WT and S100M RET POC scores for all siRNA candidates (1)

Target Symbol	WT POC score	S100M POC score
STAM2	1.06	1.13
EIF2B4	1.03	1.03
GCS1	1.06	1.11
AUP1	1.2	1
FANCL	0.91	0.94
RNF103	1.01	0.97
ATP6V1B1	1.1	1.29
SIP	1.11	1.2
ATP6V0C	1.29	1.29
ATP6V1C2	0.99	0.99
C1ORF22	0.78	0.97
DDOST	0.73	0.94
ATP6V0B	0.96	0.94
TXNDC12	0.93	0.94
MESDC2	0.67	0.9
ATF6	0.7	0.86
CASQ2	1.02	0.99
ALG5	0.83	0.81
SIL1	1.13	1
COPS5	1.19	1.12
RET	0.25	0.77
RF	1.05	1.08
COPA	0.8	1.02
CDKN2C	1.05	1.06
OPTN	1.06	1.3
GGA3	0.85	0.97
ATG4C	0.85	0.98
DJ971N18.2	0.94	0.93
SDBCAG84	1.12	1.16
BECN1	0.9	0.82
CANX	0.9	0.89
TRAF2	0.98	0.99
P4HB	1.01	1.2
OTP	0.95	1.11
CDKN1B	1.2	1.03
EIF2B1	0.86	0.91
RAB7A	1.12	1.38
RET	0.26	0.71
COPS7A	0.9	0.89
MAPK14	0.99	1.09
BAG2	0.93	0.96
HBS1L	1	1.02
MAN2A1	1.05	1.2
ETEA	1.19	0.96
GOLPH3	1.18	0.96
SKP1A,SKP1	1.04	1.01
KIAA1181	0.96	0.9
CRBN	1.04	0.97
RF	0.95	1.16
ERP44	0.62	1.03
TUSC2	0.98	1.1
ATP6V1A	1.31	1.27

Target Symbol	WT POC score	S100M POC score
EPS15L1	1.09	0.99
ATF4	1.14	1.05
ATP6V1F	1.01	1.05
EIF2AK4	1.08	1.08
ANAPC13	1	1.15
NEDD8	1.1	0.98
PRKCSH	0.91	1.01
PCIA1,DDA1	1.12	0.99
ADRM1	0.96	0.97
ATG4D	1.11	0.98
ATP6V1C2	0.85	1.02
RAB7A	1.15	1.45
MGAT1	0.86	1.04
SELS	1.12	1.19
DNAJB1	1.1	1.02
HSPBP1	1.11	1.15
VHL	1.03	1.13
EDEM1	1.07	1.09
KIDINS220	1	0.99
ERN2	1.06	0.98
RAB33A	0.84	0.97
OS-9	0.98	0.99
ERP44	0.64	1.04
ATP6V0C	1.24	1.23
DNAJB2	0.9	0.9
EDNRB	0.9	0.99
KDELR2	1.05	0.91
STAM	0.85	0.98
TXN	0.99	0.98
DYT1	1.14	1.05
GOLGA1	1.04	0.95
DERL1	0.98	1
MAP2K5	0.98	1.04
PREB	0.78	1.04
OTP	1	1.1
P4HB	1.03	1.14
BARD1	0.93	0.96
COPS4	0.93	1.05
SEC31L1	1.15	0.95
VDP,USO1	0.8	0.88
SEC24B	1.05	1.04
FLJ32115	0.92	0.95
GABARAPL1	1.04	1.28
CUL4A	1.01	0.91
TXNDC	0.95	1.07
LMAN1L	1.04	1.03
RAB7A	1.28	1.49
RET	0.31	0.71
DET1	0.94	1.02
COPS3	0.86	0.89
TP53	0.71	0.99
FKBP10	0.94	1

Table 7.6 WT and S100M RET POC scores for all siRNA candidates (2)

Target Symbol	WT POC score	S100M POC score
AKT1	0.92	0.89
NOSIP	1	1.08
RFWD2	0.96	0.89
CASQ1	1.16	1
LAP1B	1.07	1.08
GOLPH3L	0.98	0.92
RF	0.99	1.2
ERP44	0.63	0.98
IKBKE	1.02	0.97
PDIA6	0.96	0.98
ATP6V1C2	0.98	1.02
UBXD2	0.99	0.95
HSPD1	1.12	1
SUMF1	1.1	1.02
COPS7B	1.06	0.93
ATG3	1.2	0.88
EIF2A	1.06	1.11
VPRBP	1.13	1.12
ATP6V0C	1.35	1.28
ATP6V1C2	0.94	1.06
ARMET	0.82	1.02
ATG12	0.92	0.94
YIPF5	0.83	0.86
ATP6V1B2	1.24	1.07
SPFH2	1.36	1.29
UGCG	0.97	0.82
SURF4	1.24	1.15
HYOU1	0.72	0.88
SEC24D	0.96	1.07
NGLY1	0.88	0.89
RET	0.28	0.73
RF	0.91	1.05
TGOLN2	1.16	1.04
ATG10	0.9	0.94
SARA2	1.29	1.33
RABGEF1	1.19	1.03
ERP70	0.9	1.07
SEC13L1	0.95	0.95
ATP6V0C	1.16	1.17
CREB3L1	1.12	1.24
RER1	0.79	0.99
CUL4B	1	1.02
AMFR	1.08	0.88
P4HB	1.06	1.14
OTP	0.95	1.08
ATP6V0D1	1.15	1.08
STX5A	0.81	1.01
SYVN1	0.8	0.96
ZFPL1	0.85	1.03
ATF3	1.07	1.15
PPM1L	0.88	1.08
BAP1	0.95	1.03

Target Symbol	WT POC score	S100M POC score
LRPAP1	1.03	1.01
SPRY1	0.77	0.87
ANAPC10	1.03	1.05
ATP6V1C2	0.91	1.01
RAB7A	1.13	1.48
NOS3	1.06	0.9
VCP	0.9	0.97
SUGT1	0.91	1.08
TRIP15	1.17	1.06
ST5	1.03	1.01
TXNDC10	1.07	0.91
HSBP1	0.94	1.04
HSP90B1	1.04	1.02
PPIB	1.27	1.14
GRP58	0.64	0.85
ERP44	0.7	1.01
ATP6V0C	1.28	1.35
GOLGA2	1.07	0.94
NIBP	0.9	0.97
UBXD1	1.05	1.06
COPS6	1.29	1.07
ATG4B	1.1	1.04
STIP1	1.12	0.92
TNIP2	1.14	1
FEM1B	1.09	0.99
MN1	0.84	0.96
LOC204474	0.92	0.91
OTP	1.07	1.18
P4HB	1.07	1.24
HIC2	0.97	0.96
GPS1	1.19	1
MAP3K2	1	0.98
PPM1D	1.13	0.97
PTEN	1.02	1.11
RAB33B	1.24	1.1
EIF2AK3	0.94	0.95
BCMP11	1.02	0.92
FKBP2	1.09	1.2
YIF1	0.91	1.02
RAB7A	1.26	1.44
RET	0.21	0.66
ATR	0.97	1.03
VCPIP1	1.05	0.97
DDIT3	0.93	1.01
TMEM15	1.05	0.97
PTPN2	0.94	0.97
ANAPC2	1.06	0.96
SEC24C	0.69	0.87
ULK1	1.07	0.98
MAN1B1	1.41	1.21
HIC1	1.2	0.84
RF	1.06	1.1

Table 7.7 WT and S100M POC scores for all siRNA candidates (3)

Target Symbol	WT POC score	S100M POC score
ERP44	0.58	0.95
ARIH2	0.97	1.1
ERN1	0.71	0.94
CALR	0.56	0.87
YOD1	0.87	1.04
HGNT-IV-H	0.9	1.06
NPL4	0.96	0.97
DSCR2	0.92	0.9
RNF5	1.06	1
TBL3	1.25	1.19
TMED9	0.96	0.95
ATP6V0C	1.33	1.16
ATP6V1C2	0.88	1.05
HSF1	0.98	0.98
PARK2	0.87	0.96
HGS	0.99	1.07
P4HB	0.91	0.93
ANKFY1	1.03	0.89
ATP6V0C	1.22	1.21
CNO	1.05	1.09
NF2	0.94	0.96
DCC	1.16	1.08
TXNDC5	1.1	0.98
RET	0.3	0.76
RF	0.93	1.04
VHLL	0.8	0.95
SIAH1	1.17	1
ANAPC7	0.95	1.04
NF1	1.1	0.95
ATG7	1.12	1.03
ERO1L	1.05	1.02
VPS13A	1.18	1.04
LRBA	0.91	1
COPS8	0.9	1.11
UBE2J1	0.98	0.92
P4HB	1.04	1.18
OTP	0.94	0.99
MAP3K3	1	1
ATG9A	0.81	0.93
DCTN1	0.99	0.92
DOK5L	0.87	1.05
CHUK	0.92	1.04
TMX2	1.1	0.96
HSPA1A	1.15	1.14
HSPA1B	0.99	1.06
NA	1.05	0.99
NA	0.92	1.06
ATP6V1C2	0.78	0.98
RAB7A	1.16	1.38
GDNF	1.02	1.11
GFRA1	1.15	1.06
SORL1	0.81	0.84

Target Symbol	WT POC score	S100M POC score
NA	1.01	0.98
NA	1.07	0.97
NA	1	0.9
NA	1	0.96
NA	1.02	0.98
NA	1.05	1.01
NA	0.99	1.07
ERP44	0.66	1.12

Table 7.8 WT and S100M POC scores for all siRNA candidates

Reference List

ABRESCIA, C., SJOSTRAND, D., KJAER, S. & IBANEZ, C. F. 2005. Drosophila RET contains an active tyrosine kinase and elicits neurotrophic activities in mammalian cells. *FEBS Letters,* 579**,** 3789-96.

ADAMS, P. D., AFONINE, P. V., BUNKOCZI, G., CHEN, V. B., DAVIS, I. W., ECHOLS, N., HEADD, J. J., HUNG, L. W., KAPRAL, G. J., GROSSE-KUNSTLEVE, R. W., MCCOY, A. J., MORIARTY, N. W., OEFFNER, R., READ, R. J., RICHARDSON, D. C., RICHARDSON, J. S., TERWILLIGER, T. C. & ZWART, P. H. 2010. PHENIX: a comprehensive Python-based system for macromolecular structure solution. *Acta Crystallographica D Biological Crystallography,* 66**,** 213-21.

AEBI, M., BERNASCONI, R., CLERC, S. & MOLINARI, M. 2010. N-glycan structures: recognition and processing in the ER. *Trends in Biochemical Sciences,* 35**,** 74-82.

AIRAKSINEN, M. S., TITIEVSKY, A. & SAARMA, M. 1999. GDNF family neurotrophic factor signaling: four masters, one servant? *Molecular and Cellular Neuroscience,* 13**,** 313-25.

ALFANO, L., GUIDA, T., PROVITERA, L., VECCHIO, G., BILLAUD, M., SANTORO, M. & CARLOMAGNO, F. 2010. RET Is a Heat Shock Protein 90 (HSP90) Client Protein and Is Knocked Down upon HSP90 Pharmacological Block. *The Journal of Clinical Endocrinology & Metabolism,* 95**,** 3552-57.

AMIEL, J., SPROAT-EMISON, E., GARCIA-BARCELO, M., LANTIERI, F., BURZYNSKI, G., BORREGO, S., PELET, A., ARNOLD, S., MIAO, X., GRISERI, P., BROOKS, A. S., ANTINOLO, G., DE PONTUAL, L., CLEMENT-ZIZA, M., MUNNICH, A., KASHUK, C., WEST, K., WONG, K. K., LYONNET, S., CHAKRAVARTI, A., TAM, P. K., CECCHERINI, I., HOFSTRA, R. M. & FERNANDEZ, R. 2008. Hirschsprung disease, associated syndromes and genetics: a review. *Journal of Medical Genetics,* 45**,** 1-14.

AMORESANO, A., INCORONATO, M., MONTI, G., PUCCI, P., DE FRANCISCIS, V. & CERCHIA, L. 2005. Direct interactions among Ret, GDNF and GFRalpha1 molecules reveal new insights into the assembly of a functional three-protein complex. *Cellular Signaling,* 17**,** 717-27.

ANDERS, J., KJAER, S. & IBANEZ, C. 2001a. Molecular modeling of the extracellular domain of the RET receptor tyrosine kinase reveals multiple cadherin-like domains and a calcium-binding site. *The Journal of Biological Chemistry,* 276**,** 35808-17.

ANELLI, T., ALESSIO, M., BACHI, A., BERGAMELLI, L., BERTOLI, G., CAMERINI, S., MEZGHRANI, A., RUFFATO, E., SIMMEN, T. & SITIA, R. 2003. Thiol-mediated protein retention in the endoplasmic reticulum: the role of ERp44. *The EMBO Journal,* 19, 5015-22.

ANELLI, T., CEPPI, S., BERGAMELLI, L., CORTINI, M., MASCIARELLI, S., VALETTI, C. & SITIA, R. 2007. Sequential steps and checkpoints in the early exocytic compartment during secretory IgM biogenesis. *EMBO Journal,* 26**,** 4177-88.

ANTONELLI, A., BOCCI, G., LA MOTTA, C., FERRARI, S. M., FALLAHI, P., FIORAVANTI, A., SARTINI, S., MINUTO, M., PIAGGI, S., CORTI, A., ALI, G., BERTI, P., FONTANINI, G., DANESI, R., DA SETTIMO, F. & MICCOLI, P. 2011. Novel pyrazolopyrimidine derivatives as tyrosine kinase inhibitors with antitumoral activity in vitro and in vivo in papillary dedifferentiated thyroid cancer. *Journal of Clinical Endocrinology and Metabolism,* 96**,** E288-96.

APPELQVIST, H., WÄSTER, P., KÅGEDAL, K. & ÖLLINGER, K. 2013. The lysosome: from waste bag to potential therapeutic target. *Journal of Molecular Cell Biology,* 5**,** 214-26.

ARAI, K., LEE, S. R., VAN LEYEN, K., KUROSE, H. & LO, E. H. 2004. Involvement of ERK MAP kinase in endoplasmic reticulum stress in SH-SY5Y human neuroblastoma cells. *Journal of Neurochemistry,* 89**,** 232-9.

ARIGHI, E., BORRELLO, M. & SARIOLA, H. 2005. RET tyrosine kinase signaling in development and cancer. *Cytokine & Growth Factor Reviews,* 16**,** 441-67.

ASAI, N., JIJIWA, M., ENOMOTO, A., KAWAI, K., MAEDA, K., ICHIAHARA, M., MURAKUMO, Y. & TAKAHASHI, M. 2006. RET receptor signaling: dysfunction in thyroid cancer and Hirschsprung's disease. *Pathology International,* 56**,** 164-72.

AVEZOV, E., FRENKEL, Z., EHRLICH, M., HERSCOVICS, A. & LEDERKREMER, G. Z. 2008. Endoplasmic Reticulum (ER) Mannosidase I Is Compartmentalized and Required for N-Glycan Trimming to Man5–6GlcNAc2 in Glycoprotein ER-associated Degradation. *Molecular Biology of the Cell,* 19**,** 216-25.

BAINTON, D. F. 1981. The discovery of lysosomes. *The Journal of Cell Biology,* 91**,** 66s-76s.

BALLERINI, P., STRUSKI, S., CRESSON, C., PRADE, N., TOUJANI, S., DESWARTE, C., DOBBELSTEIN, S., PETIT, A., LAPILLONNE, H., GAUTIER, E. F., DEMUR, C., LIPPERT, E., PAGES, P., MANSAT-DE MAS, V., DONADIEU, J., HUGUET, F., DASTUGUE, N., BROCCARDO, C., PEROT, C. & DELABESSE, E. 2012. RET fusion genes are associated with chronic myelomonocytic leukemia and enhance monocytic differentiation. *Leukemia,* 11, 2384-89.

BALLINGER, C. A., CONNELL, P., WU, Y., HU, Z., THOMPSON, L. J., YIN, L.-Y. & PATTERSON, C. 1999. Identification of CHIP, a Novel Tetratricopeptide Repeat-Containing Protein That Interacts with Heat Shock Proteins and Negatively Regulates Chaperone Functions. *Molecular and Cellular Biology,* 19**,** 4535-45.

BERNALES, S., SCHUCK, S. & WALTER, P. 2007. ER-Phagy: Selective Autophagy of the Endoplasmic Reticulum. *Autophagy,* 3**,** 285-87.

BERNASCONI, R., GALLI, C., NOACK, J., BIANCHI, S., DE HAAN, CORNELIS A. M., REGGIORI, F. & MOLINARI, M. 2012. Role of the SEL1L:LC3-I Complex as an ERAD Tuning Receptor in the Mammalian ER. *Molecular Cell,* 46**,** 809-19.

BERTOLOTTI, A., ZHANG, Y., HENDERSHOT, L. M., HARDING, H. P. & RON, D. 2000. Dynamic interaction of BiP and ER stress transducers in the unfolded-protein response. *Nature Cell Biology,* 2**,** 326-32.

BESSET, V., SCOTT, R. P. & IBANEZ, C. F. 2000. Signaling complexes and protein-protein interactions involved in the activation of the Ras and phosphatidylinositol 3-kinase pathways by the c-Ret receptor tyrosine kinase. *The Journal of Biological Chemistry,* 275**,** 39159-66.

BOGGON, T. J., MURRAY, J., CHAPPUIS-FLAMENT, S., WONG, E., GUMBINER, B. M. & SHAPIRO, L. 2002. C-Cadherin Ectodomain Structure and Implications for Cell Adhesion Mechanisms. *Science,* 296, 1308-13*.*

BOLDEN, J. E., PEART, M. J. & JOHNSTONE, R. W. 2006. Anticancer activities of histone deacetylase inhibitors. *Nature Reviews Drug Discovery,* 5**,** 769-84.

BONANOMI, D., CHIVATAKARN, O., BAI, G., ABDESSELEM, H., LETTIERI, K., MARQUARDT, T., PIERCHALA, BRIAN A. & PFAFF, SAMUEL L. 2012. Ret Is a Multifunctional Coreceptor that Integrates Diffusible- and Contact-Axon Guidance Signals. *Cell,* 148**,** 568-82.

BORRELLO, M. G., ARDINI, E., LOCATI, L. D., GRECO, A., LICITRA, L. & PIEROTTI, M. A. 2013. RET inhibition: implications in cancer therapy. *Expert Opinion on Therapeutic Targets,* 17**,** 403-19.

BOULAY, A., BREULEUX, M., STEPHAN, C., FUX, C., BRISKEN, C., FICHE, M., WARTMANN, M., STUMM, M., LANE, H. A. & HYNES, N. E. 2008. The Ret Receptor Tyrosine Kinase Pathway Functionally Interacts with the ER{alpha} Pathway in Breast Cancer. *Cancer Research,* 68**,** 3743-51.

BRAAKMAN, I. & HEBERT, D. N. 2013. Protein Folding in the Endoplasmic Reticulum. *Cold Spring Harbor Perspectives in Biology,* 5, a013201.

BRADFORD, M. M. 1976. A rapid and sensitive method for the quantitation of microgram quantities of protein utilizing the principle of protein-dye binding. *Analytical Biochemistry,* 72**,** 248-54.

BRANDTS, J. F., BRENNAN, M. & LIN, L.-N. 1977. Unfolding and refolding occur much faster for a proline-free proteins than for most proline-containing proteins. *Proceedings of the National Academy of Sciences,* 74**,** 4178-81.

BRUNGER, A. T. 1992. Free R value: a novel statistical quantity for assessing the accuracy of crystal structures. *Nature,* 355**,** 472-75.

CAI, H., REINISCH, K. & FERRO-NOVICK, S. 2007. Coats, Tethers, Rabs, and SNAREs Work Together to Mediate the Intracellular Destination of a Transport Vesicle. *Developmental Cell,* 12**,** 671-82.

CALI, T., GALLI, C., OLIVARI, S. & MOLINARI, M. 2008. Segregation and rapid turnover of EDEM1 by an autophagy-like mechanism modulates standard ERAD and folding activities. *Biochemical and Biophysical Research Communications,* 371**,** 405-10.

CARLOMAGNO, F., DE VITA, G., BERLINGIERI, M. T., DE FRANCISCIS, V., MELILLO, R. M., COLANTUONI, V., KRAUS, M. H., DI FIORE, P. P., FUSCO, A. & SANTORO, M. 1996. Molecular heterogeneity of RET loss of function in Hirschsprung's disease. *EMBO Journal,* 15**,** 2717-25.

CARLOMAGNO, F., GUIDA, T., ANAGANTI, S., VECCHIO, G., FUSCO, A., RYAN, A. J., BILLAUD, M. & SANTORO, M. 2004. Disease associated mutations at valine 804 in the RET receptor tyrosine kinase confer resistance to selective kinase inhibitors. *Oncogene,* 23**,** 6056-63.

CARLOMAGNO, F., VITAGLIANO, D., GUIDA, T., CIARDIELLO, F., TORTORA, G., VECCHIO, G., RYAN, A. J., FONTANINI, G., FUSCO, A. & SANTORO, M. 2002a. ZD6474, an orally available inhibitor of KDR tyrosine kinase activity, efficiently blocks oncogenic RET kinases. *Cancer Research,* 62, 7284-90.

CARLOMAGNO, F., VITAGLIANO, D., GUIDA, T., NAPOLITANO, M., VECCHIO, G., FUSCO, A., GAZIT, A., LEVITZKI, A. & SANTORO, M. 2002b. The kinase inhibitor PP1 blocks tumorigenesis induced by RET oncogenes. *Cancer Research,* 62, 1077-82.

CARLSON, K. M., DOU, S., CHI, D., SCAVARDA, N., TOSHIMA, K., JACKSON, C. E., WELLS, S. A., JR., GOODFELLOW, P. J. & DONIS-KELLER, H. 1994. Single missense mutation in the tyrosine kinase catalytic domain of the RET protooncogene is associated with multiple endocrine neoplasia type 2B. *Proceedings of the National Academy of Sciences USA,* 91**,** 1579-83.

CARR, M., GILL, A. L. & WOODHEAD, S. 2004. 5-amino-2-carbonylthiophene derivatives for use as p38 map kinase inhibitors in the treatment of inflammatory diseases. Google Patents.

CARRACEDO, A., MA, L., TERUYA-FELDSTEIN, J., ROJO, F., SALMENA, L., ALIMONTI, A., EGIA, A., SASAKI, A. T., THOMAS, G., KOZMA, S. C., PAPA, A., NARDELLA, C., CANTLEY, L. C., BASELGA, J. & PANDOLFI, P. P. 2008. Inhibition of mTORC1 leads to MAPK pathway activation through a PI3K-dependent feedback loop in human cancer. *The Journal of Clinical Investigation,* 118**,** 3065-74.

CARVALHO, P., STANLEY, A. M. & RAPOPORT, T. A. 2010. Retrotranslocation of a misfolded luminal ER protein by the ubiquitin-ligase Hrd1p. *Cell,* 143**,** 579-91.

CHAKRAMA, F. Z., SEGUIN-PY, S., LE GRAND, J. N., FRAICHARD, A., DELAGE-MOURROUX, R., DESPOUY, G., PEREZ, V., JOUVENOT, M. & BOYER-GUITTAUT, M. 2010. GABARAPL1 (GEC1) associates with autophagic vesicles. *Autophagy,* 6**,** 495-505.

CHEN, H., MA, J., LI, W., ELISEENKOVA, A. V., XU, C., NEUBERT, T. A., MILLER, W. T. & MOHAMMADI, M. 2007. A molecular brake in the kinase hinge region regulates the activity of receptor tyrosine kinases. *Molecular Cell,* 27**,** 717-30.

CLARK, K., MACKENZIE, K. F., PETKEVICIUS, K., KRISTARIYANTO, Y., ZHANG, J., CHOI, H. G., PEGGIE, M., PLATER, L., PEDRIOLI, P. G., MCIVER, E., GRAY, N. S., ARTHUR, J. S. & COHEN, P. 2012. Phosphorylation of CRTC3 by the salt-inducible kinases controls the interconversion of classically activated and regulatory macrophages. *Proceedings of the National Academy of Sciences USA,* 109**,** 16986-91.

CLARK, K., PEGGIE, M., PLATER, L., SORCEK, R. J., YOUNG, E. R., MADWED, J. B., HOUGH, J., MCIVER, E. G. & COHEN, P. 2011. Novel cross-talk within the IKK family controls innate immunity. *Biochemical Journal,* 434**,** 93-104.

CLAYTON, A. H., WALKER, F., ORCHARD, S. G., HENDERSON, C., FUCHS, D., ROTHACKER, J., NICE, E. C. & BURGESS, A. W. 2005. Ligand-induced dimer-tetramer transition during the activation of the cell surface epidermal growth factor receptor-A multidimensional microscopy analysis. *The Journal of Biological Chemistry,* 280**,** 30392-99.

COLLABORATIVE COMPUTATIONAL PROJECT, Number 4. 1994. The CCP4 suite. Programs for protein crystallography. *Acta crystallographica. Section D,* 50**,** 760-63.

CONNELL, P., BALLINGER, C. A., JIANG, J., WU, Y., THOMPSON, L. J., HOHFELD, J. & PATTERSON, C. 2001. The co-chaperone CHIP regulates protein triage decisions mediated by heat-shock proteins. *Nature Cell Biology,* 3**,** 93-96.

COWAN-JACOB, S. W. 2006. Structural biology of protein tyrosine kinases. *Cellular and Molecular Life Sciences,* 63**,** 2608-25.

COWAN-JACOB, S. W., MOBITZ, H. & FABBRO, D. 2009. Structural biology contributions to tyrosine kinase drug discovery. *Current Opinion in Cell Biology,* 21**,** 280-87.

DAI, R., WILSON, D. J., GEDERS, T. W., ALDRICH, C. C. & FINZEL, B. C. 2014. Inhibition of Mycobacterium tuberculosis transaminase BioA by aryl hydrazines and hydrazides. *ChemBioChem,* 15**,** 575-86.

DAR, A. C., DAS, T. K., SHOKAT, K. M. & CAGAN, R. L. 2012. Chemical genetic discovery of targets and anti-targets for cancer polypharmacology. *Nature,* 486**,** 80-84.

DAS, T. & CAGAN, R. 2010. Drosophila as a novel therapeutic discovery tool for thyroid cancer. *Thyroid,* 20**,** 689-95.

DAWSON, D. M., LAWRENCE, E. G., MACLENNAN, G. T., AMINI, S. B., KUNG, H. J., ROBINSON, D., RESNICK, M. I., KURSH, E. D., PRETLOW, T. P. & PRETLOW, T. G. 1998. Altered expression of RET proto-oncogene product in prostatic intraepithelial neoplasia and prostate cancer. *Journal of the National Cancer Institute,* 90**,** 519-23.

DENG, X., DZAMKO, N., PRESCOTT, A., DAVIES, P., LIU, Q., YANG, Q., LEE, J. D., PATRICELLI, M. P., NOMANBHOY, T. K., ALESSI, D. R. & GRAY, N. S. 2011. Characterization of a selective inhibitor of the Parkinson's disease kinase LRRK2. *Nature Chemical Biology,* 7**,** 203-5.

DINER, P., ALAO, J. P., SODERLUND, J., SUNNERHAGEN, P. & GROTLI, M. 2012. Preparation of 3-substituted-1-isopropyl-1H-pyrazolo[3,4-d]pyrimidin-4-amines as RET kinase inhibitors. *Journal of Medicinal Chemistry,* 55**,** 4872-6.

DONIS-KELLER, H., DOU, S., CHI, D., CARLSON, K. M., TOSHIMA, K., LAIRMORE, T. C., HOWE, J. R., MOLEY, J. F., GOODFELLOW, P. & WELLS, S. A., JR. 1993. Mutations in the RET proto-oncogene are associated with MEN 2A and FMTC. *Human Molecular Genetics,* 2**,** 851-6.

DRUKER, B. J., TALPAZ, M., RESTA, D. J., PENG, B., BUCHDUNGER, E., FORD, J. M., LYDON, N. B., KANTARJIAN, H., CAPDEVILLE, R., OHNO-JONES, S. & SAWYERS, C. L. 2001. Efficacy and safety of a specific inhibitor of the BCR-ABL tyrosine kinase in chronic myeloid leukemia. *The New England Journal of Medicine,* 344**,** 1031-37.

EIGENBROT, C. & GERBER, N. 1997. X-ray structure of glial cell-derived neurotrophic factor at 1.9 A resolution and implications for receptor binding. *Nature Structural and Molecular Biology,* 4**,** 435-38.

ELLGAARD, L. & RUDDOCK, L. W. 2005. The human protein disulphide isomerase family: substrate interactions and functional properties. *EMBO Reports,* 6**,** 28-32.

ELLIS, R. J. & HARTL, F. U. 1999. Principles of protein folding in the cellular environment. *Current Opinions in Structural Biology,* 9**,** 102-10.

EMSLEY, P. & COWTAN, K. 2004. Coot: model-building tools for molecular graphics. *Acta Crystallographica D Biological Crystallography,* 60**,** 2126-32.

ESKO, J. D. & SELLECK, S. B. 2002. Order out of chaos: assembly of ligand binding sites in heparan sulfate. *Annual Review of Biochemistry,* 71**,** 435-71.

ESSEGHIR, S., TODD, S. K., HUNT, T., POULSOM, R., PLAZA-MENACHO, I., REIS-FILHO, J. S. & ISACKE, C. M. 2007. A Role for Glial Cell–Derived Neurotrophic Factor–Induced Expression by Inflammatory Cytokines and RET/GFRA1 Receptor Up-regulation in Breast Cancer. *Cancer Research,* 67, 11732-41.

EVANS, P. 2006. Scaling and assessment of data quality. *Acta Crystallographica D Biological Crystallography,* 62**,** 72-82.

EVANS, P. R. & MURSHUDOV, G. N. 2013. How good are my data and what is the resolution? *Acta Crystallographica D Biological Crystallography,* 69**,** 1204-14.

FANG, S., FERRONE, M., YANG, C., JENSEN, J. P., TIWARI, S. & WEISSMAN, A. M. 2001. The tumor autocrine motility factor receptor, gp78, is a ubiquitin protein ligase implicated in degradation from the endoplasmic reticulum. *Proceedings of the National Academy of Sciences,* 98**,** 14422-27.

FEDOROV, O., MARSDEN, B., POGACIC, V., RELLOS, P., MULLER, S., BULLOCK, A. N., SCHWALLER, J., SUNDSTROM, M. & KNAPP, S. 2007. A systematic interaction map of validated kinase inhibitors with Ser/Thr kinases. *Proceedings of the National Academy of Sciences,* 104**,** 20523-28.

FEDOROV, O., NIESEN, F. H. & KNAPP, S. 2012. Kinase inhibitor selectivity profiling using differential scanning fluorimetry. *Methods in Molecular Biology,* 795**,** 109-18.

FELDMAN, M. E., APSEL, B., UOTILA, A., LOEWITH, R., KNIGHT, Z. A., RUGGERO, D. & SHOKAT, K. M. 2009. Active-site inhibitors of mTOR target rapamycin-resistant outputs of mTORC1 and mTORC2. *PLoS Biology,* 7**,** e38.

FINLEY, D. 2009. Recognition and processing of ubiquitin-protein conjugates by the proteasome. *Annual Review of Biochemistry,* 78**,** 477-513.

FORGAC, M. 1998. Structure, function and regulation of the vacuolar (H+)-ATPases. *FEBS Letters,* 440**,** 258-63.

FRENCH, A. R., SUDLOW, G. P., WILEY, H. S. & LAUFFENBURGER, D. A. 1994. Postendocytic trafficking of epidermal growth factor-receptor complexes is mediated through saturable and specific endosomal interactions. *Journal of Biological Chemistry,* 269**,** 15749-55.

FURDUI, C., LEW, E., SCHLESSINGER, J. & ANDERSON, K. 2006. Autophosphorylation of FGFR1 kinase is mediated by a sequential and precisely ordered reaction. *Molecular Cell,* 21**,** 711-17.

GAJIWALA, K. S., WU, J. C., CHRISTENSEN, J., DESHMUKH, G. D., DIEHL, W., DINITTO, J. P., ENGLISH, J. M., GREIG, M. J., HE, Y. A., JACQUES, S. L., LUNNEY, E. A., MCTIGUE, M., MOLINA, D., QUENZER, T., WELLS, P. A., YU, X., ZHANG, Y., ZOU, A., EMMETT, M. R., MARSHALL, A. G., ZHANG, H. M. & DEMETRI, G. D. 2009. KIT kinase mutants show unique mechanisms of drug resistance to imatinib and sunitinib in gastrointestinal stromal tumor patients. *Proceedings of the National Academy of Sciences,* 106**,** 1542-47.

GAUTREAU, A., OGUIEVETSKAIA, K. & UNGERMANN, C. 2014. Function and Regulation of the Endosomal Fusion and Fission Machineries. *Cold Spring Harbor Perspectives in Biology,* 6, a016832.

GENESTE, O., BIDAUD, C., DE VITA, G., HOFSTRA, R. M., TARTARE-DECKERT, S., BUYS, C. H., LENOIR, G. M., SANTORO, M. & BILLAUD, M. 1999. Two distinct mutations of the RET receptor causing Hirschsprung's disease impair the binding of signalling effectors to a multifunctional docking site. *Human Molecular Genetics,* 8**,** 1989-99.

GHORI, K., O'DRISCOLL, J. & SHORTEN, G. 2010. The effect of midazolam on neutrophil mitogen-activated protein kinase. *European Journal of Anaesthesiology,* 27**,** 562-65.

GOH, L. K. & SORKIN, A. 2013. Endocytosis of Receptor Tyrosine Kinases. *Cold Spring Harbor Perspectives in Biology,* 5, a017459.

GONZALEZ, D. S., KARAVEG, K., VANDERSALL-NAIRN, A. S., LAL, A. & MOREMEN, K. W. 1999. Identification, Expression, and Characterization of a cDNA Encoding Human Endoplasmic Reticulum Mannosidase I, the Enzyme That Catalyzes the First Mannose Trimming Step in Mammalian Asn-linked Oligosaccharide Biosynthesis. *Journal of Biological Chemistry,* 274**,** 21375-86.

GORGUN, G., CALABRESE, E., HIDESHIMA, T., ECSEDY, J., PERRONE, G., MANI, M., IKEDA, H., BIANCHI, G., HU, Y., CIRSTEA, D., SANTO, L., TAI, Y. T., NAHAR, S., ZHENG, M., BANDI, M., CARRASCO, R. D., RAJE, N., MUNSHI, N., RICHARDSON, P. & ANDERSON, K. C. 2010. A novel Aurora-A kinase inhibitor MLN8237 induces cytotoxicity and cell-cycle arrest in multiple myeloma. *Blood,* 115**,** 5202-13.

GRAHAM, F. L., SMILEY, J., RUSSELL, W. C. & NAIRN, R. 1977. Characteristics of a human cell line transformed by DNA from human adenovirus type 5. *Journal of General Virology,* 36**,** 59-74.

GSCHWIND, A., FISCHER, O. M. & ULLRICH, A. 2004. The discovery of receptor tyrosine kinases: targets for cancer therapy. *Nature Reviews Cancer,* 4**,** 361-70.

GUPTA, R., JUNG, E. & BRUNAK, S. 2004. *Prediction of N-glycosylation sites in human proteins.* http://www.cbs.dtu.dk/services/NetNGlyc/. [Online].

HAHN, M. & BISHOP, J. M. 2001. Expression pattern of Drosophila ret suggests a common ancestral origin between the metamorphosis precursors in insect endoderm and the vertebrate enteric neurons. *Proceedings of the National Academy of Sciences,* 98**,** 1053-58.

HANKE, J. H., GARDNER, J. P., DOW, R. L., CHANGELIAN, P. S., BRISSETTE, W. H., WERINGER, E. J., POLLOK, B. A. & CONNELLY, P. A. 1996. Discovery of a novel, potent, and Src family-selective tyrosine kinase inhibitor. Study of Lck- and FynT-dependent T cell activation. *Journal of Biological Chemistry,* 271**,** 695-701.

HANSON, S. R., CULYBA, E. K., HSU, T.-L., WONG, C.-H., KELLY, J. W. & POWERS, E. T. 2009. The core trisaccharide of an N-linked glycoprotein intrinsically accelerates folding and enhances stability. *Proceedings of the National Academy of Sciences,* 106**,** 3131-36.

HARDING, H. P., ZHANG, Y. & RON, D. 1999. Protein translation and folding are coupled by an endoplasmic-reticulum-resident kinase. *Nature,* 397**,** 271-4.

HARRISON, O., JIN, X., HONG, S., BAHNA, F., AHLSEN, G., BRASCH, J., WU, Y., VENDOME, J., FELSOVALYI, K., HAMPTON, C., TROYANOVSKY, R., BEN SHAUL, A., FRANK, J., TROYANOVSKY, S., SHAPIRO, L. & HONIG, B. 2011. The extracellular architecture of adherens junctions revealed by crystal structures of type I cadherins. *Structure,* 19**,** 244-56.

HATINEN, T., HOLM, L. & AIRAKSINEN, M. S. 2007. Loss of neurturin in frog--Comparative genomics study of GDNF family ligand-receptor pairs. *Molecular and Cellular Neuroscience,* 34**,** 155-67.

HAURI, H. P., KAPPELER, F., ANDERSSON, H. & APPENZELLER, C. 2000. ERGIC-53 and traffic in the secretory pathway. *Journal of Cell Science,* 113 (Pt 4)**,** 587-96.

HAWRYLUK, M. J., KEYEL, P. A., MISHRA, S. K., WATKINS, S. C., HEUSER, J. E. & TRAUB, L. M. 2006. Epsin 1 is a polyubiquitin-selective clathrin-associated sorting protein. *Traffic,* 7**,** 262-81.

HEANUE, T. A. & PACHNIS, V. 2007. Enteric nervous system development and Hirschsprung's disease: advances in genetic and stem cell studies. *Nature Reviews Neuroscience,* 8**,** 466-79.

HEBERT, D. N., BERNASCONI, R. & MOLINARI, M. 2010. ERAD substrates: Which way out? *Seminars in Cell and Developmental Biology,* 21, 526-32.

HEBERT, D. N., FOELLMER, B. & HELENIUS, A. 1995. Glucose trimming and reglucosylation determine glycoprotein association with calnexin in the endoplasmic reticulum. *Cell,* 81**,** 425-33.

HEBERT, D. N., FOELLMER, B. & HELENIUS, A. 1996. Calnexin and calreticulin promote folding, delay oligomerization and suppress degradation of influenza hemagglutinin in microsomes. *EMBO Journal,* 15**,** 2961-68.

HENDERSHOT, L. M. 2004. The ER function BiP is a master regulator of ER function. *Mount Sinai Journal of Medicine,* 71**,** 289-97.

HIRAO, K., NATSUKA, Y., TAMURA, T., WADA, I., MORITO, D., NATSUKA, S., ROMERO, P., SLENO, B., TREMBLAY, L. O., HERSCOVICS, A., NAGATA, K. & HOSOKAWA, N. 2006. EDEM3, a Soluble EDEM Homolog, Enhances Glycoprotein Endoplasmic Reticulum-associated Degradation and Mannose Trimming. *Journal of Biological Chemistry,* 281**,** 9650-58.

HIRATA, Y., SHIMOKAWA, N., OH-HASHI, K., YU, Z. X. & KIUCHI, K. 2010. Acidification of the Golgi apparatus is indispensable for maturation but not for cell surface delivery of Ret. *Journal of Neurochemistry,* 115**,** 606-13.

HIRSCHSPRUNG, H. 1888. Stuhltragheit neugeborener in folge von dilatation und hypertrophie des colons. *Jahrb Kinderheilk,* 27**,** 1-7.

HOFSTRA, R. M., LANDSVATER, R. M., CECCHERINI, I., STULP, R. P., STELWAGEN, T., LUO, Y., PASINI, B., HOPPENER, J. W., VAN AMSTEL, H. K., ROMEO, G. & ET AL. 1994. A mutation in the RET proto-oncogene associated with multiple endocrine neoplasia type 2B and sporadic medullary thyroid carcinoma. *Nature,* 367**,** 375-76.

HORIBE, T., YOSHO, C., OKADA, S., TSUKAMOTO, M., NAGAI, H., HAGIWARA, Y., TUJIMOTO, Y. & KIKUCHI, M. 2002. The chaperone activity of protein disulfide isomerase is affected by cyclophilin B and cyclosporin A in vitro. *Journal of Biochemistry,* 132**,** 401-7.

HOSOKAWA, N., KAMIYA, Y., KAMIYA, D., KATO, K. & NAGATA, K. 2009. Human OS-9, a Lectin Required for Glycoprotein Endoplasmic Reticulum-associated Degradation, Recognizes Mannose-trimmed N-Glycans. *Journal of Biological Chemistry,* 284**,** 17061-68.

HOSOKAWA, N., TREMBLAY, L. O., SLENO, B., KAMIYA, Y., WADA, I., NAGATA, K., KATO, K. & HERSCOVICS, A. 2010. EDEM1 accelerates the trimming of α1,2-linked mannose on the C branch of N-glycans. *Glycobiology,* 20**,** 567-75.

HOSOKAWA, N., WADA, I., HASEGAWA, K., YORIHUZI, T., TREMBLAY, L. O., HERSCOVICS, A. & NAGATA, K. 2001. A novel ER α ‐ mannosidase ‐ like protein accelerates ER ‐ associated degradation. *EMBO reports,* 2**,** 415-22.

HOSOKAWA, N., WADA, I., NAGASAWA, K., MORIYAMA, T., OKAWA, K. & NAGATA, K. 2008. Human XTP3-B Forms an Endoplasmic Reticulum Quality Control Scaffold with the HRD1-SEL1L Ubiquitin Ligase Complex and BiP. *Journal of Biological Chemistry,* 283**,** 20914-24.

HUANG, F., KHVOROVA, A., MARSHALL, W. & SORKIN, A. 2004. Analysis of Clathrin-mediated Endocytosis of Epidermal Growth Factor Receptor by RNA Interference. *Journal of Biological Chemistry,* 279**,** 16657-61.

HUBBARD, S. R. 1997. Crystal structure of the activated insulin receptor tyrosine kinase in complex with peptide substrate and ATP analog. *EMBO Journal,* 16**,** 5572-81.

HUBBARD, S. R. & MILLER, W. T. 2007. Receptor tyrosine kinases: mechanisms of activation and signaling. *Current Opinions in Cell Biology,* 19**,** 117-23.

HUBBARD, S. R., WEI, L., ELLIS, L. & HENDRICKSON, W. A. 1994. Crystal structure of the tyrosine kinase domain of the human insulin receptor. *Nature,* 372**,** 746-54.

HUECKSTEADT, T., OLEFSKY, J. M., BRANDENBERG, D. & HEIDENREICH, K. A. 1986. Recycling of photoaffinity-labeled insulin receptors in rat adipocytes. Dissociation of insulin-receptor complexes is not required for receptor recycling. *Journal of Biological Chemistry,* 261**,** 8655-59.

HUSE, M. & KURIYAN, J. 2002. The conformational plasticity of protein kinases. *Cell,* 109**,** 275-82.

HUTTON, J. A., GONCALVES, V., BRANNIGAN, J. A., PAAPE, D., WRIGHT, M. H., WAUGH, T. M., ROBERTS, S. M., BELL, A. S., WILKINSON, A. J., SMITH, D. F., LEATHERBARROW, R. J., TATE, E. W. 2014. Structure-based design of potent and selective *Leishmania N*-myristoyltransferase inhibitors. *Journal of Medicinal Chemistry,* 57, 8664-70.

HYTTINEN, J. M. T., AMADIO, M., VIIRI, J., PASCALE, A., SALMINEN, A. & KAARNIRANTA, K. 2014. Clearance of misfolded and aggregated proteins by aggrephagy and implications for aggregation diseases. *Ageing Research Reviews,* 18**,** 16-28.

ITO, S., IWASHITA, T., ASAI, N., MURAKAMI, H., IWATA, Y., SOBUE, G. & TAKAHASHI, M. 1997. Biological properties of Ret with cysteine mutations correlate with multiple endocrine neoplasia type 2A, familial medullary thyroid carcinoma, and Hirschsprung's disease phenotype. *Cancer Research,* 57**,** 2870-72.

JAIN, S., ENCINAS, M., JOHNSON, E. M. & MILBRANDT, J. 2006. Critical and distinct roles for key RET tyrosine docking sites in renal development. *Genes & Development,* 20**,** 321-33.

JAIN, S., NAUGHTON, C. K., YANG, M., STRICKLAND, A., VIJ, K., ENCINAS, M., GOLDEN, J., GUPTA, A., HEUCKEROTH, R., JOHNSON, E. M. & MILBRANDT, J. 2004. Mice expressing a dominant-negative Ret mutation phenocopy human Hirschsprung disease and delineate a direct role of Ret in spermatogenesis. *Development,* 131**,** 5503-13.

JANG, K. W., LEE, J. E., KIM, S. Y., KANG, M. W., NA, M. H., LEE, C. S., SONG, K. S. & LIM, S. P. 2011. The C-terminus of Hsp70-interacting protein promotes Met receptor degradation. *Journal of Thoracic Oncology,* 6**,** 679-87.

JIANG, J., BALLINGER, C. A., WU, Y., DAI, Q., CYR, D. M., HÖHFELD, J. & PATTERSON, C. 2001. CHIP Is a U-box-dependent E3 Ubiquitin Ligase: IDENTIFICATION OF Hsc70 AS A TARGET FOR UBIQUITYLATION. *Journal of Biological Chemistry,* 276**,** 42938-44.

JOHNSON, L. N., NOBLE, M. E. M. & OWEN, D. J. 1996. Active and Inactive Protein Kinases: Structural Basis for Regulation. *Cell,* 85**,** 149-58.

KABEYA, Y., MIZUSHIMA, N., UENO, T., YAMAMOTO, A., KIRISAKO, T., NODA, T., KOMINAMI, E., OHSUMI, Y. & YOSHIMORI, T. 2000. LC3, a mammalian homologue of yeast Apg8p, is localized in autophagosome membranes after processing. *EMBO Journal,* 19**,** 5720-28.

KABSCH, W. 2010. XDS. *Acta Crystallographica D Biological Crystallography,* 66**,** 125-32.

KAJIRO, M., HIROTA, R., NAKAJIMA, Y., KAWANOWA, K., SO-MA, K., ITO, I., YAMAGUCHI, Y., OHIE, S.-H., KOBAYASHI, Y., SEINO, Y., KAWANO, M., KAWABE, Y.-I., TAKEI, H., HAYASHI, S.-I., KUROSUMI, M., MURAYAMA, A., KIMURA, K. & YANAGISAWA, J. 2009. The ubiquitin ligase CHIP acts as an upstream regulator of oncogenic pathways. *Nat Cell Biol,* 11**,** 312-319.

KANNAN, N. & NEUWALD, A. F. 2005. Did protein kinase regulatory mechanisms evolve through elaboration of a simple structural component? *Journal of Molecular Biology,* 351**,** 956-72.

KANTARDJIEFF, K. A. & RUPP, B. 2003. Matthews coefficient probabilities: Improved estimates for unit cell contents of proteins, DNA, and protein-nucleic acid complex crystals. *Protein Science,* 12**,** 1865-71.

KAWAMOTO, Y., TAKEDA, K., OKUNO, Y., YAMAKAWA, Y., ITO, Y., TAGUCHI, R., KATO, M., SUZUKI, H., TAKAHASHI, M. & NAKASHIMA, I. 2004. Identification of RET autophosphorylation sites by mass spectrometry. *Journal of Biological Chemistry,* 279**,** 14213-24.

KIKKERT, M., DOOLMAN, R., DAI, M., AVNER, R., HASSINK, G., VAN VOORDEN, S., THANEDAR, S., ROITELMAN, J., CHAU, V. & WIERTZ, E. 2004. Human HRD1 Is an E3 Ubiquitin Ligase Involved in Degradation of Proteins from the Endoplasmic Reticulum. *Journal of Biological Chemistry,* 279**,** 3525-34.

KIM, J., CHOI, T. G., DING, Y., KIM, Y., HA, K. S., LEE, K. H., KANG, I., HA, J., KAUFMAN, R. J., LEE, J., CHOE, W. & KIM, S. S. 2008. Overexpressed

cyclophilin B suppresses apoptosis associated with ROS and Ca2+ homeostasis after ER stress. *Journal of Cell Science,* 121**,** 3636-48.

KIVIRIKKO, K. I. & MYLLYHARJU, J. 1998. Prolyl 4-hydroxylases and their protein disulfide isomerase subunit. *Matrix Biology,* 16**,** 357-68.

KJAER, S., HANRAHAN, S., TOTTY, N. & MCDONALD, N. Q. 2010. Mammal-restricted elements predispose human RET to folding impairment by HSCR mutations. *Nature Structural and Molecular Biology,* 17**,** 726-31.

KJAER, S. & IBANEZ, C. F. 2003. Identification of a Surface for Binding to the GDNF-GFRa1 Complex in the First Cadherin-like Domain of RET. *Journal of Biological Chemistry,* 278**,** 47898-904.

KJAER, S. & IBANEZ, C. F. 2003a. Intrinsic susceptibility to misfolding of a hot-spot for Hirschsprung disease mutations in the ectodomain of RET. *Human Molecular Genetics,* 12, 2133-44.

KJAER, S., KUROKAWA, K., PERRINJAQUET, M., ABRESCIA, C. & IBANEZ, C. F. 2006. Self-association of the transmembrane domain of RET underlies oncogenic activation by MEN2A mutations. *Oncogene,* 25**,** 7086-95.

KLEIN, R. D., SHERMAN, D., HO, W. H., STONE, D., BENNETT, G. L., MOFFAT, B., VANDLEN, R., SIMMONS, L., GU, Q., HONGO, J. A., DEVAUX, B., POULSEN, K., ARMANINI, M., NOZAKI, C., ASAI, N., GODDARD, A., PHILLIPS, H., HENDERSON, C. E., TAKAHASHI, M. & ROSENTHAL, A. 1997. A GPI-linked protein that interacts with Ret to form a candidate neurturin receptor. *Nature,* 387**,** 717-21.

KNIGHTON, D. R., ZHENG, J., EYCK, L. F. T., ASHFORD, V. A., XUONG, N.-H., TAYLOR, S. S. & SOWADSKI, J. M. 1991. Crystal Structure of the Catalytic Subunit of Cyclic Adenosine Monophosphate-Dependent Protein Kinase. *Science,* 253**,** 407-14.

KNOWLES, P. P., MURRAY-RUST, J., KJAER, S., SCOTT, R. P., HANRAHAN, S., SANTORO, M., IBANEZ, C. F. & MCDONALD, N. Q. 2006. Structure and chemical inhibition of the RET tyrosine kinase domain. *The Journal of Biological Chemistry,* 281**,** 33577-87.

KODAMA, Y., ASAI, N., KAWAI, K., JIJIWA, M., MURAKUMO, Y., ICHIHARA, M. & TAKAHASHI, M. 2005. The RET proto-oncogene: a molecular therapeutic target in thyroid cancer. *Cancer Science,* 96**,** 143-48.

KOHNO, T., ICHIKAWA, H., TOTOKI, Y., YASUDA, K., HIRAMOTO, M., NAMMO, T., SAKAMOTO, H., TSUTA, K., FURUTA, K., SHIMADA, Y., IWAKAWA, R., OGIWARA, H., OIKE, T., ENARI, M., SCHETTER, A. J., OKAYAMA, H., HAUGEN, A., SKAUG, V., CHIKU, S., YAMANAKA, I., ARAI, Y., WATANABE, S., SEKINE, I., OGAWA, S., HARRIS, C. C., TSUDA, H., YOSHIDA, T., YOKOTA, J. & SHIBATA, T. 2012. KIF5B-RET fusions in lung adenocarcinoma. *Nature Medicine,* 18**,** 375-77.

KOMATSU, N., AOKI, K., YAMADA, M., YUKINAGA, H., FUJITA, Y., KAMIOKA, Y. & MATSUDA, M. 2011. Development of an optimized backbone of FRET

biosensors for kinases and GTPases. *Molecular Biology of the Cell,* 22**,** 4647-56.

KORAC, J., SCHAEFFER, V., KOVACEVIC, I., CLEMENT, A. M., JUNGBLUT, B., BEHL, C., TERZIC, J. & DIKIC, I. 2013. Ubiquitin-independent function of optineurin in autophagic clearance of protein aggregates. *Journal of Cell Science,* 126**,** 580-92.

KORNEV, A. P., HASTE, N. M., TAYLOR, S. S. & TEN EYCK, L. F. 2006. Surface comparison of active and inactive protein kinases identifies a conserved activation mechanism. *Proceedings of the National Academy of Sciences,* 103**,** 17783-88.

KORNEV, A. P., TAYLOR, S. S. & TEN EYCK, L. F. 2008. A helix scaffold for the assembly of active protein kinases. *Proceeding of the National Academy of Sciences,* 105**,** 14377-82.

KOZLOV, G., BASTOS-ARISTIZABAL, S., MÄÄTTÄNEN, P., ROSENAUER, A., ZHENG, F., KILLIKELLY, A., TREMPE, J.-F., THOMAS, D. Y. & GEHRING, K. 2010. Structural Basis of Cyclophilin B Binding by the Calnexin/Calreticulin P-domain. *Journal of Biological Chemistry,* 285**,** 35551-57.

KRAMER, E. R., ARON, L., RAMAKERS, G. M., SEITZ, S., ZHUANG, X., BEYER, K., SMIDT, M. P. & KLEIN, R. 2007. Absence of Ret signaling in mice causes progressive and late degeneration of the nigrostriatal system. *PLoS Biology,* 5**,** e39.

KRISHNAMOORTHY, G. P., GUIDA, T., ALFANO, L., AVILLA, E., SANTORO, M., CARLOMAGNO, F. & MELILLO, R. M. 2013. Molecular mechanism of 17-Allylamino-17-demethoxygeldanamycin (17-AAG) induced AXL degradation. *Journal of Biological Chemistry,* 288, 17481-94.

KURIYAN, J. & EISENBERG, D. 2007. The origin of protein interactions and allostery in colocalization. *Nature,* 450**,** 983-90.

LABRIOLA, C., CAZZULO, J. J. & PARODI, A. J. 1995. Retention of glucose units added by the UDP-GLC:glycoprotein glucosyltransferase delays exit of glycoproteins from the endoplasmic reticulum. *The Journal of Cell Biology,* 130**,** 771-79.

LAMARK, T. & JOHANSEN, T. 2012. Aggrephagy: selective disposal of protein aggregates by macroautophagy. *International Journal of Cell Biology,* 2012**,** 736905.

LAMPUGNANI, M. G., ORSENIGO, F., GAGLIANI, M. C., TACCHETTI, C. & DEJANA, E. 2006. Vascular endothelial cadherin controls VEGFR-2 internalization and signaling from intracellular compartments. *The Journal of Cell Biology,* 174**,** 593-604.

LAND, A., ZONNEVELD, D. & BRAAKMAN, I. 2003. Folding of HIV-1 Envelope glycoprotein involves extensive isomerization of disulfide bonds and conformation-dependent leader peptide cleavage. *The FASEB Journal,* 17**,** 1058-67.

LANG, K., SCHMID, F. X. & FISCHER, G. 1987. Catalysis of protein folding by prolyl isomerase. *Nature,* 329**,** 268-70.

LASSILA, J. K., ZALATAN, J. G. & HERSCHLAG, D. 2011. Biological phosphoryl-transfer reactions: understanding mechanism and catalysis. *Annual Review of Biochemistry,* 80**,** 669-702.

LAU, K. S., PARTRIDGE, E. A., GRIGORIAN, A., SILVESCU, C. I., REINHOLD, V. N., DEMETRIOU, M. & DENNIS, J. W. 2007. Complex N-glycan number and degree of branching cooperate to regulate cell proliferation and differentiation. *Cell,* 129**,** 123-34.

LEE, M. C., ORCI, L., HAMAMOTO, S., FUTAI, E., RAVAZZOLA, M. & SCHEKMAN, R. 2005. Sar1p N-terminal helix initiates membrane curvature and completes the fission of a COPII vesicle. *Cell,* 122**,** 605-17.

LEMMON, M. A. & SCHLESSINGER, J. 2010. Cell Signaling by Receptor Tyrosine Kinases. *Cell,* 141, 1117-34.

LEMMON, M. A., SCHLESSINGER, J. & FERGUSON, K. M. 2014. The EGFR Family: Not So Prototypical Receptor Tyrosine Kinases. *Cold Spring Harbor Perspectives in Biology,* 6, a020768.

LEPPANEN, V. M., BESPALOV, M. M., RUNEBERG-ROOS, P., PUURAND, U., MERITS, A., SAARMA, M. & GOLDMAN, A. 2004. The structure of GFRalpha1 domain 3 reveals new insights into GDNF binding and RET activation. *EMBO Journal,* 23**,** 1452-62.

LESLIE, A. G. 2006. The integration of macromolecular diffraction data. *Acta Crystallographica D Biological Crystallography,* 62**,** 48-57.

LINGWOOD, D. & SIMONS, K. 2010. Lipid rafts as a membrane-organizing principle. *Science,* 327**,** 46-50.

LIPSON, D., CAPELLETTI, M., YELENSKY, R., OTTO, G., PARKER, A., JAROSZ, M., CURRAN, J. A., BALASUBRAMANIAN, S., BLOOM, T., BRENNAN, K. W., DONAHUE, A., DOWNING, S. R., FRAMPTON, G. M., GARCIA, L., JUHN, F., MITCHELL, K. C., WHITE, E., WHITE, J., ZWIRKO, Z., PERETZ, T., NECHUSHTAN, H., SOUSSAN-GUTMAN, L., KIM, J., SASAKI, H., KIM, H. R., PARK, S. I., ERCAN, D., SHEEHAN, C. E., ROSS, J. S., CRONIN, M. T., JANNE, P. A. & STEPHENS, P. J. 2012. Identification of new ALK and RET gene fusions from colorectal and lung cancer biopsies. *Nature Medicine,* 18**,** 382-84.

LIU, F.-H., WU, S.-J., HU, S.-M., HSIAO, C.-D. & WANG, C. 1999. Specific Interaction of the 70-kDa Heat Shock Cognate Protein with the Tetratricopeptide Repeats. *Journal of Biological Chemistry,* 274**,** 34425-32.

LIU, Q., KIRUBAKARAN, S., HUR, W., NIEPEL, M., WESTOVER, K., THOREEN, C. C., WANG, J., NI, J., PATRICELLI, M. P., VOGEL, K., RIDDLE, S., WALLER, D. L., TRAYNOR, R., SANDA, T., ZHAO, Z., KANG, S. A., ZHAO, J., LOOK, A. T., SORGER, P. K., SABATINI, D. M. & GRAY, N. S. 2012. Kinome-wide selectivity profiling of ATP-competitive mammalian target of rapamycin (mTOR)

inhibitors and characterization of their binding kinetics. *Journal of Biological Chemistry,* 287**,** 9742-52.

LIU, X., VEGA, Q. C., DECKER, R. A., PANDEY, A., WORBY, C. A. & DIXON, J. E. 1996. Oncogenic RET receptors display different autophosphorylation sites and substrate binding specificities. *Journal of Biological Chemistry,* 271**,** 5309-12.

LIU, Y. & GRAY, N. S. 2006. Rational design of inhibitors that bind to inactive kinase conformations. *Nature Chemical Biology,* 2**,** 358-64.

LONGATTI, A. & TOOZE, S. A. 2009. Vesicular trafficking and autophagosome formation. *Cell Death & Differentiation,* 16**,** 956-65.

LORD, C., FERRO-NOVICK, S. & MILLER, E. A. 2013. The Highly Conserved COPII Coat Complex Sorts Cargo from the Endoplasmic Reticulum and Targets It to the Golgi. *Cold Spring Harbor Perspectives in Biology,* 5, a013367.

LUO, Y., TSUCHIYA, K. D., PARK, D. I., FAUSEL, R., KANNGURN, S., WELCSH, P., DZIECIATKOWSKI, S., WANG, J. & GRADY, W. M. 2012. RET is a potential tumor suppressor gene in colorectal cancer. *Oncogene,* 32, 2037-47*.*

MALO, N., HANLEY, J. A., CERQUOZZI, S., PELLETIER, J. & NADON, R. 2006. Statistical practice in high-throughput screening data analysis. *Nature Biotechnology,* 24**,** 167-75.

MARCOS-GUTIERREZ, C. V., WILSON, S. W., HOLDER, N. & PACHNIS, V. 1997. The zebrafish homologue of the ret receptor and its pattern of expression during embryogenesis. *Oncogene,* 14**,** 879-89.

MARMOR, M. D. & YARDEN, Y. 2004. Role of protein ubiquitylation in regulating endocytosis of receptor tyrosine kinases. *Oncogene,* 21, 2057-70*.*

MARTINEZ-MENARGUEZ, J. A., GEUZE, H. J., SLOT, J. W. & KLUMPERMAN, J. 1999. Vesicular tubular clusters between the ER and Golgi mediate concentration of soluble secretory proteins by exclusion from COPI-coated vesicles. *Cell,* 98**,** 81-90.

MAST, S. W., DIEKMAN, K., KARAVEG, K., DAVIS, A., SIFERS, R. N. & MOREMEN, K. W. 2005. Human EDEM2, a novel homolog of family 47 glycosidases, is involved in ER-associated degradation of glycoproteins. *Glycobiology,* 15**,** 421-36.

MASTERS, J. R. 2002. HeLa cells 50 years on: the good, the bad and the ugly. *Nature Review Cancer,* 2**,** 315-19.

MATSUMURA, Y., SAKAI, J. & SKACH, W. R. 2013. Endoplasmic Reticulum Protein Quality Control Is Determined by Cooperative Interactions between Hsp/c70 Protein and the CHIP E3 Ligase. *Journal of Biological Chemistry,* 288**,** 31069-79.

MATTHEWS, B. W. 1968. Solvent content of protein crystals. *Journal of Molecular Biology,* 33**,** 491-97.

MCCOY, A. J., GROSSE-KUNSTLEVE, R. W., ADAMS, P. D., WINN, M. D., STORONI, L. C. & READ, R. J. 2007. Phaser crystallographic software. *Journal of Applied Crystallography,* 40**,** 658-74.

MCKERN, N. M., LAWRENCE, M. C., STRELTSOV, V. A., LOU, M.-Z., ADAMS, T. E., LOVRECZ, G. O., ELLEMAN, T. C., RICHARDS, K. M., BENTLEY, J. D., PILLING, P. A., HOYNE, P. A., CARTLEDGE, K. A., PHAM, T. M., LEWIS, J. L., SANKOVICH, S. E., STOICHEVSKA, V., DA SILVA, E., ROBINSON, C. P., FRENKEL, M. J., SPARROW, L. G., FERNLEY, R. T., EPA, V. C. & WARD, C. W. 2006. Structure of the insulin receptor ectodomain reveals a folded-over conformation. *Nature,* 443**,** 218-21.

MCTIGUE, M., MURRAY, B. W., CHEN, J. H., DENG, Y. L., SOLOWIEJ, J. & KANIA, R. S. 2012. Molecular conformations, interactions, and properties associated with drug efficiency and clinical performance among VEGFR TK inhibitors. *Proceedings of the National Academy of Sciences,* 109**,** 18281-89.

MEDINA-KAUWE, L. K., XIE, J. & HAMM-ALVAREZ, S. 2005. Intracellular trafficking of nonviral vectors. *Gene Therapy,* 12**,** 1734-51.

MIACZYNSKA, M., PELKMANS, L. & ZERIAL, M. 2004. Not just a sink: endosomes in control of signal transduction. *Current Opinions in Cell Biology,* 16**,** 400-6.

MIDUTURU, C. V., DENG, X., KWIATKOWSKI, N., YANG, W., BRAULT, L., FILIPPAKOPOULOS, P., CHUNG, E., YANG, Q., SCHWALLER, J., KNAPP, S., KING, R. W., LEE, J. D., HERRGARD, S., ZARRINKAR, P. & GRAY, N. S. 2011. High-throughput kinase profiling: a more efficient approach toward the discovery of new kinase inhibitors. *Chemistry & Biology,* 18**,** 868-79.

MOLINARI, M., CALANCA, V., GALLI, C., LUCCA, P. & PAGANETTI, P. 2003. Role of EDEM in the release of misfolded glycoproteins from the calnexin cycle. *Science,* 299, 1397-400*.*

MOLOGNI, L., ROSTAGNO, R., BRUSSOLO, S., KNOWLES, P. P., KJAER, S., MURRAY-RUST, J., ROSSO, E., ZAMBON, A., SCAPOZZA, L., MCDONALD, N. Q., LUCCHINI, V. & GAMBACORTI-PASSERINI, C. 2010. Synthesis, structure-activity relationship and crystallographic studies of 3-substituted indolin-2-one RET inhibitors. *Bioorganic & Medicinal Chemistry,* 18**,** 1482-96.

MORANDI, A., PLAZA-MENACHO, I. & ISACKE, C. M. 2011. RET in breast cancer: functional and therapeutic implications. *Trends in Molecular Medicine,* 17**,** 149-57.

MORRIS, K. V., CHAN, S. W. L., JACOBSEN, S. E. & LOONEY, D. J. 2004. Small Interfering RNA-Induced Transcriptional Gene Silencing in Human Cells. *Science,* 305**,** 1289-92.

MOUSA, S. A., SHAQURA, M., KHALEFA, B. I., ZOLLNER, C., SCHAAD, L., SCHNEIDER, J., SHIPPENBERG, T. S., RICHTER, J. F., HELLWEG, R., SHAKIBAEI, M. & SCHAFER, M. 2013. Rab7 silencing prevents mu-opioid receptor lysosomal targeting and rescues opioid responsiveness to strengthen diabetic neuropathic pain therapy. *Diabetes,* 62**,** 1308-19.

MULLER, P., HRSTKA, R., COOMBER, D., LANE, D. P. & VOJTESEK, B. 2008. Chaperone-dependent stabilization and degradation of p53 mutants. *Oncogene,* 27**,** 3371-83.

MULLER, P., RUCKOVA, E., HALADA, P., COATES, P. J., HRSTKA, R., LANE, D. P. & VOJTESEK, B. 2013. C-terminal phosphorylation of Hsp70 and Hsp90 regulates alternate binding to co-chaperones CHIP and HOP to determine cellular protein folding/degradation balances. *Oncogene,* 32**,** 3101-10.

MULLIGAN, L. M. 2014. RET revisited: expanding the oncogenic portfolio. *Nature Reviews Cancer,* 14**,** 173-86.

MURATA, S., MINAMI, Y., MINAMI, M., CHIBA, T. & TANAKA, K. 2001. CHIP is a chaperone-dependent E3 ligase that ubiquitylates unfolded protein. *EMBO Reports,* 2**,** 1133-38.

MURRAY, C. W., VERDONK, M. L. & REES, D. C. 2012. Experiences in fragment-based drug discovery. *Trends in Pharmacological Sciences,* 33**,** 224-32.

MYERS, S. M., ENG, C., PONDER, B. A. & MULLIGAN, L. M. 1995. Characterization of RET proto-oncogene 3' splicing variants and polyadenylation sites: a novel C-terminus for RET. *Oncogene,* 11**,** 2039-45.

N-FEK, C. 1986. Total colonic aganglionosis (with or without ileal involvement): a review of 27 cases. *Journal of Pediatric Surgery,* 21**,** 251-54.

NAUGHTON, C. K., JAIN, S., STRICKLAND, A. M., GUPTA, A. & MILBRANDT, J. 2006. Glial Cell-Line Derived Neurotrophic Factor-Mediated RET Signaling Regulates Spermatogonial Stem Cell Fate. *Biology of Reproduction,* 74**,** 314-21.

NEILSON, I. R. & YAZBECK, S. 1990. Ultrashort Hirschsprung's disease: myth or reality. *Journal of Pediatric Surgery,* 25**,** 1135-38.

NIESEN, F. H., BERGLUND, H. & VEDADI, M. 2007. The use of differential scanning fluorimetry to detect ligand interactions that promote protein stability. *Nature Protocols,* 2**,** 2212-21.

NILSSON, I. M. & VON HEIJNE, G. 1993. Determination of the distance between the oligosaccharyltransferase active site and the endoplasmic reticulum membrane. *Journal of Biological Chemistry,* 268**,** 5798-801.

NIU, X. L., PETERS, K. G. & KONTOS, C. D. 2002. Deletion of the carboxyl terminus of Tie2 enhances kinase activity, signaling, and function. Evidence for an autoinhibitory mechanism. *Journal of Biological Chemistry,* 277**,** 31768-73.

NOLEN, B., TAYLOR, S. & GHOSH, G. 2004. Regulation of protein kinases: Controlling activity through activation segment conformation. *Molecular Cell,* 15**,** 661-75.

NOZAKI, C., ASAI, N., MURAKAMI, H., IWASHITA, T., IWATA, Y., HORIBE, K., KLEIN, R. D., ROSENTHAL, A. & TAKAHASHI, M. 1998. Calcium-dependent Ret activation by GDNF and neurturin. *Oncogene,* 16**,** 293-99.

OGATA, M., HINO, S., SAITO, A., MORIKAWA, K., KONDO, S., KANEMOTO, S., MURAKAMI, T., TANIGUCHI, M., TANII, I., YOSHINAGA, K., SHIOSAKA, S., HAMMARBACK, J., URANO, F. & IMAIZUMI, K. 2006. Autophagy is activated for cell survival after endoplasmic reticulum stress. *Molecular and Cellular Biol,* 26**,** 9220-31.

OGISO, H., ISHITANI, R., NUREKI, O., FUKAI, S., YAMANAKA, M., KIM, J.-H., SAITO, K., SAKAMOTO, A., INOUE, M., SHIROUZU, M. & YOKOYAMA, S. 2002. Crystal structure of the complex of human epidermal growth factor and receptor extracellular domains. *Cell,* 110**,** 775-87.

OLIVARI, S., GALLI, C., ALANEN, H., RUDDOCK, L. & MOLINARI, M. 2005. A Novel Stress-induced EDEM Variant Regulating Endoplasmic Reticulum-associated Glycoprotein Degradation. *Journal of Biological Chemistry,* 280**,** 2424-28.

OLIVER, J. D., VAN DER WAL, F. J., BULLEID, N. J. & HIGH, S. 1997. Interaction of the Thiol-Dependent Reductase ERp57 with Nascent Glycoproteins. *Science,* 275**,** 86-88.

OLKKOLA, K. T. & AHONEN, J. 2008. Midazolam and other benzodiazepines. *Handbook of Experimental Pharmacology***,** 182, 335-60.

OLZMANN, J. A., KOPITO, R. R. & CHRISTIANSON, J. C. 2013. The Mammalian Endoplasmic Reticulum-Associated Degradation System. *Cold Spring Harbor Perspectives in Biology,* 5, a013185.

OPPENHEIM, R. W., HOUENOU, L. J., PARSADANIAN, A. S., PREVETTE, D., SNIDER, W. D. & SHEN, L. 2000. Glial Cell Line-Derived Neurotrophic Factor and Developing Mammalian Motoneurons: Regulation of Programmed Cell Death Among Motoneuron Subtypes. *The Journal of Neuroscience,* 20**,** 5001-11.

OVERBYE, A., FENGSRUD, M. & SEGLEN, P. O. 2007. Proteomic analysis of membrane-associated proteins from rat liver autophagosomes. *Autophagy,* 3**,** 300-22.

PAN, S., CHENG, X. & SIFERS, R. N. 2013. Golgi-situated endoplasmic reticulum alpha-1, 2-mannosidase contributes to the retrieval of ERAD substrates through a direct interaction with gamma-COP. *Molecular Biology of the Cell,* 24**,** 1111-21.

PANDEY, U. B., NIE Z FAU - BATLEVI, Y., BATLEVI Y FAU - MCCRAY, B. A., MCCRAY BA FAU - RITSON, G. P., RITSON GP FAU - NEDELSKY, N. B., NEDELSKY NB FAU - SCHWARTZ, S. L., SCHWARTZ SL FAU - DIPROSPERO, N. A., DIPROSPERO NA FAU - KNIGHT, M. A., KNIGHT MA FAU - SCHULDINER, O., SCHULDINER O FAU - PADMANABHAN, R., PADMANABHAN R FAU - HILD, M., HILD M FAU - BERRY, D. L., BERRY DL FAU - GARZA, D., GARZA D FAU - HUBBERT, C. C., HUBBERT CC FAU - YAO, T.-P., YAO TP FAU - BAEHRECKE, E. H., BAEHRECKE EH FAU - TAYLOR, J. P. & TAYLOR, J. P. 2007. HDAC6 rescues neurodegeneration and provides an essential link between autophagy and the UPS. *Nature,* 447, 859-63.

PARATCHA, G. & LEDDA, F. 2008. GDNF and GFRalpha: a versatile molecular complex for developing neurons. *Trends in Neuroscience,* 31**,** 384-91.

PARATCHA, G., LEDDA, F. & IBANEZ, C. F. 2003. The Neural Cell Adhesion Molecule NCAM Is an Alternative Signaling Receptor for GDNF Family Ligands. *Cell,* 113, 867-79.

PARKASH, V. & GOLDMAN, A. 2009. Comparison of GFL-GFRalpha complexes: further evidence relating GFL bend angle to RET signalling. *Acta Crystallographica Section F Structural Biology and Crystallization Communications,* 65**,** 551-8.

PARKASH, V., NEN, V.-M. L., VIRTANEN, H., JURVANSUU, J. M., BESPALOV, M. M., SIDOROVA, Y. A., RUNEBERG-ROOS, P., SAARMA, M. & GOLDMAN, A. 2008. The Structure of the Glial Cell Line-derived Neurotrophic Factor-Coreceptor Complex: insights into RET signalling and heparin binding. *The Journal of Biological Chemistry,* 283, 35164-72.

PASCUAL, A., HIDALGO-FIGUEROA, M., PIRUAT, J. I., PINTADO, C. O., GOMEZ-DIAZ, R. & LOPEZ-BARNEO, J. 2008. Absolute requirement of GDNF for adult catecholaminergic neuron survival. *Nature Neuroscience,* 11**,** 755-61.

PEAT, A. J., BOUCHERON, J. A., DICKERSON, S. H., GARRIDO, D., MILLS, W., PECKHAM, J., PREUGSCHAT, F., SMALLEY, T., SCHWEIKER, S. L., WILSON, J. R., WANG, T. Y., ZHOU, H. Q. & THOMSON, S. A. 2004. Novel pyrazolopyrimidine derivatives as GSK-3 inhibitors. *Bioorganic & Medicinal Chemistry Letters,* 14**,** 2121-25.

PELET, A., GENESTE, O., EDERY, P., PASINI, A., CHAPPUIS, S., ATTI, T., MUNNICH, A., LENOIR, G., LYONNET, S. & BILLAUD, M. 1998. Various mechanisms cause RET-mediated signaling defects in Hirschsprung's disease. *The Journal of Clinical Investigation,* 101**,** 1415-23.

PIERSMA, D., BERNS, E. M., VERHOEF-POST, M., UITTERLINDEN, A. G., BRAAKMAN, I., POLS, H. A. & THEMMEN, A. P. 2006. A common polymorphism renders the luteinizing hormone receptor protein more active by improving signal peptide function and predicts adverse outcome in breast cancer patients. *The Journal of Clinical Endocrinology & Metabolism,* 91**,** 1470-76.

PLAZA-MENACHO, I., BARNOUIN, K., GOODMAN, K., MARTINEZ-TORRES, R. J., BORG, A., MURRAY-RUST, J., MOUILLERON, S., KNOWLES, P. & MCDONALD, N. Q. 2014. Oncogenic RET kinase domain mutations perturb the autophosphorylation trajectory by enhancing substrate presentation in trans. *Molecular Cell,* 53**,** 738-51.

PLAZA-MENACHO, I., BURZYNSKI, G. M., DE GROOT, J. W., EGGEN, B. J. & HOFSTRA, R. M. 2006. Current concepts in RET-related genetics, signaling and therapeutics. *Trends in Genetics,* 22**,** 627-36.

PLAZA-MENACHO, I., MOLOGNI, L., SALA, E., GAMBACORTI-PASSERINI, C., MAGEE, A. I., LINKS, T. P., HOFSTRA, R. M., BARFORD, D. & ISACKE, C. M. 2007. Sorafenib functions to potently suppress RET tyrosine kinase activity by

direct enzymatic inhibition and promoting RET lysosomal degradation independent of proteasomal targeting. *Journal of Biological Chemistry,* 282**,** 29230-40.

PLAZA-MENACHO, I., MORANDI, A., ROBERTSON, D., PANCHOLI, S., DRURY, S., DOWSETT, M., MARTIN, L. A. & ISACKE, C. M. 2010. Targeting the receptor tyrosine kinase RET sensitizes breast cancer cells to tamoxifen treatment and reveals a role for RET in endocrine resistance. *Oncogene,* 29**,** 4648-57.

POWELL, H. R. 1999. The Rossmann Fourier autoindexing algorithm in MOSFLM. *Acta Crystallographica D Biological Crystallography,* 55**,** 1690-95.

PRAKASH, C. R. & RAJA, S. 2012. Indolinones as promising scaffold as kinase inhibitors: a review. *Mini Reviews in Medicinal Chemistry,* 12**,** 98-119.

RAJAGOPALAN, S., XU, Y. & BRENNER, M. 1994. Retention of unassembled components of integral membrane proteins by calnexin. *Science,* 263**,** 387-90.

RAVID, T. & HOCHSTRASSER, M. 2008. Diversity of degradation signals in the ubiquitin-proteasome system. *Nature Reviews Molecular Cell Biology,* 9**,** 679-90.

RODRIGUES, N. R., ROWAN, A., SMITH, M. E., KERR, I. B., BODMER, W. F., GANNON, J. V. & LANE, D. P. 1990. p53 mutations in colorectal cancer. *Proceedings of the National Academy of Sciences,* 87**,** 7555-59.

RON, D. & HARDING, H. P. 2012. Protein-Folding Homeostasis in the Endoplasmic Reticulum and Nutritional Regulation. *Cold Spring Harbor Perspectives in Biology,* 4, a013177.

RUBENSTEIN, R. C., EGAN, M. E. & ZEITLIN, P. L. 1997. In vitro pharmacologic restoration of CFTR-mediated chloride transport with sodium 4-phenylbutyrate in cystic fibrosis epithelial cells containing delta F508-CFTR. *The Journal of Clinical Investigation,* 100**,** 2457-65.

RUBENSTEIN, R. C. & ZEITLIN, P. L. 2000. Sodium 4-phenylbutyrate downregulates Hsc70: implications for intracellular trafficking of ΔF508-CFTR. *American Journal of Physiology - Cell Physiology,* 278**,** C259-C267.

RUPP, B. 2010. *Biomolecular Crystallography: Principles, Practice, and Application to Structural Biology*, Garland Science.

RUSSELL, L. C., WHITT, S. R., CHEN, M.-S. & CHINKERS, M. 1999. Identification of Conserved Residues Required for the Binding of a Tetratricopeptide Repeat Domain to Heat Shock Protein 90. *Journal of Biological Chemistry,* 274**,** 20060-63.

SALVATORE, D., BARONE, M. V., SALVATORE, G., MELILLO, R. M., CHIAPPETTA, G., MINEO, A., FENZI, G., VECCHIO, G., FUSCO, A. & SANTORO, M. 2000. Tyrosines 1015 and 1062 are in vivo autophosphorylation sites in ret and ret-derived oncoproteins. *Journal of Clinical Endocrinology & Metabolism,* 85**,** 3898-907.

SALVATORE, G., NAGATA, S., BILLAUD, M., SANTORO, M., VECCHIO, G. & PASTAN, I. 2002. Generation and characterization of novel monoclonal antibodies to the Ret receptor tyrosine kinase. *Biochemical and Biophysical Research Communications,* 294**,** 813-17.

SANTORO, M. & CARLOMAGNO, F. 2013. Central Role of RET in Thyroid Cancer. *Cold Spring Harbor Perspectives in Biology,* 5, a009233.

SANTORO, M., CARLOMAGNO, F., ROMANO, A., BOTTARO, D. P., DATHAN, N. A., GRIECO, M., FUSCO, A., VECCHIO, G., MATOSKOVA, B., KRAUS, M. H. & ET AL. 1995. Activation of RET as a dominant transforming gene by germline mutations of MEN2A and MEN2B. *Science,* 267**,** 381-83.

SANTORO, M., MELILLO, R. M. & FUSCO, A. 2006. RET/PTC activation in papillary thyroid carcinoma: European Journal of Endocrinology Prize Lecture. *European Journal of Endocrinology,* 155**,** 645-53.

SARIOLA, H. & SAARMA, M. 2003. Novel functions and signalling pathways for GDNF. *Journal of Cell Science,* 116**,** 3855-62.

SATO, S., WARD, C. L., KROUSE, M. E., WINE, J. J. & KOPITO, R. R. 1996. Glycerol reverses the misfolding phenotype of the most common cystic fibrosis mutation. *Journal of Biological Chemistry,* 271**,** 635-38.

SCHACHTER, H. & WILLIAMS, D. 1982. Biosynthesis of mucus glycoproteins. *Advances in Experimental Medicine and Biology,* 144**,** 3-28.

SCHALM, S. S., BALLIF, B. A., BUCHANAN, S. M., PHILLIPS, G. R. & MANIATIS, T. 2010. Phosphorylation of protocadherin proteins by the receptor tyrosine kinase Ret. *Proceedings of the National Academy of Sciences,* 107**,** 13894-99.

SCHEFFNER, M., NUBER, U. & HUIBREGTSE, J. M. 1995. Protein ubiquitination involving an E1-E2-E3 enzyme ubiquitin thioester cascade. *Nature,* 373**,** 81-83.

SCHLEE, S., CARMILLO, P. & WHITTY, A. 2006. Quantitative analysis of the activation mechanism of the multicomponent growth-factor receptor Ret. *Nature Chemical Biology,* 2**,** 636-44.

SCHLESSINGER, J., PLOTNIKOV, A. N., IBRAHIMI, O. A., ELISEENKOVA, A. V., YEH, B. K., YAYON, A., LINHARDT, R. J. & MOHAMMADI, M. 2000. Crystal structure of a ternary FGF-FGFR-heparin complex reveals a dual role for heparin in FGFR binding and dimerization. *Molecular Cell,* 6**,** 743-50.

SCHNEIDER, C. A., RASBAND, W. S. & ELICEIRI, K. W. 2012. NIH Image to ImageJ: 25 years of image analysis. *Nature Methods,* 9**,** 671-75.

SCHNEIDER, R. 1992. The human protooncogene ret: a communicative cadherin? *Trends in Biochemical Sciences,* 17**,** 468-69.

SCHUCHARDT, A., D'AGATI, V., LARSSON-BLOMBERG, L., COSTANTINI, F. & PACHNIS, V. 1994. Defects in the kidney and enteric nervous system of mice lacking the tyrosine kinase receptor Ret. *Nature,* 367**,** 380-83.

SCHURINGA, J. J., WOJTACHNIO, K., HAGENS, W., VELLENGA, E., BUYS, C. H., HOFSTRA, R. & KRUIJER, W. 2001. MEN2A-RET-induced cellular transformation by activation of STAT3. *Oncogene,* 20**,** 5350-58.

SCOTT, R. P. & IBANEZ, C. F. 2001. Determinants of ligand binding specificity in the glial cell line-derived neurotrophic factor family receptor alpha S. *Journal of Biological Chemistry,* 276**,** 1450-58.

SHEPHERD, I. T., BEATTIE, C. E. & RAIBLE, D. W. 2001. Functional analysis of zebrafish GDNF. *Developmental Biology,* 231**,** 420-35.

SHEPHERD, I. T., PIETSCH, J., ELWORTHY, S., KELSH, R. N. & RAIBLE, D. W. 2004. Roles for GFRalpha1 receptors in zebrafish enteric nervous system development. *Development,* 131**,** 241-49.

SHIU, S. H. & LI, W. H. 2004. Origins, lineage-specific expansions, and multiple losses of tyrosine kinases in eukaryotes. *Molecular Biology and Evolution,* 21**,** 828-40.

SIN, N., KIM, K. B., ELOFSSON, M., MENG, L., AUTH, H., KWOK, B. H. & CREWS, C. M. 1999. Total synthesis of the potent proteasome inhibitor epoxomicin: a useful tool for understanding proteasome biology. *Bioorganic & Medicinal Chemistry Letters,* 9**,** 2283-88.

SLAYMAKER, I. M., BRACEY, M., MILENI, M., GARFUNKLE, J., CRAVATT, B. F., BOGER, D. L. & STEVENS, R. C. 2008. Correlation of inhibitor effects on enzyme activity and thermal stability for the integral membrane protein fatty acid amide hydrolase. *Bioorganic & Medicinal Chemistry Letters,* 18**,** 5847-50.

SMITH, D. P., HOUGHTON, C. & PONDER, B. A. 1997. Germline mutation of RET codon 883 in two cases of de novo MEN 2B. *Oncogene,* 15**,** 1213-17.

SORKIN, A., KROLENKO, S., KUDRJAVTCEVA, N., LAZEBNIK, J., TESLENKO, L., SODERQUIST, A. M. & NIKOLSKY, N. 1991. Recycling of epidermal growth factor-receptor complexes in A431 cells: identification of dual pathways. *The Journal of Cell Biology,* 112**,** 55-63.

STANLEY, P. 2011. Golgi Glycosylation. *Cold Spring Harbor Perspectives in Biology,* 3, a005199.

STOSCHECK, C. M. & CARPENTER, G. 1984. Characterization of the metabolic turnover of epidermal growth factor receptor protein in A-431 cells. *Journal of Cellular Physiology,* 120**,** 296-302.

STROBER, W. 2001. Trypan blue exclusion test of cell viability. *Current Protocols in Immunology,* Appendix 3**,** Appendix 3B.

SU, C.-H., WANG, C.-Y., LAN, K.-H., LI, C.-P., CHAO, Y., LIN, H.-C., LEE, S.-D. & LEE, W.-P. 2011. Akt phosphorylation at Thr308 and Ser473 is required for CHIP-mediated ubiquitination of the kinase. *Cellular Signalling,* 23**,** 1824-30.

SUZUKI, C. K., BONIFACINO, J. S., LIN, A. Y., DAVIS, M. M. & KLAUSNER, R. D. 1991. Regulating the retention of T-cell receptor alpha chain variants within the

endoplasmic reticulum: Ca(2+)-dependent association with BiP. *Journal of Cell Biology,* 114**,** 189-205.

SZKLARCZYK, D., FRANCESCHINI, A., WYDER, S., FORSLUND, K., HELLER, D., HUERTA-CEPAS, J., SIMONOVIC, M., ROTH, A., SANTOS, A., TSAFOU, K. P., KUHN, M., BORK, P., JENSEN, L. J. & VON MERING, C. 2014. STRING v10: protein–protein interaction networks, integrated over the tree of life. *Nucleic Acids Research,* 43, D447-52.

TAKAHASHI, M., ASAI, N., IWASHITA, T., ISOMURA, T., MIYAZAKI, K. & MATSUYAMA, M. 1993. Characterization of the ret proto-oncogene products expressed in mouse L cells. *Oncogene,* 8**,** 2925-29.

TAKAHASHI, M., BUMA, Y. & TANIGUCHI, M. 1991. Identification of the ret proto-oncogene products in neuroblastoma and leukemia cells. *Oncogene,* 6**,** 297-301.

TAKAHASHI, M. & COOPER, G. M. 1987. ret transforming gene encodes a fusion protein homologous to tyrosine kinases. *Molecular Cell Biology,* 7**,** 1378-85.

TAKEUCHI, K., SODA, M., TOGASHI, Y., SUZUKI, R., SAKATA, S., HATANO, S., ASAKA, R., HAMANAKA, W., NINOMIYA, H., UEHARA, H., LIM CHOI, Y., SATOH, Y., OKUMURA, S., NAKAGAWA, K., MANO, H. & ISHIKAWA, Y. 2012. RET, ROS1 and ALK fusions in lung cancer. *Nature Medicine,* 18**,** 378-81.

TAMURA, T., CORMIER, J. H. & HEBERT, D. N. 2011. Characterization of Early EDEM1 Protein Maturation Events and Their Functional Implications. *Journal of Biological Chemistry,* 286**,** 24906-15.

TEIS, D., SAKSENA, S. & EMR, S. D. 2009. SnapShot: The ESCRT Machinery. *Cell,* 137**,** 182-182.e1.

THORNTON, K., KIM, G., MAHER, V. E., CHATTOPADHYAY, S., TANG, S., MOON, Y. J., SONG, P., MARATHE, A., BALAKRISHNAN, S., ZHU, H., GARNETT, C., LIU, Q., BOOTH, B., GEHRKE, B., DORSAM, R., VERBOIS, L., GHOSH, D., WILSON, W., DUAN, J., SARKER, H., MIKSINSKI, S. P., SKARUPA, L., IBRAHIM, A., JUSTICE, R., MURGO, A. & PAZDUR, R. 2012. Vandetanib for the treatment of symptomatic or progressive medullary thyroid cancer in patients with unresectable locally advanced or metastatic disease: U.S. Food and Drug Administration drug approval summary. *Clinical Cancer Research,* 18**,** 3722-30.

THROWER, J. S., HOFFMAN, L., RECHSTEINER, M. & PICKART, C. M. 2000. Recognition of the polyubiquitin proteolytic signal. *EMBO Journal,* 19**,** 94-102.

TOKUNAGA, F., BROSTROM, C., KOIDE, T. & ARVAN, P. 2000. Endoplasmic Reticulum (ER)-associated Degradation of Misfolded N-Linked Glycoproteins Is Suppressed upon Inhibition of ER Mannosidase I. *The Journal of Biological Chemistry,* 275, 40757-64.

TRAINER, D. L., KLINE, T., MCCABE, F. L., FAUCETTE, L. F., FEILD, J., CHAIKIN, M., ANZANO, M., RIEMAN, D., HOFFSTEIN, S., LI, D. J. & ET AL. 1988.

Biological characterization and oncogene expression in human colorectal carcinoma cell lines. *International Journal of Cancer,* 41**,** 287-96.

TREANOR, J. J. S., GOODMAN, L., SAUVAGE, F. D., STONE, D. M., PULSEN, K. T., BECK, C. D., GRAY, C., ARMANINI, M. P., POLLOCK, R. A., HEFTI, F., PHILLIPS, H. S., GODDARD, A., MOORE, M. W., BUJ-BELLO, A., DAVIES, A. M., ASAI, N., TAKAHASHI, M., VANDLEN, R., HENDERSON, C. E. & ROSENTHAL, A. 1996. Characterization of a multicomponent receptor for GDNF. *Nature,* 382, 80-83.

TRUPP, M., ARENAS, E., FAINZILBER, M., NILSSON, A.-S., SIEBER, B.-A., GRIGORIOU, M., KILKENNY, C., SALAZAR-GRUESO, E., PACHNIS, V., ARUMAE, U., SARIOLA, H., SAARMA, M. & IBANEZ, C. F. 1996. Functional receptor for GDNF encoded by the c-ret proto-oncogene. *Nature,* 381, 785-89.

TRUPP, M., SCOTT, R., WHITTEMORE, S. R. & IBÁÑEZ, C. F. 1999. Ret-dependent and -independent Mechanisms of Glial Cell Line-derived Neurotrophic Factor Signaling in Neuronal Cells. *Journal of Biological Chemistry,* 274**,** 20885-94.

TSUI, C., SHANKLAND, S. & PIERCHALA, B. 2006. Glial cell line-derived neurotrophic factor and its receptor Ret is a novel ligand-receptor complex critical for survival response during podocyte injury. *Journal of the American Society of Nephrology,* 17, 1543-52.

TSUI-PIERCHALA, B. A., MILBRANDT, J. & JOHNSON, E. M., JR. 2002. NGF utilizes c-Ret via a novel GFL-independent, inter-RTK signaling mechanism to maintain the trophic status of mature sympathetic neurons. *Neuron,* 33**,** 261-73.

USHIODA, R., HOSEKI, J., ARAKI, K., JANSEN, G., THOMAS, D. Y. & NAGATA, K. 2008. ERdj5 Is Required as a Disulfide Reductase for Degradation of Misfolded Proteins in the ER. *Science,* 321**,** 569-72.

VAN WEERING, D. H., MOEN, T. C., BRAAKMAN, I., BAAS, P. D. & BOS, J. L. 1998. Expression of the receptor tyrosine kinase Ret on the plasma membrane is dependent on calcium. *Journal of Biological Chemistry,* 273**,** 12077-81.

VEDADI, M., NIESEN, F. H., ALLALI-HASSANI, A., FEDOROV, O. Y., FINERTY, P. J., JR., WASNEY, G. A., YEUNG, R., ARROWSMITH, C., BALL, L. J., BERGLUND, H., HUI, R., MARSDEN, B. D., NORDLUND, P., SUNDSTROM, M., WEIGELT, J. & EDWARDS, A. M. 2006. Chemical screening methods to identify ligands that promote protein stability, protein crystallization, and structure determination. *Proceedings of the National Academy of Sciences,* 103**,** 15835-40.

VON KLEIST, L., STAHLSCHMIDT, W., BULUT, H., GROMOVA, K., PUCHKOV, D., ROBERTSON, M. J., MACGREGOR, K. A., TOMILIN, N., PECHSTEIN, A., CHAU, N., CHIRCOP, M., SAKOFF, J., VON KRIES, J. P., SAENGER, W., KRAUSSLICH, H. G., SHUPLIAKOV, O., ROBINSON, P. J., MCCLUSKEY, A. & HAUCKE, V. 2011. Role of the clathrin terminal domain in regulating coated pit dynamics revealed by small molecule inhibition. *Cell,* 146**,** 471-84.

WALKER, E. H., PACOLD, M. E., PERISIC, O., STEPHENS, L., HAWKINS, P. T., WYMANN, M. P., WILLIAMS, R. L. 2000. Structural determinants of

phosphoinositide 3-kinase inhibition by wortmannin, LY294002, quercetin, myricetin and staurosporine. *Molecule Cell,* 6, 909-19.

WALLIS, A. K. & FREEDMAN, R. B. 2013. Assisting oxidative protein folding: how do protein disulphide-isomerases couple conformational and chemical processes in protein folding? *Topics in Current Chemistry,* 328**,** 1-34.

WANG, N., DANIELS, R. & HEBERT, D. N. 2005. The Cotranslational Maturation of the Type I Membrane Glycoprotein Tyrosinase: The Heat Shock Protein 70 System Hands Off to the Lectin-based Chaperone System. *Molecular Biology of the Cell,* 16**,** 3740-52.

WANG, X., BALOH, R. H., MILBRANDT, J. & GARCIA, K. C. 2006. Structure of Artemin Complexed with Its Receptor GFR[alpha]3: Convergent Recognition of Glial Cell Line-Derived Neurotrophic Factors. *Structure,* 14**,** 1083-92.

WEBB, J. L., RAVIKUMAR B FAU - ATKINS, J., ATKINS J FAU - SKEPPER, J. N., SKEPPER JN FAU - RUBINSZTEIN, D. C. & RUBINSZTEIN, D. C. Alpha-Synuclein is degraded by both autophagy and the proteasome. *Journal of Biological Chemistry,* 278, 25009-13.

WEHRMAN, T., HE, X., RAAB, B., DUKIPATTI, A., BLAU, H. & GARCIA, K. C. 2007. Structural and mechanistic insights into nerve growth factor interactions with the TrkA and p75 receptors. *Neuron,* 53**,** 25-38.

WENG, S. & SPIRO, R. G. 1996. Endoplasmic Reticulum Kifunensine-Resistant α-Mannosidase Is Enzymatically and Immunologically Related to the Cytosolic α-Mannosidase. *Archives of Biochemistry and Biophysics,* 325**,** 113-23.

WHITEHOUSE, F. R. & KERNOHAN, J. W. 1948. Myenteric plexus in congenital megacolon; study of 11 cases. *Archives of Internal Medicine (Chicago),* 82**,** 75-111.

WHITTY, A. & RIERA, T. V. 2008. New ways to target old receptors. *Current Opinion in Chemical Biology,* 12**,** 427-33.

WIESNER, S., WYBENGA-GROOT, L. E., WARNER, N., LIN, H., PAWSON, T., FORMAN-KAY, J. D. & SICHERI, F. 2006. A change in conformational dynamics underlies the activation of Eph receptor tyrosine kinases. *EMBO Journal,* 25**,** 4686-96.

WILD, P., FARHAN, H., MCEWAN, D. G., WAGNER, S., ROGOV, V. V., BRADY, N. R., RICHTER, B., KORAC, J., WAIDMANN, O., CHOUDHARY, C., DÖTSCH, V., BUMANN, D. & DIKIC, I. 2011. Phosphorylation of the Autophagy Receptor Optineurin Restricts Salmonella Growth. *Science,* 333**,** 228-33.

WILHELM, S., CARTER, C., LYNCH, M., LOWINGER, T., DUMAS, J., SMITH, R. A., SCHWARTZ, B., SIMANTOV, R. & KELLEY, S. 2006. Discovery and development of sorafenib: a multikinase inhibitor for treating cancer. *Nature Reviews Drug Discovery,* 5**,** 835-44.

WINTER, G., LOBLEY, C. M. & PRINCE, S. M. 2013. Decision making in xia2. *Acta Crystallographica D Biological Crystallography,* 69**,** 1260-73.

WISEMAN, R. L., POWERS, E. T., BUXBAUM, J. N., KELLY, J. W. & BALCH, W. E. 2007. An Adaptable Standard for Protein Export from the Endoplasmic Reticulum. *Cell,* 131**,** 809-21.

WITTMAN, M., CARBONI, J., ATTAR, R., BALASUBRAMANIAN, B., BALIMANE, P., BRASSIL, P., BEAULIEU, F., CHANG, C., CLARKE, W., DELL, J., EUMMER, J., FRENNESSON, D., GOTTARDIS, M., GREER, A., HANSEL, S., HURLBURT, W., JACOBSON, B., KRISHNANANTHAN, S., LEE, F. Y., LI, A., LIN, T. A., LIU, P., OUELLET, C., SANG, X., SAULNIER, M. G., STOFFAN, K., SUN, Y., VELAPARTHI, U., WONG, H., YANG, Z., ZIMMERMANN, K., ZOECKLER, M. & VYAS, D. 2005. Discovery of a (1H-benzoimidazol-2-yl)-1H-pyridin-2-one (BMS-536924) inhibitor of insulin-like growth factor I receptor kinase with in vivo antitumor activity. *Journal of Medicinal Chemistry,* 48**,** 5639-43.

WONG, E. & CUERVO, A. M. 2010. Integration of Clearance Mechanisms: The Proteasome and Autophagy. *Cold Spring Harbor Perspectives in Biology,* 2, a006734.

WU, H. 2013. Higher-order assemblies in a new paradigm of signal transduction. *Cell,* 153**,** 287-92.

WYBENGA-GROOT, L. E., BASKIN, B., ONG, S. H., TONG, J., PAWSON, T. & SICHERI, F. 2001. Structural basis for autoinhibition of the Ephb2 receptor tyrosine kinase by the unphosphorylated juxtamembrane region. *Cell,* 106**,** 745-57.

XU, Z., KOHLI, E., DEVLIN, K., BOLD, M., NIX, J. & MISRA, S. 2008. Interactions between the quality control ubiquitin ligase CHIP and ubiquitin conjugating enzymes. *BMC Structural Biology,* 8**,** 26.

YANG, S. Y. 2010. Pharmacophore modeling and applications in drug discovery: challenges and recent advances. *Drug Discovery Today,* 15**,** 444-50.

YE, Y., SHIBATA, Y., YUN, C., RON, D. & RAPOPORT, T. A. 2004. A membrane protein complex mediates retro-translocation from the ER lumen into the cytosol. *Nature,* 429**,** 841-47.

YEAMAN, C., GALL, A. H. L., BALDWIN, A. N., MONLAUZEUR, L., BIVIC, A. L. & RODRIGUEZ-BOULAN, E. 1997. The O-glycosylated Stalk Domain Is Required for Apical Sorting of Neurotrophin Receptors in Polarized MDCK Cells. *The Journal of Cell Biology,* 139**,** 929-40.

YIN, L., PULITI, A., BONORA, E., EVANGELISTI, C., CONTI, V., TONG, W. M., MEDARD, J. J., LAVOUE, M. F., FOREY, N., WANG, L. C., MANIE, S., MOREL, G., RACCURT, M., WANG, Z. Q. & ROMEO, G. 2007. C620R mutation of the murine ret proto-oncogene: loss of function effect in homozygotes and possible gain of function effect in heterozygotes. *International Journal of Cancer,* 121**,** 292-300.

YUAN, Z. L., GUAN, Y. J., WANG, L., WEI, W., KANE, A. B. & CHIN, Y. E. 2004. Central role of the threonine residue within the p+1 loop of receptor tyrosine

kinase in STAT3 constitutive phosphorylation in metastatic cancer cells. *Molecular Cell Biology,* 24**,** 9390-400.

YUZAWA, S., OPATOWSKY, Y., ZHANG, Z., MANDIYAN, V., LAX, I. & SCHLESSINGER, J. 2007. Structural basis for activation of the receptor tyrosine kinase KIT by stem cell factor. *Cell,* 130**,** 323-34.

ZAPF-COLBY, A. & OLEFSKY, J. M. 1998. Nerve growth factor processing and trafficking events following TrkA-mediated endocytosis. *Endocrinology,* 139**,** 3232-40.

ZENG, Q., CHENG, Y., ZHU, Q., YU, Z., WU, X., HUANG, K., ZHOU, M., HAN, S. & ZHANG, Q. 2008. The relationship between overexpression of glial cell-derived neurotrophic factor and its RET receptor with progression and prognosis of human pancreatic cancer. *Journal of International Medical Research,* 36**,** 656-64.

ZHANG, X., GUREASKO, J., SHEN, K., COLE, P. A. & KURIYAN, J. 2006. An allosteric mechanism for activation of the kinase domain of epidermal growth factor receptor. *Cell,* 125**,** 1137-49.

ZHAO, F., LIN, Z., WANG, F., ZHAO, W. & DONG, X. 2013. Four-membered heterocycles-containing 4-anilino-quinazoline derivatives as epidermal growth factor receptor (EGFR) kinase inhibitors. *Bioorganic & Medicinal Chemistry Letters,* 23**,** 5385-88.

ZHENG, J., SHEN, W.-H., LU, T.-J., ZHOU, Y., CHEN, Q., WANG, Z., XIANG, T., ZHU, Y.-C., ZHANG, C., DUAN, S. & XIONG, Z.-Q. 2008. Clathrin-dependent Endocytosis Is Required for TrkB-dependent Akt-mediated Neuronal Protection and Dendritic Growth. *Journal of Biological Chemistry,* 283**,** 13280-88.

ZHOU, N., SINGH, K., MIR, M. C., PARKER, Y., LINDNER, D., DREICER, R., ECSEDY, J. A., ZHANG, Z., TEH, B. T., ALMASAN, A. & HANSEL, D. E. 2013. The investigational Aurora kinase A inhibitor MLN8237 induces defects in cell viability and cell-cycle progression in malignant bladder cancer cells in vitro and in vivo. *Clinical Cancer Research,* 19**,** 1717-28.

ZHOU, P., FERNANDES, N., DODGE, I. L., REDDI, A. L., RAO, N., SAFRAN, H., DIPETRILLO, T. A., WAZER, D. E., BAND, V. & BAND, H. 2003. ErbB2 Degradation Mediated by the Co-chaperone Protein CHIP. *Journal of Biological Chemistry,* 278**,** 13829-37.

ZUBER, C., CORMIER, J. H., GUHL, B., SANTIMARIA, R., HEBERT, D. N. & ROTH, J. 2007. EDEM1 reveals a quality control vesicular transport pathway out of the endoplasmic reticulum not involving the COPII exit sites. *Proceedings of the National Academy of Sciences,* 104**,** 4407-12.